11-16-2011 12:00 AM

Convection Due to Spatially Distributed Heating

Mohammad Zakir Hossain
The University of Western Ontario

Supervisor
Dr. J. M. Floryan
The University of Western Ontario

Graduate Program in Mechanical and Materials Engineering
A thesis submitted in partial fulfillment of the requirements for the degree in Doctor of Philosophy

CONVECTION DUE TO SPATIALLY DISTRIBUTED HEATING

(Thesis format: Monograph)

by

MOHAMMAD ZAKIR HOSSAIN

Graduate Program
in
Engineering Science
Department of Mechanical and Materials Engineering

A thesis submitted in partial fulfillment
of the requirements for the degree of
Doctor of Philosophy

The School of Graduate and Postdoctoral Studies
The University of Western Ontario
London, Ontario, Canada

THE UNIVERSITY OF WESTERN ONTARIO
School of Graduate and Postdoctoral Studies

CERTIFICATE OF EXAMINATION

Supervisor

_____
Dr. J. M. Floryan

Supervisory Committee

_____
N/A

_____
N/A

Examiners

_____
Dr. C. Zhang

_____
Dr. K. Siddiqui

_____
Dr. G. Kopp

_____
Dr. A. Guenther

The thesis by

Mohammad Zakir Hossain

entitled:

CONVECTION DUE TO SPATIALLY DISTRIBUTED HEATING

is accepted in partial fulfillment of the
requirements for the degree of
Doctor of Philosophy

_____
Date

_____
Chair of the Thesis Examination Board

Abstract

Convection in an infinite horizontal slot subject to a spatially distributed heating has been investigated for a wide range of Prandtl numbers. The case of the lower wall subject to heating being a sinusoidal function of one of the coordinate is considered in details. The mean temperatures of both walls are set to be equal. The primary response of the system consists of convection in the form of rolls with axis orthogonal to the heating wave vector. When heating wave number α is sufficiently large the convection is found to be limited to a layer adjacent to the lower wall. Under such conditions a uniform conductive layer emerges at the upper section of the slot. Temperature field in this zone becomes independent of the character of the heating and varies in the vertical direction only.

Conditions leading to the emergence of a secondary convection have been identified using the linear stability of the above primary convection. The secondary convection gives rise either to the longitudinal rolls, or to the transverse rolls, or to the oblique rolls, or to the oscillatory mode of instability at the onset depending on the heating wave number. The longitudinal rolls are parallel to the primary rolls and the transverse rolls are orthogonal to the primary rolls, and both of them result in striped patterns. The oblique rolls lead to the formation of convection cells with aspect ratio dictated by their inclination angle. Three mechanisms of instability at the onset have been identified. In the case of small and moderate α the parametric resonance leads to the pattern of instability that is locked-in with the pattern of the heating by a subharmonic relation. The second mechanism is associated with the formation of patterns of vertical temperature gradients and patterns of the primary convection currents, operates approximately in the same range of α as the parametric resonance and provides direct modulation with structure dictated by α. The third mechanism operates in the case of large α where the instability is driven by the uniform mean vertical temperature gradient created by the primary convection and the fluid response becoming similar to that found in the case of a uniformly heated wall. Such rolls exhibit weak preference for the transverse orientation. The first two mechanisms dominate if the spatial modulation of the flow is sufficiently strong while the third one dominates in the case of weak spatial modulation. Competition

between the first and second effects gives rise to commensurable and non-commensurable states in the case of longitudinal rolls and appearance of soliton lattices. Competitions between the second and third mechanisms lead to the formation of very distorted transverse rolls. A rapid stabilization of the oblique rolls is observed when the heating wave number is reduced sufficiently, with the oscillatory mode taking the dominant role. As α becomes very small, secondary motions concentrate around the hot spots; the corresponding bifurcations may have either the supercritical pitchfork form or to the "bifurcation from infinity" form. When an external flow is introduced into the slot, the heating assists in reduction of the overall drag.

It is shown that the heating wave number α plays a role of an effective pattern control parameter and its judicious selection provides means for creation of a wide range of flow responses.

Keywords: Rayleigh-Benard convection, periodic heating, pattern control, linear stability analysis, Chebyshev collocation method, Fourier expansion.

Dedication

To my sisters Parvin and Zui.
(*we still remember you*).

Acknowledgments

I would like to express my deep gratitude to Professor J.M. Floryan for his careful supervision, constant inspiration, unceasing encouragement, invaluable suggestions and constructive criticism throughout the tenure of my doctoral research. The completion of this dissertation would not have been possible without his incomparable assistance and invaluable guidance.

I would like to thank the members of my advisory committee, Prof. A. G. Straatman and Prof. C. Zhang, for their valuable suggestions and encouragement. I would like to extend my sincerest thanks to Dr. P. Luchini for the helpful discussions with him during the development of the numerical algorithm. I am also indebted to my colleagues (past and present), Dr. S. Krol, Dr. Y. Jiang, Dr. S. Z. Husain, M. Fotia, A. Keikhaee, D. C. Del Rey Fernandez, G. Kalugin, A. Mohammadi, M. F. Bakhsheshi, H. V. Moradi, and A. Asgarian for their companionship, cooperation and insightful scientific discussions. Special thanks to A. Asgarian and D. Floryan for assisting me in some of the computations.

Last but not the least; I would like to convey my gratitude to my family, especially to my parents, to my wife R. Naznin, and to my son Zaeem, for their immense sacrifice, encouragement, tremendous patience and understanding.

This work has been carried out with support from SHARCNET and NSERC of Canada. SHARCNET of Canada provided the computing resources.

Table of Contents

List of Tables

List of Figures

List of Appendices

List of Symbols and Abbreviations

Symbols

A_p	Pressure modification gradient induced by heating
c	Specific heat per unit mass
D	d/dy
E	Quantity used for the definition of the edge of convection layer
Err	Error
F_p	Pressure force
F_s	Shear force
g	Acceleration due to gravity
h	Half-height of the slot
H	Total height of the slot
h_v	Thickness of convection layer
k_d	Thermal conductivity of the fluid
m	Fourier mode
n	Fourier mode
N_δ	Number of disturbance wavelength
N_α	Number of wavelength of primary convection
N_M	Number of Fourier modes
N_p	Number of points for “padding”
N_T	Number of Chebyshev collocation points
Nu	Nusselt number
Nu_L	Local Nusselt number
Nu_T	Special form of Nusselt number (used in Chapter 8)
Pr	Prandtl number
P_v	Dynamic pressure scale
q	Disturbance wave vector
Q	Second invariant of the velocity gradient tensor (except in chapter 9)

Q	Mass flow rate (in chapter 9)
Ra	Rayleigh number
Re	Reynolds number
S	Disturbance streamfunction at y=0
T	Temperature (dimensional)
T_d	Conductive temperature scale
T_{ref}	Reference temperature (dimensional)
T_v	Convective temperature scale
u	x-component of velocity (non-dimensional)
U_p	Velocity scale for the reference flow
U_v	Convective velocity scale
v	y-component of velocity (non-dimensional)
w	z-component of velocity (non-dimensional)
y_c	Center of the roll for primary convection

Greek symbols

α	Heating wave number
β	z-wave number of disturbances
	transverse roll wave number (in Chapter 5)
δ	x-wave number of disturbances
	longitudinal roll wave number (in Chapter 4)
ϕ	Temperature in Fourier space
η	Roll inclination angle
φ	Streamfunction in Fourier space
κ	Thermal diffusivity
λ	Wave length
μ	Dynamic viscosity
ν	Kinematic viscosity
θ	Temperature (dimensional less)
ρ	Density

σ	Eigenvalue
ω	Vorticity
ψ	Stream function
Γ	Thermal expansion coefficient
Φ	Computed quantity
ψ_{max}	Roll strength for primary convection
γ	Slope angle of lines in figures.
σ_r	Frequency of disturbances
σ_i	Growth rare of disturbances
τ	Shear stress
ϑ	Percentage drag reduction

Subscripts

1	Flow modification due to heating (except in section 2.4.2)
2	Total quantity for primary convection (except in section 2.4.2)
3	Quantity for disturbance filed
asym	Asymptotic solution
b	Lower bound
c	Critical
cr	Critical
d	Conduction
i	Imaginary
L	Lower wall
lb	Lower bound (in Chapter 4)
lc	Lock-in
m	Modulation
max	Maximum
min	Minimum
num	Numerical solution
nun	Non-uniform heating

r	Real
ref	Reference
rel	Relative
U	Upper wall
uni	Uniform
v	Convection

Superscript

(n)	Fourier mode
(m)	Fourier mode

Abbreviation

c.c.	Complex conjugate
DNA	Deoxyribonucleic acid
Eq.	Equation (used in Figure caption)
FFT	Fast Fourier Transform
Fig.	Figure (used in Figure caption)
PCR	Polymerase chain reaction
RB	Rayleigh-Benard
RF	Relaxation Factor
RHS	Right Hand Side
TOL	Tolerance

1

Introduction

1.1 Objectives

The main objective of this dissertation is to unveil the flow physics and to develop control strategies associated with convection driven by spatially distributed heating.

1.2 General introduction

Thermal convection represents one of the most common forms of fluid flow in the Universe. It has a wide range of applications, e.g., industrial appliances, crystallization processes, liquid metals, weather prediction, motion of oceans, dynamics of the interiors of planets and stars, evolution of galaxies, etc (Pal et al. 2009). Convection in a layer of fluid heated uniformly from below represents an idealized version of thermal convection, is called Rayleigh-Benard (RB) convection and has been studied for almost a century. Convective motion occurs when the so-called Rayleigh number Ra exceeds critical conditions. This motion is rotationally invariant in the plane of the layer, has form of rolls (striped pattern) and is characterized by a linear neutral stability curve with a well defined minimum which identifies the critical Rayleigh number Ra_c and the critical wave vector $\mathbf{q}_c$. Various researchers considered different configuration of RB convection and various forms of the motion, i.e., patterns, have been observed, see Bodenschatz et al. (2000) for a recent review.

1.3 Motivation

Understanding of motions of fluids over geometrically, chemically and thermally patterned surfaces is of vital interest in designing microfluidic components and devices for biological applications such as cell analyzers. Of particular importance is how convective motions develop and, in the case of droplets, how they move along regularly structured surfaces (Beltrame et al. 2011). The same issues are relevant in the development of hydrophilic surfaces. Beltrame et al. (2011) found seven distinct transition regimes for the interface depinning; this diversity shows that in addition to requiring a clear understanding of the different kinds of surface heterogeneities that may cause the pinning, the complex coupling between pinning force and surface of the fluid needs to be taken into account.

Patterned heating of surfaces offers potential to produce structured convection that provides alternative to geometric patterning. The RB convection represents a system with finite wave number instabilities. When subject to a spatially-distributed one-dimensional forcing, such system may exhibit wave number locking and responses that extend into two-spatial dimensions allowing for a wide resonance range even in the case of weak forcing (Manor et al. 2008, 2009). The understanding of such systems is still incomplete. Patterned heating leads to instability and drop formation in liquid microjets (Furlani and Hanchak 2010) by inducing a spatial variation of surface tension along the length of the jet to cause deformation of the jet (slight necking in the warmer regions and ballooning in the cooler region). The size of drops can be controlled by adjusting the heating. Such jets are used recently in integrated microfluidic inkjet devices.

1.4 Related literature survey

The existing literature on the RB convection can be categorized into two generic groups. In the first one, the bottom wall is kept under a uniform heating and in the second one various temperature modulations may occur. Few analyses focused on RB convection with modulations are available. Such modulations have been done either by (i) changing the geometry of the flow domain, or (ii) using time dependent temperature, or (iii)

applying spatial variation of temperature. Usually small amplitude modulations had been considered and the analyses had been carried out from the point of view of identification of tools for control/alteration of the pattern selection process of the reference RB convection. Pattern selection of systems affected by time-dependent forcing are considered to be well understood (Arnold 1983). In the forthcoming section we shall review the relevant literature according to the modulation techniques.

1.4.1 Modulation using geometry

We shall begin the review with the modulations created by geometrical effects. Results dealing with the RB convection modified by spatially modulated geometry are very limited.

McCoy et al. (2008) experimented with spatial modulation created by very thin stripes glued on the lower surface (using SF_6 (Pr = 0.9) as the working fluid). The periodic constraints was characterized by the wave number q_m and was applied along a selected direction, where q_m varied in a small interval around $|\mathbf{q}_c|$. Two-dimensional roll patterns with the wave vector $\mathbf{q_m}$ were observed for $Ra<<Ra_c$. Amplitude of these rolls grew with Ra until they were destabilized with various mechanisms which depended on the ratio of the wave number q_m of the imposed modulation and the critical wave number q_c of the RB convection. The wave vectors of the destabilizing modes typically formed a nonzero angle with the modulation wave vector $\mathbf{q_m}$ resulting in the formation of oblique modes producing a variety of three-dimensional patterns.

Seiden et al. (2008) studied (experimentally) the combined effect of the intrinsic symmetry breaking due to a gravity-induced shear flow and spatially one-dimensional forcing associated with surface strips attached to the bottom plate using CO_2 as the working fluid. They considered two type of forcing: (i) parallel forcing where surface corrugation is aligned parallel to the gravity component, (ii) orthogonal forcing where the corrugation is orthogonal. Depending on the inclination angle, they observed longitudinal rolls (LR), varicose pattern (VP), subharmonic resonances (SR), periodically spaced kink

lines (KL), undulations (UN) and transverse bursts (TB) for parallel forcing, and transverse rolls (TR), rhombic pattern (RO), hexarolls (HR), bimodals (BM), scepter-shaped patterns (SP), and heart-shaped patterns (HP) for orthogonal forcing.

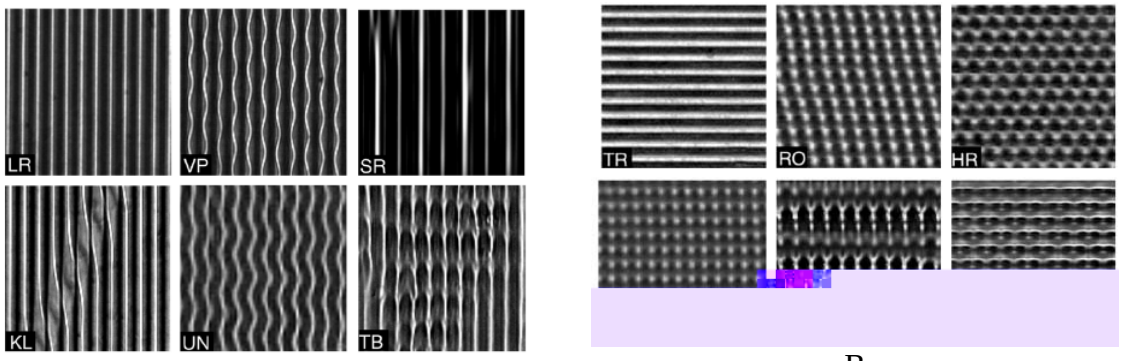

A B

Figure 1.1. *Patterns observed experimentally by Seiden et al. (2008): (A) by parallel forcing, (B) by orthogonal forcing. The patterns, starting from the top-left most of Fig.1.1A, are longitudinal rolls (LR), varicose pattern (VP), subharmonic resonances (SR), periodically spaced kink lines (KL), undulations (UN) and transverse bursts (TB); transverse rolls (TR), rhombic pattern (RO), hexarolls (HR), bimodals (BM), scepter-shaped patterns (SP), and heart-shaped patterns (HP), respectively.*

1.4.2 Time dependent modulation

Effects of time dependent modulations were studied by Or and Kelly (1999) who considered temperature of either one or both walls to vary periodically in time about the reference temperature. They considered fluids with Pr varying between 0.1 and 10. They investigated both the anti-symmetric and symmetric boundary temperatures. For symmetric modulations, they obtained alternating sequence of synchronous and sub-harmonic instabilities at low frequency modulations, but found only sub-harmonic instabilities at high frequency. In the case of anti-symmetric modulation they observed two localized disturbances, each of which was associated with a Stokes layer at the wall.

Or (2001) determined analytically the onset condition for very low modulation frequency. Liu (2004) investigated this type of modulation for a second-grade fluid. Pesch et al. (2008) studied convection in a fluid layer which was periodically accelerated in its plane.

They found that shaking in a fixed direction broke the original isotropy of the layer. At the onset of the convection and at small accelerations, they found longitudinal rolls whose axes were aligned parallel to the acceleration direction. With increasing acceleration amplitude, a shear instability took over and transverse rolls with their axes perpendicular to the shaking direction nucleated at the onset. In the case of circular shaking, the system was found to be isotropic in the time average sense and with broken chiral symmetry. The onset of convection corresponded to the transverse rolls with the rolls' axis selected spontaneously. Their study had been carried out using fluids with Pr = 0.5, 1, 2, and 6. Singh and Bajaj (2009) performed linear stability analysis of thermomagnetic convection in a ferrofluid layer subjected to time periodic modulation of temperature along the horizontal plates in the presence of an external vertical magnetic field.

1.4.3 Spatial temperature modulation

The effects of spatial variations of temperature were studied by Kelly and Pal (1978) who investigated thermal convection in a fluid contained between two rigid walls with different mean temperatures with either prescribed spatially periodic temperatures at the walls or with surface corrugations at the walls and focused on fluids with Pr = 0.025, 0.027, 0.71 and 7. The amplitudes of the spatial non-uniformities were assumed to be small and the wavelength was set to be equal to the critical wavelength for the onset of RB convection. They defined Rayleigh number based on the mean temperature difference between the two walls. When values of the Rayleigh number were close to the critical value, the effects of the non-uniformities were greatly amplified and the amplitude of convection was governed by a cubic equation. This equation yielded three supercritical states, but only the state linked to a subcritical state was found to be stable.

Killworth and Manins (1980) analyzed convection in a fluid with Pr > 1 contained in a rectangular two-dimensional box resulting from the application of a quadratic temperature variation along its lower surface. The other walls were insulated. They obtained similarity solutions for the boundary layers and a separate solution for the interior of the box. The buoyancy in the interior and the gross Nusselt number were found to be

independent of the Prandtl number but functions of the Rayleigh number (based on the horizontal length scale). The magnitude of the interior stream function was found to vary roughly proportionally to the square root of the Prandtl number in the laminar case, and to be insensitive to it in the turbulent case. In either case, magnitudes of the stream function within the thermal boundary layer were quite insensitive to changes of the Prandtl number.

Hignett et al. (1981) performed an experimental study of convection in a rotating annulus by maintaining a radial temperature gradient along the lower horizontal boundary. The vertical side walls and the upper horizontal boundary were insulated. They used water (Pr =7) and paraffin (Pr = 16.5) as the working fluids and obtained six different flow regimes parameterized by the square of the ratio of the non-rotating thermal (or buoyancy) depth scale and the Ekman-layer scale. For small values of this parameter the flow was only weakly modified by rotation but as the value of this parameter increased above unity rotation tended to thicken the thermal layer. Existence of a baroclinic wave regime was observed when the magnitude of the controlling parameter increased above a certain critical value.

Walton (1982) investigated the onset of thermal convection when the lower wall was exposed to either one ‘hot-spot’ or a periodic array of ‘hot-spots’. It was found that disturbances had the form of rolls that were largely confined to the neighborhood of the ‘hot-spots’. Mancho et al. (1997) studied convection in a container with the upper surface open to the air and heated from below using a Gaussian-like temperature distribution. They considered both buoyancy and thermo-capillarity effects and used silicon oil with Pr = 40.32 as the working fluid. A pair of rolls with the upward motion taking place above the heater and the downward motion occurring near the sidewalls was observed. An instability forming stationary rolls perpendicular to the primary ones was observed when the temperature difference at the origin increased.

To understand the ocean circulation and thermohaline overturning of the oceans Rossby (1998) carried out numerical experiments on convection in a insulated square container

whose bottom wall was exposed either to linear or to non-linear temperature distributions and contained fluids with Pr = 1-100. Mullarney et al. (2004) performed both laboratory and numerical experiments with the convective circulation that develops in a long channel driven by heating and cooling through opposite halves of the horizontal base. They considered channel with small aspect ratio, larger Rayleigh numbers and an imposed heat flux. The flow was characterized by a vigorous overturning circulation cell filling the box. A stable thermocline formed above the cooled base and was advected over the heated part of the base, where it was eroded from below by small-scale three-dimensional convection forming a 'convective mixed layer'. Wang and Huang (2005) studied experimentally circulation driven by horizontal differential heating in a tank filled with salt water. They maintained linear temperature profile either along the lower or the upper boundary. Stable thermal circulation in the form of a shallow cell adjacent to the boundary where thermal forcing was applied had been observed. Natarajan et al. (2008) performed a parametric study using computer simulations of natural convection inside a trapezoidal cavity with the bottom wall either uniformly and non-uniformly heated while the two vertical walls were maintained at constant temperatures and the top wall was insulated. They considered Rayleigh number O(100) and Pr = 0.07-100. The non-uniform heating of the bottom wall was found to produce greater heat transfer at the center of the bottom wall as compared to the uniform heating for all Rayleigh numbers but the average Nusselt number showed the overall heat transfer rate to be lower for the non-uniform heating case. The effect of variations of Prandtl number on the local and average Nusselt numbers was found to be more significant for Prandtl numbers in the range 0.07–0.7 than 10–100. Lyubimova et al. (2009) investigated steady convective flow in a horizontal channel of rectangular cross-section subjected to a uniform longitudinal temperature gradient imposed along the walls. They found that zero Prandtl number solution corresponded to a plane-parallel flow along the channel axis. In this case, the fluid moves in the direction of the imposed temperature gradient in the upper part of the channel and in the opposite direction in the lower part. At non-zero values of the Prandtl number, such solution does not exist. At low values of the Prandtl number the basic state loses its stability due to a steady hydrodynamic mode related to the formation of vortices at the interface between the both flows. The increase of the Prandtl number results in the strong

stabilization of this instability mode and, beyond a certain value of the Prandtl number depending on the cross-section aspect ratio, a new steady hydrodynamic instability mode became most unstable. This mode was characterized by concentration of perturbations near the sidewalls. At higher values of the Prandtl number, the spiral perturbations (rolls with axis parallel to the temperature gradient) became most unstable, at first the oscillatory spiral perturbations and then the Rayleigh type steady spiral perturbations.

Most recently effects of spatial temperature modulations have been studied by Freund et al. (2011) who considered temperature of the lower wall subject to a small-amplitude sinusoidal variations about a mean average. The system response consisted of a weak primary convection induced by the temperature modulations and instabilities driven by the mean temperature gradient. A competition between the pattern induced by the modulation and the preferred wave number q_c of the RB convection developed. When $q_m \approx q_c$, the RB pattern locked in with the modulation and the rolls remained stable for fairly large $Ra > Ra_c$ with the stable zone similar to the Busse balloon. For q_m slightly less than q_c the secondary motion developed in the form of cross-roll and oscillatory instabilities (Clever and Busse 1974). For q_m slightly larger than q_c skewed-varicose instability appeared but the Eckhaus and zig-zag instabilities were suppressed by the modulation. Several modes of instability directly associated with the modulation were identified for q_m away from q_c and with $Ra \approx Ra_c$. For q_m less than $0.8q_c$, the instability involved two oblique rolls; this response was originally described by Vozovoi and Nepomnyashchy (1974) and Pal and Kelly (1979). The same response was found for $1.2\ q_c < q_m < 2q_c$. Longitudinal rolls became dominant for $\sim 2q_c < q_m < \sim 2.08q_c$ and were replaced by transverse rolls for a still larger q_m. Direct numerical simulations identified several patterns of saturation states and transitions between them as a function of Ra.

1.5 Overview of the present work

The present analysis is focused on a form of convection that has yet to be studied. The lower wall is subject to a heating distributed in a selected direction with the mean temperatures of both walls being kept equal. The heating represents a simple form of one-

dimensional periodic forcing which is responsible for the system dynamics and the pattern selection. In the simplest case of sinusoidal heating the forcing is characterized by a wave number and an amplitude, resulting in a two-parameter problem. There is no reference wave number as in the case of the modulated RB convection. The wave vector of the primary convection is imposed by the external heating. A secondary convection may be generated through an instability process. Determination of conditions leading to its onset as well as determination of the pattern of this convection and its relation to the pattern of the heating are of interest. The convective system being considered can be viewed as an example of a more general dynamical system solely driven by a periodic forcing and thus the results being presented may be of a wider interest.

1.6 Outline of the dissertation

The dissertation is organized as follows. Chapter 2 provides description of the primary convection resulting from the imposition of the heating. First the primary convection problem is formulated, and then various flow characteristics of the primary convection are discussed. Chapter 3 is devoted to the formulation of the linear stability problems and description of solution methodology that permits identification of conditions leading to the onset of the secondary convection. Different forms of instability at the onset are discussed in Chapters 4, 5, 6, and 7. In particular, longitudinal rolls are discussed in Chapter 4, transverse rolls are discussed in Chapter 5, oblique rolls are discussed in Chapter 6, and oscillatory mode of instability is discussed in Chapter 7. Flow bifurcations occurring at long wavelength heating are described in Chapter 8. Finally, changes of the system response associated with presence of an external flow are elucidated in Chapter 9. A short summary of the main conclusions, suggested applications of the results and recommendations for the future work are presented in Chapter 10.

2

Primary Convection

This chapter deals with the convection due to the presence of the distributed heating. We refer to such convection as the 'primary convection'. In Section 2.1 we discuss about the steady convection problem description, Section 2.2 is devoted to devise the governing equations, method of solution is described in Section 2.3, and the characters of the flow and temperature fields are elucidated in Section 2.4. A short summary of the main conclusions is presented in Section 2.5.

2.1 Steady convection

Consider steady motion of fluid contained in a slot between two plane parallel plates extending to $\pm\infty$ in the x-direction and placed at a distance 2h apart from each other with the gravitational acceleration g acting in the negative y-direction, as shown in **Figure 2.1**. Motion of the fluid is driven by buoyancy forces resulting in the formation of convective rolls. The fluid is incompressible, Newtonian, with thermal conductivity k_d, specific heat c, thermal diffusivity $\kappa = k_d/\rho c$, kinematic viscosity ν, dynamic viscosity μ, thermal expansion coefficient Γ and variations of the density ρ follow the Boussinesq approximation. All material properties need to be evaluated at the reference temperature defined below. The plates are subject to a distributed heating with temperatures of the lower (θ_L) and upper (θ_U) plates described by the following relations

$$\theta_L(x) = \sum_{n=-\infty}^{n=+\infty} \theta_L^{(n)} e^{in\alpha x}\ ,\ \theta_U(x) = \sum_{n=-\infty}^{n=+\infty} \theta_U^{(n)} e^{in\alpha x}\ , \tag{2.1}$$

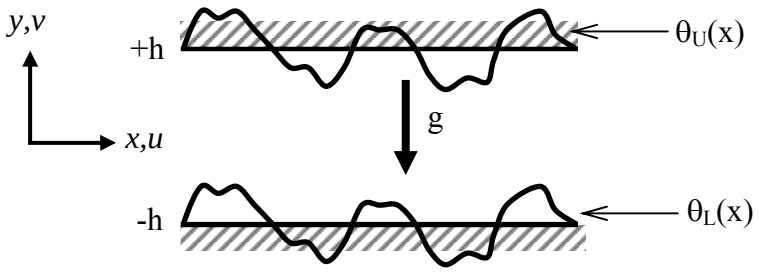

Figure 2.1. *Parallel plates subject to spatially distributed heating.*

where α stands for the wave number of the heating, θ denotes the relative temperature, i.e., $\theta=T-T_{ref}$, T denotes the temperature and T_{ref} denotes the reference temperature. The reality condition has the form $\theta^{(n)} = \theta^{(-n)^*}$ where star denote complex conjugates. The wavelength of the heating is denoted as $\lambda = 2\pi/\alpha$. It is assumed that the mean temperatures of the both plates are equal, i.e., $\theta_U^{(0)} = \theta_L^{(0)} = 0$ and this defines the reference temperature.

2.2 Problem formulation

The temperature field is represented as a sum of the conductive field θ_0 and deviations θ_1 associated with the convective effects. We introduce two temperature scales, i.e., we use the amplitude of the temperature variations along the plates as the conductive temperature scale T_d and $T_v = T_d\nu/\kappa$ as the convective temperature scale, where $T_v/T_d=Pr$, with $Pr=\nu/\kappa$ denoting the Prandtl number. We select half distance h between the plates as the length scale, $U_v = \nu/h$ as the (convective) velocity scale and $P_v = \rho U_v^2$ as the (dynamic) pressure scale.

The complete dimensionless temperature is scaled using the convective scale, i.e.,

$$\theta(x,y) = Pr^{-1}\,\theta_0(x,y) + \theta_1(x,y) \tag{2.2}$$

where the conductive temperature θ_0 is a solution of the following problem

$$\frac{\partial^2\theta_0}{\partial x^2}+\frac{\partial^2\theta_0}{\partial y^2}=0\,,\quad \theta_0(x,-1)=\sum_{n=-\infty}^{n=+\infty}\theta_L^{(n)}e^{in\alpha x}\,,\qquad \theta_0(x,1)=\sum_{n=-\infty}^{n=+\infty}\theta_U^{(n)}e^{in\alpha x} \tag{2.3}$$

and has the form

$$\begin{aligned}\theta_0(x,y)&=\sum_{n=-\infty}^{n=+\infty}\theta_0^{(n)}(y)\,e^{in\alpha x}\\&=\sum_{n=-\infty}^{n=+\infty}\left[\left(\theta_U^{(n)}-\theta_L^{(n)}\right)\frac{\sinh(n\alpha y)}{2\sinh(n\alpha)}+\left(\theta_U^{(n)}+\theta_L^{(n)}\right)\frac{\cosh(n\alpha y)}{2\cosh(n\alpha)}\right]e^{in\alpha x}\end{aligned} \tag{2.4}$$

with $\theta_0^{(0)}(y)=0$.

The dimensionless field equations describing motion of the fluid and the resulting changes in the temperature field have the form

$$u\frac{\partial u}{\partial x}+v\frac{\partial u}{\partial y}=-\frac{\partial p}{\partial x}+\nabla^2 u\,, \tag{2.5a}$$

$$u\frac{\partial v}{\partial x}+v\frac{\partial v}{\partial y}=-\frac{\partial p}{\partial y}+\nabla^2 v+Ra\,\theta_1+Ra\,Pr^{-1}\,\theta_0\,, \tag{2.5b}$$

$$Pr\left(u\frac{\partial\theta_1}{\partial x}+v\frac{\partial\theta_1}{\partial y}\right)+u\frac{\partial\theta_0}{\partial x}+v\frac{\partial\theta_0}{\partial y}=\nabla^2\theta_1\,, \tag{2.5c}$$

$$\frac{\partial u}{\partial x}+\frac{\partial v}{\partial y}=0\,, \tag{2.5d}$$

where **v** = (u,v) denotes the velocity vector, p stands for the pressure, $Ra = g\Gamma h^3 T_d/\nu\kappa$ is the Rayleigh number, ∇^2 denotes the Laplace operator and dissipation effects have been neglected in the energy equation. The boundary conditions take the form

$$u(\pm1)=0,\quad v(\pm1)=0,\quad \theta_1(\pm1)=0\,. \tag{2.6}$$

The reader may note that the above problem represents a forced response problem as the motion occurs regardless of the amplitude of heating, i.e., one does not need to meet any critical heating conditions as in the case of the classical problem of plates subject to a uniform heating.

2.3 Method of solution

We shall use combination of three techniques in order to determine system response.

2.3.1 Method 1: Finite difference-complex notation

We define the stream function $\psi(x,y)$ in the usual manner, i.e., $u = \partial\psi / \partial y$, $v = -\partial\psi / \partial x$, and eliminate pressure from the momentum equations resulting in the following form of the governing equations

$$\frac{\partial\psi}{\partial y}\frac{\partial}{\partial x}\left(\nabla^2\psi\right) - \frac{\partial\psi}{\partial x}\frac{\partial}{\partial y}\left(\nabla^2\psi\right) = \nabla^4\psi - \mathrm{Ra}\frac{\partial\theta_1}{\partial x} - \mathrm{Ra}\,\mathrm{Pr}^{-1}\frac{\partial\theta_0}{\partial x}, \tag{2.7a}$$

$$\mathrm{Pr}\left(\frac{\partial\psi}{\partial y}\frac{\partial\theta_1}{\partial x} - \frac{\partial\psi}{\partial x}\frac{\partial\theta_1}{\partial y}\right) + \frac{\partial\psi}{\partial y}\frac{\partial\theta_0}{\partial x} - \frac{\partial\psi}{\partial x}\frac{\partial\theta_0}{\partial y} = \nabla^2\theta_1. \tag{2.7b}$$

The solution is assumed to be in the form of Fourier expansions, i.e.,

$$\psi = \sum_{n=-\infty}^{n=+\infty}\varphi^{(n)}(y)e^{in\alpha x}, \quad \theta_1 = \sum_{n=-\infty}^{n=+\infty}\phi^{(n)}(y)e^{in\alpha x}. \tag{2.8}$$

Substitution of (2.8) into (2.7) and separation of Fourier components result in the following system of ordinary differential equations

$$D_n^2\varphi^{(n)} - in\alpha Ra\phi^{(n)} - i\alpha\sum_{m=-\infty}^{m=+\infty}\left[mD\varphi^{(n-m)}D_m\varphi^{(m)} - (n-m)\varphi^{(n-m)}D_m\left(D\varphi^{(m)}\right)\right] = in\alpha Ra\,Pr^{-1}\theta_0^{(n)}\,, \tag{2.9a}$$

$$D_n\phi^{(n)} - i\alpha\sum_{m=-\infty}^{m=+\infty}\left[Pr\left(m\phi^{(m)}D\varphi^{(n-m)} - (n-m)\varphi^{(n-m)}D\phi^{(m)}\right) + \left(m\theta_0^{(m)}D\varphi^{(n-m)} - (n-m)\varphi^{(n-m)}D\theta_0^{(m)}\right)\right] = 0. \tag{2.9b}$$

where $-\infty<n<+\infty$, $D=d/dy$ and $D_n=D^2-n^2\alpha^2$. The required boundary conditions have the form

$$\varphi^{(n)}(\pm1)=0, \quad D\varphi^{(n)}(\pm1)=0, \quad \phi^{(n)}(\pm1)=0\,, \quad \text{for } -\infty<n<+\infty\,. \tag{2.10a-c}$$

The system (2.9) together with the boundary conditions (2.10) needs to be solved numerically. The solution method uses variable-step-size, finite-difference discretization based on the Simpson method with deferred corrections (Kierzenka and Shampine, 2001, 2008) with the resulting algebraic system being solved using a simplified Newton (chord) method with residual control. The value of the residual set at 10^{-6} was found to be sufficient in most of the computations (see Appendix E for discussion of numerical accuracy). The selection of the number and distribution of grid points is done automatically so that the specified error bounds are met. The number of Fourier modes used in the solution was selected through numerical experiments so that the flow quantities of interest were determined with at least six digits accuracy.

2.3.2 Method 2: Finite difference-real notation

Technique presented in this section is more efficient as it deals with real numbers and is specialized to sinusoidal temperature distributions only. The solution is assumed to be in the form of Fourier expansions defined as

$$\psi = \sum_{n=0}^{n=+\infty} \varphi^{(n)}(y)\sin(n\alpha x),\ \theta_1 = \sum_{n=0}^{n=+\infty} \phi^{(n)}(y)\cos(n\alpha x). \tag{2.11}$$

Substitution of (2.11) into (2.7) and separation of Fourier components result in the following system of ordinary differential equations

$$\begin{aligned} 2D_n^2\varphi^{(n)} + 2n\alpha Ra\phi^{(n)} - \alpha \sum_{m=0}^{m=+\infty} \Big\{ &\left[mD\varphi^{(n-m)} D_m\varphi^{(m)} - (n-m)\varphi^{(n-m)} D_m\left(D\varphi^{(m)}\right)\right] \\ &+ \left[mD\varphi^{(m-n)} D_m\varphi^{(m)} + (m-n)\varphi^{(m-n)} D_m\left(D\varphi^{(m)}\right)\right] \\ &- \left[mD\varphi^{(n+m)} D_m\varphi^{(m)} + (n+m)\varphi^{(n+m)} D_m\left(D\varphi^{(m)}\right)\right]\Big\} = -2n\alpha Ra\,\mathrm{Pr}^{-1}\,\theta_0^{(n)}, \end{aligned} \tag{2.12a}$$

$$\begin{aligned} 2D_n\phi^{(n)} + \alpha \sum_{m=0}^{m=+\infty} \Big\{ &\left(D\varphi^{(m-n)} + D\varphi^{(m+n)} - D\varphi^{(n-m)}\right)\left(\theta_0^{(m)} + \mathrm{Pr}\,\phi^{(m)}\right) \\ &+ \left[(m-n)\varphi^{(m-n)} + (m+n)\varphi^{(m+n)} + (n-m)\varphi^{(n-m)}\right]\left(D\theta_0^{(m)} + \mathrm{Pr}\,D\phi^{(m)}\right)\Big\} = 0 \end{aligned} \tag{2.12b}$$

where $0<n<+\infty$, $D=d/dy$ and $D_n=D^2-n^2\alpha^2$. The required boundary conditions have the form

$$\varphi^{(n)}(\pm1)=0, \quad D\varphi^{(n)}(\pm1)=0, \quad \phi^{(n)}(\pm1)=0, \quad \text{for } 0<n<+\infty. \tag{2.13a-c}$$

Here the reader may note that Eq. (2.12b) is valid for $n>0$. The Eq. (2.12b) takes the following form for $n=0$,

$$2D_0\phi^{(0)} + m\alpha \sum_{m=0}^{m=+\infty} \left\{ D\varphi^{(m)}\left(\theta_0^{(m)} + \mathrm{Pr}\,\phi^{(m)}\right) + \varphi^{(m)}\left(D\theta_0^{(m)} + \mathrm{Pr}\,D\phi^{(m)}\right)\right\} = 0 \tag{2.14}$$

The system (2.12)-(2.14) together with the boundary conditions (2.13) needs to be solved numerically. The solution method used is the same as described in the previous section.

2.3.3 Method 3: Spectral complex notation

Equation (2.7) is written in the form

$$\nabla^4\psi - \mathrm{Ra}\frac{\partial\theta_1}{\partial x} - \mathrm{Ra}\,\mathrm{Pr}^{-1}\frac{\partial\theta_0}{\partial x} = N_\psi, \tag{2.15a}$$

$$\nabla^2\theta_1 = \mathrm{Pr}\,N_{\theta 1} + N_{\theta 0} \tag{2.15b}$$

where terms involving products and nonlinearities are expressed as

$$N_\psi = \frac{\partial}{\partial y}\left(\frac{\partial}{\partial x}\langle uu\rangle + \frac{\partial}{\partial y}\langle uv\rangle\right) - \frac{\partial}{\partial x}\left(\frac{\partial}{\partial x}\langle uv\rangle + \frac{\partial}{\partial y}\langle vv\rangle\right),$$

$$N_{\theta 1} = \frac{\partial}{\partial x}\langle u\theta_1\rangle + \frac{\partial}{\partial y}\langle v\theta_1\rangle,$$

$$N_{\theta 0} = \frac{\partial}{\partial x}\langle u\theta_0\rangle + \frac{\partial}{\partial y}\langle v\theta_0\rangle.$$

The solution is assumed to be in the form of Fourier expansions, as discussed in the Section 2.3.1, i.e.,

$$\begin{aligned}
&\psi(x,y) = \sum_{n=-\infty}^{n=+\infty}\varphi^{(n)}(y)e^{in\alpha x},\ \theta_1(x,y) = \sum_{n=-\infty}^{n=+\infty}\phi^{(n)}(y)e^{in\alpha x},\\
&u(x,y) = \sum_{n=-n}^{n=+\infty}u^{(n)}(y)e^{in\alpha x},\ v(x,y) = \sum_{n=-\infty}^{n=+\infty}v^{(n)}(y)e^{in\alpha x}
\end{aligned} \tag{2.16}$$

where $u^{(n)} = D\varphi^{(n)}$ and $v^{(n)} = -in\alpha\varphi^{(n)}$. The nonlinear and product terms are also expressed in terms of Fourier expansions in the form

$$\begin{aligned}
&\langle uu\rangle(x,y) = \sum_{n=-\infty}^{n=+\infty}\langle uu\rangle^{(n)}(y)e^{in\alpha x},\ \langle uv\rangle(x,y) = \sum_{n=-\infty}^{n=+\infty}\langle uv\rangle^{(n)}(y)e^{in\alpha x},\\
&\langle vv\rangle(x,y) = \sum_{n=-\infty}^{n=+\infty}\langle vv\rangle^{(n)}(y)e^{in\alpha x},\ \langle u\theta_1\rangle(x,y) = \sum_{n=-\infty}^{n=+\infty}\langle u\theta_1\rangle^{(n)}(y)e^{in\alpha x},
\end{aligned} \tag{2.17}$$

$$\langle v\theta_1\rangle(x,y)=\sum_{n=-\infty}^{n=+\infty}\langle v\theta_1\rangle^{(n)}(y)e^{in\alpha x}\ ,\langle u\theta_0\rangle(x,y)=\sum_{n=-\infty}^{n=+\infty}\langle u\theta_0\rangle^{(n)}(y)e^{in\alpha x}\ .$$

Substitution of (2.16)-(2.17) into (2.15) and separation of Fourier components result in the following system of ordinary differential equations for the modal functions

$$D_n^2\varphi^{(n)}-in\alpha Ra\phi^{(n)}=in\alpha Ra\,Pr^{-1}\theta_0^{(n)}+N_\psi^{(n)}, \tag{2.18a}$$

$$D_n\phi^{(n)}=N_{\theta 0}^{(n)}+Pr\,N_{\theta 1}^{(n)} \tag{2.18b}$$

where $0\le|n|<+\infty$, $D=d/dy$, $D^2=d^2/dy^2$, $D_n=D^2-n^2\alpha^2$,

$$N_\psi^{(n)}=in\alpha D\langle uu\rangle^{(n)}+D^2\langle uv\rangle^{(n)}+in^2\alpha^2\langle uv\rangle^{(n)}-in\alpha D\langle vv\rangle^{(n)},$$

$$N_{\theta 1}^{(n)}=in\alpha\langle u\theta_1\rangle^{(n)}+D\langle v\theta_1\rangle^{(n)},$$

$$N_{\theta 0}^{(n)}=in\alpha\langle u\theta_0\rangle^{(n)}+D\langle v\theta_0\rangle^{(n)}.$$

The unknown linear terms have been placed on the left hand side, and the nonlinear and product terms have been placed on the right hand side. Equations (2.10) provide the required boundary conditions.

For the purpose of numerical solution, expansions (2.16)-(2.17) have been truncated after N_M Fourier modes. The discretization method uses Chebyshev collocation technique based on the Gauss-Chebyshev-Lobatto points (Trefethen 2000) whose locations were computed from the formula

$$y_k=\sin\left(\frac{\pi(N_T+1-2k)}{2(N_T-1)}\right),\quad k=0,1,2,\ldots N_T \tag{2.19}$$

which is advantageous in the floating-point arithmetic (Weideman and Reddy 2000). The resulting nonlinear algebraic system was solved using an iterative technique combined with under-relaxation in the form

$$\Phi_{j+1} = \Phi_j + RF\left(\Phi_{comp} - \Phi_j\right) \tag{2.20}$$

where $\Phi = \left\{\varphi^{(n)}, \phi^{(n)}\right\}$, Φ_{comp} denotes the current solution, Φ_j denotes the previous solution, Φ_{j+1} stands for the accepted value of the next iteration and RF denotes the relaxation factor.

The solution process starts with solution of (2.18) with the RHS terms assumed to be zero. Once solution of this problem has been completed, the first approximation of the RHS terms is computed on the basis of the available approximation of the velocity and temperature fields and the system (2.18) is resolved with the new approximation of the RHS. This process is continued, with the update of the RHS terms taking place after each iteration, until a convergence criterion in the form $\max\left(\left|\Phi_{comp} - \Phi_j\right|\right) < TOL$ is satisfied. TOL denotes difference between solutions obtained in two consecutive iterations and its value set at 10^{-6} was found to be sufficient in most of the computations (see Appendix E for the discussion on numerical accuracy). The number of collocation points and the number of Fourier modes used in the solution were selected through numerical experiments so that the flow quantities of interest were determined with at least six digits accuracy.

The evaluation of the RHS terms requires evaluation of products of two Fourier series. It is more efficient to evaluate these products in the physical space rather than in the Fourier space (Canuto et al. 2006). The required flow quantities, i.e., u, v, θ_1, were computed in the physical space on a suitable grid based on the collocation points in the y-direction and a uniformly distributed set of points in the x-direction, and the required products were evaluated at the grid points. The Fast Fourier Transform (FFT) algorithm was used to express these products in terms of Fourier expansions (2.17). The aliasing error was controlled using "padding" (Canuto et al. 2006), i.e., using of a discrete FFT transform with N_p rather than N_M points, where $N_p \geq 3N_M / 2$. Zeros were added for the additional Fourier modes as required.

2.4 Description of the flow and temperature fields

We focus our attention on the simplest reference case as shown in **Figure 2.2** where the temperature distribution along the bottom plate is expressed by one Fourier mode and the temperature of the upper plate is constant and equal to the average temperature of the lower plate, i.e.,

$$\theta_L(x) = \tfrac{1}{2}\cos(\alpha x)\,,\ \theta_U(x) = 0. \tag{2.21}$$

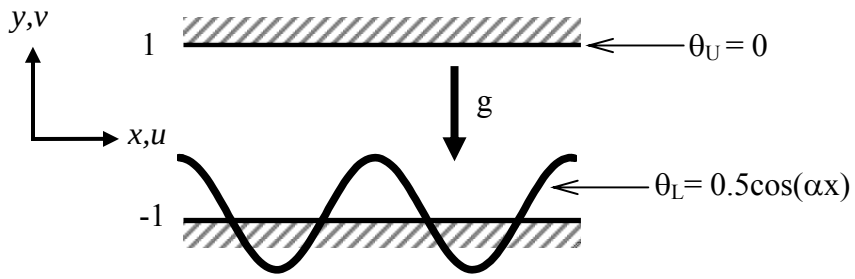

Figure 2.2: *Parallel plates subject to periodic heating defined by equation* (2.21).

We refer the above spatial distribution of heating as "periodic heating". We know that if the heating wave number α is large, the wavelength of heating will be small, and vice versa. We shall discuss the pattern of the convection due to the presence of periodic heating applied at the bottom wall in two parts depending on the magnitude of the heating wave number. In first part, we discuss the "small" wavelength heating which will cover $\alpha \geq 3$, and in the second part we discuss the "long" wavelength heating for which $\alpha \approx 0$ to 0.5. It may be noted that there is no significant change in flow properties in the range of the heating wave number $0.5<\alpha<3$.

2.4.1 Short wavelength heating

For the arrangement shown in **Figure 2.2**, the amplitude of temperature variations along the lower wall represents the conductive temperature scale T_d and this amplitude is

expressed in terms of Rayleigh number in the dimensionless formulation. The structure of the temperature field in the absence of convection shown in **Figure 2.3** demonstrates that the space between the plates can be separated into the heated and cooled zones resulting in the buoyancy force changing direction along the length of the slot. Such distribution of the driving force results in the onset of convection regardless of the amplitude of the heating. A more detail physical explanation on how the onset of convection takes place is given in the Section 2.4.2.

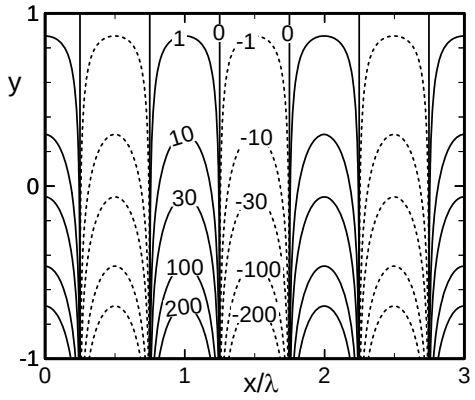

Figure 2.3. *Isotherms of the conductive temperature field for the heating wave number $\alpha = 3$. Solid lines denote positive temperatures (hot) and dashed lines denote negative temperature (cold). Temperature magnitudes are multiplied by 1000.*

Convective motion has a fairly simple topology for this heating, as illustrated in **Figures 2.4-2.5**. The fluid rises above the hot zones in the lower wall (due to upward buoyancy force at the hot zones) and descends above the cold zones (due to downward buoyancy force at the cold zones) forming closed, counter-rotating rolls. When the intensity of the heating increases (Ra increases), centers of the rolls move upwards and towards to the hot zones. The fluid movement concentrates closer to the lower wall as the heating wave number α increases. Increase of the Prandtl number produces the same effect.

It will be shown in the subsequent chapters that the convective rolls are subject to an instability for sufficiently high Ra and thus we limit our consideration to $Ra<10^4$.

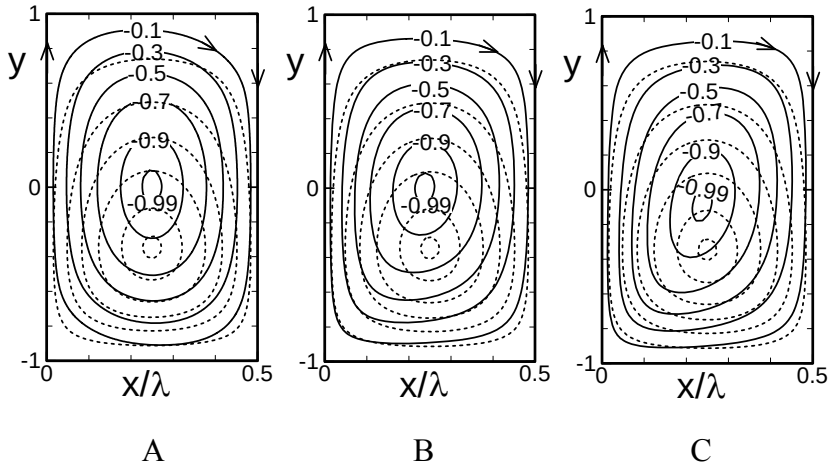

Figure 2.4. *Flow topology for the heating wave number α = 3 and the Rayleigh numbers Ra=1 (dotted lines) and Ra = 10,000 (solid lines). Stream function is normalized with its maximum ψ_{max} . Fig.2.4A corresponds to Pr = 0.01 (ψ_{max} = 0.128, 580.1 for Ra = 1, 10000),Fig.2.4B corresponds to Pr = 0.71 (ψ_{max} = 0.0017, 10.43 for Ra = 1, 10000), Fig.2.4C corresponds to Pr = 1000 (ψ_{max} = 1.22e-6, 7.3e-3 for Ra = 1, 10000).*

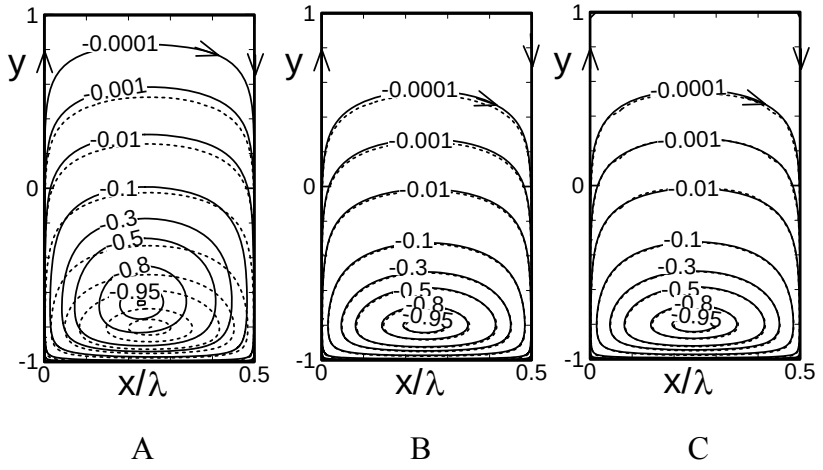

Figure 2.5. *Flow topology for the heating wave number α = 10 and the Rayleigh numbers Ra = 1 (dotted lines) and Ra = 10,000 (solid lines). Stream function is normalized with its maximum ψ_{max} . Fig.2.5A corresponds to Pr = 0.01 (ψ_{max} =3.38e-3, 26.37 for Ra = 1, 10000), Fig.2.5B corresponds to Pr = 0.71 (ψ_{max} = 4.77d-5, 0.4683 for Ra = 1, 10000), Fig.2.5C corresponds to for Pr = 1000 (ψ_{max} = 3.38e-8, 3.32e-4 for Ra = 1, 10000).*

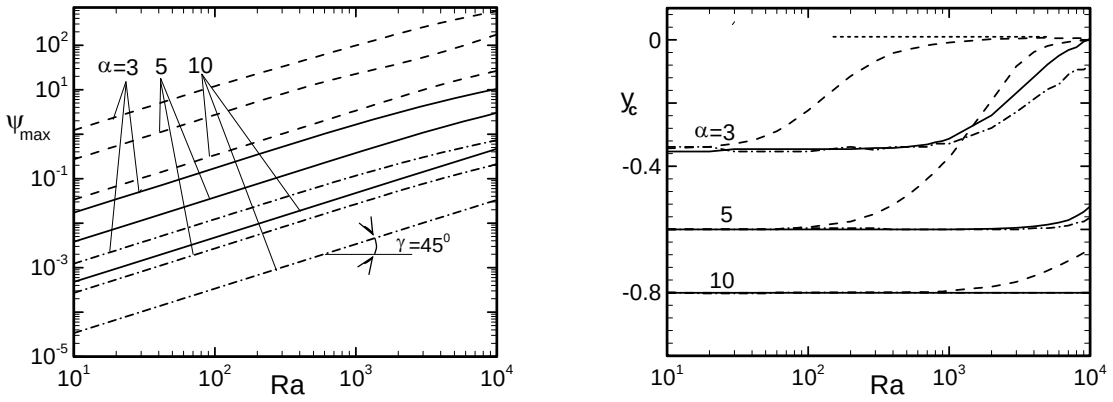

Figure 2.6. *Variations of the roll strength (as measured by the maximum of the stream function ψ_{max} , Fig.2.6A), and of the location of the coordinate y_c of the roll center (Fig.2.6B) as a function of the Rayleigh number Ra for selected values of the heating wave number α. Dash, continuous and dash-dot lines correspond to the Prandtl numbers Pr = 0.01, 0.71 and 10, respectively. Data for the last two values of Pr overlap in Fig.2.6B.*

Results displayed in **Figure 2.6**A demonstrate that the strength of the rolls, as measured by the maximum of the stream function, increases linearly with the Rayleigh number Ra. This intensity increases when Prandtl number Pr of the fluid is lowered. Results displayed in **Figure 2.6**B illustrate variations in the location of the vortex center as a function of the Rayleigh number Ra. It can be seen that this location remains constant for low values of Ra but, once a certain critical value of Ra is reached, the vortex center starts moving upwards and reaches to the center of the slot for high enough Ra. Increase of the heating wave number α causes this transition to take place at higher values of Ra (see **Figure 2.6**B).

Results displayed in **Figure 2.7** illustrate changes in the convection due to variations of the heating wave number α. It can be see that the strength of the convection decreases proportionally to α^{-3} for all values of Ra and Pr of interest, with the convection for the lowest value of Pr considered being strongest. The center of the vortex moves downwards with an increase of α and it follows an asymptote in the form $y_c=-1+2.07\alpha^{-1}$ for large

enough α regardless of the values of Ra and Pr. The approach to the asymptote is slowest for the smallest value of Pr considered.

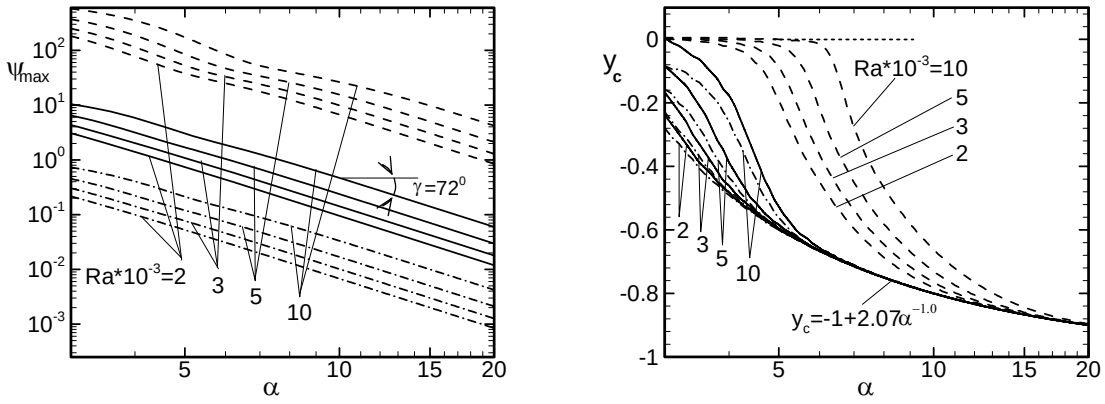

Figure 2.7. *Variations of the roll strength (as measured by the maximum of the stream function ψ_{max} , Fig.2.7A) and of the location of the roll center identified by its coordinate y_c (Fig. 2.7B) as a function of the heating wave number α for selected values of the Rayleigh number Ra. Dash, continuous and dash-dot lines correspond to the Prandtl numbers Pr = 0.01, 0.71 and 10, respectively.*

We have seen from **Figures 2.6A** and **2.7A** that the strength of the rolls increases linearly with Ra (for a fixed α) and decreases proportionally to α^{-3} (for a fixed Ra). To obtain the combined effect of Ra and α on the strength of the rolls it is convenient to introduce a Rayleigh number Ra_λ based on the heating wavelength where $Ra = Ra_\lambda \alpha^3$. In the limit $\alpha \to \infty$, ψ_{max} approaches a constant Ra_λ-dependent value. A simple correlation in the form

$$\psi_{max} = 0.0467\ Ra/\alpha^3 = 0.0467\ Ra_\lambda \qquad (2.22)$$

describes the strength of convection in this limit for the fluid with Pr = 0.71. The range of validity of correlation (2.22) is surprisingly large, as shown in **Figure 2.8**.

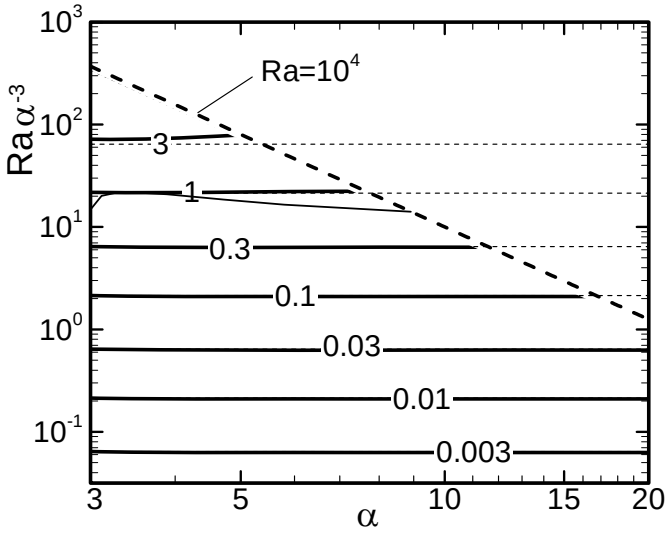

Figure 2.8. *Variations of the roll strength measured by the stream function maximum ψ_{max} as a function of the heating wave number α and the Rayleigh number based the heating wavelength $Ra_\lambda = Ra/\alpha^3$ for a fluid with the Prandtl number Pr = 0.71. The dash line corresponds to the maximum of Ra being considered. The dotted lines describe asymptotes (2.22). Thin solid line identifies conditions where the difference between the actual value of ψ_{max} and the value computed from (2.22) is equal to 1%.*

The effects of variations of the Prandtl number on the roll strength and on the roll center are illustrated explicitly in **Figure 2.9**. It can be seen that the strength of convection decreases linearly with an increase of Pr. Vortex centers are located at the middle of the slot for small enough values of Pr and move to a new, Pr-independent location for high enough values of Pr (see **Figure 2.9**B). This new location is a function of the heating wave number α. The transition between the two limiting locations occurs for values of Pr between ~0.01 and ~0.2.

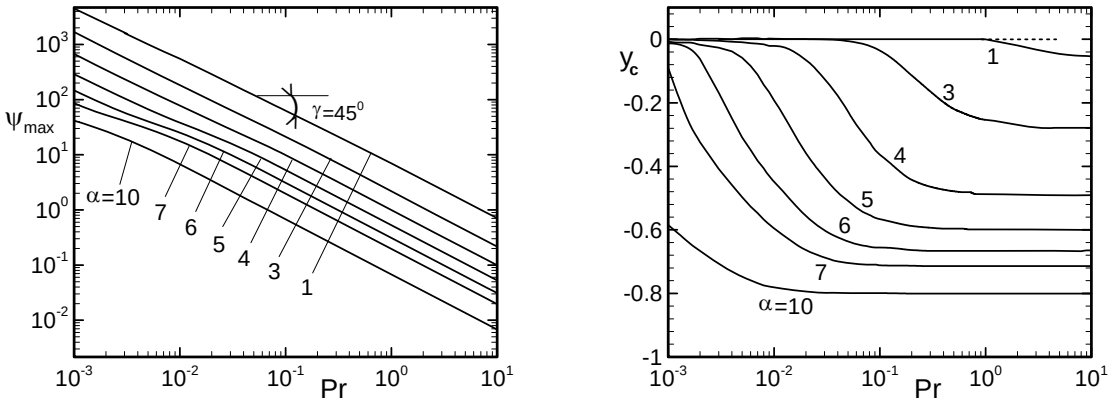

Figure 2.9. *Variations of the roll strength as measured by the maximum of the stream function ψ_{max} (Fig.2.9A) and of the location of the roll center identified by its coordinate y_c (Fig.2.9B) as a function of the Prandtl number Pr. All results are for the Rayleigh number Ra = 2000 and selected values of the heating wave numbers α.*

The topology of the temperature field is more complex. **Figure 2.3** displays conductive temperature field. As the heating intensity increases, the convective effects alter this field as shown in **Figure 2.10**A. Further increase of the Rayleigh number Ra leads to the formation of saddle points that are already well developed at Ra = 100 (see **Figure 2.10**B). Plumes over the heated portions of the wall increase in size and the heated fluid occupies most of the space in the slot. Further increase of Ra leads to a re-arrangement in the character of the temperature field. Temperature in the top portion of the slot looses x-dependence and assumes form associated with conductive heat transfer between walls of constant but different temperatures (see **Figure 2.10**C). Convection is contained in the bottom portion of the slot and the temperature here has a strong x-dependence. Further increase of Ra leads to the penetration of the convective effects back to the top portion of the slot (see **Figure 2.10**D). While the evolution of the structure of the temperature field as a function of Ra is qualitatively similar for different values of the heating wave number α and for fluids with different Prandtl numbers Pr, the quantitative differences can be significant. In the case of smaller wave numbers, i.e., α = 3 (see **Figure 2.11** A and B), the plumes of the heated fluid are more pronounced, cool fluid occupies relatively less

space and formation of the conduction-like zone is not observed. In the case of larger heating wave numbers, i.e., α = 10 (see **Figure 2.11** C and D), formation of the conduction-like zone is observed for much smaller values of Ra with the convection contained in a zone very closed to the bottom wall.

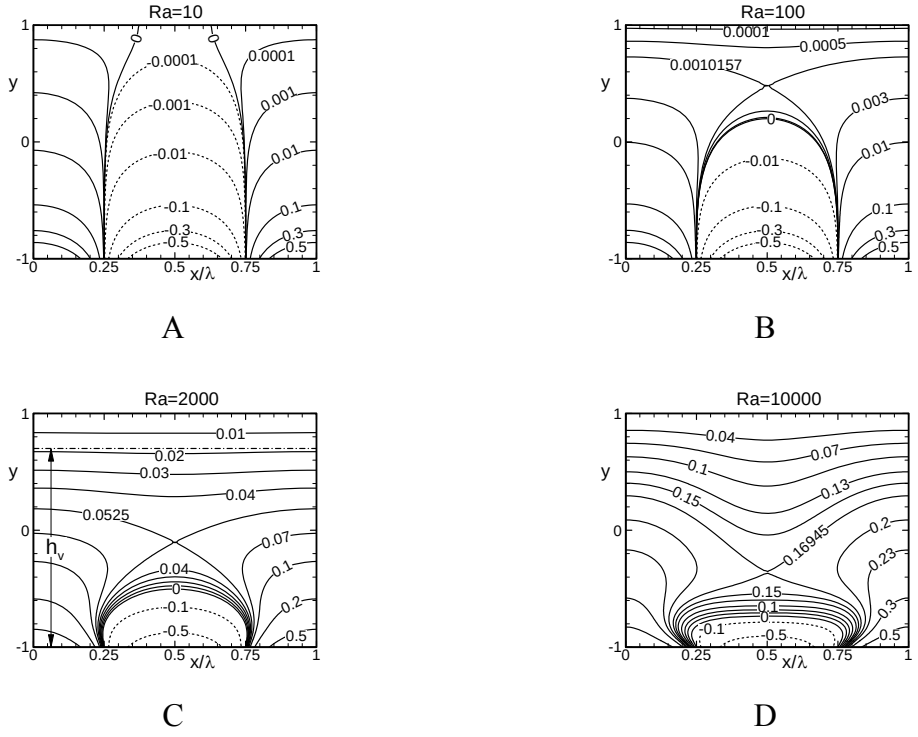

Figure 2.10. *Temperature fields resulting from the heating with the wave number α = 5 in the case of fluid with the Prandtl number Pr = 0.71. Results displayed in Figs 2.10A,B,C and D correspond to the amplitude of heating described by the Raleigh numbers Ra = 10, 100, 2000 and 10000, respectively. Solid and dash lines correspond to the positive and negative values of the temperature, respectively. The temperatures have been normalized with the factor $(2*Pr)^{-1}$ resulting in the displayed values changing between -1 and +1. The thickness of the convection layer is denoted as h_v.*

Formation of the conduction-like zone in the upper portion of the slot is illustrated in **Figure 2.12**A which displays the y-derivative of the zero-order modal function in the temperature field $d\phi^{(0)}/dy$. This modal function determines the net heat flow between both walls. It can be seen that as the heating wave number α increases, $d\phi^{(0)}/dy$ assumes a constant value in the upper portion of the slot. **Figure 2.12**B displays derivative of the

first four modal functions in the temperature field, i.e., $d\phi^{(0)}/dy$ for n=0, 1, 2, 3, for the heating wave number $\alpha = 5$. The corresponding temperature field is shown in **Figure 2.10**C. It can be seen that the magnitudes of the modal functions other than $d\phi^{(0)}/dy$ quickly decrease as one moves away from the lower wall and thus the dominant heat transport in the upper portion of the slot is by conduction and only in the vertical direction. The temperature field in the lower portion of the slot is very complex and strongly affected by the convective effects. This "convective layer" is seen by the upper portion of the slot as a "wall with a constant and uniform temperature" and this leads to the heat transport in the upper part of the slot by conduction only.

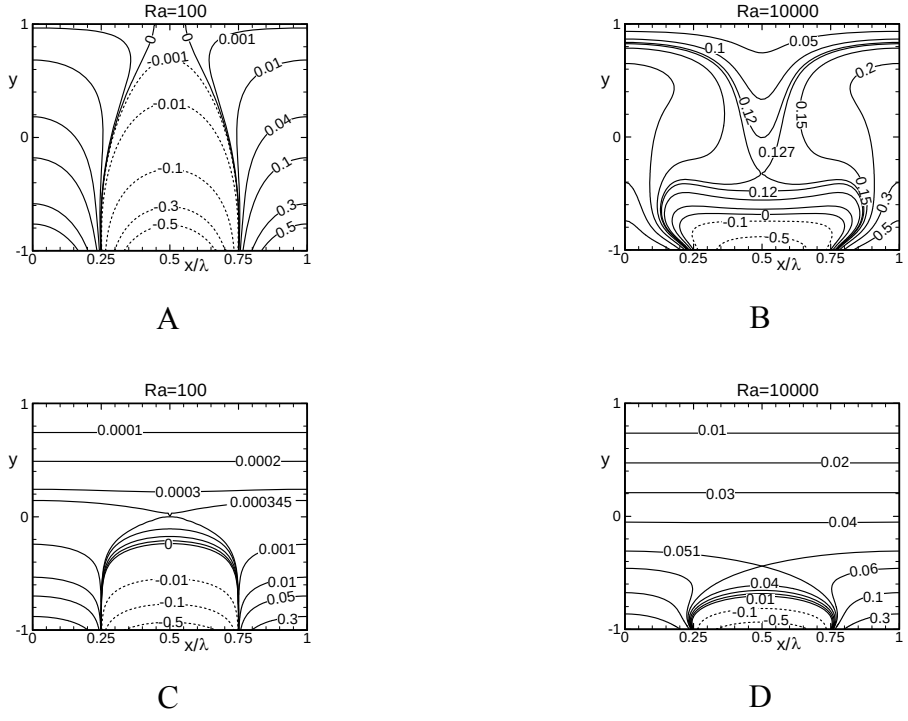

Figure 2.11. *Temperature fields resulting from the heating with the wave number $\alpha = 3$ (Figs 2.10A and B) and $\alpha = 10$ (Figs 2.11C and D). Figures 2.11A and C are for Ra = 100, and 2.10B and D for Ra = 10000. Other parameters as in Fig.2.10.*

Variations of the thickness of the convective layer h_v (see **Figure 2.10**C) are of interest for quantitative description of changes in the temperature field. This thickness is determined by comparing heat flow carried by mode zero with the heat flow carried by

the remaining modes. Because the heat flow carried by higher modes quickly decreases with distance away from the lower wall (see **Figure 2.12**B), only the first three modes have been used in the actual calculations. According to the notation used in Section 2.3.2, a quantity E defined below expresses ratio of both heat flows, i.e.,

$$E = \left\{ \left[\alpha\phi'^{(1)} + 2\alpha\phi^{(2)} \right]^2 + \left[D\phi'^{(1)} + D\phi^{(2)} \right]^2 \right\}^{1/2} / \left| D\phi^{(0)} \right| \tag{2.23}$$

with $\phi'^{(1)} = \mathrm{Pr}^{-1}\,\theta_0^{(1)} + \phi^{(1)}$ and location where E = 0.05 has been adopted as the definition of the edge of the convective layer. The 5% criterion has been chosen rather arbitrarily but it well illustrates evolution of the structure of the temperature field.

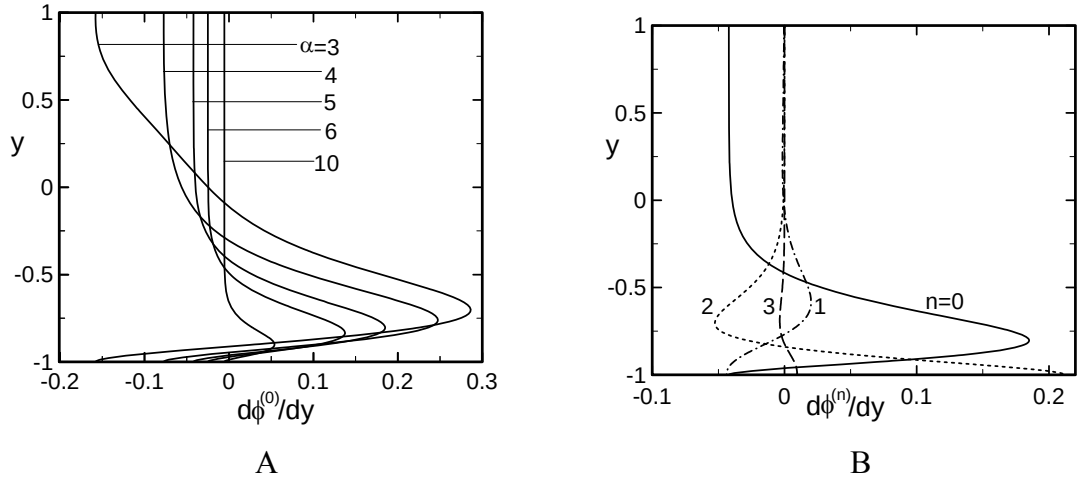

Figure 2.12. *Derivatives of the zero modal function of the temperature field $d\phi^{(0)}/dy$ for selected values of the wall heating wave number α (Fig.2.12A) and of the first four modal functions for the wave number α = 5 (Fig.2.12B) for the heating amplitude corresponding to the Rayleigh number Ra = 2000 for the fluid with the Prandtl number Pr = 0.71.*

Variations of the thickness h_v of the convective layer as a function of the Rayleigh number Ra are illustrated in **Figure 2.13** for Pr = 0.71. It can be seen that the heat is carried by convection in the whole slot for the heating wave numbers α<4.5. A distinct conduction layer can be identified for α = 4.5, but only for a finite range of Ra, i.e., for Ra$\in$(~500,~2500). The range of Ra that gives rise to conduction layer expands towards

smaller and larger values as α increases. For $\alpha = 10$ this range reaches Ra<1 on the low end and Ra>10^4 on the high end. The character of the curves suggest that the conductive zone will disappear if Ra reaches a sufficiently high value even for large values of α, e.g., $\alpha = 10$. **Figure 2.14** illustrates effects of variations of the Prandtl number Pr on the thickness of the convection layer h_v for Ra = 2000. It can be seen that variations of Pr cease to affect the structure of the temperature field for Pr>~0.2 regardless of the value of the heating wave number α, major changes of the temperature field occur for Pr<~0.2 and these changes are more pronounced when α assumes smaller values.

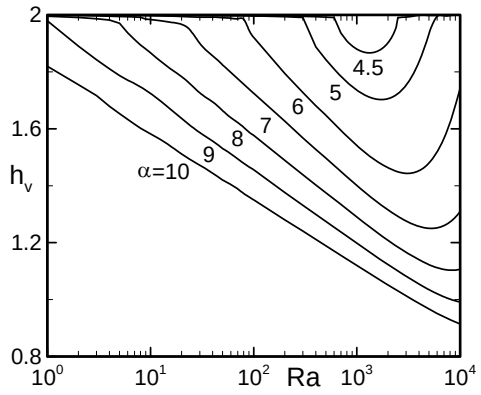

Figure 2.13. *Variations of the thickness h_v of the convection layer as a function of the heating wave number α and the heating amplitude expressed in terms of the Rayleigh number Ra for the fluid with the Prandtl number Pr = 0.71.*

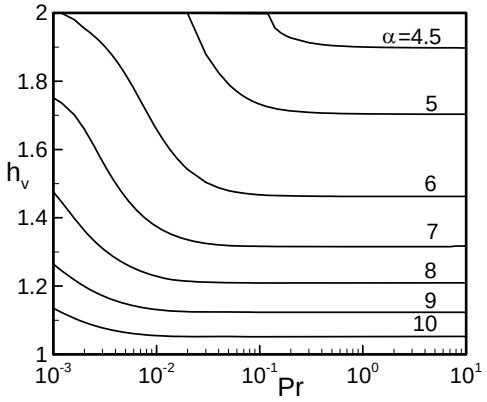

Figure 2.14. *Variations of the thickness h_v of the convection layer as a function of the fluid Prandtl number Pr and the heating wave number α for the heating amplitude corresponding to the Rayleigh number Ra = 2000.*

The variations of the net heat flow between the both wall per unit length across the slot as a function of the Rayleigh number Ra and the heating wave number α are illustrated in **Figure 2.15**. This heat flow is expressed in terms of Nusselt number defined as

$$\mathrm{Nu} = \frac{\mathrm{Pr}}{\lambda}\int_0^{\lambda}\left(-\left.\frac{d\theta}{dy}\right|_{y=-1}\right)dx = -\mathrm{Pr}\left.\frac{d\phi^{(0)}}{dy}\right|_{y=-1} \tag{2.24}$$

and is based on conductive temperature scale.

It can be seen that generally Nu increases when α decreases and when Ra increases. Changes of Nu as a function of Ra are more rapid for smaller values of α. Lines of constant Nu have the form $\mathrm{Ra} \sim \alpha^3, \alpha^3, \alpha^4$ for Pr = 0.01, 0.71, 10, respectively.

To obtain the combined effect of Ra and α on heat transfer we perform the similar analysis as the roll strength for the fluid with Pr = 0.71. The system reaches a asymptotic state for sufficiently large α where variations of the Nusselt number are described by a simple relation in the form

$$\mathrm{Nu} = 0.00192\ \mathrm{Ra}/\alpha^3 = 0.00192\ \mathrm{Ra}_\lambda. \tag{2.25}$$

The functional form of this relation is the same as for the strength of convection given by (2.22), which is not unexpected as the heat transfer is dominated by convection. The range of validity of correlation (2.25) is illustrated in **Figure 2.16**.

The character of variations of Nu is similar for all values of Pr considered with Nu increasing with an increase of Pr. The effects of variations of Pr are explicitly illustrated in **Figure 2.17**. It can be seen that Nu has weak dependence on the Prandtl number for Pr>~0.2 in the range of α being considered in this study, however, the heat flow changes rapidly for Pr between 10^{-2} and 10^{-1}.

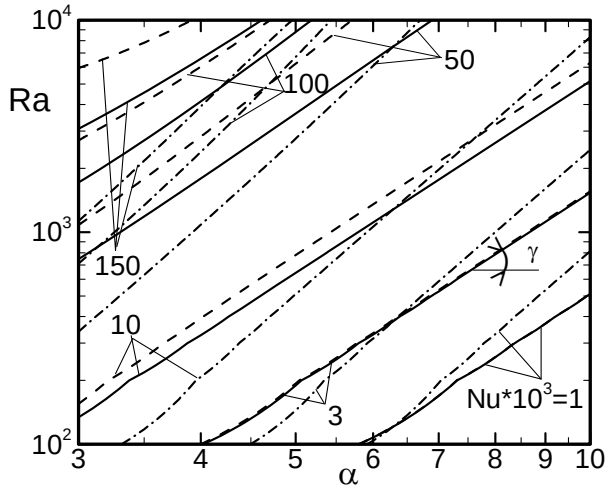

Figure 2.15. *Variations of the net heat flow $Nu*10^3$ between the lower and upper walls per unit length of the slot as a function of the heating wave number α and the heating amplitude expressed in terms of the Rayleigh number Ra for the fluid with the Prandtl numbers Pr = 0.01 (dash lines), 0.71 (solid lines) and 10 (dash-dot lines). Maxima of $Nu*10^3$ occur for the conditions corresponding to the upper left corner of the plot and take values $Nu_{max}*10^3$ = 178.7, 258.4, 600.5 for Pr = 0.01, 0.71, 10, respectively. Slopes of the lines Nu = const are γ = 72°, 72° and 76° for Pr = 0.01, 0.71, 10, respectively.*

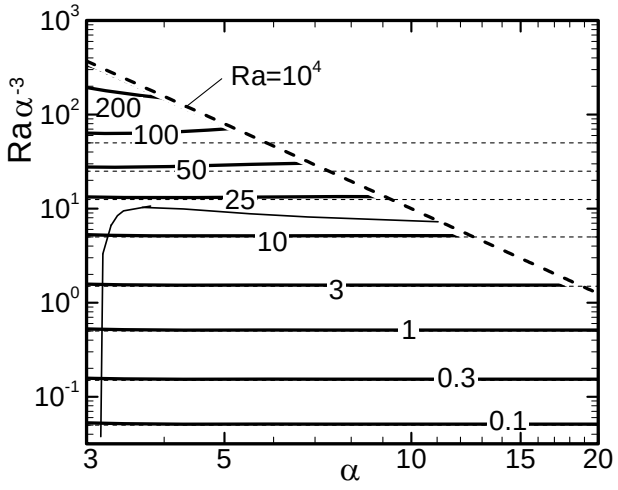

Figure 2.16. *Variations of the heat flow $Nu*10^3$ between the walls per unit length as a function of the heating wave number α and the Rayleigh number based the heating wavelength $Ra_\lambda = Ra/\alpha^3$ for the fluid with Pr = 0.71. The dash line corresponds to the maximum value of Ra being considered. The dotted lines describe asymptotes (2.25). Thin solid line identifies conditions where the difference between the actual value of Nu and the value computed from Eq. (2.25) is equal to 1%.*

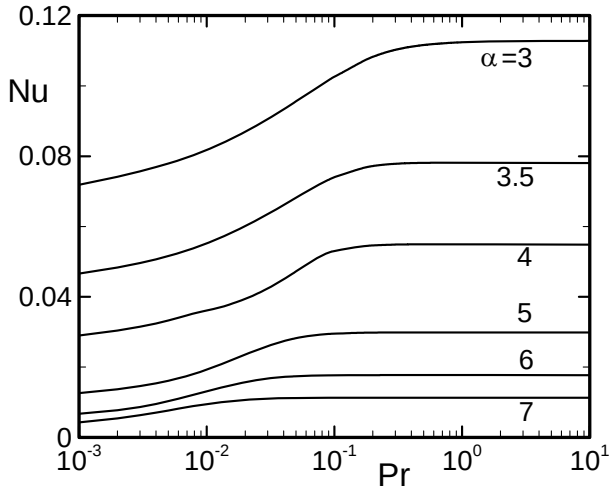

Figure 2.17. *Variations of the heat flow Nu between the lower and upper walls per unit length of the slot as a function of the fluid Prandtl number Pr for selected values of the heating wave number α for the heating amplitude corresponding to the Rayleigh number Ra = 2000.*

2.4.2 Long wavelength heating

Long wavelength heating pattern exhibits different form of response as compared to the short wavelength heating. We begin discussion with the formal analysis of the structure of primary convection in the limit $\alpha \to 0$ and focus presentation of results on the fluid with the Prandtl number Pr = 0.71.

2.4.2.1 Asymptotic analysis of the limit $\alpha \to 0$

To proceed with the asymptotic analysis for the limiting case $\alpha \to 0$, we rescale the x-coordinate with a length scale L, where h/L = α, resulting in the following form of the governing equations

$$\alpha u \frac{\partial u}{\partial X} + v \frac{\partial u}{\partial y} = -\alpha \frac{\partial p}{\partial X} + \alpha^2 \frac{\partial^2 u}{\partial X^2} + \frac{\partial^2 u}{\partial y^2}, \qquad (2.26a)$$

$$\alpha u\frac{\partial v}{\partial X}+v\frac{\partial v}{\partial y}=-\frac{\partial p}{\partial y}+\alpha^2\frac{\partial^2 v}{\partial X^2}+\frac{\partial^2 v}{\partial y^2}+Ra\theta_1+RaPr^{-1}\theta_0, \tag{2.26b}$$

$$Pr\left(\alpha u\frac{\partial\theta_1}{\partial X}+v\frac{\partial\theta_1}{\partial y}\right)+\alpha u\frac{\partial\theta_0}{\partial X}+v\frac{\partial\theta_0}{\partial y}=\alpha^2\frac{\partial^2\theta_1}{\partial X^2}+\frac{\partial^2\theta_1}{\partial y^2}, \tag{2.26c}$$

$$\alpha\frac{\partial u}{\partial X}+\frac{\partial v}{\partial y}=0, \tag{2.26d}$$

where X denotes the x-coordinate scaled using the new length scale. For the heating pattern considered in (2.21) the conductive temperature field described by (2.4) can be approximated in the limit $\alpha\to 0$ as

$$\theta_0=\theta_{00}+O(\alpha^2)=\frac{1}{4}(1-y)\cos(X)+O(\alpha^2). \tag{2.27}$$

We assume the flow quantities as asymptotic expansions in terms of α in the form,

$$u=U_0+\alpha U_1+\alpha^2U_2+\cdots,\quad v=V_0+\alpha V_1+\alpha^2V_2+\cdots \tag{2.28a-b}$$

$$p=P_0+\alpha P_1+\alpha^2P_2+\cdots,\quad \theta_1=\Theta_0+\alpha\Theta_1+\alpha^2\Theta_2+\cdots. \tag{2.28c-d}$$

Substituting the asymptotic expansions in the governing equations (2.26), performing the order analysis, we obtain the following reduced form of the asymptotic expansions,

$$u=\alpha U_1+O(\alpha^3),\ v=\alpha^2V_2+O(\alpha^4),\ p=P_0+O(\alpha^2),\ \theta_1=\alpha^2\Theta_2+O(\alpha^4). \tag{2.29a-d}$$

Substitution of (2.27) and (2.29) into (2.26) and retention of the leading order terms lead to the following form of the field equations

$$\frac{\partial P_0}{\partial y}=\frac{Ra}{Pr}\theta_{00}, \tag{2.30a}$$

$$\frac{\partial P_0}{\partial X} = \frac{\partial^2 U_1}{\partial y^2}, \tag{2.30b}$$

$$\frac{\partial U_1}{\partial X} + \frac{\partial V_2}{\partial y} = 0, \tag{2.30c}$$

$$U_1 \frac{\partial \theta_{00}}{\partial X} + V_2 \frac{\partial \theta_{00}}{\partial y} = \frac{\partial^2 \Theta_2}{\partial y^2}, \tag{2.30d}$$

where (2.30a-d) originate from the y-momentum, x-momentum, continuity and energy equations, respectively. The boundary conditions can be easily deduced from (2.6) and need to be supplemented by condition expressing zero mass flux in the x-direction. Solution of (2.30) has the form

$$P_0 = \frac{Ra}{4\,Pr}\cos(\alpha x)\left[-\frac{1}{2}y^2 + y + \frac{1}{10}\right], \tag{2.31a}$$

$$U_1 = -\frac{Ra}{4\,Pr}\sin(\alpha x)\left[-\frac{1}{24}y^4 + \frac{1}{6}y^3 + \frac{1}{20}y^2 - \frac{1}{6}y - \frac{1}{120}\right], \tag{2.31b}$$

$$V_2 = \frac{Ra}{4\,Pr}\cos(\alpha x)\left[-\frac{1}{120}y^5 + \frac{1}{24}y^4 + \frac{1}{60}y^3 - \frac{1}{12}y^2 - \frac{1}{120}y + \frac{1}{24}\right], \tag{2.31c}$$

$$\begin{aligned}\Theta_2 = \frac{Ra}{32\,Pr}\Bigg\{&\frac{1}{40}\left[\frac{1}{21}y^7 - \frac{1}{3}y^6 + \frac{1}{5}y^5 + y^4 - y^3 - y^2 + \frac{79}{105}y + \frac{1}{3}\right] \\ &- \frac{1}{3}\cos(2\alpha x)\left[\frac{1}{420}y^7 - \frac{1}{60}y^6 + \frac{1}{50}y^5 + \frac{1}{30}y^4 - \frac{1}{12}y^3 + \frac{1}{30}y^2 + \frac{32}{525}y - \frac{1}{15}\right]\Bigg\}.\end{aligned} \tag{2.31d}$$

The physical interpretation of the asymptotic equations (2.31) state that the flow forcing in the form of externally imposed conductive temperature (see (2.27)) generates a pressure field as dictated by the y-momentum equation (see (2.30a)), this pressure field drives motion in the x-direction as dictated by the x-momentum equation (see (2.30b)), the complementary motion in the y-direction is determined by the continuity equation

(see (2.30c)), and the overall motion creates a correction in the imposed conductive temperature field as dictated by the energy equation (see (2.30d)).

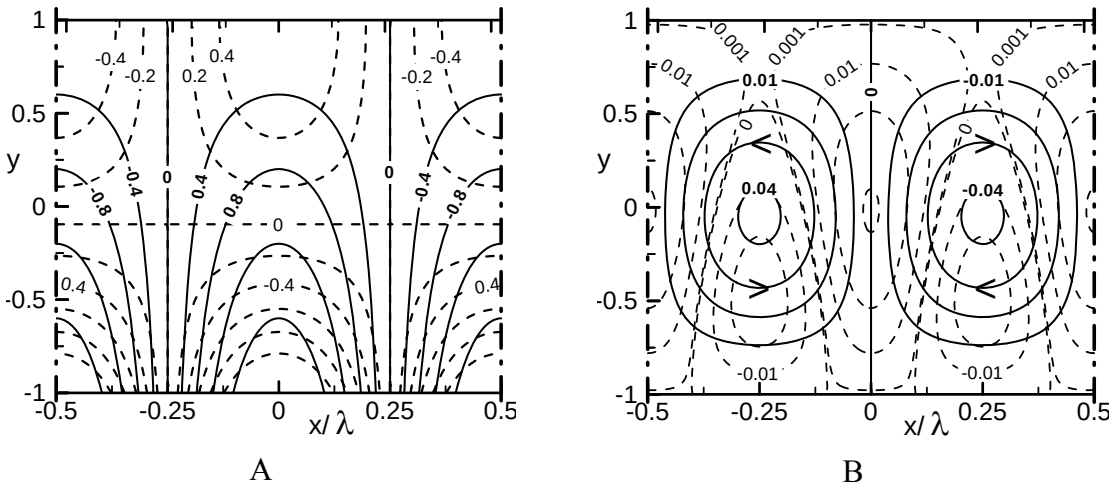

Figure 2.18. *Convection patterns described by the asymptotic solutions (2.27) and (2.31). Conductive temperature $4*\theta_{00}$ and pressure $P_0(4Pr/Ra)$ are shown in Fig.2.18A using solid lines with step size 0.4 and dash lines with step size 0.2, respectively. Stream function $\psi/(\alpha Ra/4Pr)$ and isotherms of the convective temperature $\Theta_2(32Pr/Ra)$ are displayed in Fig.2.18B using solid lines with step size 0.01 and dash lines with step size 0.01 (unless otherwise shown), respectively.*

The conductive temperature field obtained from the asymptotic solution (using (2.27)) is illustrated in **Figure 2.18**A (the plot extends over one wavelength of the heating from $-\lambda/2$ to $+\lambda/2$). It generates a buoyancy force acting upwards at x = 0 and downwards at $x = \lambda/2$; this force is responsible for driving the fluid upwards at x = 0 and downwards at $x = \lambda/2$. Since motion in the y-direction is restricted due to the presence of the walls, an opposing pressure force is generated which forces the fluid to turn around before reaching walls. This leads to the formation of the y- and x-pressure gradients as illustrated in **Figure 2.18**A. The overall flow pattern has the form of rolls depicted in **Figure 2.18**B. Fluid motion transports energy and creates changes in the temperature field displayed in **Figure 2.18**B. It can be seen that hot fluid rises at x = 0 creating positive correction in the temperature field. This fluid turns sideways as it approaches the upper wall but still

creates positive temperature correction as it flows towards zones with lower conductive temperatures. The fluid turns downwards around x = ±λ/2 and again creates positive temperature correction as it flows in the direction of decreasing conductive temperature. The final turn occurs at the lower wall and the fluid flows into the zone of higher conductive temperature field creating a negative temperature correction.

2.4.2.2 Range of validity of the asymptotic solution

The range of validity of the above analytical solution can be determined by comparing it to the complete solution determined numerically. **Figure 2.19** displays patterns of conductive and convective temperature fields, and pressure and velocity fields determined numerically for α = 0.5. One can observe that centers of the rolls move closer to the hot spots as α increases from α ≈ 0 (see **Figure 2.18**) to α ≈ 0.5 (see **Figure 2.19**) but otherwise the patterns do not change significantly.

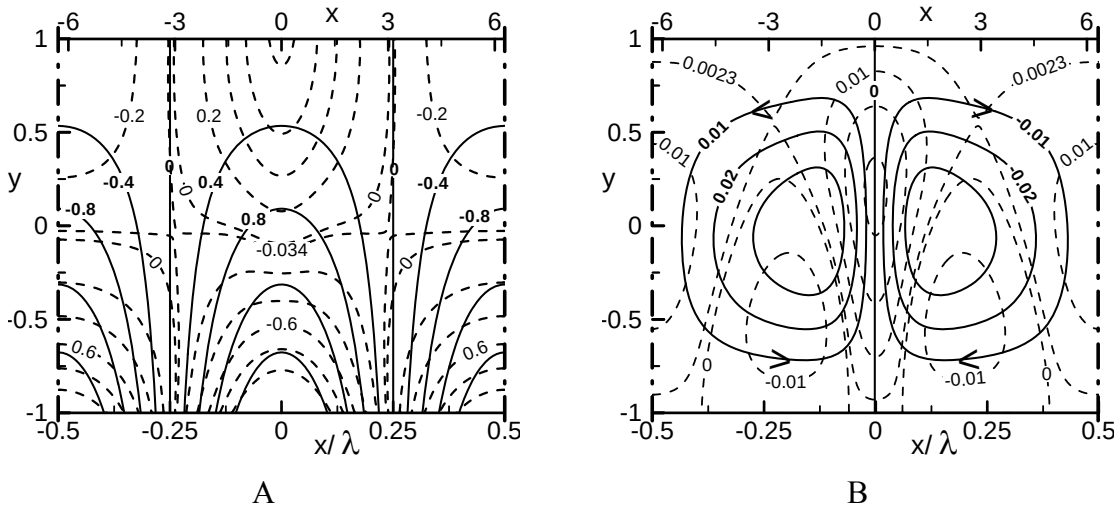

Figure 2.19. *Convection patterns described by the complete field equations for a fluid with Prandtl number Pr = 0.71 subject to heating corresponding to the Rayleigh number Ra = 400 and the heating wave number α = 0.5. Other conditions as in Fig.2.18.*

To provide a quantitative measure of the range of validity of the asymptotic solution, we define the relative error of the asymptotic solution as

$$\mathrm{Err}_{\mathrm{rel}} = \underbrace{\max}_{-1<y<1}\left|\frac{|\Phi_{\mathrm{num}}| - |\Phi_{\mathrm{asym}}|}{|\Phi_{\mathrm{num}}|}\right| \tag{2.32}$$

where Φ stands either for u evaluated at $x = \lambda/4$ or for any of the remaining quantities evaluated at $x = \lambda/8$, and subscripts "num" and "asym" denote quantities computed on the basis of the complete and asymptotic equations, respectively. It is noted that u is evaluated at a different point ($x = \lambda/4$) for better resolution. **Figure 2.20**A illustrates variations of the relative error of the asymptotic solution as a function of α. It can be seen that the relative error is less than 0.1 for $\alpha \approx 0.2$ even when Ra = 400. Variations of the relative error as a function of the Rayleigh number Ra for selected values of the heating wave number α are illustrated in **Figure 2.20**B. The error rises with an increase of Ra but remains below 0.1 even for $\alpha = 0.2$ and Ra = 400.

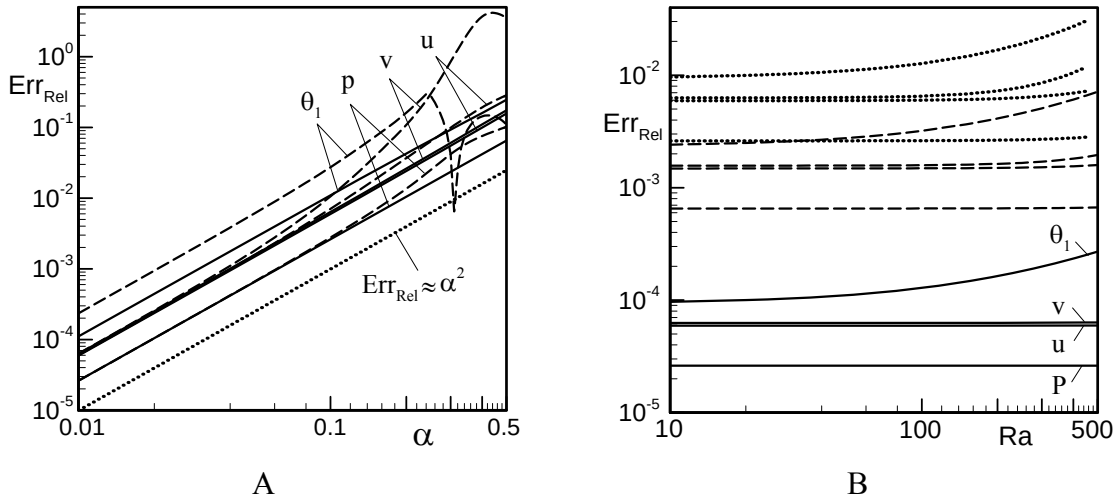

Figure 2.20. *Variations of the relative error of the asymptotic solution for p, u, v and θ_1 for a fluid with Pr = 0.71 as a function of the heating wave number α for selected values of the Rayleigh number Ra and as a function of the Rayleigh number Ra for selected values of the heating wave number α. Solid and dash lines are used for Ra = 50, 400 in Fig.2.20A, respectively and for α = 0.01, 0.05 in Fig.2.20A, respectively. The dotted line with slope ~α^2 is shown in Fig.2.20A for reference purposes.*

2.4.2.3 Heat transfer in the asymptotic limit

The net heat transfer across the slot is expressed by the global (mean) Nusselt number as defined in (2.24). For the asymptotic solution, Nusselt number has the following form,

$$\mathrm{Nu}_{\mathrm{asym}} \to \frac{1}{1400}\alpha^2 \mathrm{Ra} \quad \text{when} \quad \alpha \to 0. \tag{2.33}$$

Figure 2.21 illustrates variations of Nu/Ra as a function of α for selected values of Ra. It can be seen that variations of Nu can be predicted using asymptotic theory from Section 2.4.2.1 as long as Ra < 427. When Ra > 427, Nu branches off and approaches other asymptotic, Ra-dependent limits as $\alpha \to 0$. The branching occurs at larger values of α when the intensity of heating, as measured by the Rayleigh number Ra, increases. The branching process results in the formation of two families of solutions that keep intersecting each other as α decreases, as illustrated in **Figure 2.21**B. These families exist for all values of Ra > 427 and "distance" between them increases with an increase of Ra, but decreases with a decrease of α. This distance is non-zero for all finite values of α considered and the solutions keep intersecting each other as α decreases.

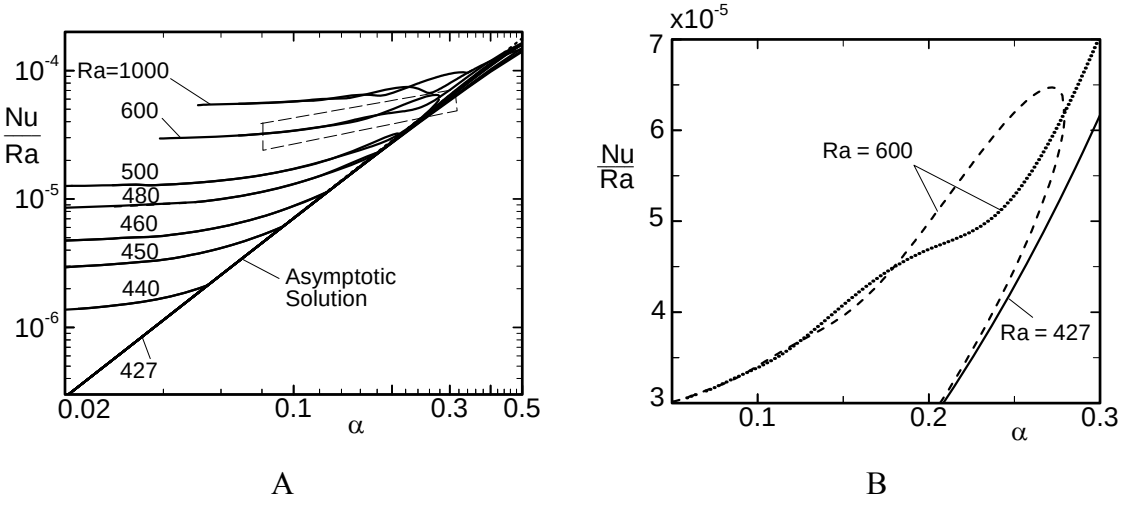

Figure 2.21. *Variations of the Nusselt number as a function of the heating wave number α for selected values of the Rayleigh number Ra. Enlargement of the box marked in Fig.2.21A is displayed in Fig.2.21B.*

Analysis of the conductive temperature field in the limit of $\alpha \to 0$ (shown in (2.27)) expressed in terms of the original length scale demonstrates that zones of length $O(\alpha^{-1})$ on both sides of hot spots are subject to an almost uniform heating and similar zones centered around cold spots are subject to an almost uniform cooling. When the magnitude of the heating is sufficiently large, the zones around the hot spots may be subject to the RB-type instability. The critical Rayleigh number expressed in terms of thickness of the slot for a uniformly heated wall is $Ra_{uni} = 1708$ (Drazin and Reid 1981). This number expressed using the present scaling takes value $Ra_{cr} = 427$. Results shown in **Figure 2.21** suggest that an instability does take place (as it is evident from the branching of the Nu plot). Conditions leading to the onset of such an instability need to be investigated numerically, and will be discussed in a separate chapter.

2.5 Summary

In this chapter the two-dimensional flow response due to the presence of spatially distributed heating applied at the bottom wall has been discussed. The mean temperatures of both walls are kept the same thus the convection occurs only due to the spatial variability of the heating. Spatial distribution of heating is controlled by the heating wave number α, and intensity (amplitude) of the heating is controlled by the Rayleigh number Ra. The case of sinusoidal (periodic) heating has been considered for a wide range of Prandtl number varying from 10^{-3} to 10^{3}. It has been found that the convective motion occurs regardless of the amplitude of heating (i.e. regardless of the magnitude of the Rayleigh number Ra) unlike the RB convection with uniform heating where a critical Rayleigh number is needed for initiation of convection. The convection has the form of counter rotating rolls with axis orthogonal to the heating wave vector $(\alpha,0)$. The convective effects give rise to the mean vertical temperature gradient that results in a net heat transfer between both walls, with the heat flow being larger for smaller α. It is shown that convection is limited to a layer adjacent to the lower wall when α is sufficiently large. Under such conditions a uniform conductive layer emerges at the upper section of the fluid layer with temperature field in this zone becoming independent of the

spatial variations of the heating and varying in the vertical direction only. For $\alpha \to 0$, an asymptotic analysis is performed to compute the flow quantities. The trend of the heat transfer characteristic at a sufficiently small α, i.e., at long wavelength heating, suggests that for supercritical values of Ra (Ra>427) some form of RB-type instability may occur.

3

Onset of Secondary Convection

In this chapter, we examine stability of the primary convection (discussed in the previous chapter). Imposition of small disturbances may initiate instability of the primary convection rolls which may give rise to various forms of 'secondary convection'. Conditions that lead to the onset of a secondary convection is determined using the linear stability theory. This theory provides a good tool for detecting physical growth mechanisms and identifying dominant disturbance types (Schmid and Henningson 2000). In Section 3.1 we formulate the two-dimensional stability equations, the three dimensional equations are discussed in Section 3.2, the method of solution of the stability equations are presented in Section 3.3, a more general form of stability equations are shown in Section 3.4, a summary of the stability analysis is given in Section 3.5, and, finally, in Section 3.6, various instabilities that have been found in this work are reported.

3.1 Formulation of the two-dimensional stability problem

The analysis begins with the momentum equations expressed in terms of the stream function and energy equation. Unsteady, two-dimensional disturbances are super-imposed on the base flow (primary convection) in the form (Floryan 2005)

$$\psi = \psi_2(x, y) + \psi_3(x, y, t), \tag{3.1a}$$

$$\theta = \theta_2(x, y) + \theta_3(x, y, t), \tag{3.1b}$$

where subscripts 2 and 3 refer to the base flow and the disturbance field, respectively. The assumed form (3.1) of the flow quantities is substituted into the field equations, the

base part (primary convection) is subtracted, and the equations are linearized. The resulting disturbance equations have the form

$$\frac{\partial}{\partial t}\left(\nabla^2\psi_3\right)+\frac{\partial\psi_2}{\partial y}\cdot\frac{\partial}{\partial x}\left(\nabla^2\psi_3\right)+\frac{\partial\psi_3}{\partial y}\cdot\frac{\partial}{\partial x}\left(\nabla^2\psi_2\right)-\frac{\partial\psi_2}{\partial x}\cdot\frac{\partial}{\partial y}\left(\nabla^2\psi_3\right)-\frac{\partial\psi_3}{\partial x}\cdot\frac{\partial}{\partial y}\left(\nabla^2\psi_2\right)=\nabla^2\left(\nabla^2\psi_3\right)-\mathrm{Ra}\frac{\partial\theta_3}{\partial x}\,, \tag{3.2a}$$

$$\mathrm{Pr}\left(\frac{\partial\theta_3}{\partial t}+\frac{\partial\psi_2}{\partial y}\cdot\frac{\partial\theta_3}{\partial x}+\frac{\partial\psi_3}{\partial y}\cdot\frac{\partial\theta_2}{\partial x}-\frac{\partial\psi_2}{\partial x}\cdot\frac{\partial\theta_3}{\partial y}-\frac{\partial\psi_3}{\partial x}\cdot\frac{\partial\theta_2}{\partial y}\right)=\nabla^2\theta_3\,, \tag{3.2b}$$

and are subject to the homogeneous boundary conditions $\psi_3 = 0$, $\partial\psi_3/\partial y = 0$, $\theta_3 = 0$ at the two walls. The partial differential equations (3.2) have coefficients that are functions of y and x, with the dependence on the x-coordinate being periodic. Because of that, the time dependence can be separated in the usual manner and the x-dependence can be expressed as a product of an exponential function and an x-periodic amplitude (Floryan 2005), resulting in the solution in the form,

$$\psi_3(x,y,t)=\Phi_3(x,y)e^{i(\delta x-\sigma t)}+\text{c.c.}\,, \tag{3.3a}$$

$$\theta_3(x,y,t)=\Theta_3(x,y)e^{i(\delta x-\sigma t)}+\text{c.c.}\ . \tag{3.3b}$$

The exponent δ is real and accounts for the x-periodicity of the disturbance field, $\Phi_3(x,y)$ and $\Theta_3(x,y)$ are the x-periodic amplitude functions expressing modulation of the disturbance field by the spatially distributed heating, exponent σ is assumed to be complex ($\sigma = \sigma_r + i\sigma_i$) and its imaginary part denoted by σ_i and real part denoted by σ_r describe the rate of growth and the frequency of disturbances, respectively, and c.c. denotes the complex conjugate. If $\sigma_i > 0$ the disturbance motion is unstable with the disturbances growing exponentially, while $\sigma_i < 0$ indicates exponential decay of the disturbances to make the motion stable and $\sigma_i = 0$ refers to neutral stability that disturbances neither grow nor decay. Whereas σ_r determines the kinematic character of the disturbance field. If $\sigma_r \neq 0$ then the disturbances have the form of the traveling wave

(the speed of this wave in x-direction is equal to σ_r / δ). Such disturbances are also called the oscillatory ones because at any fixed point is space one observes time-periodic modulation of the disturbance amplitude (superimposed on the exponential decay or growth). If $\sigma_r = 0$ then time variation of the amplitude of disturbances at any space location is monotonic (non-oscillatory); such disturbances are sometimes called stationary, and their physical structure usually look likes rolls or vortices.

For the problem considered here, (δ, σ) represent eigenvalues for the specified flow conditions which are characterized in terms of (Pr, Ra, α), and the relevant eigenvalue problem for the partial differential equations describing $\Phi_3(x,y)$ and $\Theta_3(x,y)$ can be easily derived. Rather than solving this problem directly, we take advantage of the periodicity of the amplitude functions and represent them as

$$\Phi_3(x,y) = \sum_{m=-\infty}^{m=+\infty} \varphi_3^{(m)}(y) e^{im\alpha x}\ ,\ \Theta_3(x,y) = \sum_{m=-\infty}^{m=+\infty} \phi_3^{(m)}(y) e^{im\alpha x}\ . \tag{3.4a-b}$$

This leads to the following form of the disturbance quantities

$$\psi_3(x,y,t) = \sum_{m=-\infty}^{m=+\infty} \varphi_3^{(m)}(y) e^{i[(\delta+m\alpha)x-\sigma t]} + c.c.\ , \tag{3.5a}$$

$$\theta_3(x,y,t) = \sum_{m=-\infty}^{m=+\infty} \phi_3^{(m)}(y) e^{i[(\delta+m\alpha)x-\sigma t]} + c.c.\ . \tag{3.5b}$$

Substitution of (3.5a-b) into the disturbance equations (3.2a-b) and separation of Fourier components result, after a rather lengthy algebra, in a system of linear homogeneous ordinary differential equations in the form

$$\begin{aligned} B^{(m)}\varphi_3^{(m)} - it_m\theta_3^{(m)} = i\sum_{n=-\infty}^{n=+\infty} \Big[& t_n D\varphi_2^{(m-n)} H^{(n)}\varphi_3^{(n)} + (m-n)\alpha I^{(m-n)}\varphi_2^{(m-n)} D\varphi_3^{(n)} \\ & - (m-n)\alpha\varphi_2^{(m-n)} H^{(n)} D\varphi_3^{(n)} - t_n I^{(m-n)} D\varphi_2^{(m-n)}\varphi_3^{(n)} \Big] \end{aligned} \tag{3.6a}$$

$$C^{(m)}\theta_3^{(m)} = i\,Pr\sum_{n=-\infty}^{n=+\infty}\Big[t_n D\varphi_2^{(m-n)}\theta_3^{(n)} + (m-n)\alpha\theta_2^{(m-n)}D\varphi_3^{(n)} - (m-n)\alpha\varphi_2^{(m-n)}D\theta_3^{(n)} - t_n D\theta_2^{(m-n)}\varphi_3^{(n)}\Big] \tag{3.6b}$$

where $B^{(m)} = \left(D^2 - t_m^2\right)^2 + i\sigma\left(D^2 - t_m^2\right)$,

$C^{(m)} = D^2 - t_m^2 + i\,Pr\,\sigma$,

$H^{(m)} = D^2 - t_m^2$,

$I^{(m-n)} = D^2 - (m-n)^2\alpha^2$,

$t_m = \delta + m\alpha$.

The boundary conditions take the form

$$\varphi_3^{(n)}(\pm 1) = 0,\ \ D\varphi_3^{(n)}(\pm 1) = 0,\ \phi_3^{(n)}(\pm 1) = 0 \quad \text{for } -\infty<n<+\infty. \tag{3.7}$$

3.2 Formulation of the three-dimensional stability problem

We consider three-dimensional linear stability of the primary convection discussed in the previous section. The analysis begins with the governing equations in the form of vorticity transport, energy and continuity equations.

$$\frac{\partial\overline{\omega}}{\partial t} - (\overline{\omega}\bullet\nabla)\overline{v} + (\overline{v}\bullet\nabla)\overline{\omega} = \nabla^2\overline{\omega} + \nabla\times(Ra\theta\,\overline{j}),\quad \nabla\bullet\overline{v} = 0,\quad \overline{\omega} = \nabla\times\overline{v}, \tag{3.8a-c}$$

$$\frac{\partial\theta}{\partial t} + (\overline{v}\bullet\nabla)\theta = Pr^{-1}\nabla^2\theta. \tag{3.8d}$$

where $\overline{j}$ is the unit vector along the vertical (y) direction, $\overline{\omega}$ is the vorticity vector, $\overline{v}$ is the velocity vector, respectively.

Unsteady, three-dimensional disturbances are super-imposed on the base flow in the form (Floryan 2003)

$$\left.\begin{aligned}\overline{\omega} &= \overline{\omega}_2(x,y) + \overline{\omega}_3(x,y,z,t),\\ \overline{v} &= \overline{v}_2(x,y) + \overline{v}_3(x,y,z,t),\\ \theta &= \theta_2(x,y) + \theta_3(x,y,z,t)\end{aligned}\right\} \qquad (3.9a\text{-}c)$$

where subscripts 2 and 3 refer to the base flow and the disturbance field, respectively. The assumed form (3.9) of the flow quantities is substituted into the field equations (3.8), the base part (primary convection) is subtracted, and the equations are linearized. The resulting disturbance equations have the form

$$\frac{\partial\overline{\omega}_3}{\partial t} + (\overline{v}_2 \bullet \nabla)\overline{\omega}_3 - (\overline{\omega}_3 \bullet \nabla)\overline{v}_2 + (\overline{v}_3 \bullet \nabla)\overline{\omega}_2 - (\overline{\omega}_2 \bullet \nabla)\overline{v}_3 = \nabla^2\overline{\omega}_3 + \nabla\times(Ra\theta_3\bar{j}) \quad , \qquad (3.10a)$$

$$\nabla \bullet \overline{v}_3 = 0 \quad , \qquad \overline{\omega}_3 = \nabla\times\overline{v}_3 \quad , \qquad (3.10b\text{-}c)$$

$$\frac{\partial\theta_3}{\partial t} + (\overline{v}_3 \bullet \nabla)\theta_2 + (\overline{v}_2 \bullet \nabla)\theta_3 = Pr^{-1}\nabla^2\theta_3 \qquad (3.10d)$$

and are subject to the homogeneous boundary conditions $\overline{v}_3 = 0, \quad \theta_3 = 0$ at the two walls.

The disturbance equations (3.10) have coefficients that are functions of x and y only, with the dependence on the x-coordinate being periodic. Thus the solution can be written in the following form

$$\overline{v}_3(x,y,z,t) = \overline{G}_3(x,y)e^{i(\delta x+\beta z-\sigma t)} + c.c. \quad , \qquad (3.11a)$$

$$\theta_3(x,y,z,t) = \Theta_3(x,y)e^{i(\delta x+\beta z-\sigma t)} + c.c. \quad . \qquad (3.11b)$$

The exponents δ and β are real and account for the x- and z-periodicity of the disturbance field. $\overline{G}_3(x,y)$ and $\Theta_3(x,y)$ are the x-periodic disturbance amplitude functions expressing

modulation of disturbances by the heating, exponent σ is assumed to be complex as mention in Section 3.1, and c.c. denotes the complex conjugate. (δ, β, σ) represent eigenvalues for the specified flow conditions which are characterized in terms of (Pr, Ra, α). The relevant eigenvalue problem for the partial differential equations (3.10) describing $\overline{G}_3(x,y)$ and $\Theta_3(x,y)$ can be easily derived. Rather than solving this problem directly, we take advantage of the periodicity of the amplitude functions and represent them as

$$\overline{G}_3(x,y)=\sum_{m=-\infty}^{m=+\infty}\left[g_u^{(m)}(y),g_v^{(m)}(y),g_w^{(m)}(y)\right]e^{im\alpha x},\quad \Theta_3(x,y)=\sum_{m=-\infty}^{m=+\infty}g_\theta^{(m)}(y)e^{im\alpha x}. \tag{3.12a-b}$$

This leads to the following form of the disturbance quantities

$$\overline{v}_3(x,y,z,t)=\sum_{m=-\infty}^{m=+\infty}\left[g_u^{(m)}(y),g_v^{(m)}(y),g_w^{(m)}(y)\right]e^{i[(\delta+m\alpha)x+\beta z-\sigma t]}+c.c.\ , \tag{3.13a}$$

$$\theta_3(x,y,z,t)=\sum_{m=-\infty}^{m=+\infty}g_\theta^{(m)}(y)\,e^{i[(\delta+m\alpha)x+\beta z-\sigma t]}+c.c.\ . \tag{3.13b}$$

Substitution of (3.13a-b) into the disturbance equations (3.10) and separation of Fourier components result, after a rather lengthy algebra, in a system of linear homogeneous ordinary differential equations in the form

$$A^{(m)}\zeta^{(m)}=\sum_{n=-\infty}^{n=+\infty}\left[H_\zeta^{(m-n)}\zeta^{(m-n)}+H_v^{(m-n)}g_v^{(m-n)}\right] \tag{3.14a}$$

$$B^{(m)}g_v^{(m)}-Rak_m^2g_\theta^{(m)}=-\sum_{n=-\infty}^{n=+\infty}\left[I_\zeta^{(m-n)}\zeta^{(m-n)}+I_v^{(m-n)}g_v^{(m-n)}\right] \tag{3.14b}$$

$$it_mg_u^{(m)}+Dg_v^{(m)}+i\beta g_w^{(m)}=0 \tag{3.14c}$$

$$C^{(m)}g_\theta^{(m)}=Pr\sum_{n=-\infty}^{n=+\infty}\left[J_\zeta^{(m-n)}\zeta^{(m-n)}+J_v^{(m-n)}g_v^{(m-n)}+J_\theta^{(m-n)}g_\theta^{(m-n)}\right] \tag{3.14d}$$

where, $A^{(m)} = D^2 - k_m^2 + i\sigma$,

$$B^{(m)} = \left(D^2 - k_m^2\right)^2 + i\sigma\left(D^2 - k_m^2\right),$$

$$C^{(m)} = D^2 - k_m^2 + i\,Pr\,\sigma,$$

$$\zeta^{(m)} = t_m g_w^{(m)} - \beta g_u^{(m)},$$

$$t_m = \delta + m\alpha,\ k_m^2 = t_m^2 + \beta^2,$$

$$H_\zeta^{(m-n)} = it_m f_u^{(n)} + k_{m-n}^{-2}\left(\beta^2 + t_{m-n}t_m\right)f_v^{(n)}D,$$

$$H_v^{(m-n)} = -\beta D f_u^{(n)} + in\alpha\beta k_{m-n}^{-2} f_v^{(n)} D^2,$$

$$I_\zeta^{(m-n)} = n\alpha\beta\, k_{m-n}^{-2}\left(2t_{m-n}f_u^{(n)}D + \left(t_m + t_{m-n}\right)Df_u^{(n)} - ik_m^2 f_v^{(n)} - if_v^{(n)}D^2\right),$$

$$\begin{aligned} I_v^{(m-n)} = {} & k_{m-n}^{-2}\left[in\alpha\left(\beta^2 - t_m t_{m-n}\right)Df_u^{(n)}D + k_m^2\left(\beta^2 + t_{m-n}t_{m-2n}\right)f_v^{(n)}D\right] \\ & + k_{m-n}^{-2}\left[i\left(-k_{m-n}^2 t_m + 2n\alpha\beta^2\right)f_u^{(n)}D^2 + \left(n\alpha t_{ml} - k_m^2\right)f_v^{(n)}D^3\right], \\ & + ik_m^2 t_{m-2n}f_u^{(n)} + it_m D^2 f_u^{(n)} \end{aligned}$$

$$J_\zeta^{(m-n)} = -in\alpha\beta k_{m-n}^{-2} f_\theta^{(n)},$$

$$J_v^{(m-n)} = -n\alpha k_{m-n}^{-2} t_{m-n} f_\theta^{(n)} D + Df_\theta^{(n)},$$

$$J_\theta^{(m-n)} = it_{m-n}f_u^{(n)} + f_v^{(n)}D.$$

The boundary conditions take the form

$$\zeta^{(n)}(\pm 1) = 0,\ g_v^{(n)}(\pm 1) = 0,\ Dg_v^{(n)}(\pm 1) = 0,\ g_\theta^{(n)}(\pm 1) = 0 \qquad \text{for } -\infty<n<+\infty. \tag{3.15}$$

It may be noted that, in this work, the stability analysis is limited to two-dimensional primary convection only. Consequently, the required expressions for the basic state (primary convection) to use in (3.14) have the form

$$\bar{v}_2(x,y) = \sum_{n=-\infty}^{n=+\infty}\left[f_u^{(n)}(y), f_v^{(n)}(y), 0\right]e^{in\alpha x} \tag{3.16a}$$

$$\theta_2(x,y) = \sum_{n=-\infty}^{n=+\infty} f_\theta^{(n)}(y)\, e^{in\alpha x} \tag{3.16b}$$

where, $f_u^{(n)} = D\varphi^{(n)}$, $f_v^{(n)} = -in\alpha\varphi^{(n)}$, and $f_\theta^{(n)} = Pr^{-1}\theta_0^{(n)} + \phi^{(n)}$.

3.3 Method of solution

Equations (3.6) (or (3.14)) together with the boundary conditions (3.7) (or (3.15)) are truncated after N_M modes. The resulting system has a nontrivial solution only for certain combinations of parameters Ra, Pr, δ, β, α and σ. The required dispersion relation has to be determined numerically through solution of the relevant eigenvalue problem. For the purposes of calculations, the problem is posed as an eigenvalue problem for σ. Equations (3.6) and (3.14) are discretized with spectral accuracy using Chebyshev collocation method with N_T collocation points (Canuto et al. 2006). The relevant numerical parameters (i.e., N_M and N_T) have been selected through numerical convergence studies as shown in Appendix E.

The above discretization procedure results in a matrix eigenvalue problem in the form

$$\Omega x = 0, \tag{3.17}$$

where $\Omega(\sigma)$ represents the coefficient matrix. This matrix is linear in σ, i.e.,

$$\Omega = \Omega_0 + \Omega_1\sigma, \tag{3.18}$$

where $\Omega_0 = \Omega(0)$, $\Omega_1 = \Omega(1) - \Omega_0$.

Using the property (3.18) of the coefficient matrix, finally we end up with a generalized eigenvalue problem in the form,

$$\Omega_0 x = \sigma\Omega_1 x. \tag{3.19}$$

3.3.1 Evaluation of eigenvalue

From a numerical point of view, there are two general concepts of finding the eigenvalues of a discretized stability equation (Schmid and Henningson 2000). The first method, the local method, starts with an initial guess of the eigenvalue or the eigenvector, and uses iteration procedure to converge to the true eigenvalue or the eigenvector. Local method may be employed either by using the Newton-Raphson search method which uses an initial guess of the eigenvalue, or by using 'inverse iteration' technique which uses eigenvector as the initial guess. The second method, the global method, uses complete discretized stability equation and computes spectrum of the resulting matrix. The advantage of the local method is that it is high in accuracy and requires less computational time but it computes only one eigenvalue or one set of eigenvectors, whereas the global method is computationally expensive but it computes the full spectrum. The virtue of full spectrum computations is that they provide the safest means of identifying all possible instability modes. Situations have arisen in the literatures in which iterative computations (local method) led to the most important branch of eigenvalues being missed (Ding and Kawahara 1998). Of no less significance is the fact that full spectrum information aids in the classification of different branches of eigenvalue, corresponding to different physical phenomena (Theofilis 2011). It may be noted that full spectrum computations help to assess the effect of grid-resolution (see Appendix E). Details of the aforementioned methods are given in Appendix D, in the next sections we describe them only briefly.

3.3.2 Full spectrum computation

The σ-spectrum is determined by solving a general eigenvalue problem (3.19). Since the eigenvalues are complex in nature, we use the method described in (Golub and Loan 1996). From computed eigenvalues, the top 100 eigenvalues are further refined (to test their sensitivity) using the 'inverse iteration' technique as described in (Saad 2011).

3.3.3 Newton-Raphson search method

In this method, we alter flow conditions and produce an approximation for the eigenvalue which is then improved iteratively by searching for the near-by zero of the determinant using a Newton–Raphson search procedure (for details see Appendix D). A reasonable guess for the unknown eigenvalue is essential for the convergence of this search routine.

3.3.4 Inverse iteration method

We compute an approximation for the eigenvector Λ_a corresponding to the unknown eigenvalue σ_a using an iterative process in the form $(\Omega_0 - \sigma_0\Omega_1)\Lambda^{(n+1)} = \Omega_1\Lambda^{(n)}$ where σ_0 and $\Lambda^{(0)}$ are the eigenvalue and the eigenvector (an eigenpair) corresponding to the unaltered flow. If σ_a is the eigenvalue closest to σ_0, $\Lambda^{(n)}$ converges to Λ_a. The eigenvalue σ_a is evaluated using formula $\sigma_a = \Lambda_a^* \Omega_0 \Lambda_a / \Lambda_a^* \Omega_1 \Lambda_a$ where asterisk denotes the complex conjugate transpose. The inverse iterations method was found to be generally more efficient.

3.3.5 Eigenvalue tracing

To produce various stability diagrams we need to trace the eigenvalues in the parameter space. For the tracing of the eigenvalues we use a special version of the Newton-Raphson search procedure described in Appendix D.

3.4 General stability formulation

The distributed heating considered so far is one-dimensional, i.e., it varies only in the longitudinal direction x. If we consider a two-dimensional heating pattern, i.e., heating which varies both in longitudinal (x) and transverse (z) directions, then the primary convection has also a three-dimensional character. Therefore, a more general form of

stability equations has been derived by considering three-dimensional primary convection. Details are shown in Appendix B and C.

3.5 Summary of stability analysis

In this section we summarize the general steps that are used in the stability analysis in the pictorial form.

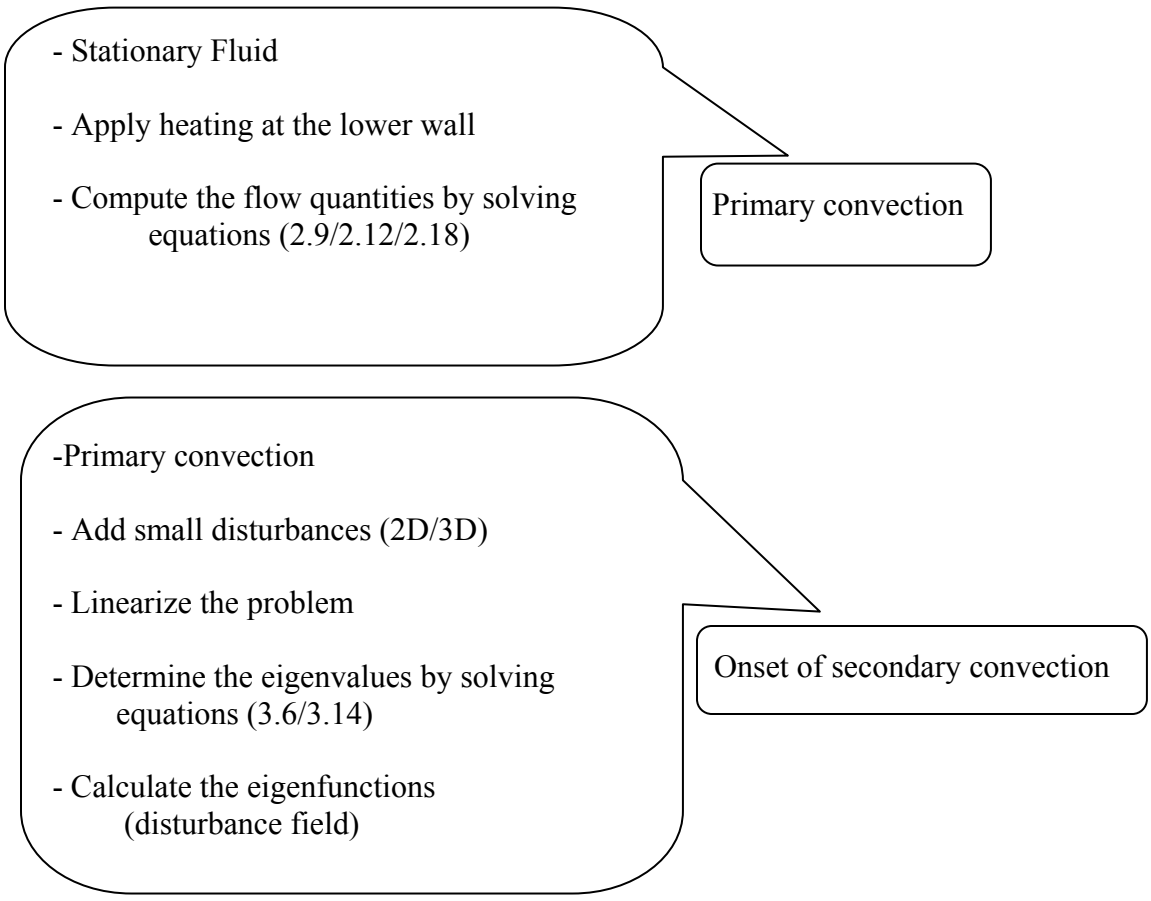

Figure 3.1. *Summary of general steps used for stability analysis.*

3.6 Types of instability identified

From chapter 2 we have seen that the primary convection has the form of rolls whose topology is tightly coupled to the heating pattern. These rolls are subject to instabilities that give rise to various forms of secondary convection. We performed various tests in the parameter space to obtain the stability characteristics of the primary convection. We have identified that the following four types of instability emerge for the spatially periodic heating pattern considered in this work,

i. Longitudinal roll instability,
ii. Transverse roll instability,
iii. Oblique roll instability,
iv. Oscillatory mode of instability.

Details of each of the instabilities will be discussed in the subsequent chapters.

4

Longitudinal Roll

In this chapter, we discuss the longitudinal roll instability, i.e., instability that gives rise to secondary rolls with axis parallel to the axis of the primary rolls. The onset of the longitudinal roll instability can be predicted using the two-dimensional stability theory (Floryan 2005) described in Chapter 3 (see Section 3.1). Various test calculations and scans through the parameter space suggest that there exist only stationary disturbances of such form, i.e., $\sigma_r = 0$. No travelling wave disturbances have been found. Characteristics of this instability for fluids with the Prandtl number Pr = 0.71 are discussed in Section 4.1, for Pr = 7 in Section 4.2, for Pr = 0.04 in Section 4.3, for Pr = 0.25 in Section 4.4 and for fluids with arbitrary Prandtl numbers in Section 4.5. A short summary is given in Section 4.6.

4.1 Fluids with the Prandtl number Pr=0.71

To discuss the longitudinal roll instability of the fluid with Pr = 0.71 which approximates properties of Air, we begin with **Figure 4.1** which shows the amplification rate σ_i of the longitudinal roll as a function of the heating wave number α, and the roll wave number δ for a fixed intensity of the heating corresponding to the Rayleigh number Ra = 3900. It can be seen that there exists a finite range of α that results in the instability. The instability does not occur if the heating pattern is characterized by a wavelength that is either too long or too short. The range of wavelengths of the rolls that may emerge from this instability is also finite with the most amplified wave number corresponds to $\delta \approx 2$.

A set of neutral curves (curves corresponding to $\sigma_i = 0$) for a sequence of Rayleigh numbers is displayed in **Figure 4.2**. It can be seen that a decrease of the heating intensity (decrease of Ra) results in the reduction of the range of the heating patterns (reduction of the range of the heating wave numbers) that can lead to the instability and, at the same time, reduction in the range of the roll wave numbers δ that can be produced by the instability. The instability does not occur at all for Ra < ~3100.

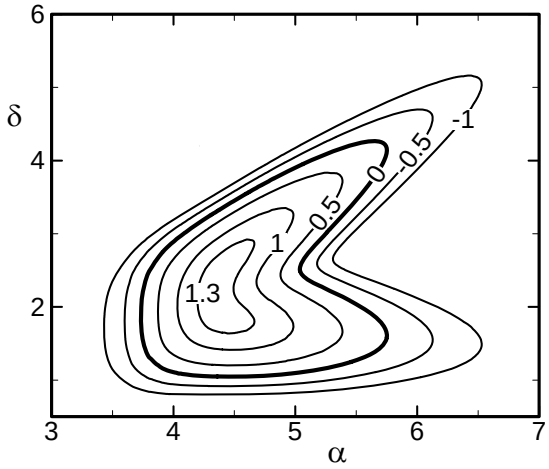

Figure 4.1. *Variations of the amplification rate σ_i of the longitudinal rolls as a function of the heating wave number α and the longitudinal roll wave number δ for the Rayleigh number Ra = 3900 and fluids with the Prandtl number Pr = 0.71.*

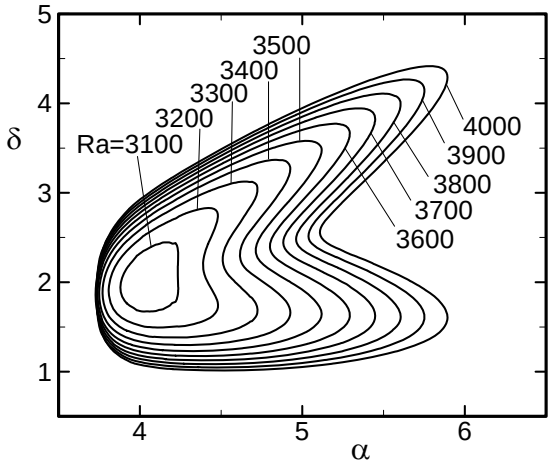

Figure 4.2. *Variations of the neutral stability conditions defined by $\sigma_i = 0$ as a function of the heating wave number α and the longitudinal roll wave number δ for selected values of the Rayleigh number Ra for fluids with the Prandtl number Pr = 0.71.*

One can identify the upper and lower limits of the unstable range of α for each value of Ra and the corresponding values of δ to produce plots displayed in **Figure 4.3**. Such plots identify the critical conditions leading to the onset of the longitudinal roll instability. The intensity of the heating required to induce roll instability, as measured by Ra_{cr}, is a strong function of the heating wave number α. It can be seen that there is a certain minimum heating intensity defined by $Ra_{min} = Ra_A = 3031.6$ (point A in **Figure 4.3**A) and a corresponding very specific heating pattern corresponding to $\alpha_{min} = \alpha_A = 4.03$ that are required in order to initiate the instability. An increase of Ra above 3031.6 increases the range of heating patterns that can induce this instability. The critical curve steeply rises when α is reduced below α_{min} and, as a matter of fact, this instability does not occur when $\alpha < \alpha_{lb} = 3.72$ in the range of Ra considered in this analysis. An increase of α above $\alpha_A = 4.03$ results in a gradual increase of the critical value of Ra_{cr}; when α is big enough, the increase of Ra_{cr} can be approximated by an asymptotic relation obtained numerically from the character of change of Ra_{cr} and the asymptote has the following form

$$Ra_{cr} \rightarrow 236\ \alpha^{1.5} \text{ as } \alpha \rightarrow \infty. \tag{4.1}$$

In summary, spatial pattern of heating corresponding to $\alpha_{min} = \alpha_A = 4.03$ is the most efficient in inducing instability and any other pattern requires a more intense heating. It appears that heating patterns with a small α are unable to create longitudinal rolls at all.

The structure of the disturbance motion, as described by the critical roll wave number δ_{cr}, is also a strong function of the heating wave number α (see **Figure 4.3**B). When $\alpha < \alpha_{lc} = 4.2$ the heating pattern and the disturbance pattern are locked-in according to the relation $\delta_{cr} = \alpha/2$. When $\alpha > \alpha_{lc}$, the lock-in is broken and there is no obvious relation between the heating pattern and the disturbance pattern. When $\alpha \rightarrow \infty$, variations of δ_{cr} follow the asymptote in the form $\delta_{cr} = 1.56 + 7.05\ e^{-0.85\alpha}$ and, in the limit, the critical wave number reaches value of $\delta_{cr} = 1.56$, which is the same as found in the case of the classical RB convection (Drazin and Reid 1981). This result suggests that there is an analogy between the periodically heated and the uniformly heated fluids for large α.

Results presented in Chapter 2 have already demonstrated that periodic heating in the limit of $\alpha \to \infty$ produces uniform mean vertical temperature gradient with spatial modulations being confined to a very thin layer adjacent to the lower wall. As a result, the convective effects make the lower wall appear to the fluid above as a wall with a uniform temperature.

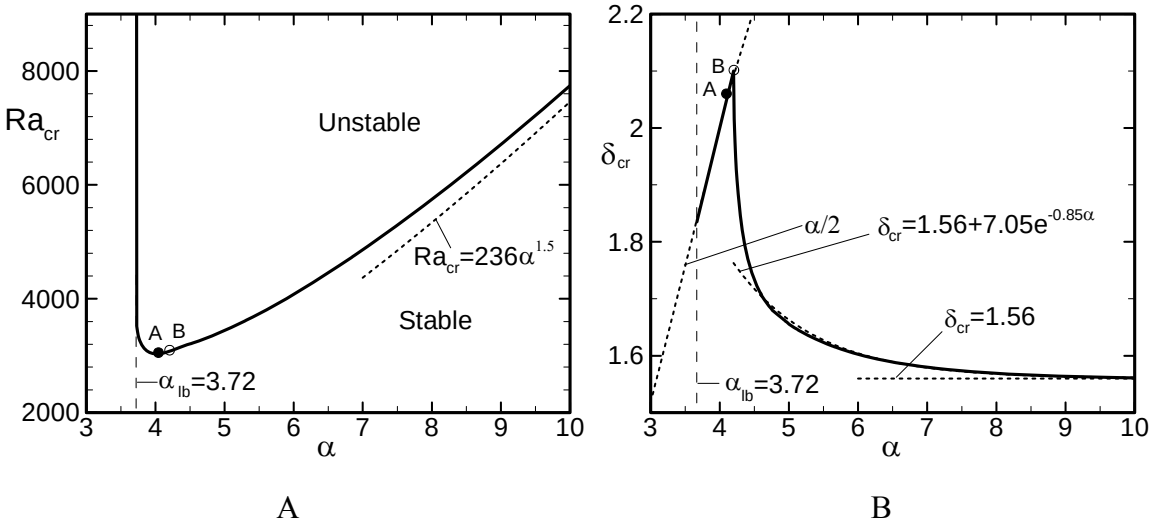

Figure 4.3. *Variations of the critical Rayleigh number Ra_{cr} (Fig.4.3A) and the critical disturbance wave number δ_{cr} (Fig.4.3B) as functions of the heating wave number α for a fluid with the Prandtl number Pr = 0.71 for the longitudinal roll instability. Points A and B are located at (Ra_A=3031.6, α_A=4.03, δ_A=2.015), (Ra_B=3078.3, α_B=4.2, δ_B=2.1).*

Selected properties of the basic state (primary convection) evaluated along the critical curve are displayed in **Figure 4.4**. It can be seen that the net heat flow across the wall Nu, roll strength ψ_{max}, and thickness of the convection layer h_v vary along the critical curve according to the asymptotic relation in the form

$$Nu \to 0.4531\alpha^{-1.5},\ \psi_{max} \to 12.6\,\alpha^{-1.5},\ \ h_v \to 7.2\,\alpha^{-0.81} \ \text{ as } \alpha \to \infty. \qquad (4.2a\text{-}c)$$

The asymptotic relation of Nu (4.2a) can also be obtained by combining variations of Ra_{cr} (4.1) with the correlation (2.25). It also permits to express Ra used in this analysis in terms of the Rayleigh number Ra_{uni} used to describe the classical RB convection. The

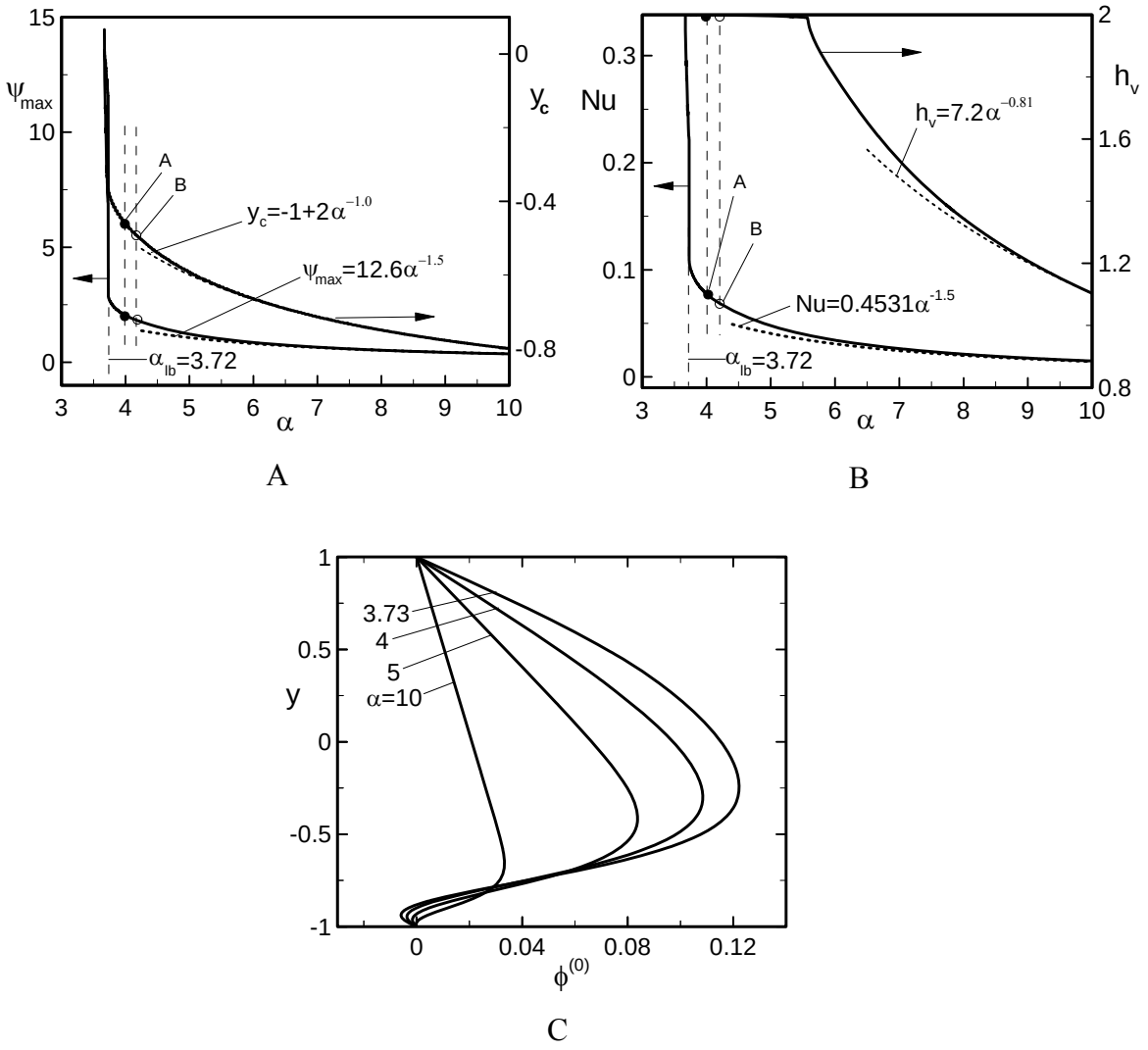

Figure 4.4. *Variations of the selected primary convection properties for conditions corresponding to the onset of the longitudinal roll instability for Pr = 0.71. Fig.4.4A - roll strength as measured by the maximum of the stream function ψ_{max} and location of the center of the roll identified by its coordinate y_c. Fig.4.4B - net heat flow Nu and thickness of the convective layer h_v (determined using Eq. 2.23 with E = 0.01). Fig.4.4C- Distributions of the 0^{th} modal function of the primary convection temperature $\phi^{(0)}$ for selected values of the heating wave number α. (Ra,α) = (7744.4, 10), (3435.2, 5), (3041.8, 4), (3663.4, 3.73). Points A and B in Fig.4.4A,B correspond to points A and B in Fig.4.3.*

latter one is based on the thickness of the complete layer H = 2h as the length scale and its critical value of Ra_{uni} = 1708 can be expressed in terms of Ra as

$$Ra = Ra_{uni} (2\ Nu)^{-1} [h/H]^3 = 235.6\ \alpha^{1.5} \text{ when } \alpha \to \infty. \quad (4.3)$$

The relation (4.3) is in good agreement with the relation (4.1). Detail derivation of (4.3) is shown in Appendix F.

The form of the critical curve displayed in **Figure 4.3**A shows rapid flow stabilization when the heating wave number α decreases a bit below the lock-in value of $\alpha_{lc} = 4.2$. It is to be mentioned that lock-in occurs when the heating pattern and the disturbance pattern follow the subharmonic relation $\delta_{cr} = \alpha/2$, i.e., each disturbance roll carries two primary rolls. The minimum value of Ra_{cr} is reached when $\alpha = 4.03$ and further decreases of α causes rapid increase of Ra_{cr}. One could suppose that the tight lock-in of the basic state (structure of the primary convection) and the disturbance structures is responsible for the rapid stabilization. Another effect that also contributes to the flow stabilization is associated with the re-arrangement of the primary temperature field. To understand this effect we refer to **Figure 2.11** which illustrates large differences in the temperature fields associated with different values of α, and **Figure 4.4**C which displays variations of the mean temperature of the primary convection as a function of α at the onset of the longitudinal roll instability. It can be seen that reduction of α results in an increase of thickness of the part of the fluid layer that has stable mean temperature gradient and this contributes to the flow stabilization.

The occurrence of the lock-in is related to the spatial modulation of the primary convection (Manor et al. 2008, 2009). The modulation is very strong when $\alpha = O(1)$; an increase of α reduces its strength and eventually leads to the break of the lock-in. The break up is not directly related to the appearance of the conductive zone in the primary state temperature as results for h_v (see **Figure 4.4**B) clearly show that the convective effects persist everywhere in the fluid for up to $\alpha \approx 5.5$ while the lock-in occurs only for

$\alpha < \alpha_B = 4.2$. It may be concluded that the breakup of the lock-in is related to the weakening of the spatial flow modulation.

Analysis of results presented in **Figures 4.3-4.4** shows that there are two competing effects that produce the instability mitigated by changes in the mean vertical temperature gradient. In the case of large α the instability is driven by the mean vertical temperature difference created by the primary convection. In the case of α = O(1) the secondary convection is driven by the spatial parametric-like resonance. The conditions that separate the locked-in and unlocked zones (point B in **Figures 4.3-4.4**) may be considered as an approximate boundary between the zones of dominance of either of these two effects.

Pattern of disturbance motion changes considerably with the change of the heating wave number. The pattern for the lock-in situation is rather simple and is illustrated in **Figure 4.5** for α = 4.1, which is just below the lock-in value of α_B = 4.2. The sub-harmonic relation between the primary convection and the disturbance pattern is clearly visible.

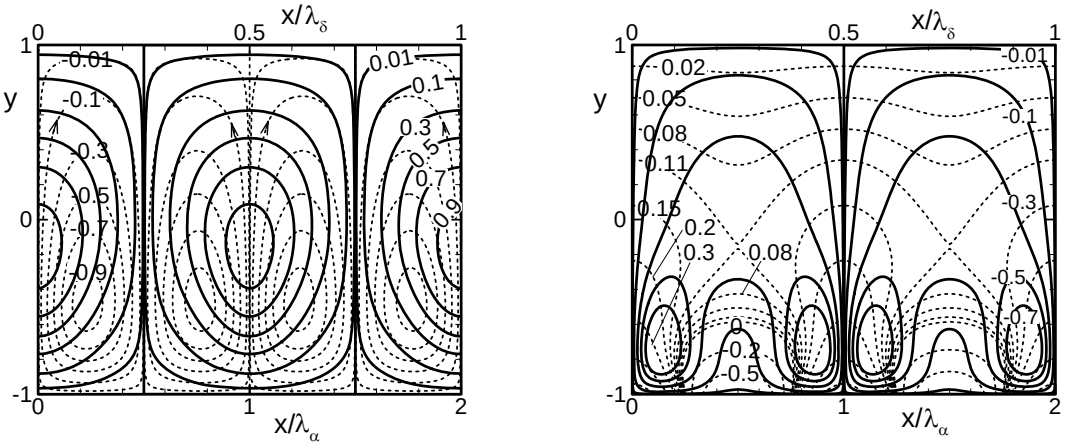

Figure 4.5. *Disturbance streamlines (Fig.4.5A) and isotherms (Fig.4.5B) for the heating wave number α = 4.1 and the Prandtl number Pr = 0.71 at the onset of the longitudinal roll instability*, i.e., for Ra = 3042.3. *These conditions are marked with letter L in Fig.4.8. The primary flow and disturbance quantities are represented using dash and solid lines, respectively. The stream functions and the temperatures are normalized with their maxima for presentations purposes. The maximum values for the primary convection are ψ_{max} = 1.9091 and θ_{max} = 0.7042.*

There are many possible disturbance patterns for the unlocked situation as they result from an interplay between the disturbance wave number δ_{cr} and the modulation (heating) wave number α. These patterns are functions of α and the functional relation is linked to the dispersion relation $\delta_{cr} = \delta_{cr}(\alpha)$. While this relation has been determined numerically, it exhibits properties of a continuous function. In the limit of $\alpha \to \infty$ the relation assumes a very simple form, i.e., $\delta_{cr} \to 1.56$. The numerical results show that this limit is effectively reached for $\alpha > 9$. As $\delta_{cr} = 1.56$ for large α, the system may exhibit commensurable (periodic) and non-commensurable (quasi-periodic) states; only commensurable states can be accessed by the computations. The heating wave number α is the control parameter that provides means for re-arrangement of the system states. It is convenient to categorize commensurable states using wavelength of the flow system expressed either in terms of the number of the disturbance wavelengths N_δ or in terms of the number of the heating wavelengths N_α. The possible system wavelengths can be divided into an infinite sequence of bands associated with each value of N_δ. There is an infinite number of N_α's corresponding to each N_δ, i.e., $N_\alpha = \alpha\, N_\delta / 1.56$ as α can be selected arbitrarily. Since N_α must be integer, it is better to write this relation as $\alpha = 1.56\, N_\alpha / N_\delta$ in order to identify suitable values of α corresponding to N_δ and N_α of interest. Results displayed in **Figure 4.6** illustrate the possible periodic states for each α corresponding to $N_\delta <= 39$.

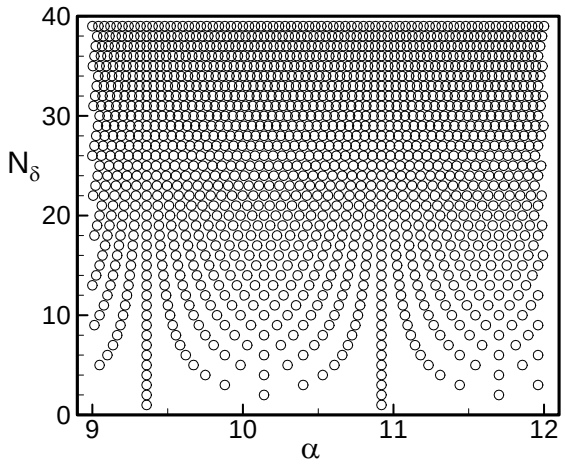

Figure 4.6. *The possible x-periodic states of the system in the "large α" regime. The wavelength of the system is expressed in terms of the number of disturbance wavelengths N_δ.*

A qualitatively similar situation has been analyzed by Freund et al. (2011) who considered modifications of the RB convection near the onset induced by addition of periodic temperature modulations of small amplitude imposed at the lower wall. As the wave number of modifications increased, they observed a continuous bifurcation to longitudinal rolls with the wave number 1.56 followed by bifurcations to transverse rolls with the same wave number. The critical value of Ra_{uni} slightly decreased as compared with the pure RB convection. Results discussed in Chapter 2 demonstrate that temperature modulations with large α create an additional mean vertical temperature gradient which reinforces the gradient created by the uniform heating. This effect is responsible for the reduction of Ra_{uni} required for the onset of the instability reported by Freund et al. (2011), i.e., the lower wall looks slightly hotter to the bulk of the fluid due to the modulation effect. The imposed spatial modulations are confined to a very thin layer and thus give very weak preference to either longitudinal or transverse rolls. The vertical temperature gradient in the case of purely periodic heating considered in the present analysis is created solely by the nonlinear effects and this requires heating more intense than the equivalent uniform heating in order to reach the critical conditions (see equation (3.9) and **Figure 4.4**A).

When α is large the flow patterns are rather simple as depicted in **Figure 4.7** and consist of rolls with the wave number $\delta_{cr} = 1.56$ occupying most of the space between the walls with spatial modulations (which dictate the overall system periodicity) confined to a small neighborhood of the heated wall.

Application of the heating with the wave number between the lock-in value of $\alpha_B = 4.2$ and the effective "large α" limit, i.e., $\alpha \approx 9$, produces a number of intriguing flow structures. Commensurable states are illustrated in **Figure 4.8** where N_δ has been determined by looking for the lowest common denominator of α and δ_{cr} (Floryan 1997, 2005). The structures form bands in the (N_δ, α) plane that can be categorized by looking at the corresponding N_δ at the large α limit. The bands have been determined numerically and search for the pairs (δ_{cr}, α) that correspond to the band of interest involves a trial and error. Data presented in **Figure 4.8** have been determined by varying α with constant step

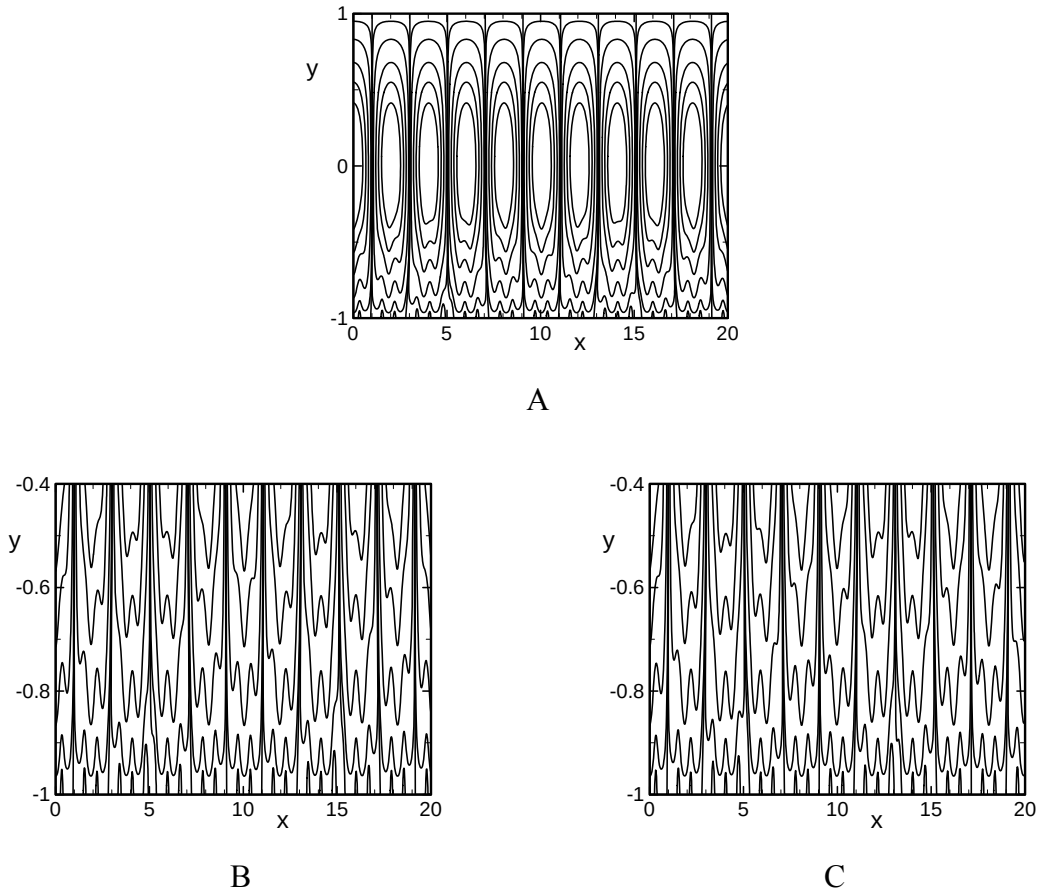

Figure 4.7. *Disturbance flow fields in the "large α" regime at the onset of the longitudinal roll instability. Fig.4.7A: (α, δ_{cr}, Ra_{cr}) = (10.01, 1.56, 7749), complete layer is shown. Fig. 4.7B,C: (α, δ_{cr}, Ra_{cr}) = (10, 1.56, 7738), (10.083, 1.56, 7827),respectively; only zone next to the lower wall is shown. The contour lines correspond to $\psi_3(x,y)$ = 0, 0.01, 0.1, 0.3, 0.5, 0.7 of the respective maxima. Conditions in Fig.4.7A, B, C correspond to the wavelength bands N_δ = 156, 39, 468 (point E, J, K in Fig.4.8), respectively.*

sizes of $\Delta\alpha$ = 1/100 and $\Delta\alpha$ = 1/12. Only certain bands can be reached through such a process as the numerical evaluation of δ_{cr} is done with a finite accuracy. δ_{cr} had been evaluated with an accuracy of four decimal points but only two decimal points were retained for evaluation of N_δ. Results displayed in **Figure 4.8** clearly show bands starting at large α and extending down to the lock-in condition. The bands that have been identified by the above process correspond to N_δ = 39, 78, 117, 156, 234, 468, ... The same bands correspond to $N_\alpha = 25\alpha, 50\alpha, 75\alpha, 100\alpha, 150\alpha, 300\alpha$, ..., i.e., they are linear

functions of the heating wave number α. The same results also show existence of additional bands that do not exist in the large α limit.

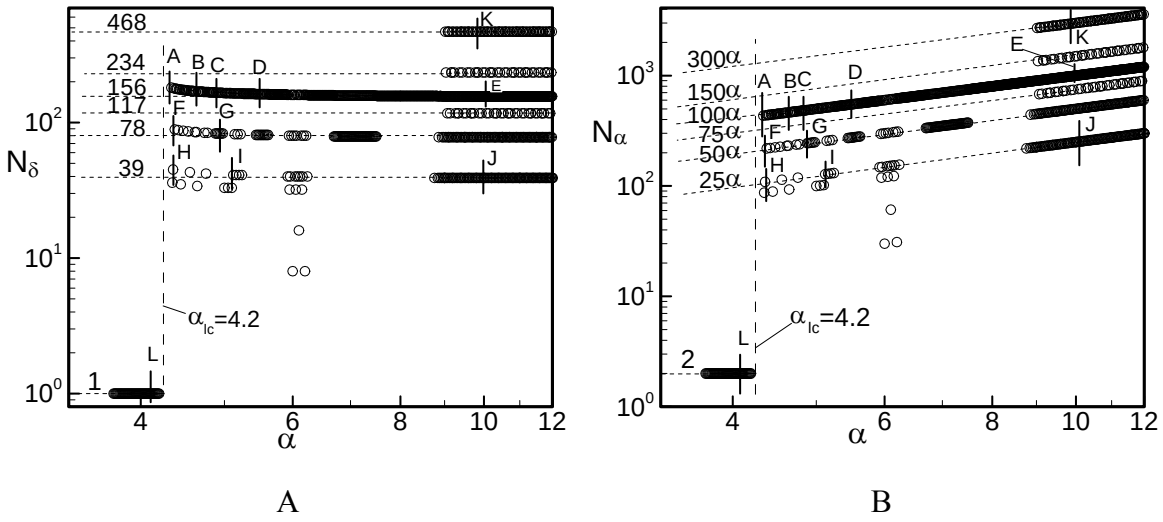

Figure 4.8. *Variations of the wavelength of the disturbance flow structures for the longitudinal roll instability as a function of the heating wave number α at the onset conditions measured using the number of the disturbance wavelengths N_δ (Fig.4.8A) and the number of the heating wavelengths N_α (Fig.4.8B) for fluids with Pr=0.71. Additional information about the structure of the unstable motion corresponding to conditions marked with letters A, ..., E is displayed in Fig.4.9, for F, G is displayed in Fig.4.13, for H and I in Fig.4.14, for J and K in Fig.4.7, and for L in Fig.4.5. The reader should note logarithmic scale on the α-axis.*

Structure of the disturbance field undergoes interesting changes as a function of α for each band. Variations of the disturbance stream function ψ_3 for disturbances belonging to the band $N_\delta = 156$ demonstrate a "beating" pattern for α slightly above α_B (**Figure 4.9**A), followed by a pattern that is not easily categorized (**Figure 4.9**B) for larger α, then followed by a "wavy" pattern for still larger α (**Figure 4.9**C), and followed by a still another not easily categorized pattern (**Figure 4.9**D) and leading to a pattern dominated by δ_{cr} for sufficiently high α (**Figure 4.9**E). While the terms "beating" and "wavy" are rather arbitrary, they nevertheless well capture changes in the amplitude of disturbances. Streamlines for the "beating" pattern displayed in **Figure 4.10** show that the disturbance

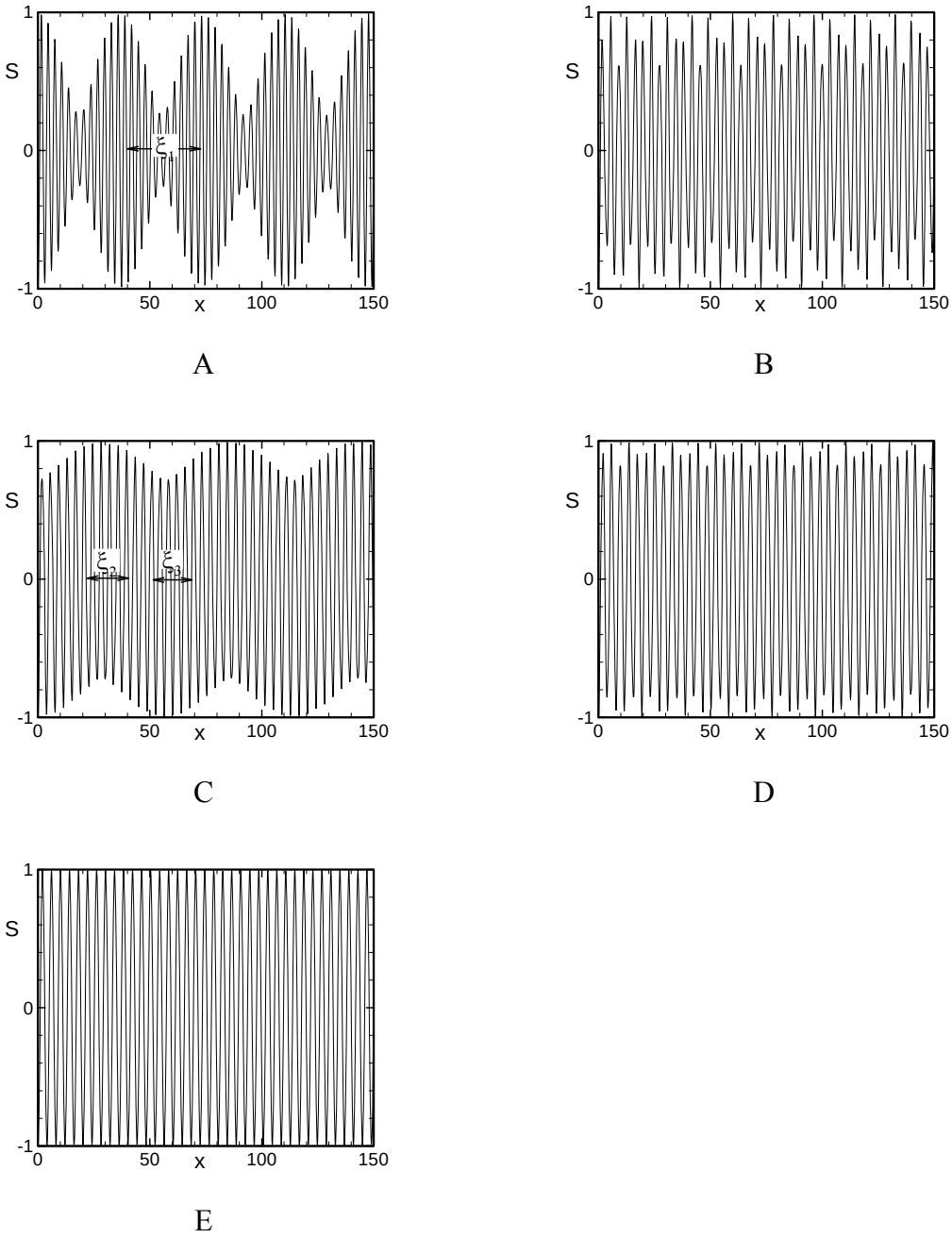

Figure 4.9. *Variations of the disturbance stream function $S = \psi_3(x,0)$ at $y = 0$ for the wavelength band corresponding to $N_\delta = 156$ for $Pr = 0.71$. Results shown in Figs 4.9A, B, C, D, E correspond to the onset conditions, i.e., (α, δ_{cr}, Ra_{cr}) = (4.21, 2.02, 3083), (4.5,1.73, 3208), (4.9, 1.67, 3389), (5.51,1.62, 3742) and (10.01,1.56, 7749), respectively, and are marked with letters A, B, C, D, E in Fig.4.8, respectively.*

field consists of rolls of almost the same topology but with their strength changing in a periodic manner along the layer. One can easily identify zones with high and low intensities of instability. Streamlines for the "wavy" pattern displayed in **Figure 4.11** show that the disturbance flow field consists of pairs of rolls rotating in the opposite directions with "opposite" characteristics, i.e., at the beginning of the spatial cycle one roll is larger but has less intense motion and the other one is smaller and has more intense motion. Their characters are reversed after half cycle, with the smaller roll expanding and motion in its interior slowing down and the larger one contracting and motion in its interior intensifying.

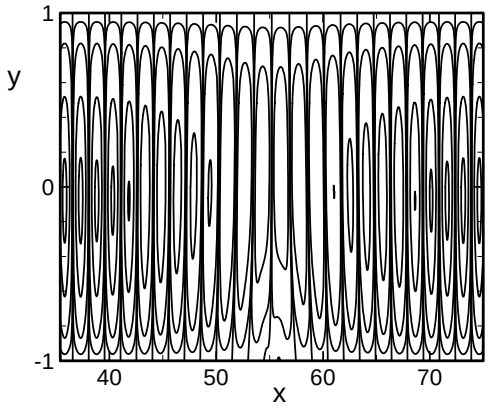

Figure 4.10. *Disturbance flow field corresponding to the "beating" pattern at the critical point (α, δ_{cr}, Ra_{cr}) = (4.21, 2.02, 3083) and for the fluid with the Prandtl number Pr = 0.71. The contour lines shown correspond to $\psi_3(x,y)$ = 0, 0.01, 0.1, 0.5, 0.7 of its maximum. The range of x used for display is marked using symbol ξ_1 in Fig.4.9A. This pattern belongs to the wavelength band N_δ = 156.*

An insight into the patterns is provided by modulations of the phase illustrated using the local wave number δ_{local} determined on the basis of zero's of the disturbance stream function displayed in **Figure 4.9**. One may observe a competition between the locked-in wave number $\delta_{cr} = \alpha/2$ and the "large α" wave number $\delta_{cr} = 1.56$. In the case of the "beating" pattern (**Figure 4.9**A, $\alpha = 4.21$) the system is still strongly influenced by the lock-in effect producing wide and flat maxima with $\delta_{local} \sim 2.08$ separated by narrow minima with $\delta_{local} \sim 1.8$ giving appearance of a solitary phase modulation (see **Figure**

4.12A). These solitons form a lattice that is parallel to the rolls. Solitons are known to mediate transition between the commensurate and non-commensurate patterns and have been observed in pattern forming hydrodynamic instabilities, e.g., Lowe and Gollub (1985), Seiden et al. (2008) and McCoy et al. (2008). The maxima of δ_{local} correlate with the areas of high intensity motion and the minima correspond to the zones of low intensity motion. In the case of the "wavy" pattern (**Figure 4.9**C, $\alpha = 4.9$), both effects are at par resulting in a continuous and rapid adjustment of δ_{local} between 1.56 and 1.8 (see **Figure 4.12**B) that is repeated periodically in the x-direction and forms a lattice. The minima of the amplitude of variations of δ_{local} correspond to zones where the rolls with the clockwise and counter clockwise rotations have similar intensity while maxima identify regions with a preferred direction of rotation. In the large alpha zone (**Figure 4.9**E) δ_{local} overlaps with $\delta_{cr} = 1.56$ within the numerical accuracy.

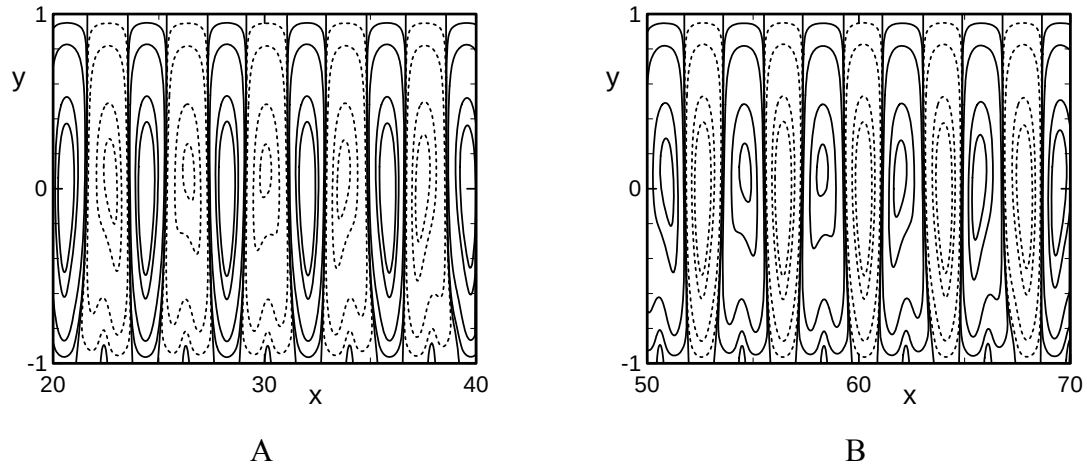

Figure 4.11. *Disturbance flow field corresponding to the "wavy" pattern at the critical point (α, δ_{cr}, Ra_{cr}) = (4.9, 1.67, 3389) and for the fluid with Pr = 0.71. The contour lines shown correspond to $\psi_3(x,y)$ = 0, 0.01, 0.1, 0.5, 0.7 of its maximum. Solid and dot lines are used to identify rolls rotating in the opposite directions. Results displayed in Fig.4.11A and 4.11B correspond to the ranges of x marked with symbols ξ_2 and ξ_3 in Fig.4.9C, respectively. This pattern belongs of the wavelength band $N_\delta = 156$.*

Analysis of disturbance field for disturbances belonging to band $N_\delta = 78$ shows existence of structures similar to those found for $N_\delta = 156$. Both the "beating" and the "wavy"

patterns are clearly visible in **Figure 4.13**, however, they have different wavelengths as compared with the case of $N_\delta = 156$. Similar analysis carried out for the band $N_\delta = 39$ (see **Figure 4.14**) shows existence of the "wavy" pattern while the "beating" pattern is less clear; it is believed that a clear "beating" pattern can be determined using more accurate evaluation of the pair (δ_{cr}, α). These results indicate that the "beating" and "wavy" patterns are likely to occur for all bands of N_δ, but with a different spatial wavelengths and amplitudes which depend of the particular value of N_δ. This conclusion is supported by results obtained for other values of the Prandtl number discussed in the following sections.

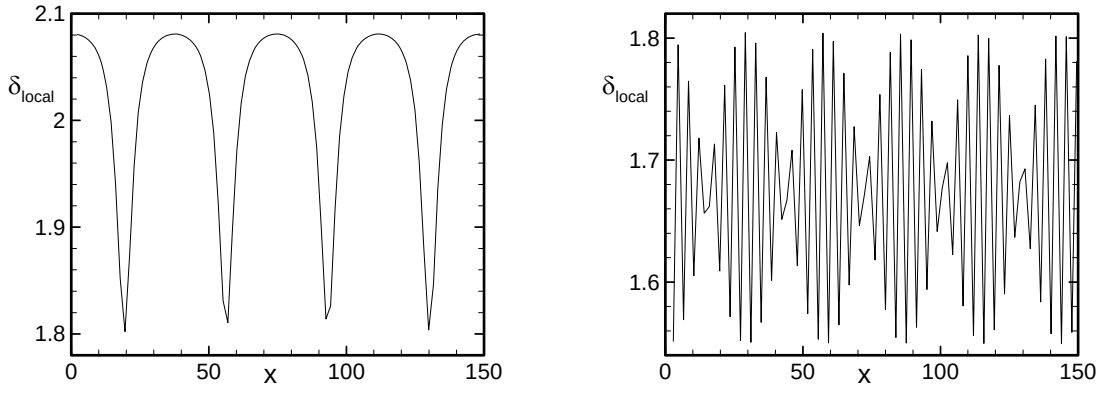

A B

Figure 4.12. *Solitary roll structure. Results displayed in Figs 4.12A, B have been extracted from the data displayed in Figs 4.9A and C, respectively.*

Results displayed in **Figure 4.9**E show that for large α the disturbance pattern around the center of the slot is dominated by δ_{cr}. This pattern is modulated by wall heating, however, modulation is contained in a thin layer adjacent to the lower wall. **Figure 4.7** displays disturbance streamlines for $\alpha \approx 10$ in the zone adjacent to the lower wall for disturbance bands corresponding to $N_\delta = 39$ and $N_\delta = 468$. It can be seen that both patterns are very similar, despite large difference of N_δ, and cannot be easily categorized.

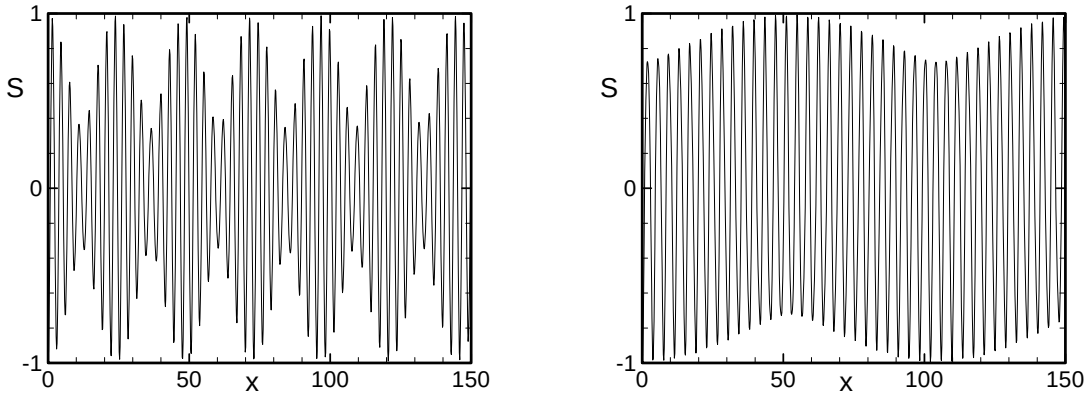

Figure 4.13. *Variations of the disturbance stream function $S = \psi_3(x,0)$ at $y = 0$ for the wavelength band corresponding to $N_\delta = 78$ for the fluid with $Pr = 0.71$. Results shown in Figs 4.13A, B correspond to the onset conditions, i.e., $(\alpha, \delta_{cr}, Ra_{cr}) = (4.22, 1.98, 3086)$, $(4.92, 1.66, 3399)$, respectively, and are marked with letters F, G in Fig.4.8, respectively.*

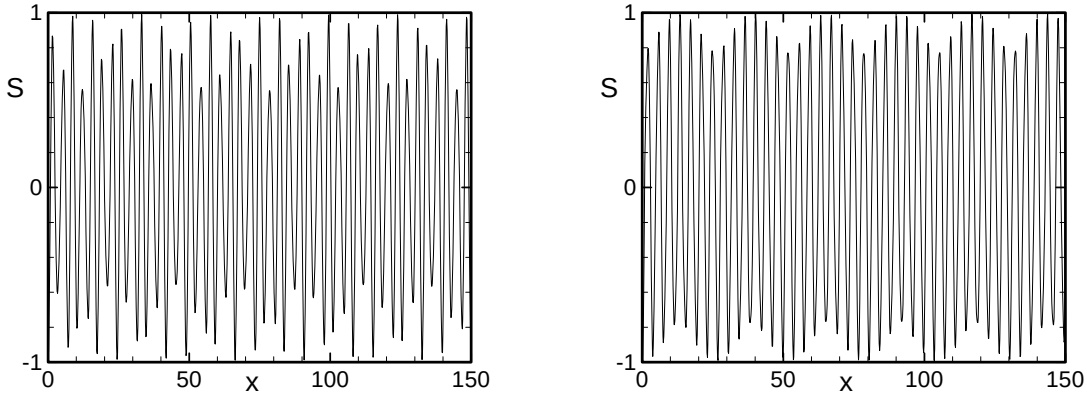

Figure 4.14. *Variations of the disturbance stream function $S = \psi_3(x,0)$ at $y = 0$ for the wavelength band corresponding to $N_\delta = 39$ for the fluid with $Pr = 0.71$. Results shown in Figs 4.14A, B correspond to the onset conditions, i.e., $(\alpha, \delta_{cr}, Ra_{cr}) = (4.36, 1.8, 3151)$, $(5.16, 1.64, 3532)$, respectively, and are marked with letters H, I in Fig.4.8, respectively.*

4.2 The Case of Pr=7

This particular value of the Prandtl number well approximates properties of water. It also serves as an example of large Pr fluids as differences found in the stability characteristics for fluids with Pr = 7 and Pr = 100 are rather small.

Variations of the critical Rayleigh number Ra_{cr} and the critical wave number δ_{cr} as a function of the heating wave number α are displayed in **Figure 4.15**. The forms of these curves are qualitatively very similar to the case of Pr = 0.71 shown in **Figure 4.3**. The minimum heating intensity required to initiate the longitudinal roll instability for fluid with Pr = 7 is $Ra_{min} = Ra_A = 2901.2$ (point A) and it occurs for $\alpha_{min} = \alpha_A = 3.93$. The complete stabilization occurs for $\alpha < \alpha_{lb} = 3.6$ in the range of Ra subject to this investigation. The lock-in occurs at point B for $\alpha < \alpha_B = 4.37$. The asymptotes for large α are $Ra_{cr} \rightarrow 236\ \alpha^{1.5}$ and $\delta_{cr} \rightarrow 1.56$.

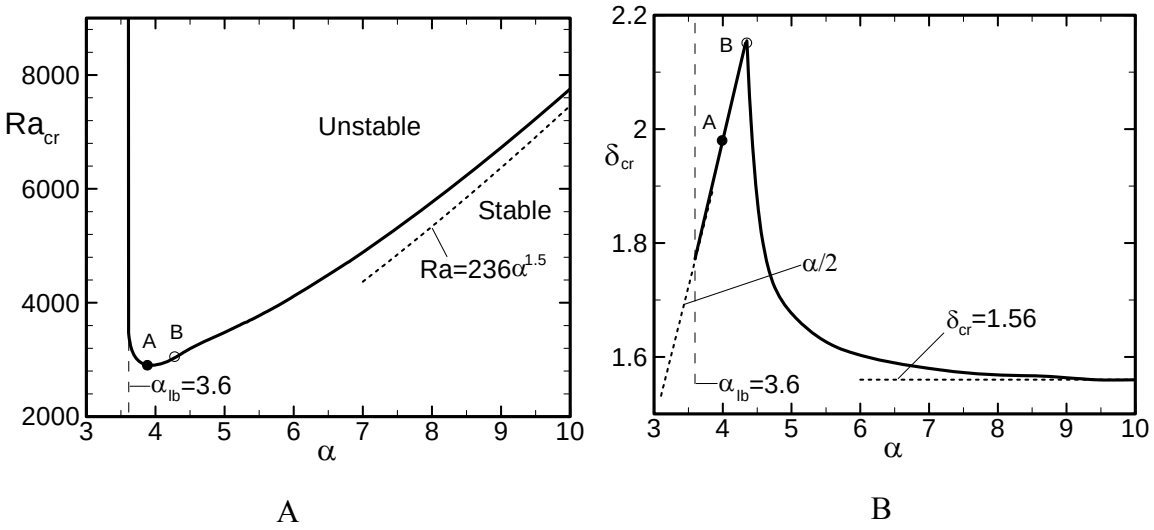

Figure 4.15. *Variations of the critical Rayleigh number Ra_{cr} (Fig.4.15A) and the critical disturbance wave number δ_{cr} (Fig.4.15B) as functions of the heating wave number α for Pr = 7. Points A and B are located at (Ra_A=2901.2, α_A=3.93, δ_A=1.965), (Ra_B=3100.9, α_B=4.37, δ_B=2.185).*

After performing the analysis similar to the fluid with Pr = 0.71, the commensurable states (in term of N_δ) and the patterns of the disturbance motion for the fluid with Pr = 7 in the no-lock zone are illustrated in **Figures 4.16** and **4.17**. It can be seen that for large α disturbance patterns can be divided into an infinite number of branches with the first five corresponding to N_δ = 39, 78, 156, 234, 468, similarly as in the case of Pr = 0.71. These branches extend to smaller α, up to its lock-in value of α_{lc} = 4.37, and exhibit both the "beating" and the "wavy" patterns (see **Figures 4.17**). The reader may observe large differences in the amplitudes of these patterns.

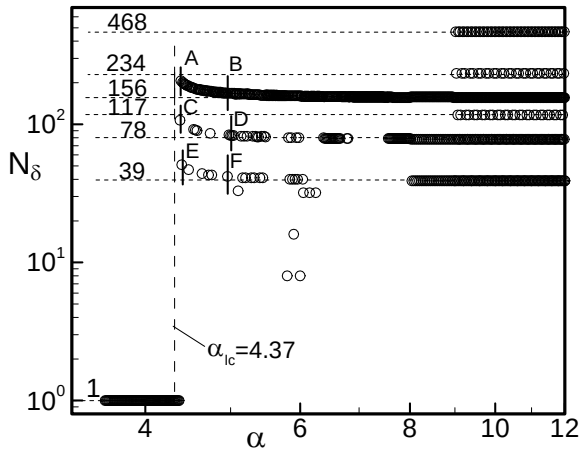

Figure 4.16. *Variations of the wavelength of the disturbance flow structures for the longitudinal roll instability as a function of the heating wave number α at the onset conditions measured using the number of the disturbance wavelengths N_δ for Pr = 7. Additional information about the structure of the unstable motion corresponding to conditions marked with letters A, ..., F is displayed in Fig.4.17. The reader should note logarithmic scale on the α-axis.*

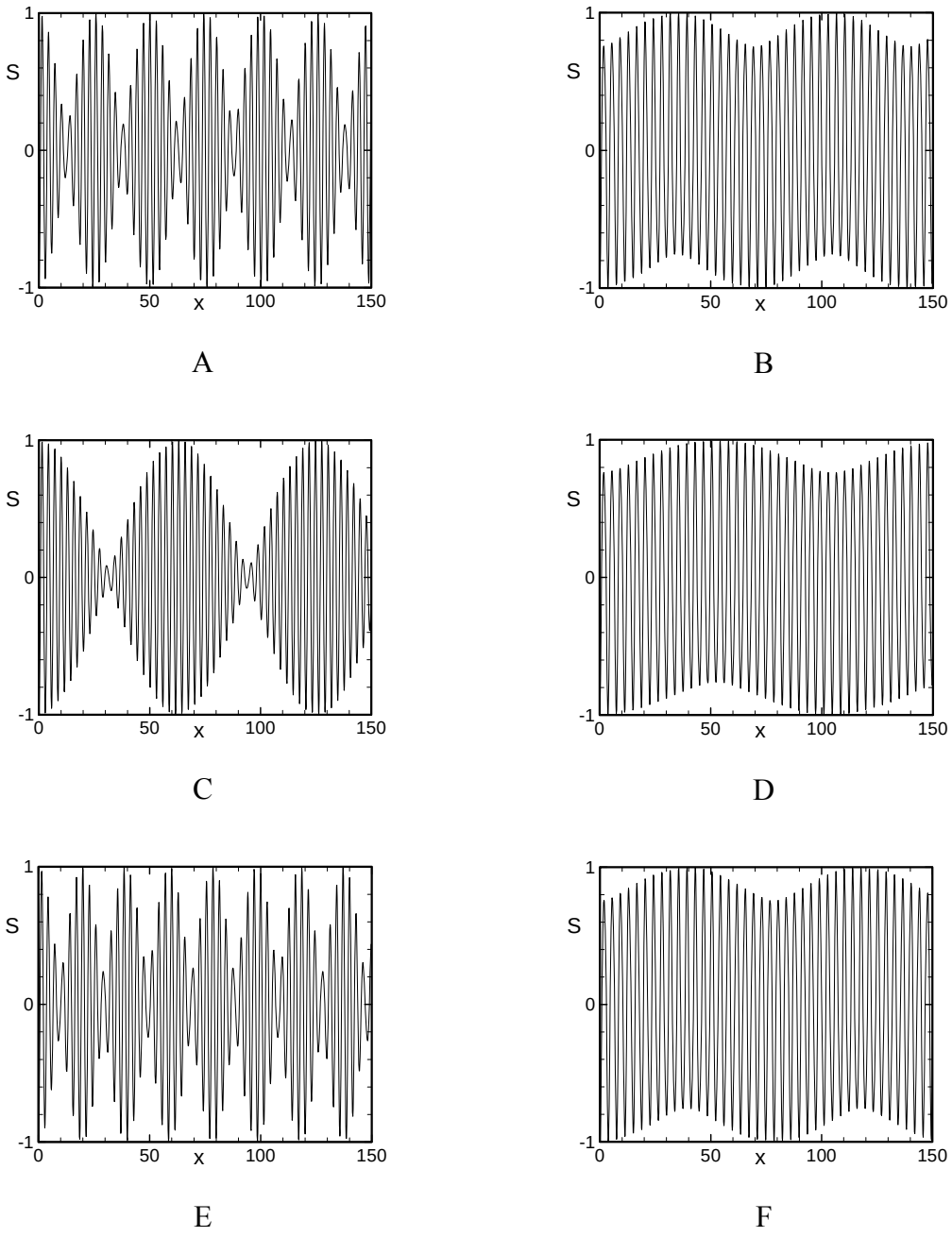

Figure 4.17. *Variations of the disturbance stream function $S = \psi_3(x,0)$ at $y = 0$ for $Pr = 7$. Results shown in Fig.4.17A,B belong to the wavelength band $N_\delta = 156$ and correspond to the onset conditions, i.e., $(\alpha, \delta_{cr}, Ra_{cr}) = (4.39, 2.07, 3116.8), (4.95, 1.68, 3454.1)$, and are marked with symbols A, B in Fig.4.16, respectively. Results shown in Fig.4.17C, D belong to $N_\delta = 78$ and correspond to the onset conditions, i.e., $(\alpha, \delta_{cr}, Ra_{cr}) = (4.38, 2.14, 3108.9), (4.98, 1.68, 3469.9)$, and are marked with symbols C, D in Fig.4.16, respectively. Results shown in Fig.4.17E, F belong to $N_\delta = 39$ and correspond to the onset conditions, i.e., $(\alpha, \delta_{cr}, Ra_{cr}) = (4.4, 2.04, 3124.5), (4.96, 1.68, 3459.6)$, and are marked with symbols E, F in Fig.4.16, respectively.*

4.3 The Case of Pr=0.04

This particular value of the Prandtl number has been selected to represent low Pr fluids and is typical for liquid metals. Variations of the critical Rayleigh number Ra_{cr} and the critical wave number δ_{cr} as a function of the heating wave number α are displayed in **Figure 4.18** and demonstrate qualitatively different responses of the system. Two critical branches have been identified. The first one describes system response for smaller heating wave numbers, i.e., $\alpha < \alpha_B = 8.76$, where rolls that are locked-in with the heating pattern according to a sub-harmonic relation in the form $\delta_{cr} = \alpha/2$. The minimum value of Ra for this branch is $Ra_{min,1} = Ra_A = 1087.7$ and it occurs at $\alpha_{min,1} = \alpha_B = 4.04$. The rolls are fully stabilized for $\alpha < \alpha_{lb} = 3.8$ for the range of Ra considered and the critical Rayleigh number increases as $Ra_{cr} = 9.8\alpha^{3.1}$ for $\alpha \to \infty$ The second branch describes critical conditions for larger heating wave numbers, i.e., $\alpha > \alpha_B = 8.76$, where the rolls are not locked-in with the heating. The minimum value of Ra for this branch is $Ra_{min,2} = Ra_C = 6289.4$, it corresponds to the minimum value of the disturbance wave number $\delta_{cr} = \delta_{min,2} = 0.96$ and it occurs at $\alpha_{min,2} = \alpha_C = 9.8$. The Rayleigh number increases as $Ra_{cr} \to 236\alpha^{1.5}$ and $\delta_{cr} \to 1.56$ when $\alpha \to \infty$. Two different disturbance structures co-exist at the onset of instability for the heating wave number $\alpha = \alpha_B = 8.76$, i.e., the locked-in structure characterized by $\delta_{B,1} = 4.38$ and the unlocked structure described by $\delta_{B,2} = 1.61$.

The disturbance velocity and temperature fields for the locked-in patterns (branch one) at the onset of instability are illustrated in **Figure 4.19** for conditions corresponding to $\alpha_A = 4.04$ and in **Figure 4.20** for conditions corresponding to the intersection of both branches, i.e., $\alpha_B = 8.76$. The sub-harmonic relation between the primary convection and the disturbance field is clearly visible. The emergence of the second layer of rolls at the top of the slot for larger heating wave numbers is observed.

Commensurable states (in term of N_δ) of the disturbance field for the second instability branch are illustrated in **Figure 4.21**. These patterns can be divided for large α into an infinite number of branches with the first five corresponding to N_δ = 39, 78, 156, 234, 468, similarly as in the case of Pr = 0.71 and Pr = 7. These branches extend to smaller α but do not intersect with the locked-in branch. Pattern corresponding to the intersection of both branches, i.e., α_B = 8.76, corresponds to N_δ = 156 and is displayed in **Figure 4.22**. This pattern is markedly different from the branch one pattern at the intersection point displayed in **Figure 4.20** and its form is difficult to characterize. Increase of α above α_B = 8.76 leads to the appearance of the "beating" patterns for the lowest three branches considered, as shown in **Figure 4.23**. No "wavy" patterns have been found.

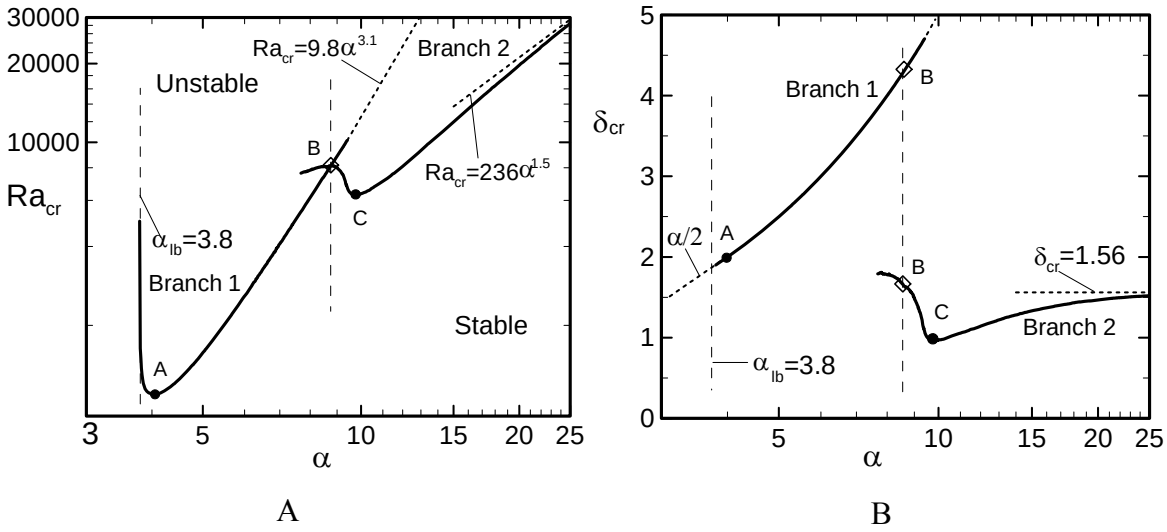

Figure 4.18. *Variations of the critical Rayleigh number Ra_{cr} (Fig.4.18A) and the critical disturbance wave number δ_{cr} (Fig.4.18B) as functions of the heating wave number α for Pr = 0.04. Points A and B are located at (Ra_A=1087.7, α_A=4.04, δ_A=2.02), (Ra_B=8142.9, α_B=8.76, $\delta_{B,1}$=4.38, $\delta_{B,2}$=1.61), (Ra_C=6289.4, α_C=9.8, δ_C=0.96). The reader should note logarithmic scales on the α- and Ra_{cr} -axes, and two values of δ_B for Branch 1 and Branch2.*

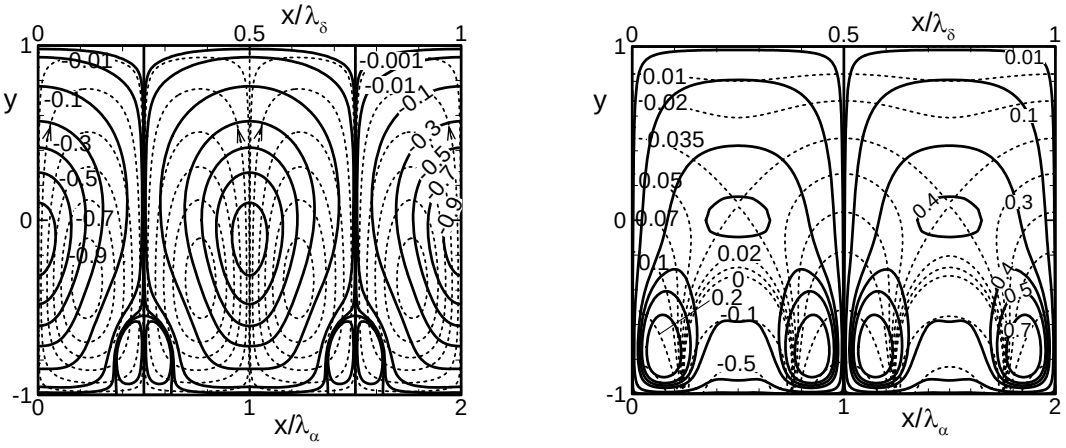

A B

Figure 4.19. *Disturbance streamlines (Fig.4.19A) and isotherms (Fig.4.19B) for branch one of the instability for the heating wave number* $\alpha = \alpha_A = 4.04$ *and the Rayleigh number* $Ra_{cr} = Ra_A = 1087.7$ *for the fluid with the Prandtl number Pr = 0.04. These conditions correspond to point A in Fig.4.21. Primary flow and disturbance quantities are represented using dash and solid lines, respectively. The stream functions and the temperatures are normalized with their maxima for presentations purposes. The maximum values for the primary convection are* $\psi_{max} = 13.13$ *and* $\theta_{max} = 12.5$.

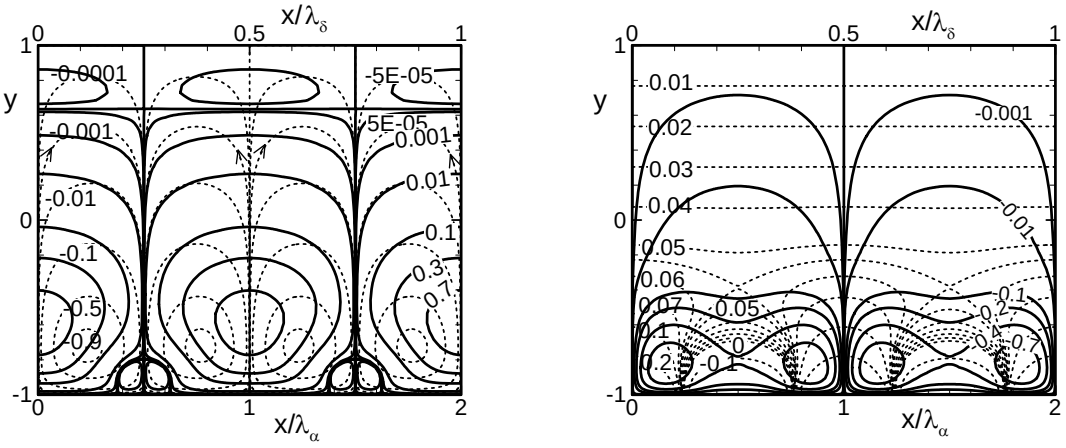

A B

Figure 4.20. *Disturbance streamlines (Fig.4.20A) and isotherms (Fig.4.20B) for branch one of the instability for conditions corresponding to the intersection of both branches, i.e., for the heating wave number* $\alpha = \alpha_B = 8.76$ *and the Rayleigh number* $Ra_{cr} = Ra_B = 8142.9$ *for the fluid with the Prandtl number Pr = 0.04. These conditions correspond to point B in Fig.4.21. Primary flow and disturbance quantities are represented using dash and solid lines, respectively. The stream functions and the temperatures are normalized with their maxima for presentations purposes. The maximum values for the primary convection are* $\psi_{max} = 9.828$ *and* $\theta_{max} = 12.5$.

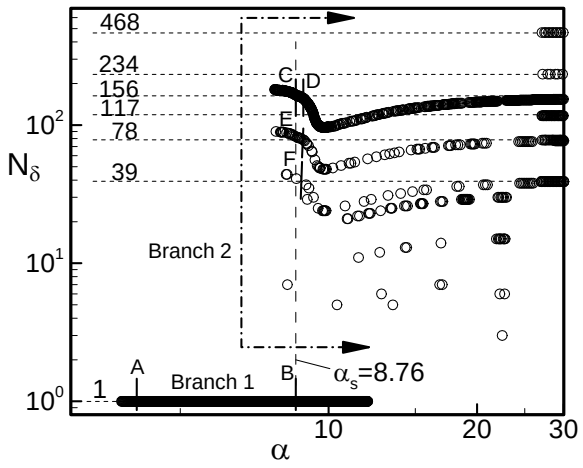

Figure 4.21. *Variations of the wavelength of the disturbance flow structures for the longitudinal roll instability as a function of the heating wave number α at the onset conditions measured using the number of the disturbance wavelengths N_δ for Pr = 0.04. Additional information about the structure of the unstable motion corresponding to conditions marked with letter A is displayed in Fig.4.19, letter B in Fig.4.20, letter C in Fig.4.22 and letters D, E and F in Fig.4.23.*

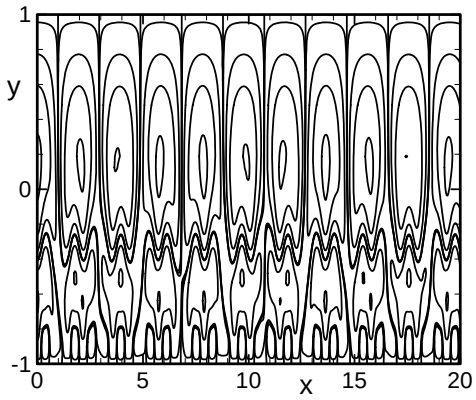

Figure 4.22. *Disturbance flow field for branch two of the instability for conditions corresponding to the intersection of both branches, i.e., for the heating wave number $\alpha = \alpha_B = 8.76$, the Rayleigh number $Ra_{cr} = Ra_B = 8142.9$ and the critical disturbance wave number $\delta_{B,2} = 1.61$ for the fluid with the Prandtl number Pr = 0.04. These conditions correspond to point C in Fig.4.21 and belong to branch $N_\delta = 156$. The contour lines shown correspond to $\psi_3(x,y) =$ 0, 0.01, 0.2, 0.5, 0.9 of its maximum.*

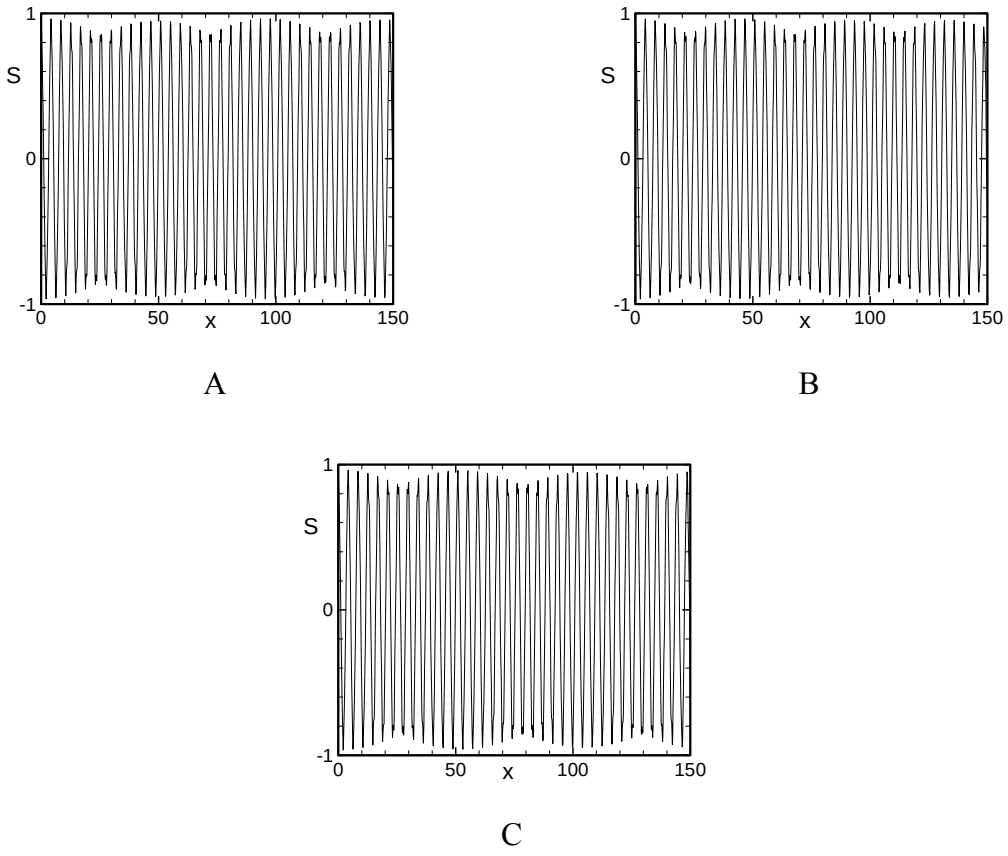

Figure 4.23. *Variations of the disturbance stream function $S = \psi_3(x,0)$ at $y = 0$ for the fluid with Pr = 0.04. Results shown in Figs 4.23 A, B, C belong to the wavelength bands N_δ = 156, 78, 39, correspond to the onset conditions, i.e., (α, δ_{cr}, Ra_{cr}) = (9.01, 1.48, 7961.4), (9.02, 1.48, 7950.2), (9.0, 1.48, 8013.2), and are marked with letters D, E and F in Fig.4.21, respectively.*

4.4 The Case of Pr = 0.25

This particular value of Pr has been selected to illustrate the wealth of possible system responses. Variations of the critical Rayleigh number Ra_{cr} and the critical wave number δ_{cr} as a function of the heating wave number α are displayed in **Figure 4.24** and demonstrate that the lock-in phenomenon does not occur for such fluids. The minimum value of the critical Rayleigh number is $Ra_{min} = Ra_A = 2826.8$ and it occurs for $\alpha_{min} = \alpha_A = 3.97$. The complete stabilization occurs for $\alpha < \alpha_{lb} = 3.58$ in the range of Ra subject to this investigation. The asymptotes for large α are $Ra_{cr} \rightarrow 236\ \alpha^{1.5}$ and $\delta_{cr} \rightarrow 1.56$.

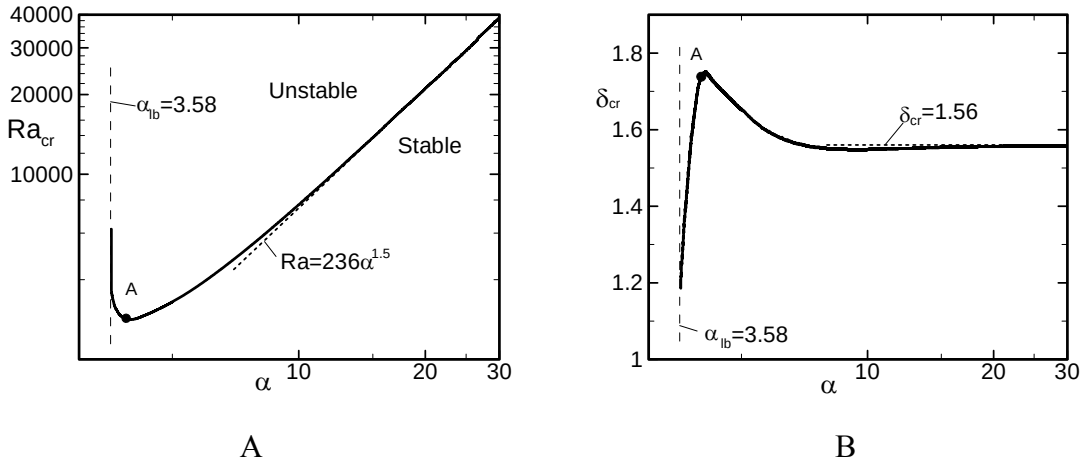

Figure 4.24. *Variations of the critical Rayleigh number Ra_{cr} (Fig.4.24A) and the critical disturbance wave number δ_{cr} (Fig.4.24B) as functions of the heating wave number α for Pr = 0.25. Point A is located at (Ra_A=2826.8, α_A=3.97, δ_A=1.72).*

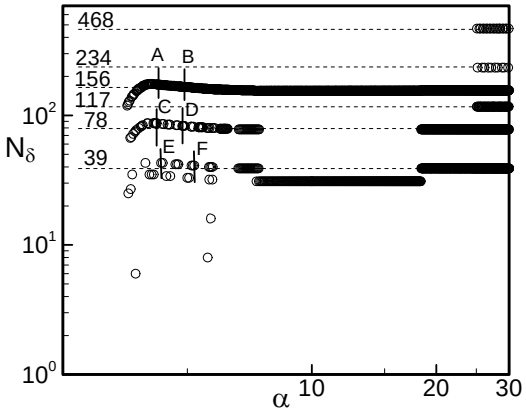

Figure 4.25. *Variations of the wavelength of the disturbance flow structures for the longitudinal roll instability as a function of the heating wave number α at the onset conditions measured using the number of the disturbance wavelengths N_δ for Pr = 0.25. Additional information about the structure of the unstable motion corresponding to conditions marked with letters A, ..., F is displayed in Fig.4.26.*

Similar to the previous sections dealing with Pr = 0.71, 7 and 0.04, commensurable states of the disturbance motion in terms of N_δ are illustrated in **Figure 4.25**. It can be seen that for large α these patterns can be divided into an infinite number of branches with the first five corresponding to N_δ = 39, 78, 156, 234, 468, similarly as for all values of Pr discussed so far. These branches extend to smaller values of α and produce patterns

different from those identified so far. Branch $N_\delta = 156$ gives rise to the "double-wavy" and the "wavy-like" patterns illustrated in **Figures 4.26**A and **4.26**B, respectively. The term "double wavy" can be better justified by looking at the enlargement of the pattern from **Figure 4.26**A displayed in **Figure 4.27**. This pattern involves sets of four rolls as shown in **Figure 4.28**. Each set has one "intense" narrow roll with high intensity of motion surrounded by two a bit wider and less "intense" rolls rotating in the opposite direction, and bordered by much "wider" rolls with similar intensities of motion, a separation bubble at the bottom and rotating in the same direction as the "intense" roll (see **Figure 4.28**A). One of the wide rolls belongs to the next set. After a quarter of the spatial cycle, one of the less "intense" rolls becomes wider and slows down while the adjacent former "wide" roll narrows down and accelerates producing a double separation bubble at the bottom. The other less "intense" roll accelerates (see **Figure 4.28**B). After half spatial cycle the pattern is reversed as compared with the beginning of the cycle but the equivalent rolls rotate in the opposite directions (see **Figure 4.28**C). In the "wavy-like" pattern the disturbance field consists of sets of two rolls, one narrow and intense and the other one wide, less intense and with a separation bubble at the bottom. These rolls are subject to modulation along the length of the slot and after half of the spatial cycle their characteristics are reversed, i.e., the former narrow roll acquires characteristics of the former wide roll and the former wide roll looks like the former narrow roll, as illustrated in **Figure 4.29**. This evolution is qualitatively similar to the "wavy" pattern shown in **Figures 4.9C** and **4.11**, but sufficiently different as to justify a different name, e.g., compare **Figures 4.9C** and **4.26B** and observe "sharp corners" in the pattern in **Figure 4.26**B. Branch $N_\delta = 78$ gives rise to the "double-parallel" and the "wavy-like" patterns illustrated in **Figures 4.26**C and D. Disturbance field in the "doubly-parallel" pattern consists of sets of four rolls repeated sequentially and involving a narrow and intense roll surrounded by two less intense rolls rotating in the opposite direction and bordered by wide rolls with a separation bubble at the bottom with one of these rolls belonging to the next set, as illustrated in **Figure 4.30**. Branch $N_\delta = 39$ gives rise to the "double-wavy" and "wavy-like" patterns illustrated in **Figures 4.26E** and **4.26F**, respectively, but with wavelengths and amplitudes different from those associated with the other branches. No other patterns have been identified for the branches in question.

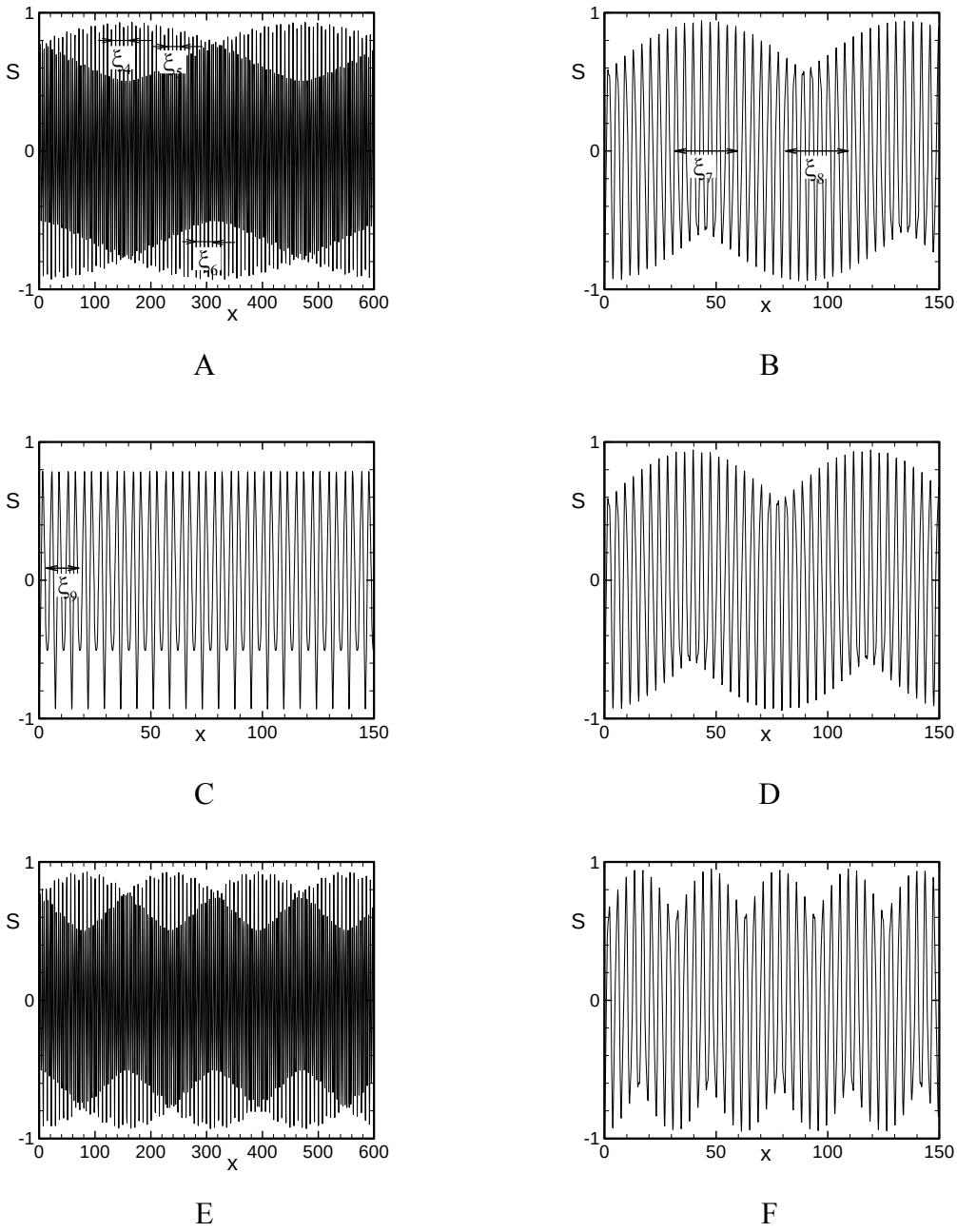

Figure 4.26. *Variations of the disturbance stream function $S = \psi_3(x,0)$ at $y = 0$ for the fluid with $Pr = 0.25$. Results shown in Fig.4.26 A, B belong to the wavelength band $N_\delta = 156$, correspond to the onset conditions, i.e., (α, δ_{cr}, Ra_{cr}) = (4.31, 2939.3, 1.72), (4.91, 3244.2, 1.66), and are marked with letters A, B in Fig.4.25, respectively. Results shown in Fig. 4.26 C, D belong to $N_\delta = 78$, correspond to the onset conditions, i.e., (α, δ_{cr}, Ra_{cr}) = (4.3, 2934.8, 1.72), (4.9, 3238.5, 1.66), and are marked with letters C, D in Fig.4.25, respectively. Results shown in Fig. 4.26 E, F belong to $N_\delta = 39$, correspond to the onset conditions, i.e., (α, δ_{cr}, Ra_{cr}) = (4.32, 2943.2, 1.71), (5.12, 3372.2, 1.64), and are marked with letters E, F in Fig.4.25, respectively.*

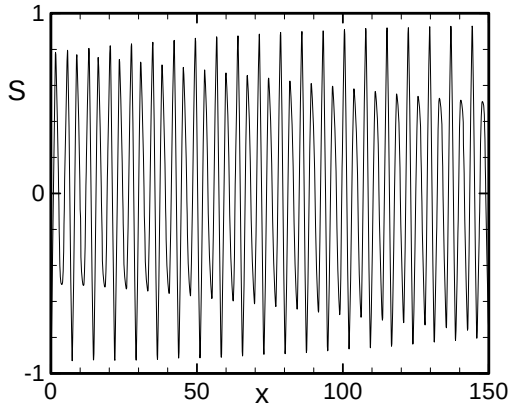

Figure 4.27. *Enlargement of the stream function pattern shown in Fig.4.26A.*

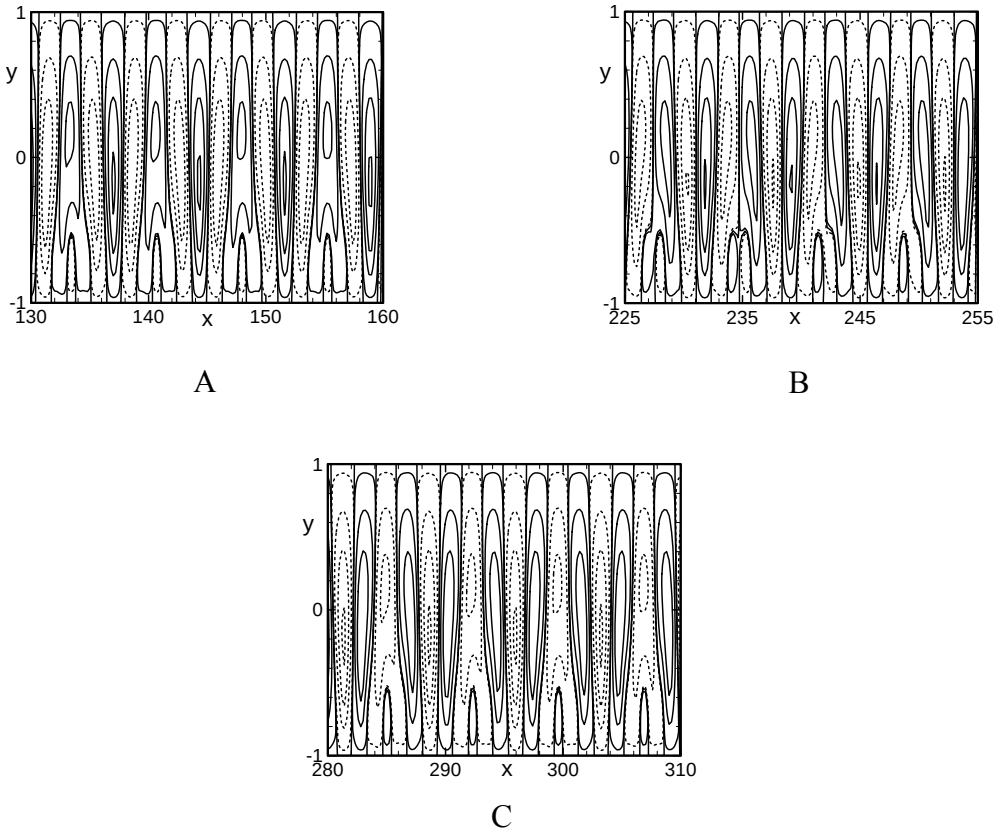

Figure 4.28. *Disturbance flow field corresponding to the "double wavy" pattern at the critical point (α, δ_{cr}, Ra_{cr}) = (4.31, 2939.3, 1.72) for the fluid with the Prandtl number Pr = 0.25. The contour lines shown correspond to $\psi_3(x,y)$ = 0, 0.01, 0.2, 0.5, 0.9 of its maximum. Solid and dot lines are used to identify rolls rotating in the opposite directions. Results displayed in Fig.4.28A,B,C correspond to the ranges of x marked with symbols ξ_4, ξ_5 and ξ_6 in Fig.4.26A, respectively. This pattern belongs of the wavelength band N_δ = 156.*

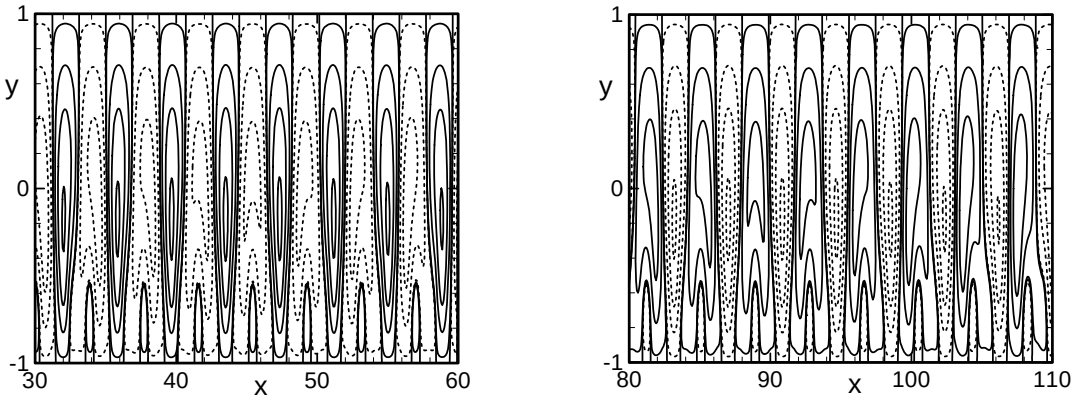

Figure 4.29. *The disturbance flow field corresponding to the "wavy-like" pattern at the critical point (α, δ_{cr}, Ra_{cr}) = (4.91, 3244.2, 1.66) for the fluid with the Prandtl number Pr = 0.25. The contour lines shown correspond to $\psi_3(x,y)$ = 0, 0.01, 0.1, 0.5, 0.9 of its maximum. Solid and dot lines are used to identify rolls rotating in the opposite directions. Results displayed in Figs 4.29A,B correspond to the ranges of x marked with symbols ξ_7 and ξ_8 in Fig.4.26B, respectively. This pattern belongs of the wavelength band N_δ = 156.*

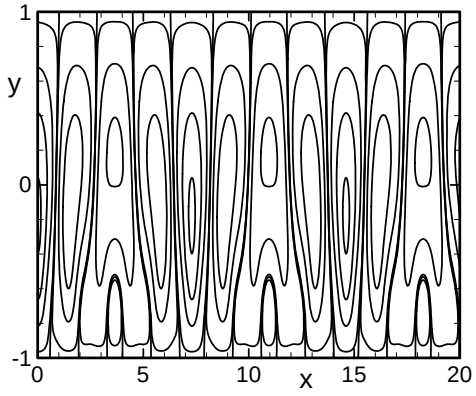

Figure 4.30. *The disturbance flow field corresponding to the "double-parallel" pattern at the critical point (α, δ_{cr}, Ra_{cr}) = (4.3, 2934.8, 1.72) for the fluid with the Prandtl number Pr = 0.25. The contour lines shown correspond to $\psi_3(x,y)$ = 0, 0.01, 0.1, 0.5, 0.9 of its maximum. The range of x used for display is marked as ξ_9 in Fig.4.26C. This pattern belongs of the wavelength band N_δ = 78.*

4.5 Arbitrary Prandtl number

Discussion presented in the previous sections shows existence of two qualitatively different mechanisms of instability motion at the onset of longitudinal roll. In the case of medium heating wave numbers the form of the motion is tightly locked-in with the structure of the heating and exhibits spatial structure determined by the pattern of heating where $\delta_{cr} = \alpha/2$. In the case of large α the pattern of motion is not directly related to the pattern of heating and the fluid response is similar to that found in the case of a uniform wall heating, i.e., $\delta_{cr} \rightarrow 1.56$ and $Ra_{cr} \rightarrow 236\alpha^{1.5}$ when $\alpha \rightarrow \infty$ regardless of the value of Pr. Transition between these two forms of response takes place somewhere between these two limits and precise conditions leading to this transition are determined by the strength of spatial flow modulation. This modulation increases with a decrease of the Prandtl number as this increases the strength of conduction effects, an increase of the heating wave number decreases spatial modulation as convection leads to an increase of mixing, and an increase of the Rayleigh number initially decreases spatial modulation while its further increase eventually increases spatial modulation (see **Figure 2.13**). All these effects are present simultaneously and thus it is difficult to predict system response without detailed analysis of any case of interest.

Analysis of the lock-in conditions, i.e., variations of the lock-in heating wave number α_{lc} and of the associated critical Rayleigh number Ra_{lc}, as a function of the Prandtl number, permit identification of four types of response (see **Figure 4.31**). Type A occurs for $Pr >\sim 0.4$ and is characterized by a very weak dependence of Ra_{lc} and α_{lc} on Pr. Type B occurs approximately for $Pr \in (\sim 0.19, \sim 0.4)$ and is characterized by the absence of the lock-in. Type C is observed for $Pr \in (\sim 0.08, \sim 0.19)$ and is similar to type A with Ra_{lc} being a strong function of Pr. Type D is observed for $Pr < \sim 0.08$ and is characterized by the existence of two branches of the critical curve, with branch one corresponding to the locked-in pattern and branch two corresponding to the no locked-in pattern, and both patterns co-existing at a specific, Pr-depend value of α (intersection of both branches). Type A has been discussed in Sections 4.1 and 4.2 in the context of fluids characterized

by Pr = 0.71 and Pr = 7, type B occurs for Pr = 0.25 and has been discussed in Section 4.4, and type D occurs for Pr = 0.04 and has been discussed in Section 4.3.

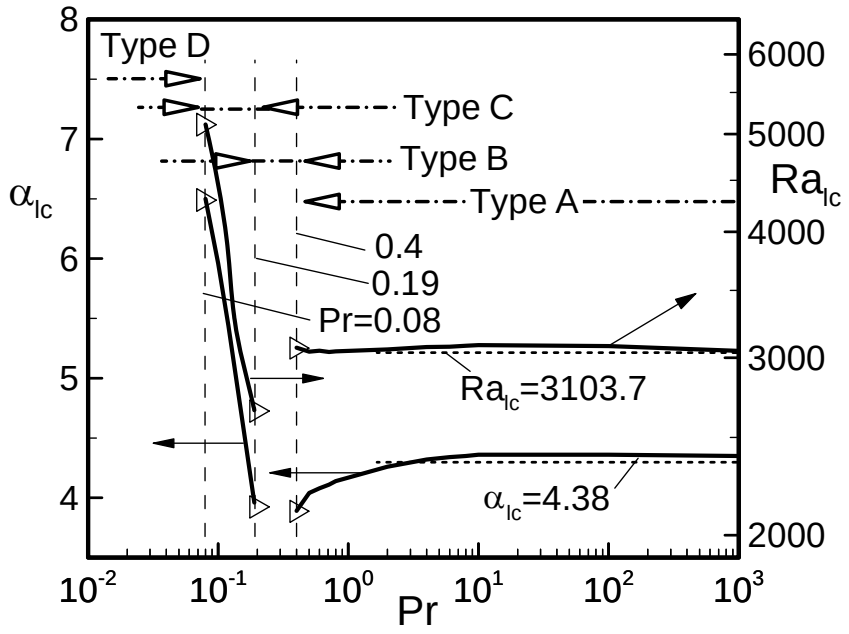

Figure 4.31. *Variations of conditions leading to the occurrence of the lock-in phenomenon, i.e., the lock-in heating wave number α_{lc} and the critical Rayleigh number at the lock-in point Ra_{lc}, as a function of the Prandtl number Pr. Triangles identify ends of intervals where the lock-in occurs.*

Critical stability curves for Pr varying between 0.01 and 1000 are displayed in **Figure 4.32**. Single, smooth critical curves exist for type A (curves corresponding to Pr ≥10, 0.71, 0.5, and 0.4) response where the disturbance pattern is locked-in with the heating pattern over a certain range of heating wave numbers α and there is no lock-in over the rest of the α-range. Type B (curves corresponding to Pr = 0.25 and 0.2) also has single, smooth critical curves but its characteristic signature involves curves describing critical wave numbers δ_{cr} which turn downwards (without the presence of any lock-in) in a characteristic manner as α decreases (see **Figure 4.32**B). Type C (curves corresponding to Pr = 0.15, 0.12, 0.1 and 0.08) is characterized by the critical curves displaying a characteristic bump, with the size of this bump increasing and moving towards larger

values of α as Pr decreases (see **Figure 4.32**A). Type D (curves corresponding to Pr = 0.07, 0.06, 0.04, 0.03, 0.02 and 0.01) is characterized by the existence of two branches of the critical curve as discussed above.

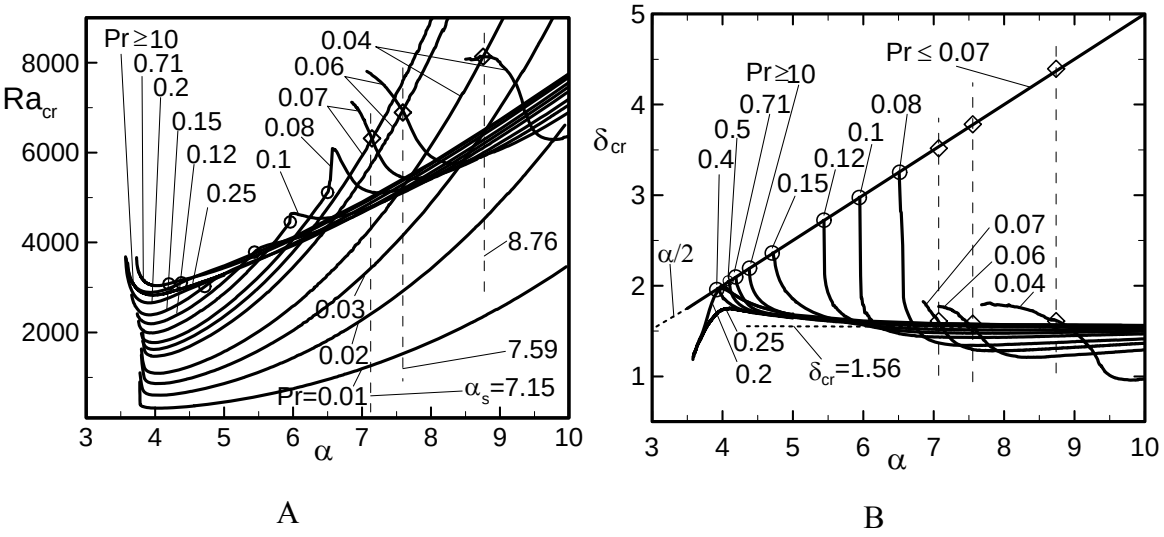

Figure 4.32. *Variations of the critical Rayleigh number Ra_{cr} (Fig.4.32A) and the critical disturbance wave number δ_{cr} (Fig.4.32B) as functions of the heating wave number α for selected values of the Prandtl number Pr in the range from Pr $\in$ (0.01, 1000) for longitudinal rolls. Lock-in points are marked with circles and points where two different disturbance structures co-exist are marked with diamonds. Curves for Pr = 0.4, 0.5 have been omitted from Fig.4.32A as they nearly overlap with the curve for Pr = 0.71.*

Competition between the locked-in and the no locked-in patterns exists under all conditions but is explicitly visible in type C response. When $\alpha \approx 4.5$ the disturbance pattern is locked-in with the heating pattern. An increase of α automatically increases δ_{cr} and the difference between this value and the no-lock value of $\delta_{cr} \approx 1.56$ increases continuously. Eventually this difference becomes too large and both patterns may not be able to "attract" each other, i.e., one pattern may not be able to morph into the other. The case of Pr = 0.08 represents the limiting case where both patterns can morph and the relevant critical curves are displayed in **Figure 4.33**. For large α the pattern is dominated by $\delta_{cr} \approx 1.56$. A decrease of α to around 6.58 produces minor changes in δ_{cr} (see **Figure 4.33**B). Further decrease of α results in a rapid increase of $\delta_{cr,}$ and at the same time, a

rapid decrease of Ra_{cr}. Point A in **Figure 4.33**B marks the beginning of the rise of δ_{cr} and corresponds to the "corner" in the plot of Ra_{cr} in **Figure 4.33**A. The disturbance flow field displayed in **Figure 4.34**A shows that its pattern is still dominated by $\delta_{cr} = 1.56$ (due to the presence of big envelop-rolls containing small three cells, each pair of the envelop-roll has wavelength approximately equal to $2\pi/1.56$). A decrease of α from 6.57 (point A) to 6.56 (point B) shows that the direct disturbance modulation by the heating expands rapidly to the complete slot (see **Figure 4.34**B). This rapid change (increase of δ_{cr} and decrease of Ra_{cr}) continues until the lock-in occurs (point C in **Figure 4.33**, $\alpha_{lc} = 6.51$). The reader should note that point A in the Ra_{cr} plot represents a corner within numerical accuracy while the same curve around point C has just a large gradient. A decrease of Pr from 0.08 to 0.07 breaks the ability of both patterns to morph into each other, as shown in **Figure 4.32**, and leads to the formation of two separate branches of the critical curve.

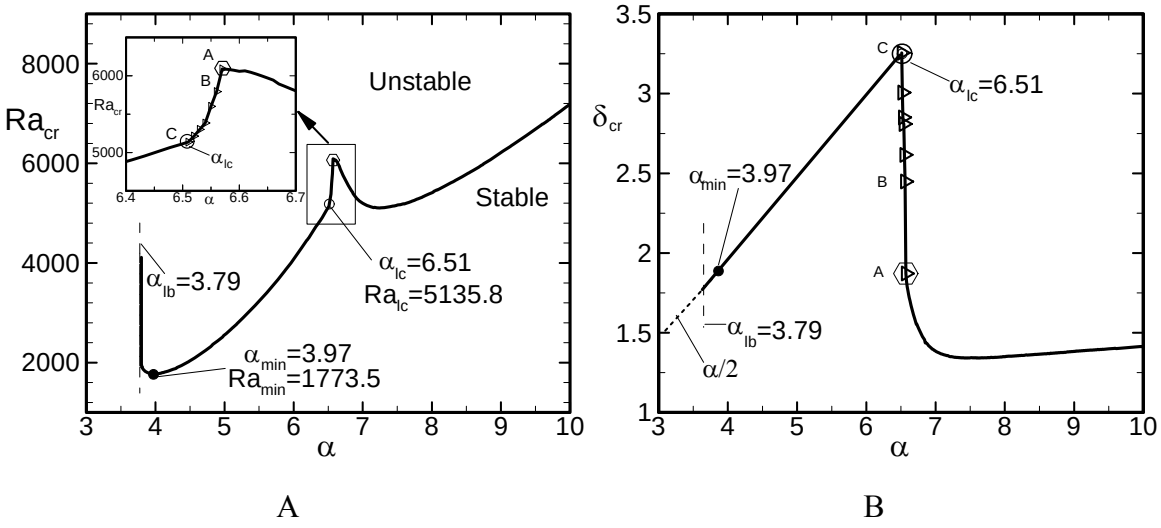

Figure 4.33. *Variations of the critical Rayleigh number Ra_{cr} (Fig.4.33A) and the critical disturbance wave number δ_{cr} (Fig.4.33B) as functions of the heating wave number α for Pr = 0.08. Triangles mark computed points between points A and C. Circle marks the lock-in point. Hexagon marks the "corner" in the Ra_{cr} plot.*

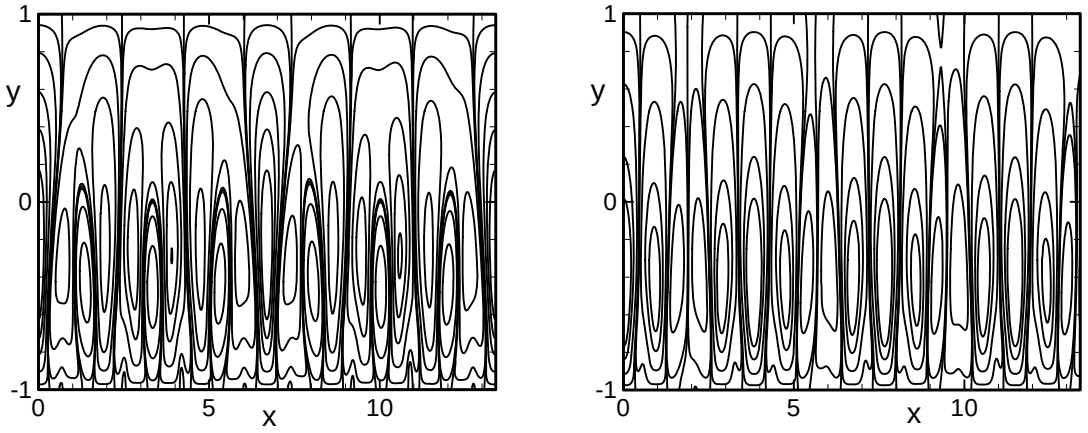

Figure 4.34. *The disturbance flow at the critical points (α, Ra_{cr}, δ_{cr}) = (6.57, 6138.2, 1.87), (6.56, 5794, 2.45) in Figs 4.34A and B, respectively, for the fluid with the Prandtl number Pr = 0.08. The contour lines shown correspond to $\psi_3(x,y)$ = 0, 0.01, 0.1, 0.3, 0.5, 0.7 of their maxima in Fig.4.34A and to 0, 0.01, 0.1, 0.3, 0.5 in Fig.4.34B, respectively. These patterns belong to the wavelength band N_δ = 156.*

The net heat flow Nu across the slot and the thickness of the convection layer h_v along the critical curves for selected values of Pr are displayed in **Figure 4.35**. The characteristic of this figure provides a limited insight into the conditions that may lead to the lock-in effect. It can be seen that type D response occurs when a sufficiently thick uniform conduction layer forms in the upper section of the slot, i.e, when Prandtl number takes sufficiently small values. No other explicit correlation can be made between the properties of the primary convection and the onset of the lock-in phenomenon.

Figure 4.36 provides information that permits a more accurate identification of conditions required for the occurrence of type B response. This figure displays variations of the critical disturbance wave number δ_{cr} as a function of Prandtl number Pr for selected values of the heating wave number α. It can be seen that the locked-in condition may or may not be reached when α decreases from α = 7.15 (largest value displayed) while keeping a fixed value of Pr. The locked-in condition is never reached for Pr in the range from approximately ~0.19 to approximately ~0.4.

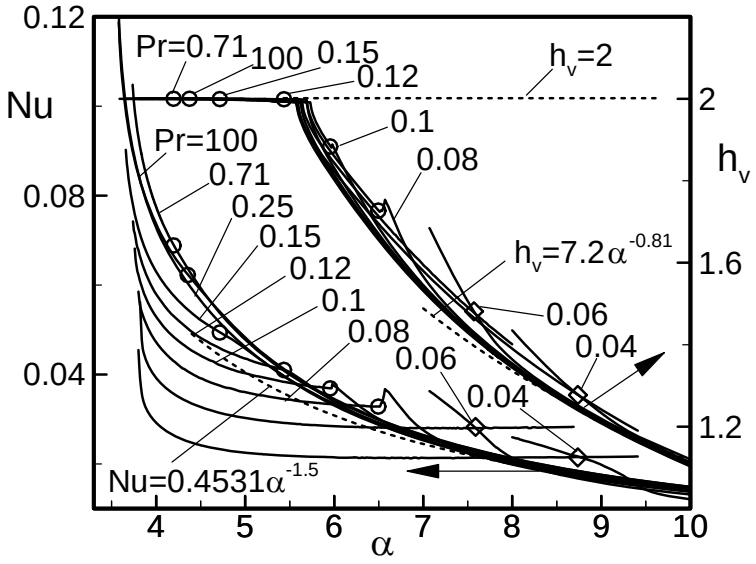

Figure 4.35. *Variations of the net heat flow Nu between the plates forming the slot and thickness of the convective layer h_v (determined using Eq.2.23 with E = 0.01) along the critical stability curves for selected values of the Prandtl number. Circles mark locations of the lock-in points and diamonds identify conditions when two disturbance structures co-exist at the instability onset. Curve for Pr = 0.25 has been omitted from the h_v plot as it mostly overlaps with the curve for Pr = 0.71 (the lock-in does not occur for Pr = 0.25).*

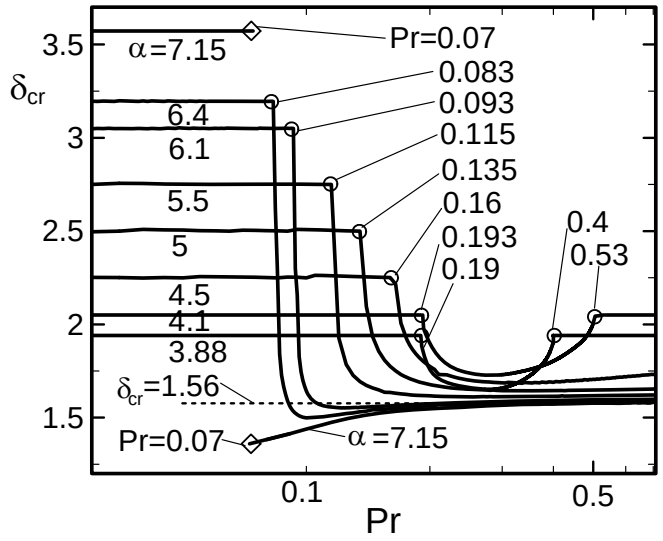

Figure 4.36. *Variations of the critical wave number δ_{cr} at the onset of the instability as a function of the Prandtl number Pr for selected values of the heating wave number α. Diamonds identify conditions where the locked-in and the no-locked-in structures co-exist. Circles denote locations of the lock-in points.*

4.6 Summary

In this chapter the linear stability of the primary convection for the conditions leading to the emergence of the longitudinal roll instability has been presented for the case of periodic heating applied at the lower wall. The system response is a strong function of the Prandtl number, especially for smaller values of Pr. Two mechanisms of instability at the onset have been identified depending on the pattern of the resulting instability motion. This pattern can be either directly forced in by the pattern of the heating or can be independent of the form of the heating. In the case of moderate α the parametric resonance leads to the pattern of instability that is generally locked-in with the pattern of the heating according to the relation $\delta_{cr} = \alpha/2$. This resonance may be combined with variations in patterns of vertical temperature gradients, and patterns and strength of the primary convection currents. The second mechanism is active in the case of large α, where the instability is driven by the mean vertical temperature gradient created by the primary convection with the magnitude of the critical disturbance wave number approaching limiting value of $\delta_{cr} = 1.56$. It has been shown that in this case the critical value of Ra increases proportionally to $\alpha^{1.5}$ for all values of Pr which suggests that under such conditions the lower wall acts as a uniformly heated wall. This "conversion" is associated with concentration of convective effects in a thin layer next to the lower wall and dominance of the uniform conduction in the remaining part of the slot.

The first mechanism referred to above dominates if the spatial modulation of the flow is sufficiently strong while the second one occurs for weak spatial modulations. The strength of the modulation is a monotonic function of Pr and α but a non-monotonic function of Ra. The possible responses for different fluids can be divided into four types. In type A, which occurs for fluids with Pr > ~0.4, the pattern of instability is locked-in with the pattern of heating for smaller values of α and no direct relation between both patterns exists for larger values of α. In type B, which occurs for Pr between ~0.4 and ~0.19, the lock-in does not occur at all. In type C, which occurs for ~0.08 < Pr < ~0.19, the pattern of instability is locked-in with the pattern of the heating for a range of small

α's and both pattern exhibit no direct relation for large α's, similarly as in type A. The difference between types A and C involves rate of change of the lock-in conditions as a function of Pr; this change is very rapid for type C and insignificant for type A. In type D, which occurs for Pr < 0.08, two critical instability branches have been identified. Branch one determines critical conditions for lower values of α and corresponds to disturbances whose structure is locked-in with the heating pattern. Branch two determines critical conditions for larger values of α and describes disturbance patterns that have no direct relation with the heating patterns. Critical conditions when both disturbance patterns, i.e., the locked-in and the unlocked-in patterns, co-exist have been identified. Morphing between different patterns of instability motion may occur in response to change in the heating pattern in types A and C, while such process is not possible in types B and D.

There is a wealth of possible patterns of disturbance motion occurring under the no lock-in conditions and these patterns can be categorized into distinct branches on the basis of asymptotic analysis for $\alpha\rightarrow\infty$ as δ_{cr} reaches the value of $\delta_{cr} = 1.56$ in this limit. These branches are categorized according to the wavelength of the flow system N_δ measured using the disturbance wavelength as a length scale. Branches corresponding to N_δ = 39, 78, 156, 234 and 468 (i.e., the lowest braches) have been explored in details. When α is large enough the modulation of instability motion is always limited to the zone around the lower (heated) wall and the flow structures in the rest of the slot are dominated by δ_{cr}. A decrease of α causes the flow pattern to evolve and this evolution may eventually lead to the morphing into the locked-in pattern for certain ranges of Pr. Several characteristic patterns associated with this evolution have been identified, i.e., "beating", "wavy", "double wavy", "wavy-like" and "double-parallel" patterns. In the case of Pr = 0.71 and 7 all N_δ-branches produced "beating" and "wavy" patterns but with a wide range of amplitudes and wavelengths. More complex patterns are found in fluids with smaller Pr. In the case of Pr = 0.25 the complex patterns occur because the lock-in phenomenon does not take place at all and the unlocked patterns persist into fairly small values of α. The case of Pr = 0.08 represents a limiting case where the lock-in still occurs but the morphing between the locked-in and unlocked patterns is very rapid due to a large

difference between $\delta_{cr} = \alpha/2$ and $\delta_{cr} = 1.56$ around the lock-in point. In the case of very small Pr, e.g., Pr = 0.04, only beating patterns with small amplitudes and wavelengths similar for all N_δ-branches have been found.

5

Transverse Roll

This chapter deals with the transverse roll instability, i.e., instability that gives rise to secondary rolls with axis perpendicular to the axis of the primary rolls. To predict onset of the transverse roll instability we use the three-dimensional stability theory discussed in Section 3.2 with $\delta = 0$. Only stationary disturbances ($\sigma_r = 0$) have been found. Characteristics of this instability for fluids with the Prandtl number Pr = 0.71 are described in details in Section 5.1, and for Pr = 7 in Section 5.2. Short discussion of results for Prandtl numbers Pr = 0.12, 0.08, and 0.06 is given in Section 5.3, 5.4, and 5.5, respectively. Section 5.6 is devoted to direct analysis of Prandtl number effects. A short summary is given in Section 5.7.

5.1 Fluids with the Prandtl number Pr=0.71

We start with description of variations of the the amplification rate σ_i of the transverse roll instability as a function of the heating wave number α and the roll wave number β for a fixed intensity of the heating corresponding to the Rayleigh number Ra = 3980 as shown in **Figure 5.1**. It can be seen that, analogously to the longitudinal rolls, there exists a finite range of α that results in the instability. The instability does not occur if the heating pattern is characterized by a wavelength that is either too long or too short. The wavelengths of the rolls that emerge from this instability also have a finite bandwidth; the most amplified wave number corresponds to $\beta \approx 1.7$.

A set of neutral curves for the transverse roll instability for a sequence of Rayleigh numbers is displayed in **Figure 5.2**. It can be seen that a decrease of the heating intensity (decrease of Ra) results in the reduction of the range of heating patterns, i.e., reduction of

the range of the heating wave numbers, that can lead to the instability and, at the same time, reduction in the range of the roll wave numbers that can be produced by the instability. The instability does not occur at all for Ra < ~3200.

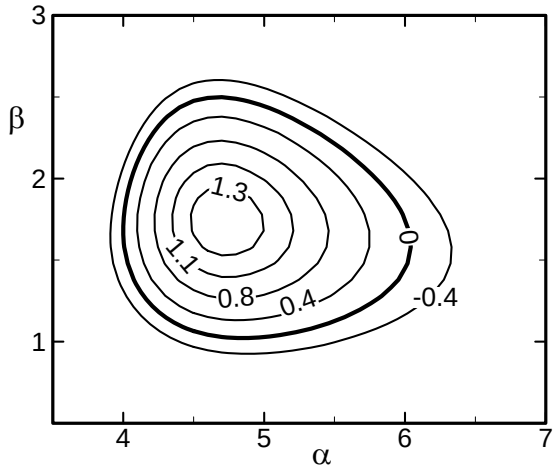

Figure 5.1. *Variations of the amplification rate σ_i of the transverse rolls as a function of the heating wave number α and the transverse roll wave number β for the Rayleigh number Ra = 3980 and fluids with the Prandtl number Pr = 0.71.*

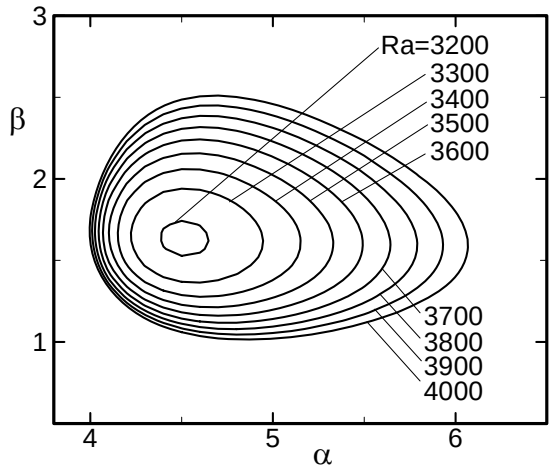

Figure 5.2. *Variations of the neutral stability conditions as a function of the heating wave number α and the transverse roll wave number β for selected values of the Rayleigh number Ra for fluids with the Prandtl number Pr = 0.71.*

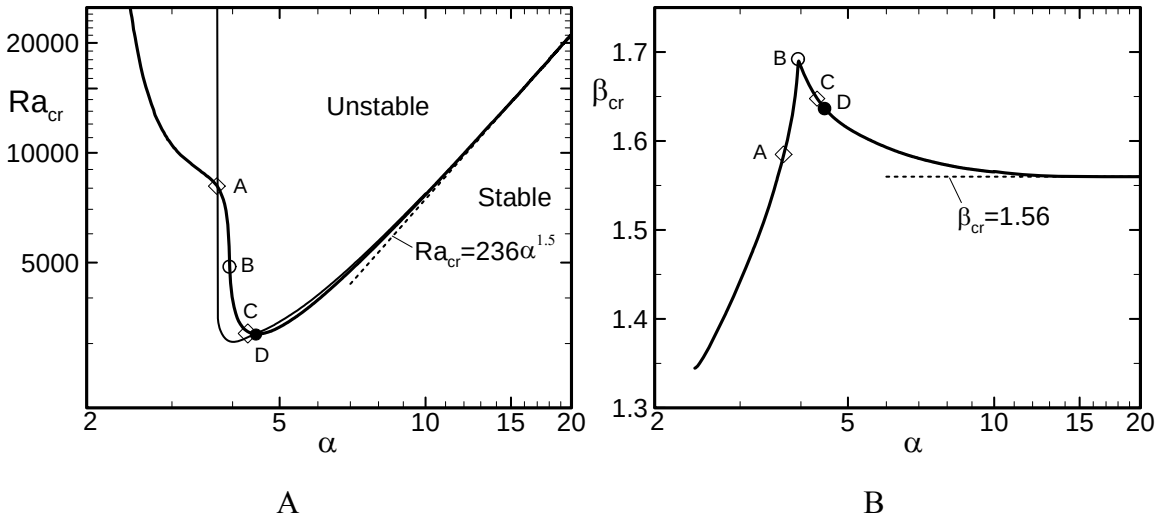

Figure 5.3. *Variations of the critical Rayleigh number Ra_{cr} (Fig.5.3A) and the critical disturbance wave number β_{cr} (Fig.5.3B) as functions of the heating wave number α for the fluid with the Prandtl number Pr = 0.71. Thick and thin lines correspond to the transverse roll instability and to the longitudinal roll instability, respectively. Points A, B, C, D are located at (Ra_A=8099.0, α_A=3.72, β_A=1.59), (Ra_B=4823.9, α_B=3.95, β_B=1.69), (Ra_C=3191.8, α_C=4.46, β_C=1.64), (Ra_D=3188.6, α_D=4.51, β_D=1.63), respectively.*

One can identify the upper and lower limits of the unstable range of α for each value of Ra and the corresponding values of β to produce plots displayed in **Figure 5.3**A. Such plots identify the critical conditions leading to the onset of the transverse roll instability. The same figure displays critical curves for the longitudinal roll instability studied in Chapter 4 for comparison purposes. The minimum heating intensity required to induce this instability corresponds to $Ra_{min} = Ra_D = 3188.6$ (point D in **Figure 5.3**A) but the instability will occur only if the heating pattern corresponds to $\alpha_{min} = \alpha_D = 4.51$. No transverse roll instability can be initiated for Ra < 3188.6 regardless of the pattern of heating. An increase of Ra above 3188.6 increases the range of heating patterns that can induce this instability. The critical curve steeply rises when α is reduced below $\alpha_D = 4.51$ but this rise becomes less extreme for $\alpha < \sim 3.6$. An increase of α above $\alpha_D = 4.51$ results in a gradual increase of the value of Ra_{cr}; when α is big enough, the increase follows the asymptote $Ra_{cr} \rightarrow 236\ \alpha^{1.5}$ as $\alpha \rightarrow \infty$. The reader may note that the spatial pattern of the

heating corresponding to $\alpha_{min} = \alpha_D = 4.51$ is the most efficient in inducing transverse roll instability and any other pattern requires more intense heating. It appears that patterns with small α are not effective at all in producing transverse rolls.

Comparison of the longitudinal roll and the transverse roll instabilities (see **Figure 5.3**A) shows that the transverse roll instability dominates for $\alpha < \alpha_A = 3.72$, there is a range of alpha ($\alpha_A = 3.72 < \alpha < \alpha_C = 4.46$) where the longitudinal roll instability dominates, and the transverse roll instability dominates again for $\alpha > \alpha_C = 4.46$. Both types of instability have the same asymptotes with $Ra_{cr} \rightarrow 236\alpha^{1.5}$ as $\alpha \rightarrow \infty$ with the critical values of Ra_{cr} for the transverse rolls being always lower than Ra_{cr} for the longitudinal rolls at the same α. A small preference for the transverse rolls was also reported by Freund et al. (2010) in the case of the RB convection with high wave number temperature modulations, as discussed in the Section 4.1.

The structure of the disturbance motion, as described by the critical transverse roll wave number β_{cr}, is also a strong function of the heating wave number α (see **Figure 5.3**B). Categorization of these structures is simpler than those associated with the longitudinal rolls as they are uniquely determined by β_{cr}. One can identify two intervals with qualitatively different forms of variations of β_{cr}, with a sharp transition at $\alpha = \alpha_B = 3.95$ (point B in **Figure 5.3**B). Value of β_{cr} decreases from the "transitional" value of $\beta_B = 1.69$ as one moves away from α_B along the α-axis in both directions. No characteristic relation can be found between β_{cr} and α in either of these directions. This separates the transverse roll instability from the longitudinal roll instability (discussed in Chapter 4) where a sub-harmonic lock-in between the roll wave number and the heating wave number has been found for moderate α. When α decreases below α_B, β_{cr} rapidly decreases suggesting a rapid increase in the wavelength of the most unstable transverse rolls, and the corresponding value of Ra_{cr} rapidly increases demonstrating a strong stabilization. When α increases above α_B, the corresponding β_{cr} smoothly decreases and in the limit of $\alpha \rightarrow \infty$

approaches the limiting value of $\beta_{cr} = 1.56$, which is the same as for the longitudinal roll instability.

The net heat flow (denoted by the Nusselt number) across the slot induced by the primary convection at the onset of the transverse roll instability is shown in **Figure 5.4**. It is found that when $\alpha \to \infty$ the net heat flow changes as $Nu \to 0.4531\alpha^{-1.5}$. This asymptotic relation is the same as the case of the longitudinal roll instability; hence we obtain the same asymptotic relation for Ra_{cr} for both type of instability.

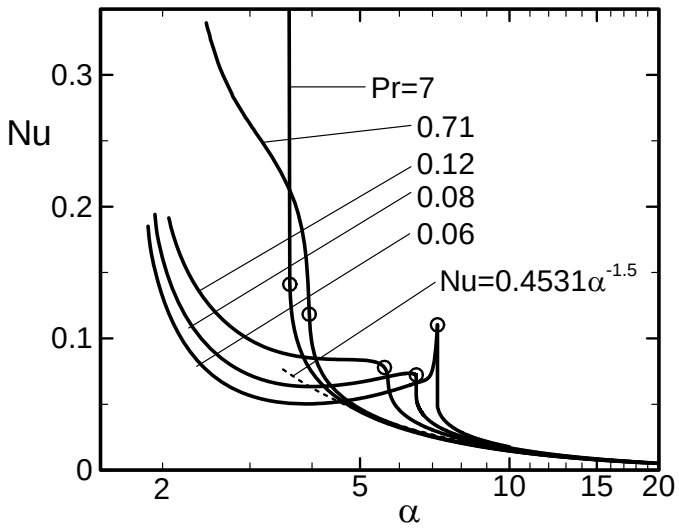

Figure 5.4. *Variations of the Nusselt number Nu for the primary convection as a function of the heating wave number α for the critical values of the Rayleigh number Ra_{cr} for the transverse roll instability. Circles mark conditions when transition between the different characters of variations of the critical roll wave number β_{cr} take place.*

Topologies of the disturbance velocity fields and how they change as a function of α at the onset are illustrated in **Figures 5.5-5.7** using the second invariant of the velocity gradient tensor (Dubief and Delcayre 2000) Q defined as

$$Q = \frac{1}{2}\left(\varpi_{ij}\varpi_{ij} - R_{ij}R_{ij}\right) \tag{5.1}$$

where $\varpi_{ij} = \frac{1}{2}\left(u_{i,j} - u_{j,i}\right)$, $R_{ij} = \frac{1}{2}\left(u_{i,j} + u_{j,i}\right)$. Explicit form of Q can be written for disturbance velocity fields as

$$\begin{aligned} Q = {} & \frac{1}{4}\left[\left(\frac{\partial u_3}{\partial y} - \frac{\partial v_3}{\partial x}\right)^2 + \left(\frac{\partial u_3}{\partial z} - \frac{\partial w_3}{\partial x}\right)^2 + \left(\frac{\partial v_3}{\partial z} - \frac{\partial w_3}{\partial y}\right)^2\right] \\ & - \frac{1}{2}\left[\left(\frac{\partial u_3}{\partial x}\right)^2 + \left(\frac{\partial v_3}{\partial y}\right)^2 + \left(\frac{\partial w_3}{\partial z}\right)^2\right] - \\ & - \frac{1}{4}\left[\left(\frac{\partial u_3}{\partial y} + \frac{\partial v_3}{\partial x}\right)^2 + \left(\frac{\partial u_3}{\partial z} + \frac{\partial w_3}{\partial x}\right)^2 + \left(\frac{\partial v_3}{\partial z} + \frac{\partial w_3}{\partial y}\right)^2\right]. \end{aligned} \tag{5.2}$$

The disturbance velocity field has been normalized with the condition max($g_u^{(0)}$)=1 for display purposes. The same figures display topology of the primary velocity field for comparison purposes. When the heating wave number α is large, the primary convection at the onset is concentrated very close to the heated wall (**Figure 5.5**A) and is unable to modulate the disturbance velocity field which is centered in the middle of the layer (**Figure 5.5**B). Reduction of α leads to a rapid increase of the strength of the primary convection; data shown in **Figure 2.7** documents its increase as being proportional to α^{-3} even while keeping Rayleigh number Ra constant. As a result the secondary rolls are pushed upwards by strong up swells above the hot spots and downwards by strong down swells above the cold spots (**Figure 5.6**B). Further reduction of α continues this process, i.e., the primary convection becomes stronger and fills in the whole fluid layer (**Figure 5.7**A), the up and down swells produce more extreme deformation of the secondary rolls, the rolls contract and deform in locations where they are pushed against the walls, the z-wavelength of the system increases as a result of these deformations, and cores of the rolls expand significantly in the zones where vertical motion is minimal (**Figure 5.7**B). A more intense heating is required to sustain such deformed rolls leading to an rapid increase of Ra_{cr}, as shown in **Figure 5.3**.

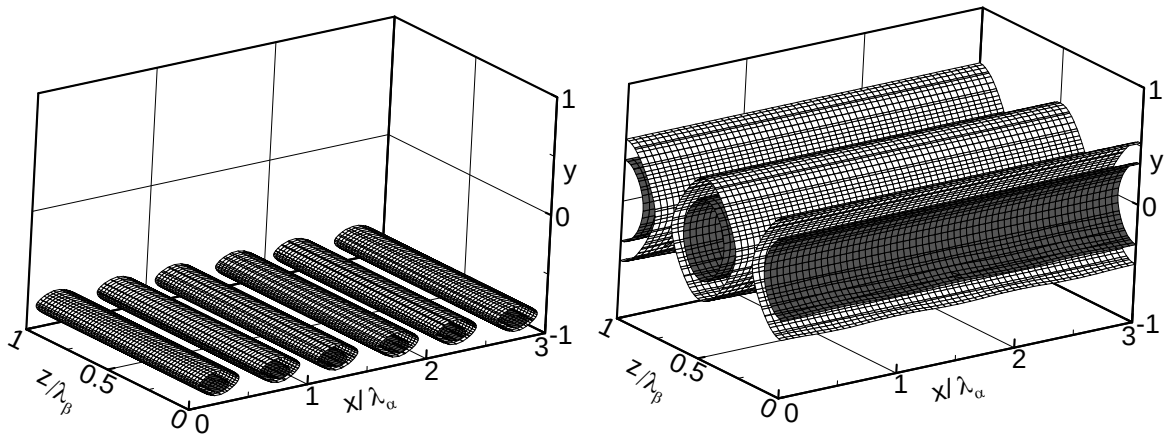

Figure 5.5. *Flow structures created by the primary convection (Fig.5.5A) and by the secondary convection in the form of transverse rolls (Fig.5.5B) generated by the heating with the wave number α = 10 at the onset, i.e., for the Rayleigh number Ra_{cr} = 7667.4. The critical roll wave number is β_{cr} = 1.56. Iso-surfaces with Q = 0.1, 0.5 and Q = 0.2, 0.7 (see Eq.5.2) are displayed in Fig.5.5A and B, respectively.*

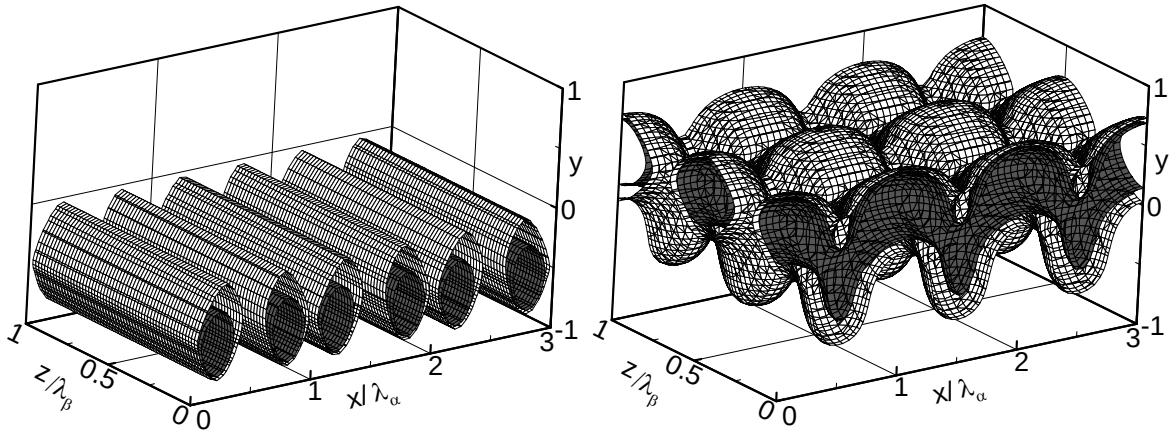

Figure 5.6. *Flow structures created by the primary convection (Fig.5.6A) and by the secondary convection in the form of transverse rolls (Fig.5.6B) generated by the heating with the wave number α = 3.95 at the onset, i.e., for the Rayleigh number Ra_{cr} = 4823.9. The critical roll wave number is β_{cr} = 1.69. Iso-surfaces with Q = 0.1, 0.3 and Q = 0.1, 0.3 (see Eq.5.2) are displayed in Fig.5.6A and B, respectively.*

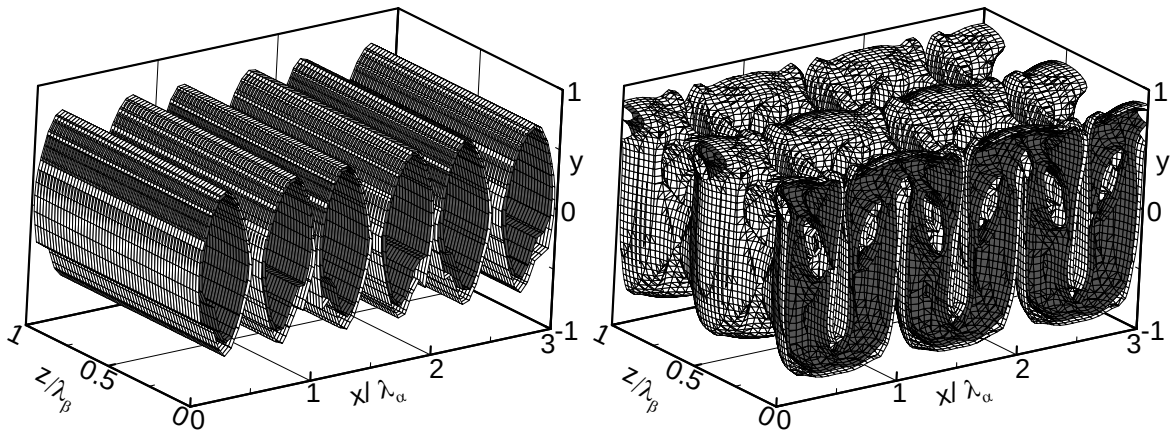

Figure 5.7. *Flow structures created by the primary convection (Fig.5.7A) and by the secondary convection in the form of transverse rolls (Fig.5.7B) generated by the heating with the wave number α = 2.47 at the onset, i.e., for the Rayleigh number Ra_{cr} = 24166.5. The critical roll wave number is β_{cr} = 1.35. Iso-surfaces with Q = 0.2, 0.45 and Q = 0.12, 0.3 (see Eq.5.2) are displayed in Fig.5.7A and B, respectively.*

To visualize the convection patterns in experiments shadowgraph method is generally utilized. Patterns observed by experiments may be produced in numerical simulations by taking the snapshot of the temperature field in a suitable plane, or by using the vertical average of the whole temperature field (Trainoff and Cannel 2002, Paul et al. 2003, Jenkins 1988). In the present analysis, we use temperature snapshot at the vertical mid-plane. **Figure 5.8** shows patterns that one may observe in experiments for the flow structures shown in **Figures 5.5-5.7**. The reader may note that the primary convection always produce longitudinal rolls, so one will always see the longitudinal striped pattern similar to the pattern shown in **Figure 5.8**A regardless of the heating wave number α. For disturbance patterns, at large α, the topology of the disturbance field looks like straight transverse roll (see **Figure 5.5**B) so the stripes are oriented along the x-direction as depicted in **Figure 5.8**B. As the heating wave number α decreases these rolls are modulated and this modulation is clearly visible in the pattern shown in **Figure 5.8**C. With the further reduction of α, the rolls become increasingly stretched near the colder

regions and, as a result, one does not see continuous stripes along the x-direction but dimple-like shapes concentrated at the colder regions. It may be noted that the patterns documented in **Figures 5.8**A-B are similar to the shadowgraph images obtained in experiments for longitudinal and transverse rolls, respectively (see **Figure 1.1**).

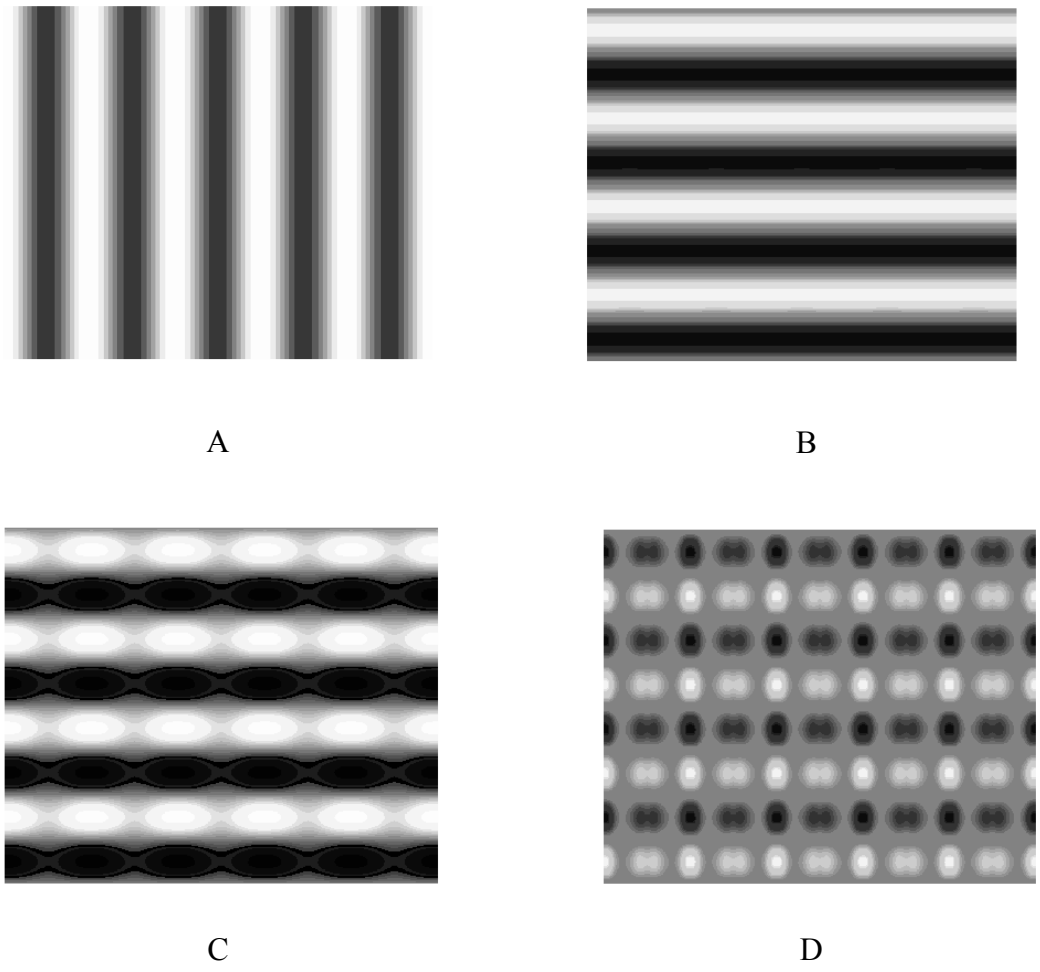

Figure 5.8. *Snapshots of the temperature field at the mid-plane (y = 0 i.e. x-z plane). Darker color corresponds to colder fluid. Figures 5.8A,B,C and D are for conditions of Fig.5.6A, Fig 5.5B, Fig.5.6B, and Fig.5.7B, respectively. Figure 5.8A is produced using the total temperature field of the primary convection defined by Eq. (2.2), and the remaining figures are produced using the disturbance temperature fields. Horizontal direction corresponds to the x-axis. The display extends for five heating wavelengths along the x-direction and four disturbance wavelengths along the z-direction.*

The transverse roll instability is driven in the "large α" zone by the uniform mean vertical temperature created by the primary convection. It appears that the vertical temperature gradient still drives the secondary convection in the case of $\alpha = O(1)$, however, this gradient is strongly modulated in the x-direction and rolls are exposed to strong, x-periodic convection currents. It may be concluded that the transverse rolls are primarily driven by the vertical temperature gradients and modulated by a combination of the spatial distribution of these gradients and convection currents created by the primary convection. Conditions where the character of variations of the critical roll wave number β_{cr} changes qualitatively (point B in **Figure 5.3**B) may be considered as a boundary between zones of dominance of these two effects. Location of this point shown in **Figure 5.4** supports conclusion that point B approximately corresponds to conditions where the primary convection starts to develop a meaningful mean vertical temperature gradient.

5.2 Fluids with the Prandtl number Pr=7

This particular value of the Prandtl number well approximates properties of water where conductive effects are relatively weaker as compared with the convective effects. The critical stability curve shown in **Figure 5.9** is qualitatively similar to the critical stability curve for Pr = 0.71 (see **Figure 5.3**). The transition point that separates zones of dominance of both instability mechanisms (point B, $\alpha_B = 3.611$) is shifted towards smaller values of α as the conduction-dominated spatial modulation is weaker. No instability occurs for $\alpha < \alpha_A = 3.6$ in the range of Ra of interest. The minimum critical Rayleigh number is $Ra_{min} = Ra_D = 2859.8$ and the corresponding most destabilizing heating pattern is described by $\alpha_{min} = \alpha_D = 4.18$. Longitudinal rolls play the role of critical disturbances for $\alpha < \alpha_C = 3.98$ while transverse rolls dominate for $\alpha > \alpha_C = 3.98$. The critical Rayleigh number approaches the same asymptote $Ra_{cr} \rightarrow 236\alpha^{1.5}$ when $\alpha \rightarrow \infty$ but more rapidly when compared with the case of Pr = 0.71. The critical roll wave number approaches the same limit, i.e., $\beta_{cr} \rightarrow 1.56$ when $\alpha \rightarrow \infty$, but again more rapidly when compared with the case of Pr = 0.71.

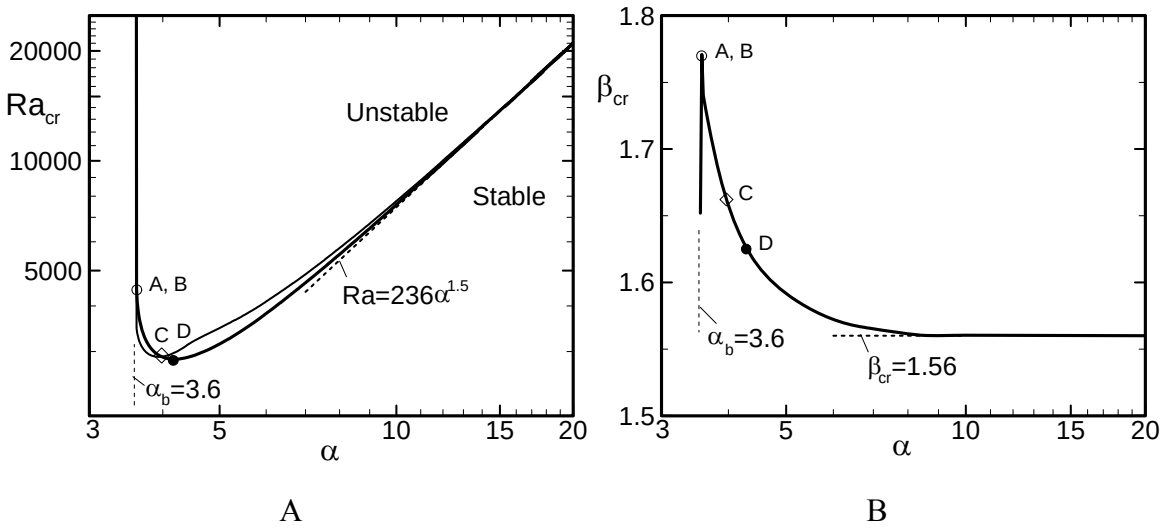

Figure 5.9. *Variations of the critical Rayleigh number Ra_{cr} (Fig.5.9A) and the critical disturbance wave number β_{cr} (Fig.5.9B) as functions of the heating wave number α for a fluid with the Prandtl number Pr = 7. Thick and thin lines correspond to the transverse roll instability and to the longitudinal roll instability, respectively. Points A, B, C, D are located at (Ra_A=4472.9, α_A=3.61, β_A=1.77), (Ra_B=4472.9, α_B=3.61, β_B=1.77), (Ra_C=2904.4, α_C=3.98, β_C=1.66), (Ra_D=2859.8, α_D=4.18, β_D=1.63), respectively.*

5.3 Fluids with the Prandtl number Pr=0.12

Reduction of the Prandtl number Pr increases the strength of the spatial modulation. As a result, compared with the cases of Pr = 7 and 0.71, the zone of instability at the left end shifts towards smaller α, and conditions required for the creation of the mean vertical temperature gradient to be meaningful shift towards higher α. **Figure 5.10** displays the resulting stability diagram. The critical curve can be divided into two segments, one with a minimum at $\alpha = \alpha_A = 2.65$ and the other one with a minimum at $\alpha = \alpha_E = 6.46$. These two segments are joined together at $\alpha = \alpha_D = 5.6$ where a qualitative change in the character of variations of the critical roll wave number β_{cr} takes place (see point D in **Figure 5.10**B). Point D is the transition point and this transition occurs at a higher value of α when compared with fluids with higher values of Pr. The modulation mechanism dominates under conditions corresponding to the left part of the critical curve

(for $\alpha < \alpha_D = 5.6$) while the effects associated with the mean vertical temperature gradient dominate under conditions associated with the right part of the curve (for $\alpha > \alpha_D = 5.6$). The change in the dominant effects is underscored by the change in the character of variations of the Nusselt number Nu of the primary convection (see **Figure 5.4**) where different types of variations are found on both sides of the transition point $\alpha_D = 5.6$. The reader may also note the emergence of a zone of heating patterns centered around $\alpha \approx 5$ where neither of the mechanisms is particularly effective.

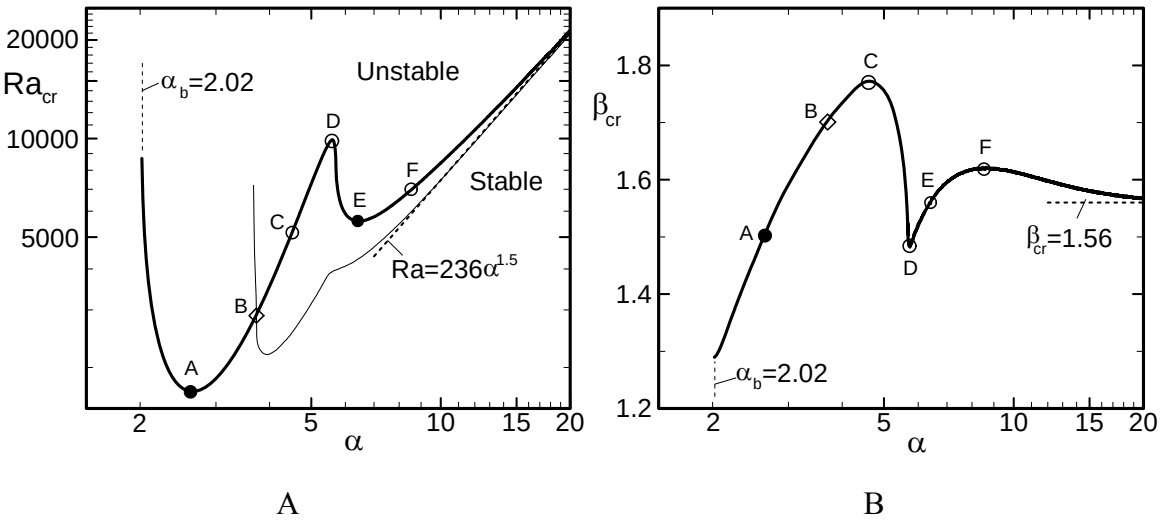

Figure 5.10. *Variations of the critical Rayleigh number Ra_{cr} (Fig.5.10A) and the critical disturbance wave number β_{cr} (Fig.5.10B) as functions of the heating wave number α for a fluid with the Prandtl number Pr = 0.12. Thick line corresponds for the transverse roll instability, and the thin line corresponds for the longitudinal roll instability. Points A, B, C, D, E, F are located at (Ra_A=1691.2, α_A=2.65, β_A=1.5), (Ra_B=2902.4, α_B=3.73, β_B=1.71), (Ra_C=5232.1, α_C=4.53, β_C=1.77), (Ra_D=9921.8, α_D=5.6, β_D=1.48), (Ra_E=5595.3, α_E=6.46, β_E=1.57), (Ra_F=7068.1, α_F=8.64, β_F=1.62), respectively.*

The effect of modulation is active over a finite range of the heating wave numbers $\alpha < \alpha_D = 5.6$ (see **Figure 5.10**A). It is most effective for the heating pattern corresponding to $\alpha_{min1} = \alpha_A = 2.65$ resulting in the critical Rayleigh number $Ra_{min1} = Ra_A = 1691.2$. It weakens as one moves away from this point in either direction along the α-axis. This mechanism is not able to destabilize the primary convection for $\alpha < \alpha_b = 2.02$ in the range of Ra of interest and is overcomed by the mean-temperature-gradient mechanism when α

increases above $\alpha_D = 5.6$. The critical roll wave number starts around $\beta_{cr} \approx 1.3$ and initially increases, it reaches a maximum of $\beta_{cr} = \beta_C = 1.77$ at $\alpha = \alpha_C = 4.53$, and then decreases to $\beta_{cr} = \beta_D = 1.48$ at $\alpha = \alpha_D = 5.6$ as one traverses the modulation-dominated zone in the direction of increasing α suggesting a rather large change in the wavelength of the critical rolls depending on the pattern of heating.

The mean-temperature-gradient mechanism dominates for heating patterns corresponding to $\alpha > \alpha_D = 5.6$. This mechanism is most effective for $\alpha_{min2} = \alpha_E = 6.46$ resulting in the critical Rayleigh number $Ra_{min2} = Ra_E = 5595.3$. Variations of Ra_{cr} follow the same asymptote for large values of α as in the cases of Pr = 0.71 and Pr = 7, i.e., $Ra_{cr} \rightarrow 236\alpha^{1.5}$ when $\alpha \rightarrow \infty$. The critical roll wave number β_{cr} varies from $\beta_{cr} = \beta_D = 1.48$ at the beginning to the mean-temperature gradient dominated interval, then increases until it reaches maximum of $\beta_{cr} = \beta_F = 1.62$ at $\alpha = \alpha_F = 8.64$ and monotonically decreases to the asymptotic limit of $\beta_{cr} \rightarrow 1.56$ when $\alpha \rightarrow \infty$. This limit is the same as for other values of Pr. Changes of the wavelengths of the critical rolls are therefore much smaller than those associated with the modulation mechanism and they are centered around the asymptotic value of $\beta_{cr} \approx 1.56$.

The form of the critical curve shows that the modulation mechanism is centered around $\alpha \approx 2.5$ and it shifts towards smaller α with reduction of Pr in direct response to the stronger modulation. The location of the most active mean-temperature gradient mechanism depends on the overall convection dynamics and it shifts towards higher values of α as Pr decreases. It smoothly overlaps with the modulation mechanism for Pr = 7 (**Figure 5.9**), some distinction begins to emerge for Pr = 0.71 (**Figure 5.3**) and two separate zones are clearly visible for Pr = 0.12 (**Figure 5.10**). We shall come back to this question in Section 5.6.

Comparison of the critical curves for the longitudinal and transverse roll instabilities (see **Figure 5.10**) shows that the transverse rolls play critical role when $\alpha < \alpha_B = 3.73$ while the longitudinal rolls dominate for $\alpha > \alpha_B = 3.73$.

5.4 Fluids with the Prandtl number Pr=0.08

The form of the critical curve displayed in **Figure 5.11**A is similar to that found in the case of Pr = 0.12 but distinctions between responses associated with both instability mechanisms are more pronounced. The modulation effect becomes stronger as evidenced by reduction of the minimum possible Ra_{cr}, its center identified by the location of the $Ra_{min1} = Ra_A$ shifts towards smaller α and its reach expands to α as small as $\alpha_b = 1.93$. The emergence of the mean-temperature gradient occurs at higher α and this pushes the transition point (point D) up in α. As a results, the zone where neither of the instability mechanisms is particularly effective widens and pushes the corresponding $Ra_{cr} = Ra_D$ to a higher level.

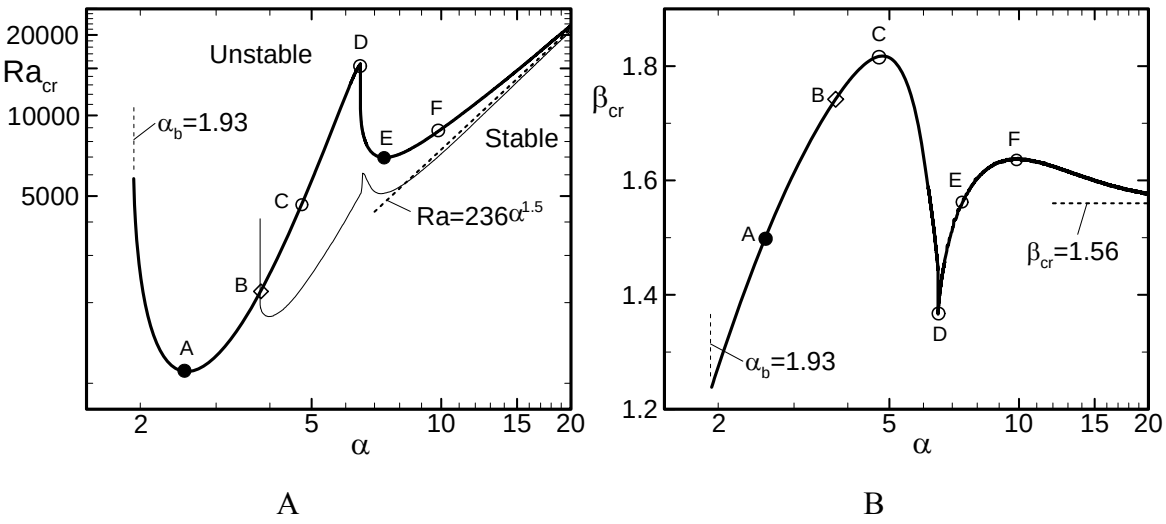

Figure 5.11. *Variations of the critical Rayleigh number Ra_{cr} (Fig.5.11A) and the critical disturbance wave number β_{cr} (Fig.5.11B) as functions of the heating wave number α for a fluid with the Prandtl number Pr = 0.08. Thick line corresponds for the transverse roll instability, and the thin line corresponds for the longitudinal roll instability. Points A, B, C, D, E, F are located at (Ra_A=1105.8, α_A=2.56, β_A=1.5), (Ra_B=2194.0, α_B=3.8, β_B=1.75), (Ra_C=4882.0, α_C=4.8, β_C=1.83), (Ra_D=15588.6, α_D=6.48, β_D=1.37), (Ra_E=6963.1, α_E=7.4, β_E=1.56), (Ra_F=8840.4, α_F=9.95, β_F=1.64), respectively.*

The modulation effect dominates for $\alpha < \alpha_D = 6.48$, it is most effective for $\alpha = \alpha_A = 2.56$ resulting in the critical Rayleigh number $Ra_{min1} = Ra_A = 1105.8$, and it cannot destabilize

the primary convection for $\alpha < \alpha_b = 1.93$. The range of variations of β_{cr} (**Figure 5.11**B) extends beyond that found for Pr = 0.12.

The mean-temperature gradient mechanism dominates for $\alpha > \alpha_D = 6.48$, it is most effective for $\alpha = \alpha_E = 7.4$ resulting in the critical Rayleigh number $Ra_{min2} = Ra_E = 6963.1$, Ra_{cr} follows the same asymptote and β_{cr} approaches the same limit for $\alpha \to \infty$ as in the case of other values of Pr. The range of variations of β_{cr} is similar to that found in the case of Pr = 0.12. The transverse rolls dominate for $\alpha < \alpha_B = 3.8$ while the longitudinal rolls play critical role for $\alpha > \alpha_B = 3.8$.

5.5 Fluids with the Prandtl number Pr=0.06

The critical curve displayed in **Figure 5.12**A has the same qualitative form as in the case of Pr = 0.08 but with more pronounced features. The zone where the mean-temperature gradient dominates moves further towards higher α and thus widens the zone where the modulation mechanism dominates. The modulation effect becomes relatively stronger as it can produce the instability at smaller α, i.e., down to $\alpha = \alpha_b = 1.87$, can reduce Ra_{cr} down to $Ra_{min1} = Ra_A = 825.6$ at $\alpha_{min1} = \alpha_A = 2.53$ (point A), and the transition to the mean-temperature gradient zone occurs at larger α, i.e., $\alpha = \alpha_D = 7.16$, although the last effect is more due to the retreat of the mean-temperature gradient mechanism to higher α. Corresponding variations of β_{cr} extend from 1.2 to 1.87 and down to 1.24 (see **Figure 5.12**B) as one traverses this zone in the direction of increasing α. The character of variations of the critical conditions in the mean-temperature gradient zone remains approximately the same as for Pr = 0.08. The zone where neither of the instability mechanisms is particularly effective widens and pushes the corresponding Ra_{cr} up to $Ra_D = 34677.1$.

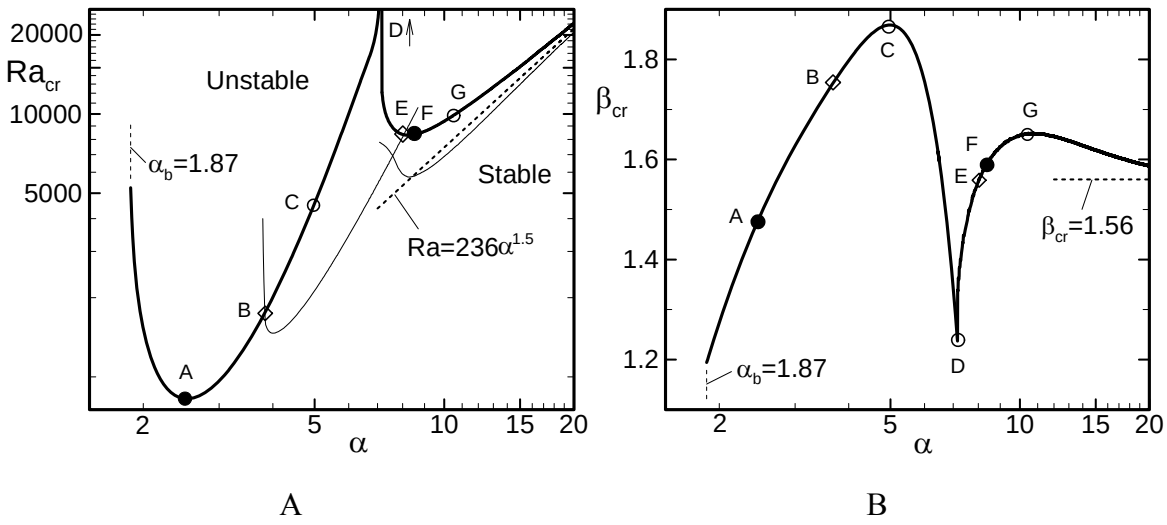

Figure 5.12. *Variations of the critical Rayleigh number Ra_{cr} (Fig.5.12A) and the critical disturbance wave number β_{cr} (Fig.5.12B) as functions of the heating wave number α for a fluid with the Prandtl number Pr = 0.06. Thick line corresponds for the transverse roll instability, and the thin line corresponds for the longitudinal roll instability. Points A, B, C, D, E, F,G are located at (Ra_A=825.6, α_A=2.53, β_A=1.5), (Ra_B=1695.0, α_B=3.79, β_B=1.77), (Ra_C=4468.1, α_C=4.97, β_C=1.87), (Ra_D=34667.1, α_D=7.16, β_D=1.24), (Ra_E=8336.1, α_E=8.06, β_E=1.56), (Ra_F=8299.2, α_F=8.26, β_F=1.58), (Ra_G=9836.3, α_G=10.46, β_G=1.65), respectively.*

5.6 Fluids with an arbitrary Prandtl number

Evolution of fluid response as a function of the Prandtl number Pr and the interplay between both mechanisms producing secondary convection are illustrated in **Figure 5.13**. The increase of the strength of the modulation effect and its small shift towards smaller α can be easily followed. At Pr > 2 the zones of activity of both mechanisms overlap producing critical curve with one minimum in the range of Ra subject to this investigation. A small shift of the modulation effect towards smaller α can be seen at Pr = 1 as the small-α end of the critical curve starts to bends towards small α. This shift becomes more pronounced as Pr further decreases with the critical curve acquiring two minima at Pr ≈ 0.5, one at a smaller α associated with the modulation effect and one at a higher α that can be attributed to the mean-temperature gradient effect. The former minimum becomes the overall minimum for Pr <~0.25. Further decrease of Pr

continuously increases the strength of the modulation effect expanding the zone of instability to smaller α's and reducing the corresponding minimum Ra_{cr}. At the same time the mean-temperature gradient effect becomes relatively weaker and retreats towards larger α; the corresponding minimum of Ra_{cr} continuously increases with reduction of Pr. The shift of the mean-temperature gradient effect towards larger α is not compensated by the equivalent expansion of the modulation effect towards larger α creating a fairly stable, in-between zone of heating patterns where the transverse roll instability occurs only at a fairly large Ra_{cr}.

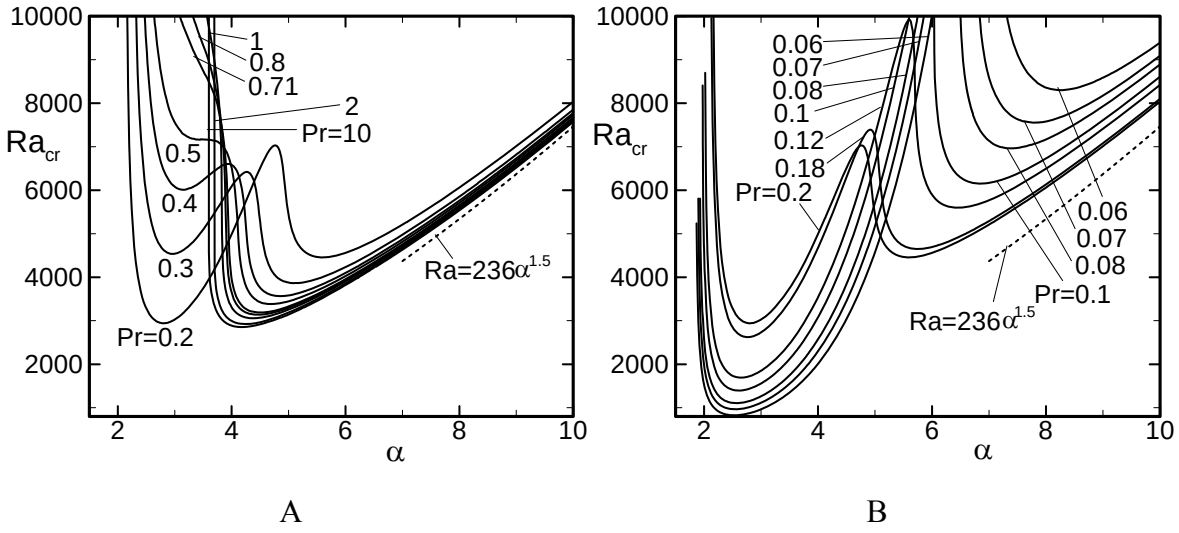

Figure 5.13. *Variations of the critical Rayleigh number Ra_{cr} as functions of the heating wave number α for selected values of the Prandtl number Pr (Fig.5.13A - Pr=10-0.2, Fig,5.13B - Pr=0.2-0.06).*

Evolution of the critical roll wave number β_{cr} as a function of Pr is illustrated in **Figure 5.14**. The reader may note formation of the transition point between zones dominated by different instability mechanism starting with Pr ≈ 0.4 (**Figure 5.14**B) with the distinction increasing with any further decrease of Pr. Another process appears to take place when Pr increases above 0.4 as a clear distinction between zones where each mechanism plays a leading role disappears (**Figure 5.15**). Both mechanisms coexists, however, modulation effect takes over for a sufficiently large Pr resulting in a rapid drop

of β_{cr}. This change occurs for large Ra outside the range of interest in the current work as other processes not related to the transverse roll instability are likely to dominate the flow response.

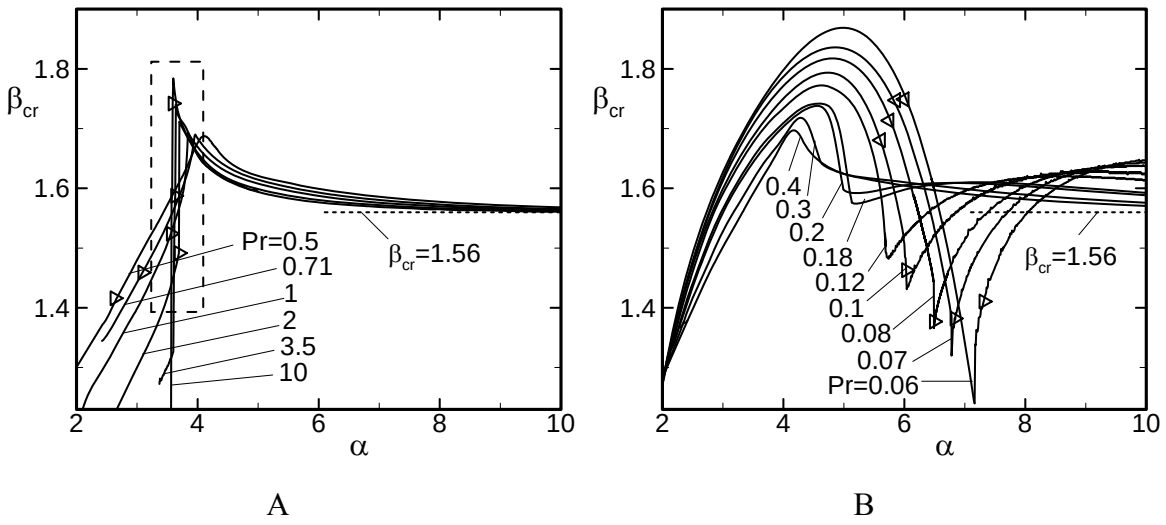

Figure 5.14. *Variations of the critical wave number β_{cr} as functions of the heating wave number α for selected values of the Prandtl number Pr (Fig.5.14A - Pr=10-0.5, Fig.5.14B - Pr=0.5-0.06). Enlargement of the box marked in Fig.5.14A is displayed in Fig.5.15. Zones between triangles in Fig.5.14B correspond to $Ra_{cr} > 10^4$.*

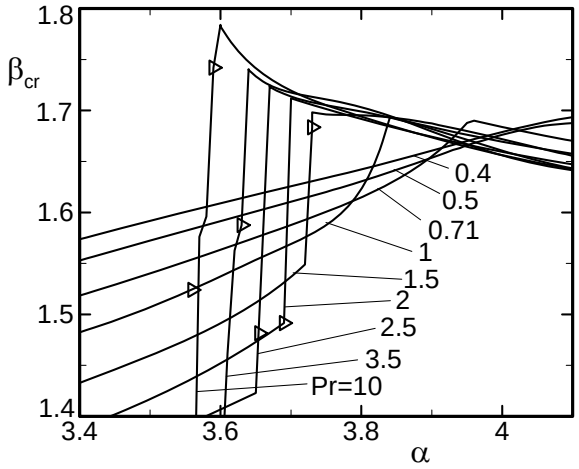

Figure 5.15. *Enlargement of the box marked in Fig.5.14A. Zones to the left of triangles correspond to $Ra_{cr} > 10^4$.*

5.7 Summary

Onset of the transverse roll instability in an infinite slot subject to a sinusoidal heating at the lower wall has been considered in this chapter for a wide range of Prandtl numbers Pr. Two instability mechanisms contributing to the onset of such convection have been identified. The first mechanism is based on effect of the modulation associated with the spatial pattern of the heating. This mechanism is active for heating patterns corresponding to the heating wave numbers O(1) for all types of fluids considered (with properties characterized in terms of the Prandtl number Pr). The second mechanism is associated with the mean vertical temperature gradient created by the primary convection and the zone where this mechanism is active shifts towards higher values of the heating wave number as Pr decreases. The interplay between both mechanisms results in a single-minimum critical curve for values of Pr where both mechanisms are active in the same range of the heating wave numbers, and a two-minimum critical curve where both mechanisms are active in distinctly different ranges of the heating wave numbers. A zone of a fairly stable primary convection occurs in the latter case for the heating patterns corresponding to the heating wave numbers from the in-between zone.

A decrease of Pr produces primary convection with a stronger spatial modulation. As a result, the modulation effect mechanism becomes stronger reducing the minimum critical Rayleigh number required for the onset of the secondary convection. Because of the strong spatial modulation, the formation of the mean vertical temperature gradient shifts towards higher values of the heating wave numbers resulting in the higher critical Rayleigh numbers required for the onset of the secondary convection under conditions when the modulation effect is weak.

6

Oblique Roll

In this chapter we shall turn our attention to the secondary rolls with an arbitrary orientation, i.e., rolls characterized by the wave vector **q** = (δ, ±β) with the magnitude $|\mathbf{q}| = \left(\beta^2 + \delta^2\right)^{1/2}$ and the inclination angle η = ± $\tan^{-1}$(β/δ). According to this notation longitudinal rolls correspond to η = 0° and transverse rolls to η = 90°. Similar to the longitudinal and transverse rolls instabilities, there exist only stationary disturbances, i.e., σ_r = 0. No travelling wave disturbances have been found. Characteristics of oblique rolls for fluids with the Prandtl number Pr = 0.71 are described in details in Section 6.1 and form a reference point. Characteristics of this instability for high Prandtl number fluids, e.g., for Pr = 7, 3 and 2 are discussed in Section 6.2. Characteristics for small Prandtl number fluids, e.g., Pr = 0.12, 0.08, and 0.06, are discussed in Section 6.3, 6.4, and 6.5, respectively. Section 6.6 is devoted to discussion of Prandtl number effects. A short summary is given in Section 6.7. The reader may note that the cost of evaluation of eigenvalues for the oblique roll instability is considerably higher as one has to consider both the x- and z-components of the wave vector (i.e., δ and β) of disturbances.

6.1 Fluids with the Prandtl number Pr=0.71

All physical mechanisms discussed so far contribute to the dynamics of the oblique rolls, including parametric resonance as well as direct modulation by patterns of vertical temperature gradients and distribution of convection currents.

We begin our discussion with **Figure 6.1** which illustrates the evolution of the neutral surfaces in the $\left(\mathrm{Ra}, |\mathbf{q}|, \eta\right)$ space for selected values of the heating wave number.

Figure 6.1A displays neutral surface for $\alpha = 10$ ("large α" zone). It can be seen that the minimum of Ra corresponds to $|\mathbf{q}| = 1.56$ and $\eta = 90°$ (transverse rolls). This minimum is fairly flat in the η direction with the change of Ra between $\eta = 90°$ and $\eta = 0°$ being ~130 which demonstrates a rather week preference for the transverse rolls. The minimum is rather steep in the $|\mathbf{q}|$ direction showing a strong preference for the size of the rolls. Reduction of the heating wave number to $\alpha = 5$ (**Figure 6.1**B) demonstrates emergence of two local minima, one centered at $\eta = 0°$, $|\mathbf{q}| \approx 1.7$ and the other at $\eta = 90°$, $|\mathbf{q}| \approx 1.6$. The transverse rolls with slightly higher $|\mathbf{q}|$ continue to play the critical role. Gradients in the η and $|\mathbf{q}|$ directions remain similar showing weak preference for the orientation of the rolls but strong preference for the size. Further reduction of the heating wave number to $\alpha = 4.4$ shows existence of similar two local minima but with the minimum at $\eta = 0°$ becoming the global minimum and the longitudinal rolls playing the critical role (see **Figure 6.1**C). When the heating wave number reaches value $\alpha = 4$ (**Figure 6.1**D) the global minimum moves from $\eta = 0°$ to $\eta \approx 8°$ showing that the oblique rolls begin to play the critical role; these rolls become a bit smaller as the corresponding wave number increases to $|\mathbf{q}| \approx 2.1$. Further reduction of the heating wave number to $\alpha = 3.5$ shows existence of a single minimum at $\eta \approx 28°$ and a slight reduction of $|\mathbf{q}|$ (**Figure 6.1**E). The minimum of Ra_{cr} is reached at $\alpha = 2.69$ (not shown) and further decrease of the heating wave number leads to the increase of Ra_{cr}, a small increase of the inclination angle η and a fairly large decrease of the roll wave number $|\mathbf{q}|$ as illustrated in **Figure 6.1**F for $\alpha = 2.5$.

Variations of the global and local minima as functions of the heating wave number are illustrated in **Figure 6.2** and identify the critical stability conditions. It can be seen that the transverse rolls play the critical role for $\alpha > \alpha_D = 4.46$, the longitudinal rolls dominate for $\alpha_D = 4.46 > \alpha > \alpha_B = 4.07$ and the oblique rolls become dominant for $\alpha < \alpha_C = 4.03$ (the minimum Rayleigh number point for the longitudinal roll). Reduction of α below $\alpha_C = 4.03$, i.e., use of heating pattern that gives rise to oblique rolls, leads to the reduction

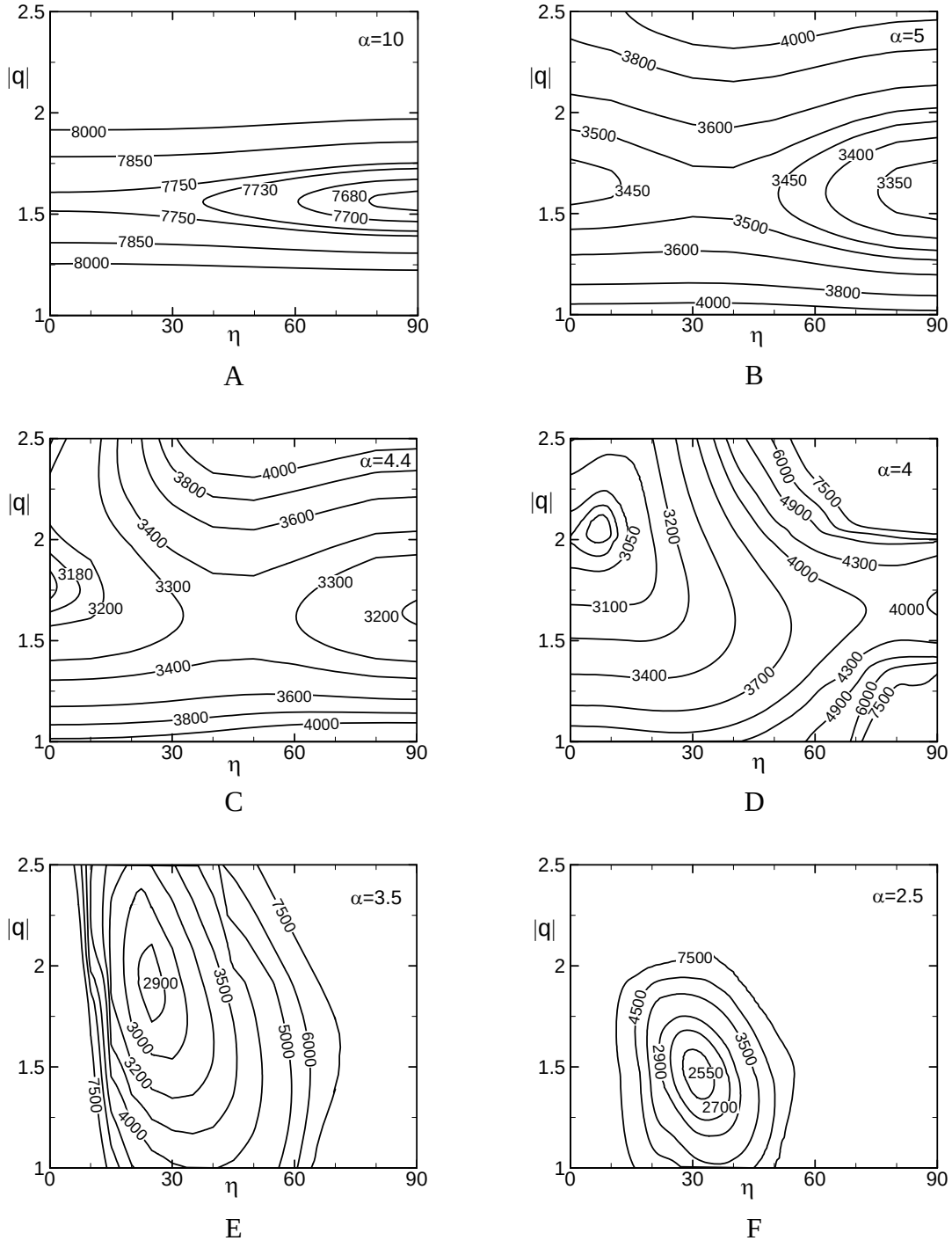

Figure 6.1. *Neutral surfaces in the space formed by the roll wave number* $|\mathbf{q}|$*, the roll inclination angle* η *and the Rayleigh number Ra for selected values of the heating wave number* α *for the fluid with the Prandtl number Pr=0.71.*

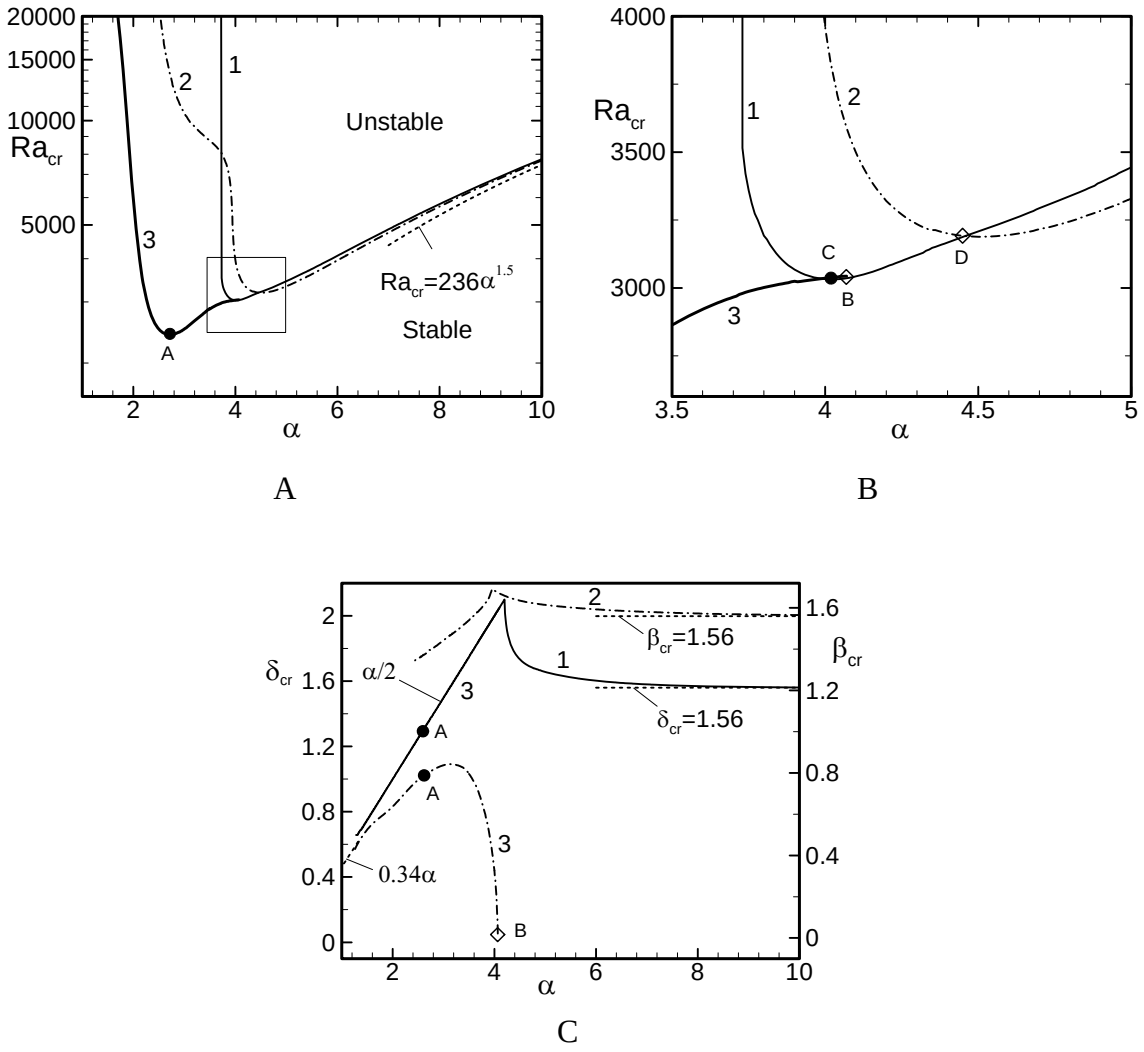

Figure 6.2. *Variations of the critical Rayleigh number Ra_{cr} (Fig.6.2A,B) and the critical wave numbers δ_{cr} (solid line) and β_{cr} (dash-dot lines) (Fig.6.2C) as functions of the heating wave number α for the fluid with the Prandtl number Pr = 0.71. Enlargement of the box shown in Fig.6.2A is displayed in Fig.6.2B. Curves 1, 2, 3 correspond to the longitudinal, transverse and oblique rolls, respectively. Points A, B,C and D are located at (Ra_A=2411.2, α_A=2.69, δ_A=1.345, β_A=0.8), (Ra_B=3043.6, α_B=4.07, δ_B=2.035, β_B=0), (Ra_C=3031.6, α_C=4.03, δ_C=2.015, β_C=0), and, (Ra_D=3191.4, α_D=4.46, δ_D=0, β_D=1.64).*

of Ra_{cr}. The most efficient pattern for formation of oblique rolls corresponds to $\alpha = \alpha_A$ = 2.69 and results in $Ra_{cr} = Ra_A$ = 2411.2. A rapid stabilization of the primary convection is observed when the heating wave number is reduced below $\alpha \approx$ ~2.2 with no instability

found for α <~1.75 in the range of Ra considered. This stabilization is remarkable as no rolls may appear if α is sufficiently small. A possible reason for elimination of secondary rolls is illustrated in **Figure 6.3** which displays variations of the mean vertical temperature created by the primary convection at the onset. It can be seen that the zone with an unstable temperature gradient becomes thinner for smaller α leading to reduction of the driving force and, at the same time, increase of the opposing force.

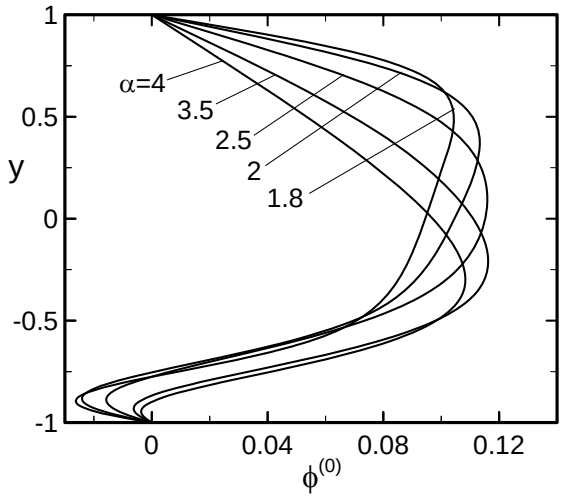

Figure 6.3. *Distributions of the 0th modal function of the primary convection temperature $\phi^{(0)}$ for selected values of the heating wave number α corresponding to the onset of the oblique rolls for the fluid with the Prandtl number Pr = 0.71, i.e. (Ra, α) = (3035.7, 4), (2863.7, 3.5), (2505.7, 2.5), (5918.9, 2), (14030.3, 1.8).*

Variations of the critical wave numbers for the longitudinal and transverse rolls have been already described in Chapters 4 and 5. When the oblique rolls dominate, the x-component of the wave vector is locked-in with the heating wave number according to the relation $\delta_{cr} = \alpha/2$ (similar relation exhibits in the case of longitudinal rolls) while the z-component does not exhibit any correlation with α (**Figure 6.2**C). β_{cr} increases rapidly from 0 to about 0.8 when the heating wave number decreases from α_B = 4.07 down to $\alpha \approx 3$ resulting in a rapid rotation of the critical roll up to orientation corresponding to $\eta \approx 30°$ (see **Figure 6.4**). Further decrease of α causes small increase of the inclination angle

while the roll wave number decreases according to the relation $|\mathbf{q}| \approx \alpha / 1.65$.

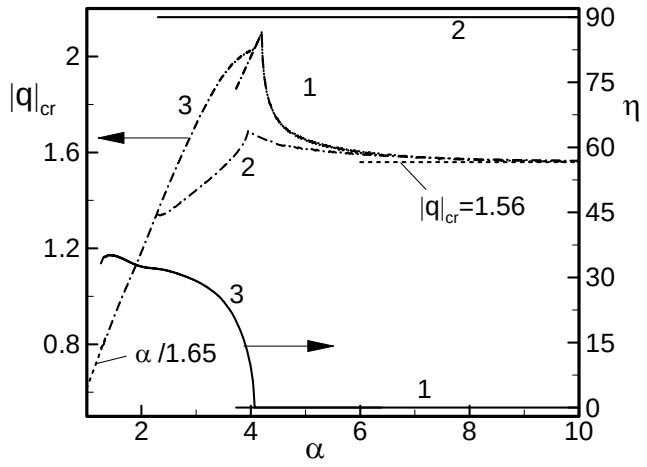

Figure 6.4. *Variations of the critical roll wave number* $|\mathbf{q}|_{cr}$ *(dash-dot lines) and the roll inclination angle* η *(solid lines) as a function of the heating wave number* α *at the onset conditions for the fluid with the Prandtl number Pr = 0.71. Lines 1, 2, 3 correspond to the longitudinal, transverse and oblique rolls, respectively.*

Pattern associated with a single oblique roll is similar to the transverse roll shown in **Figure 5.7**B. Since oblique rolls appear in pairs with the wave vectors $\mathbf{q}_{1,2} = (\delta_{cr}, \pm\beta_{cr})$ (Freund et al. 2010, Tao and Busse 2009), the secondary convection takes the form of finite cells of rectangular shape rather than the infinite rolls. The aspect ratio x/z of the rectangle approaches 0.7 as α decreases. The topology resulting from superposition of two oblique rolls is shown in **Figure 6.5**A where the rectangular cells are clearly visible. The length of the rectangular cells in z-direction increases with the increase of the heating wave number α, and at $\alpha = \alpha_B = 4.07$ they form continuous rolls, i.e., they smoothly morph into longitudinal rolls as shown in **Figure 6.5**B. To determine orientation angle of the rectangular cells, a snapshot of the disturbance temperature field is shown in **Figure 6.6**.

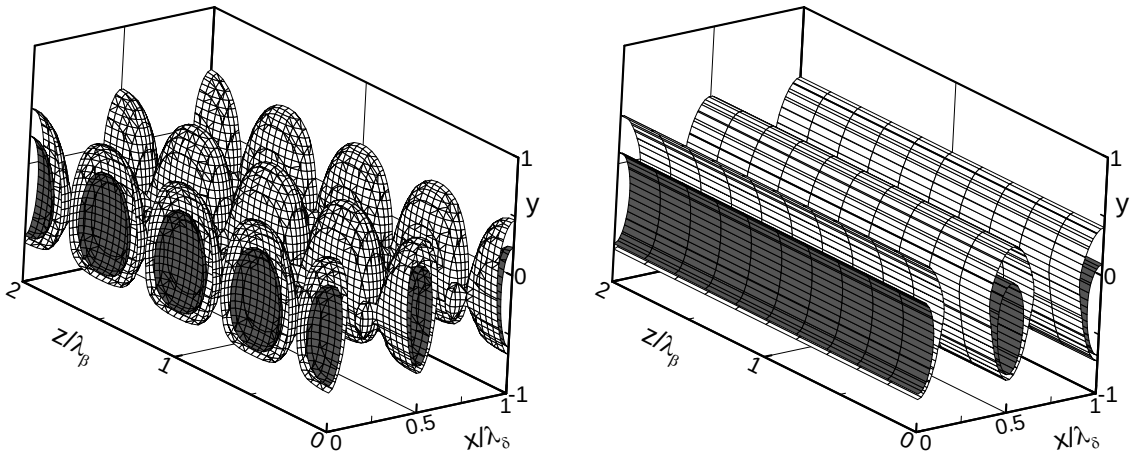

Figure 6.5. *Flow structures created by the secondary convection in the form of oblique rolls (Fig.6.5A) and longitudinal rolls (Fig.6.5B) generated by the heating with the wave numbers α = 3.2 and 4.07 at the onset, i.e., for the Rayleigh number Ra_{cr} = 2645.7 and 3043.6, respectively, for the fluid with the Prandtl number Pr = 0.71. The critical roll wave numbers are δ_{cr} = 1.6 and 2.035, β_{cr} = ±0.841 and 0, respectively. Iso-surfaces with Q = 0.05, 0.3 (see Eq.5.2) are displayed in both figures.*

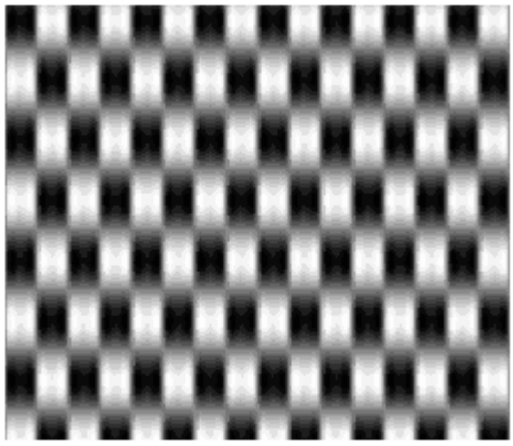

Figure 6.6. *Snapshot of the disturbance temperature field at the mid-plane (y = 0) for the flow conditions shown in Fig.6.5A. Dark color identifies colder fluid and white color identifies hotter fluid. Eight disturbance wavelengths were used for plotting in the x-direction and four disturbance wavelengths were used along the z-direction.*

6.2 High Prandtl number fluids

In this section we discuss instability in high Prandtl number fluids, e.g., in fluids with Pr = 7, 3, and 2, where conductive effects are weaker than convective effects. The critical stability curves are shown in **Figure 6.7**A-C. It can be seen that the zone where the oblique rolls play the critical role expands as Pr decreases, i.e., values of α_B increase with a decrease of Pr. At the same time the critical value of Ra at $\alpha = \alpha_B$ decreases which demonstrates that the oblique rolls become more important for smaller values of Pr. The most efficient heating pattern for creation of oblique rolls corresponds to $\alpha = \alpha_A = 2.64$ and remains unchanged for all values of Pr.

Variations of the critical wave numbers are shown in **Figure 6.7**D. Since the primary computed quantities are the x-and z-components of the wave vector δ_{cr} and β_{cr}, we report and discuss their variations in this section. We shall discuss the roll wave number $|\mathbf{q}|$ and the inclination angle η in a later section. It is clear that the subharmonic relation $\delta_{cr} = \alpha/2$ for the critical x-component of the wave vector holds for high Prandtl number fluids. The critical z-component of the wave vector β_{cr} increases with an increase of the heating wave number α unlike the case of Pr = 0.71 where β_{cr} rapidly decreased to 0 around $\alpha \sim 4$ causing a smooth transition from the oblique roll to the longitudinal roll. There is no smooth transition between various types of rolls for high Prandtl number fluids.

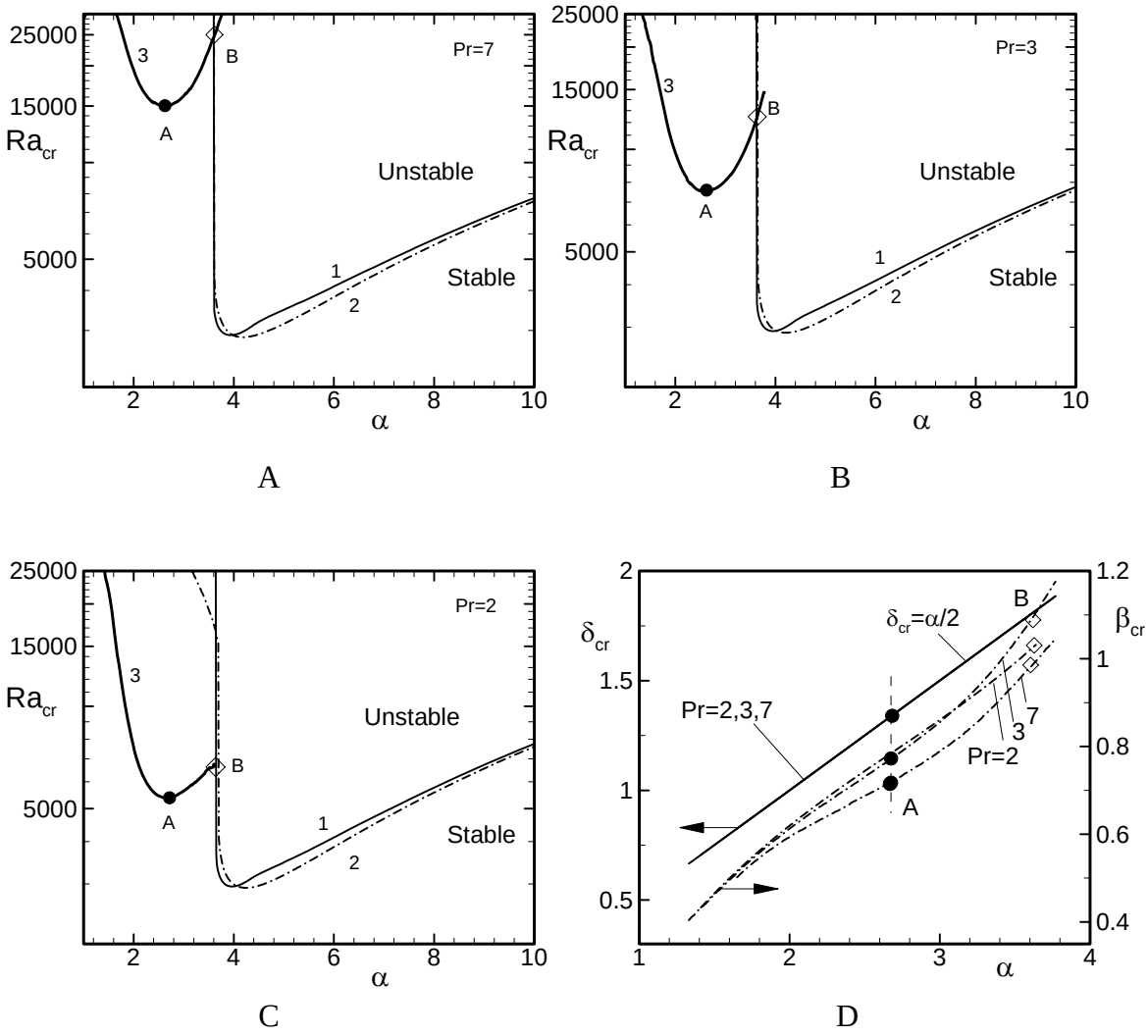

Figure 6.7. *Variations of the critical Rayleigh number Ra_{cr} (Fig.6.7A,B,C) and the critical wave numbers δ_{cr} (solid line) and β_{cr} (dash-dot lines) (Fig.6.7D) as functions of the heating wave number α for fluids with the Prandtl number Pr = 7,3,2, respectively. Lines 1, 2, 3 in Fig. 6.7A,B,C correspond to the longitudinal, transverse and oblique rolls, respectively. Fig. 6.7D is only for the oblique rolls. Points A and B are located at (Ra_A=14982.36, α_A=2.64, δ_A=1.32, β_A=0.712) and (Ra_B=24497.45, α_B=3.6, δ_B=1.8, β_B=0.979) for Pr=7(Fig.6.7A); (Ra_A=7507.28, α_A=2.64, δ_A=1.32, β_A= 0.763) and (Ra_B=12245.14, α_B=3.62, δ_B=1.81, β_B=1.095) for Pr=3(Fig.6.7B); and (Ra_A=5369.2, α_A=2.64, δA=1.32, βA=0.776) and (Ra_B=6658.62, α_B=3.64, δ_B=1.82, β_B=1.023) for Pr=2(Fig.6.7C).*

6.3 Fluids with the Prandtl number Pr=0.12

We have already pointed out that reduction of the Prandtl number Pr increases the strength of the spatial modulation. **Figure 6.8**A displays stability diagram for Pr = 0.12. Here we observe that the oblique rolls play a dominant role for $\alpha < \alpha_B = 5.79$, and no instability occurs for $\alpha < \alpha_b = 1.69$. The most effective heating pattern to induce the oblique roll instability corresponds to $\alpha = \alpha_A = 2.75$ and requires heating intensity $Ra_{cr} = Ra_A = 753.9$. This intensity is 55% smaller than the intensity required by the transverse roll instability created by its most efficient heating pattern. The critical x-component of the disturbance wave vector δ_{cr} also follows relation $\delta_{cr} = \alpha/2$. The critical z-component of the disturbance wave vector β_{cr} increases with an increase of the heating wave number α which demonstrates that there is no continuous transformation of the oblique rolls into the longitudinal rolls.

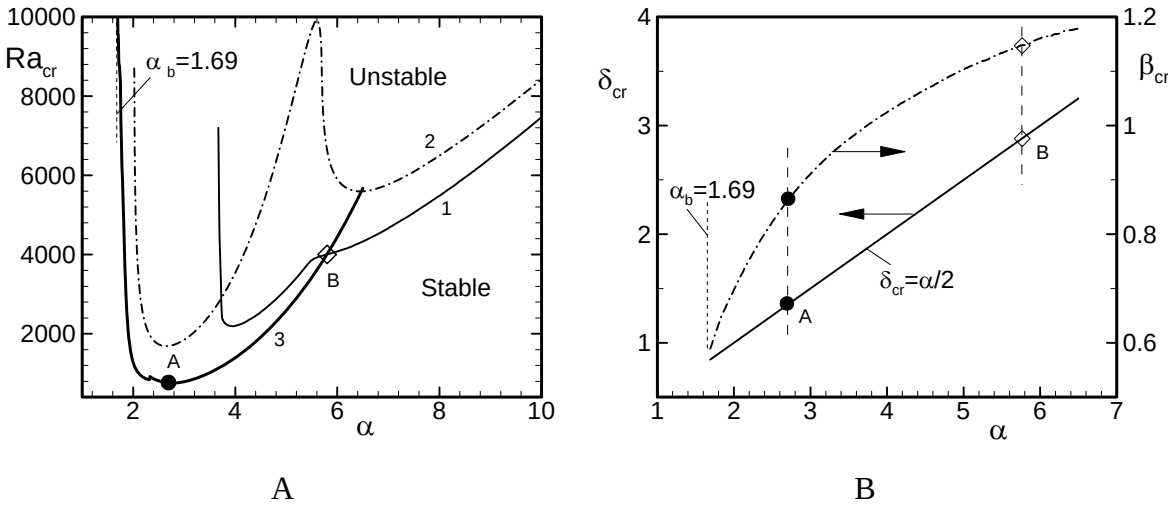

Figure 6.8. *Variations of the critical Rayleigh number Ra_{cr} (Fig.6.8A) and the critical wave numbers δ_{cr} (solid line) and β_{cr} (dash-dot lines) (Fig.6.8B) as functions of the heating wave number α for a fluid with the Prandtl number Pr = 0.12. Lines 1, 2, 3 in Fig.6.8A correspond to the longitudinal, transverse and oblique rolls, respectively. Fig.6.8B is only for the oblique rolls. Points A and B are located at (Ra_A=753.9, α_A=2.75, δ_A=1.375, β_A=0.87) and (Ra_B=3990.1, α_B=5.79, δ_B=2.895, β_B=1.147).*

6.4 Fluids with the Prandtl number Pr=0.08

The form of the critical stability curve displayed in **Figure 6.9**A is similar to that found for the fluid with Pr = 0.12. The zone of dominance of the oblique roll is increased compared with the case of Pr = 0.12 as the oblique rolls play the critical role for the heating wave numbers up to $\alpha = \alpha_B = 6.97$. At the same time the instability can be induced by heating with the wave numbers as small as $\alpha = \alpha_b = 0.96$. The most efficient heating pattern as far as instability is concerned corresponds to $\alpha = \alpha_A = 2.35$ with the corresponding heating intensity described by $Ra_{cr} = Ra_A = 521.9$. Approximately 53% less heating is required to induce the oblique roll instability compared with the transverse roll at its most efficient heating patterns. The x-component of the critical disturbance wave vector δ_{cr} follows the same relation as for other values of Pr, i.e., $\delta_{cr} = \alpha/2$. The z-component of the critical wave vector β_{cr} increases with an increase of the heating wave number α and this increase is almost linear for $\alpha > \alpha_B$.

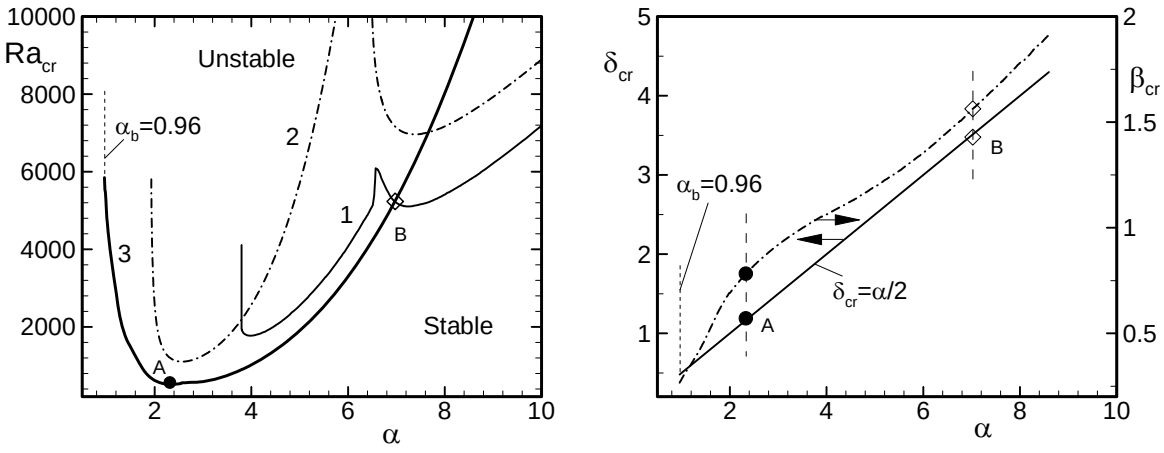

Figure 6.9. *Variations of the critical Rayleigh number Ra_{cr} (Fig.6.9A) and the critical wave numbers δ_{cr} (solid line) and β_{cr} (dash-dot lines) (Fig.6.9B) as functions of the heating wave number α for the fluid with the Prandtl number Pr = 0.08. Lines 1, 2, 3 in Fig.6.9A correspond to the longitudinal, transverse and oblique rolls, respectively. Fig.6.9B is only for the oblique rolls. Points A and B are located at (Ra_A=521.9, α_A=2.35, δ_A=1.175, β_A= 0.786) and (Ra_B=5239.5, α_B=6.97, δ_B=3.485, β_B=1.552).*

6.5 Fluids with the Prandtl number Pr=0.06

The critical stability curve displayed in **Figure 6.10**A has the same qualitative characteristics as for fluids with Pr = 0.08. The zone of dominance of the oblique rolls is further expanded as now the upper bound for the zone where the oblique rolls play the critical role moves to α_B = 7.91, and the lower bound moves to α_b = 0.94. The most efficient heating pattern corresponds to $\alpha = \alpha_A$ = 2.31 and the corresponding heating intensity is described by $Ra_{cr} = Ra_A$ = 387.6. Approximately 53% less heating is required to induce the oblique roll instability compared with the transverse roll at its most efficient heating patterns. The x-component of the critical disturbance wave vector δ_{cr} changes according to the relation $\delta_{cr} = \alpha/2$. The z-component of the critical disturbance wave vector β_{cr} increases with an increase of the heating wave number α and this increase is linear for $\alpha > \alpha_B$.

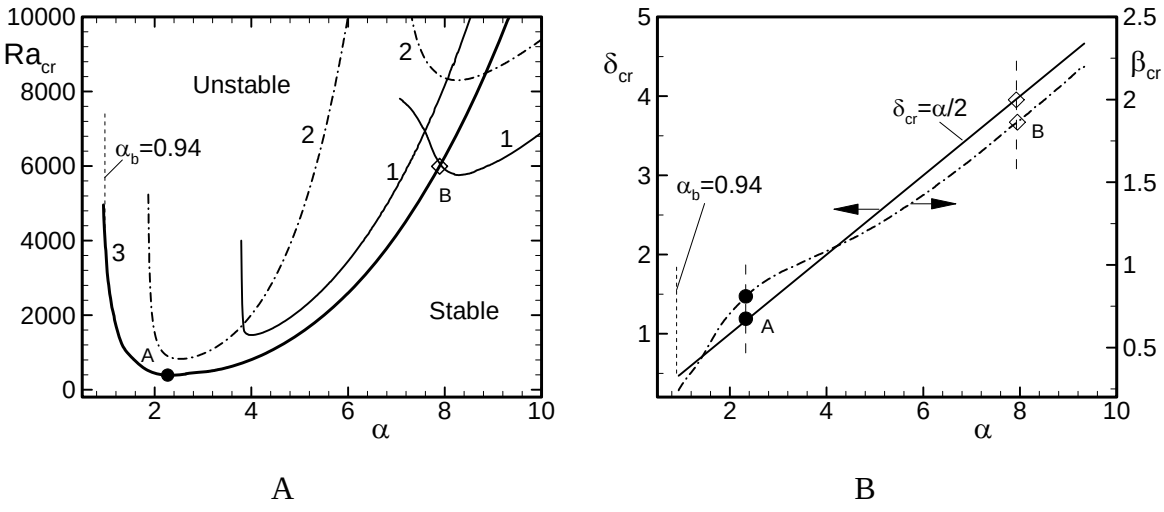

Figure 6.10. *Variations of the critical Rayleigh number Ra_{cr} (Fig.6.10A) and the critical wave numbers δ_{cr} (solid line) and β_{cr} (dash-dot lines) (Fig.6.10B) as functions of the heating wave number α for the fluid with the Prandtl number Pr = 0.06. Lines 1, 2, 3 in Fig.6.10A correspond to the longitudinal, transverse and oblique rolls, respectively. Fig.6.10B is only for the oblique rolls. Points A and B are located at (Ra_A=387.6, α_A=2.31, δ_A=1.155, β_A=0.8) and (Ra_B=6035.8, α_B=7.91, δ_B=3.955, β_B=1.855).*

6.6 Fluids with an arbitrary Prandtl number

Evolution of fluid responses as a function of the Prandtl number Pr are illustrated in **Figure 6.11**A for the zone (i.e., range of α) of dominance of the oblique roll instability. It is observed that the zone of dominance gradually increases with a decrease of Pr. Most of the increase occurs at the high α end with very small increase at the low α end. The x-component of the critical disturbance wave vector δ_{cr} always changes according to the relation $\delta_{cr} = \alpha/2$ regardless of the value of Pr (not shown in the figure). **Figure 6.11**B demonstrates that a smooth and gradual transition from the oblique roll to the longitudinal roll (i.e., the oblique roll morphs into the longitudinal roll) occurs for the fluid with ~0.3<Pr<~1. Above and below this range of Pr there is no smooth transition between different types of rolls.

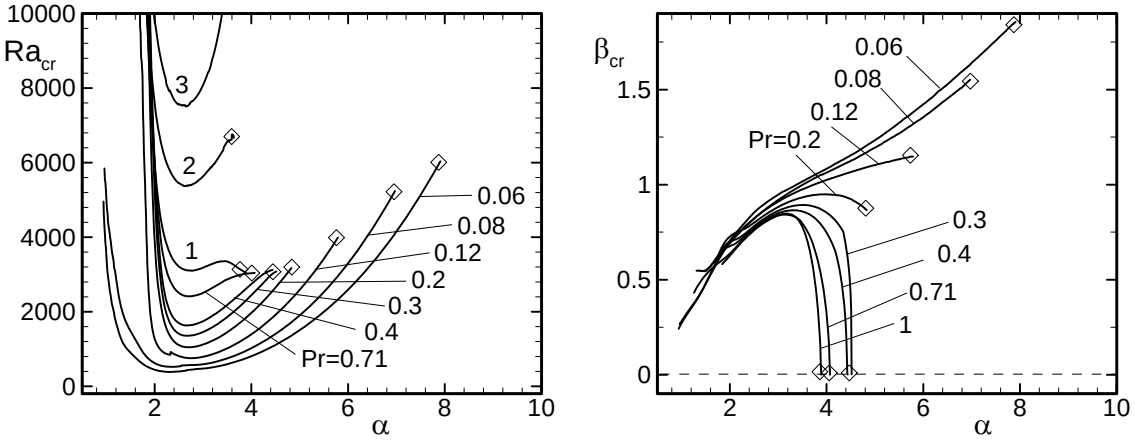

Figure 6.11. *Variations of the critical Rayleigh number Ra_{cr} (Fig.6.11A) and the critical z-component of the wave vector β_{cr} (Fig.6.11B) as functions of the heating wave number α for selected values of the Prandtl number Pr for the zone of dominance of the oblique roll. Diamond symbols denote the upper bound of the zone of dominance of the oblique roll. Note that the critical x-component of the wave vector δ_{cr} holds the relation '$\delta_{cr}=\alpha/2$' for all of the Prandtl numbers considered and not shown in this figure. The variation of β_{cr} for Pr =2 and 3 are omitted for the clarity of the figure (they are shown in Fig.6.7D).*

At this point, we focus discuss on the variations of the critical oblique roll wave number and its inclination angle as shown in **Figure 6.12**. It is observed that for high Pr number fluids, e.g., Pr >~2, the inclination angle η varies very little with the change of the heating wave number α. It varies around $\eta \sim 30^0$ ($\pm 1^0$) in the range of Pr considered here. For moderate Pr number fluids, i.e., ~0.3<Pr<~1, this angle varies from 0^0 to 35^0 which causes the oblique rolls to morph smoothly into the longitudinal rolls. For low Pr number fluids, i.e., Pr <~0.2, the inclination angle varies between 20^0 and 35^0 (this range is reduced to 25^0 to 35^0 for Pr = 0.06). The critical roll wave number $|\mathbf{q}|_{cr}$ varies mostly in a linear form that can be approximated as $|\mathbf{q}|_{cr} = 0.55\alpha + 0.02$ with a branching off around the upper end of α-zone where oblique rolls play the dominant role. This branching is in the upward direction for high Prandtl numbers (Pr >~2), and in the downward direction for moderate Prandtl numbers (~0.3<Pr<~1), and is negligible for small Prandtl numbers (Pr <~0.2).

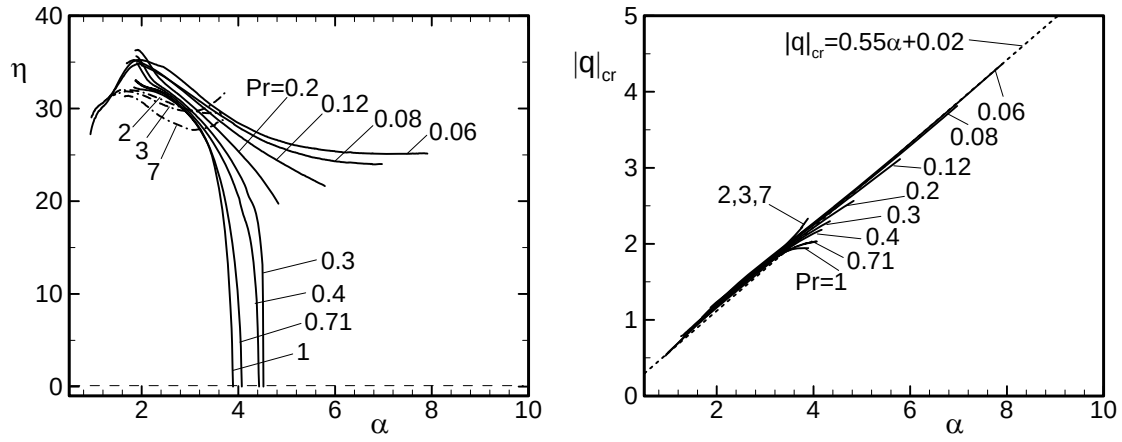

A B

Figure 6.12. *Variations of the roll inclination angle η (Fig. 6.12A) and the critical oblique roll wave number* $|\mathbf{q}|_{cr}$ *(Fig.6.12B) as functions of the heating wave number α for selected values of the Prandtl number Pr for the zone of dominance of the oblique roll. In Fig.6.12A dash-dotted lines are used for Pr=2,3,7 to distinguish the lines from other Pr.*

6.7 Summary

Onset of the secondary rolls oblique to the primary convection rolls in an infinite slot subject to a sinusoidal heating at the lower wall has been elucidated in this chapter for a wide range of Prandtl numbers Pr. The oblique rolls lead to the formation of convection cells with aspect ratio dictated by their inclination angle. It has been found that for fluids with Pr = 0.71 these rolls can change orientation from 0° to 30° with respect to the primary rolls depending on the heating wave number within the range of Ra being of interest. A rapid stabilization of the primary convection is observed when the heating wave number is sufficiently small. Analysis of the temperature field created by the primary convection at the onset suggests that reduction of the thickness of the zone with an unstable temperature gradient is likely responsible for the observed stabilization.

High Prandtl number fluids require substantial amount of heating to induce the oblique roll instability. A decrease of Pr reduces the amount of heating required to induce the oblique roll instability. The zone of dominance of oblique rolls expands toward larger α with a decrease of Pr. The x-component of the critical wave vector δ_{cr} always satisfies relation $\delta_{cr} = \alpha/2$ regardless of the value of Pr. A continuous morphing between the oblique rolls and the longitudinal rolls occurs only for the fluid with $\sim 0.3 < Pr < \sim 1$.

7

Oscillatory Mode

The previous chapters demonstrate that all forms of rolls are stabilized if the heating wave number α is reduced sufficiently. The small α regime is characterized by the appearance of an oscillatory mode of the secondary convection and description of this mode is the main focus of this chapter. Unlike the roll instabilities discussed in the previous chapters, the disturbances for the oscillatory mode are not stationary in nature, i.e., $\sigma_r \neq 0$, and they oscillate in time. The frequency of the oscillation σ_r may have both sign, so the instability can manifest itself as a wave travelling in the either direction along the axis of the primary rolls or as a standing wave. This type of instability has been found by Busse and Clever (1979) in the stability analysis of two-dimensional convective rolls for the case of uniformly heated wall for fluids with Prandtl number Pr <~1. We investigate the characteristics of this mode for fluids with the Prandtl number Pr = 0.71 only and discuss results in Section 7.1. A short summary follows in Section 7.2. The reader may note that the cost of computing of characteristics of the oscillatory mode is even higher than the cost of computing of characteristics of the oblique rolls (see Appendix E).

7.1 Fluids with the Prandtl number Pr=0.71

The critical stability conditions for the onset of the oscillatory mode of instability have been determined using a process similar to that used in the case of rolls. Variations of the critical Rayleigh number displayed in **Figure 7.1** show that the oscillatory mode is centered around $\alpha = \alpha_A = 0.25$ and plays the critical role for $\alpha < \alpha_B = 1.73$. Reduction of α below this value results in a rapid destabilization with the critical Rayleigh number reaching the minimum value of $Ra_{cr} = Ra_A = 2056.6$ at $\alpha = \alpha_A = 0.25$. Further reduction of

α increases Ra_{cr}.

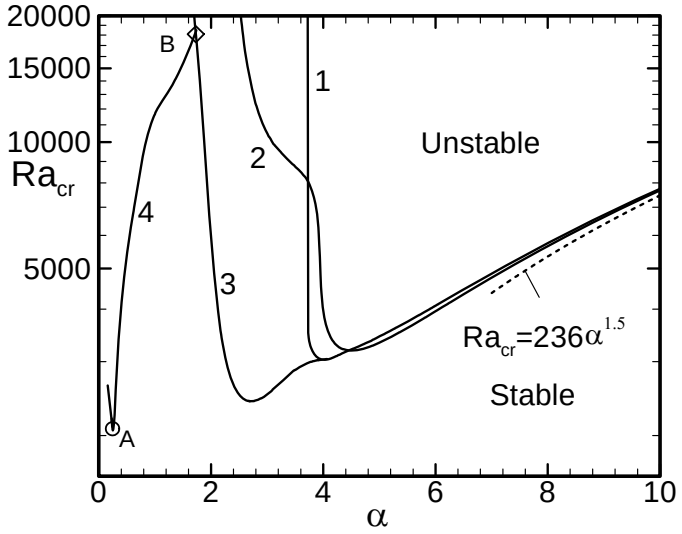

A

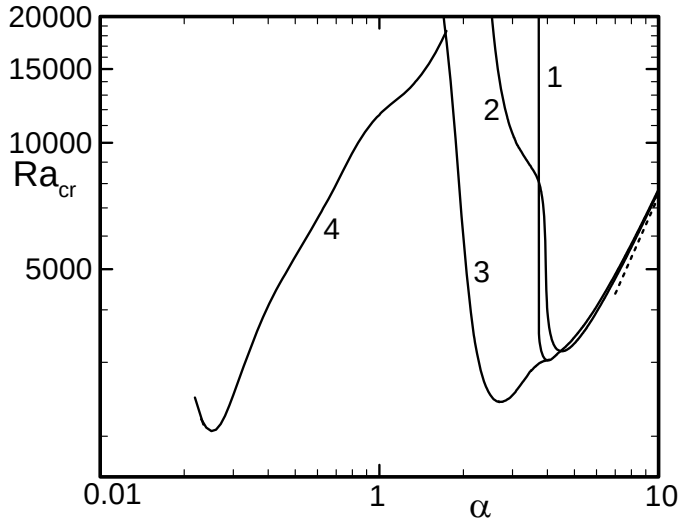

B

Figure 7.1. *Variations of the critical Rayleigh number Ra_{cr} as a function of the heating wave number for fluids with the Prandtl number Pr = 0.71. Curves 1, 2, 3, 4 correspond to the longitudinal, transverse and oblique rolls, and for the oscillatory mode of instability, respectively. Points A and B are located at (Ra_A=2056.6, α_A=0.25), (Ra_B=18347, α_B=1.73), respectively. In Fig.7.1B α-axis has logarithmic scale in order to magnify the small α zone where the oscillatory instability dominates.*

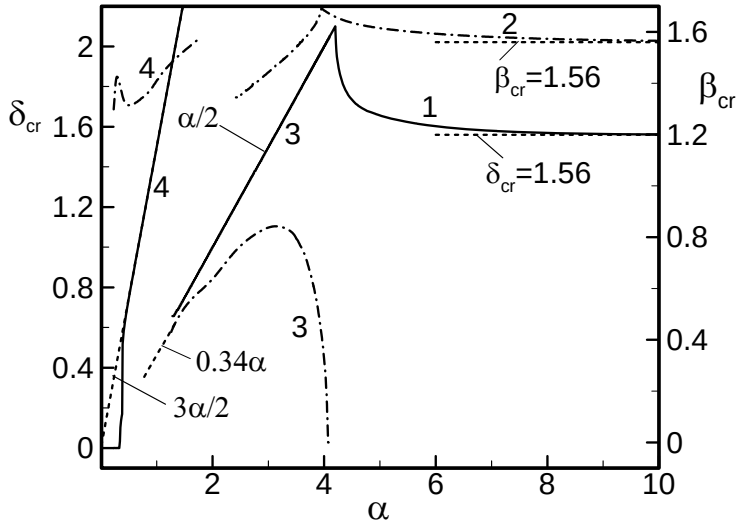

A

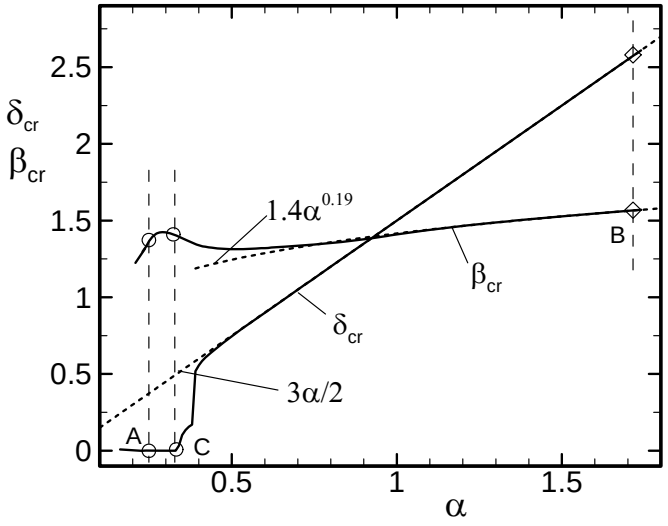

B

Figure 7.2. *Variations of the critical wave numbers δ_{cr} and β_{cr} as functions of the heating wave number α at the onset for fluids with the Prandtl number Pr = 0.71. Curves 1, 2, 3, 4 in Fig.7.2A correspond to the longitudinal, transverse and oblique rolls, and for the oscillatory mode of instability, respectively. Solid and dash-dot lines in Fig.7.2A correspond to δ_{cr} and β_{cr}, respectively. Figure 7.2B is only for the oscillatory mode of instability; points A, B are located at (α_A=0.25, δ_A=0, β_A=1.37), (α_B=1.73, δ_B=2.595, β_B=1.57), respectively, and point C is located at (α_C, β_C, δ_C, Ra_C)= (0.33, 1.4, 0, 2989.6).*

Variations of the critical wave numbers at the onset are shown in **Figure 7.2**. It has been found that δ_{cr} varies according to the relation $\delta_{cr} = 3\alpha/2$ for $\alpha >\sim 0.5$; for smaller α, δ_{cr} starts to decrease and finally reaches the limiting value of $\delta_{cr} = 0$ at $\alpha = \alpha_c = 0.33$ and remains unchanged with any further decrease of α. The z-component of the critical wave vector β_{cr} varies as $\beta_{cr} = 1.4\alpha^{0.19}$ for $\alpha >\sim 0.7$. Variations of the critical roll wave number $|\mathbf{q}|_{cr}$ and the roll inclination angle η are shown in **Figure 7.3**. It is observed that the inclination angle η varies from $\sim 30^0$ to 90^0, i.e., the rolls gradually orients themselves along the transverse direction.

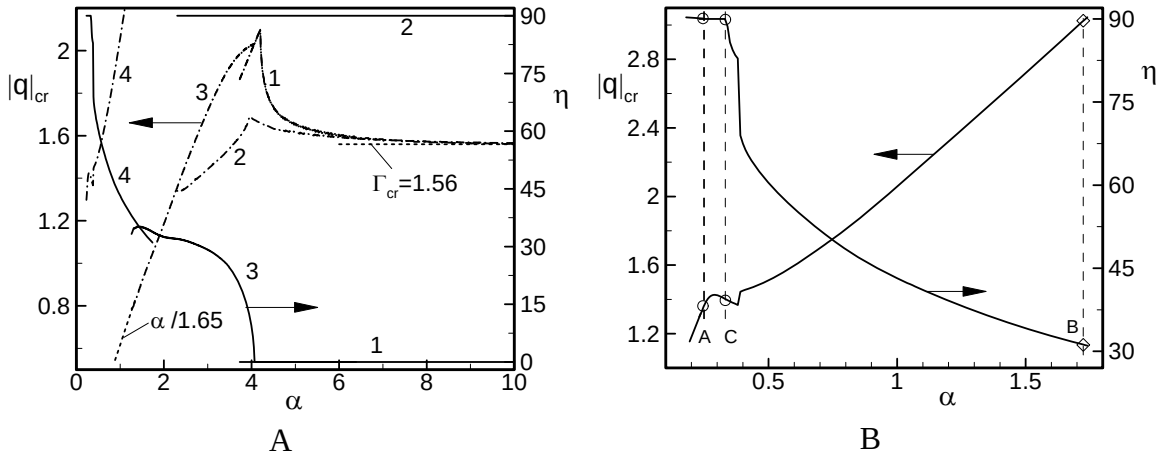

Figure 7.3. *Variations of the critical roll wave number* $|\mathbf{q}|_{cr}$ *(dash-dot lines) and the roll inclination angle* η *(solid lines) as functions of the heating wave number* α *at the onset conditions for fluids with the Prandtl number Pr = 0.71. Lines 1, 2, 3, 4 in Fig.7.3A correspond to the longitudinal, transverse and oblique rolls, and for the oscillatory mode of instability, respectively. Fig.7.3B is only for the oscillatory mode of instability.*

Variation of frequency of disturbances at the onset of the oscillatory mode of instability is illustrated in **Figure 7.4**. It is apparent from this figure that with the decrease of the heating wave number α, the magnitude of the frequency σ_r is reduced. If α is sufficiently small, the frequency σ_r follows the asymptotic relation $81.3\alpha^{1.7}$.

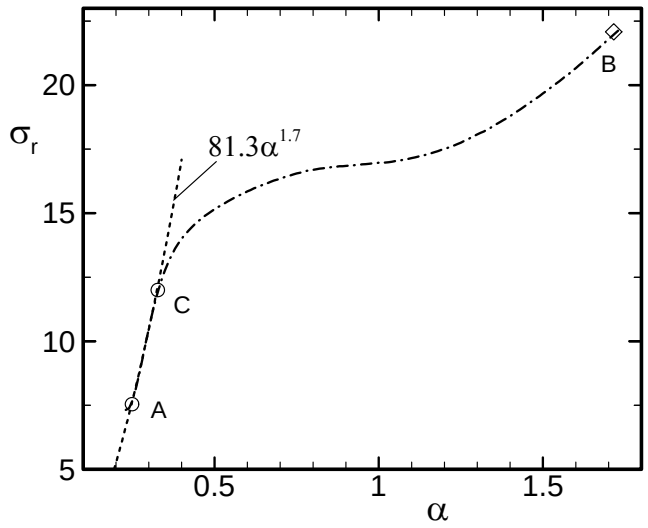

Figure 7.4. *Variation of the frequency σ_r = Real(σ_{cr}) for the oscillatory mode of instability as a function of the heating wave number α at the onset conditions for the fluid with the Prandtl number Pr = 0.71. Points A, B, and C correspond to the same points as in Fig.7.2.*

The evolution of the disturbance structures at the onset is complex and not easily identifiable, especially for $\alpha > \alpha_C$. We illustrate qualitative features of this motion using the two-dimensional snapshots of the disturbance temperature field as shown in **Figure 7.5**. At relatively high α, the oblique roll-like and very distorted structures are observed (see **Figure 7.5**A), whereas at low α, simple and easily identifiable structures are visible (see **Figure 7.5**B). In the latter case, i.e., at sufficiently low α, one may notice that roll-like structures are formed locally at the hot spots and that these structures are aligned horizontally and looking like transverse rolls.

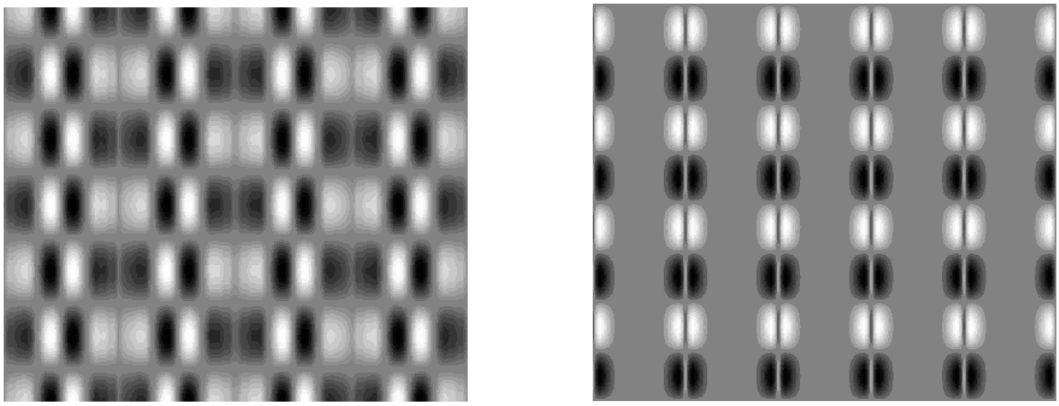

A B

Figure 7.5. *Snapshots of the disturbance temperature field at the mid-plane (y = 0 i.e. x-z plane) for the heating wave number α = 1(Fig.7.5A) and 0.3(Fig.7.5B) at the onset of the oscillatory mode of instability. Dark color identifies colder fluid and white color identifies hotter fluid. Horizontal direction represents x-axis. Five heating wavelengths and four disturbance wavelengths were used for plotting in the x- and z-directions, respectively. Flow conditions (α, δ_{cr}, β_{cr}, Ra_{cr}) for Figs 7.5A,B are (1,1.5,1.4,11721.6) and (0.3,0,1.42, 2506.8), respectively.*

7.2 Summary

Onset of the oscillatory secondary convection in an infinite slot subject to a sinusoidal heating at the lower wall has been explored in this chapter. The analysis is limited to fluids with the Prandtl number Pr = 0.71. It has been established that the convective structures can change orientation from 30° to 90° with respect to the primary rolls, depending on the heating wave number, within the range of Ra being of interest. The x-component of the critical wave vector δ_{cr} changes according to the relation $\delta_{cr} = 3\alpha/2$, but at sufficiently small α, a rapid decrease of δ_{cr} to zero is observed. The frequency of oscillations decreases with reduction of α. At sufficiently small α, roll-like structures emerge locally around the hot spots suggesting formation of transverse roll-like structures.

8

Long Wavelength Heating: Bifurcation*

The heating pattern dictated by a sufficiently small heating wave number, i.e., long wavelength heating, exhibits some interesting phenomena and requires separate investigation. Here we summarize key findings. As mentioned in Chapter 2, when the wavelength of the heating becomes very large the zones centered around the hot spots are subject to an almost uniform heating and similar zones centered around cold spots are subject to an almost uniform cooling. If the magnitude of the heating is sufficiently large, the zones around the hot spots may be subject to the RB-type instability (the critical Rayleigh number in the present scale is $Ra_{cr} = 427$). For the "supercritical" values of Ra ($Ra > 427$) multiple solutions of the primary convection exist depending on the history of the heating; this history can be controlled by using different initialization conditions, different continuation strategies in the parameters space as well as by using different numerical solvers presented Section 2.3. Various convective motions are depicted using bifurcation diagrams. The mean Nusselt number defined by equation (2.24) is not suitable to construct the bifurcation diagrams. A local Nusselt number Nu_L based on the conductive temperature scale and defined as

$$Nu_L = -Pr\left.\frac{d\theta}{dy}\right|_{x=0,\, y=-1} \tag{8.1}$$

is used for this purpose.

* Some of the material discussed in this chapter is the outcome from the collaborative research between the author and Mr. Ali Asgarian who presented it for his M.A.Sc. Dissertation at The University of Western Ontario, London, ON, Canada.

This chapter is organized as follows. In Sections 8.1 we discuss in details bifurcation diagrams generated by changing the heating wave number α in (Nu_L, α) space for fluids with the Prandtl number Pr = 0.71. Bifurcation diagrams produced by changing the intensity of the heating Ra in (Nu_L, Ra) space are discussed in Section 8.2. Effects of variations of the Prandtl number are considered in Section 8.3. A short summery is presented in Section 8.4. Computations are restricted to Ra < 1000 in this chapter. The relevant numerical issues are addressed in the Appendix E.

8.1 Bifurcation diagram in (Nu_L, α) space

The reader may note that the slot is filled with primary convection rolls regardless of how small α is (see **Figure 2.18**). Strength of these rolls decreases with a decrease of α and increases with an increase of Ra. The secondary rolls may emerge only locally around the hot spots. These rolls may emerge if α is sufficiently small and at the same time Ra is sufficiently large. The former condition is required in order to create a sufficiently long, almost uniformly heated segment of the slot so that the edge effects associated with longitudinal variations of temperature play no role. The second condition is required in order to overcome viscous and thermal dissipations and effects associated with existence of the primary rolls.

Variations of Nu_L for "supercritical" values of Ra, i.e., Ra > 427, are illustrated in **Figure 8.1**. It is observed that when α > 0.3 the solution is unique in the range of Ra subject to this analysis. Reduction of α leads to two types of bifurcations depending on the value of Ra, i.e., supercritical pitchfork bifurcation for Ra < ~470 and "bifurcation from infinity" (Rosenblat and Davis 1979) for larger values of Ra. In this discussion we shall refer to direction of decreasing α (increasing wavelength of the heating) as the positive direction of the parameter.

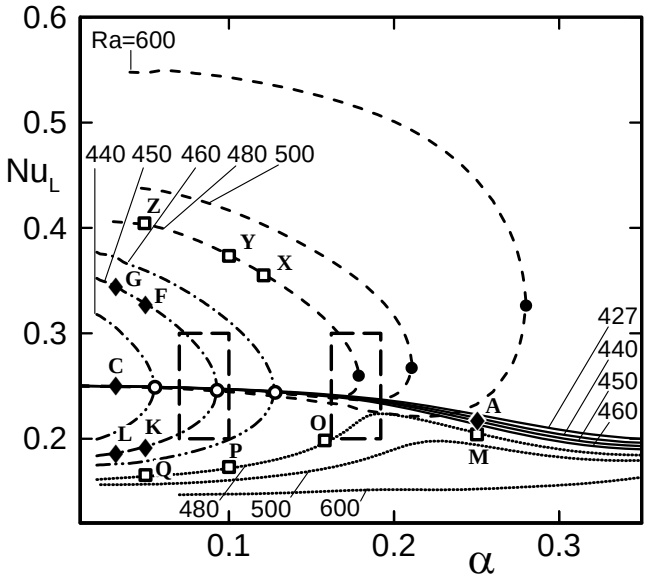

Figure 8.1. *Variations of the local Nusselt number Nu_L at x = 0, y = -1 as a function of the heating wave number α for fluids with the Prandtl number Pr = 0.71 subject to heating corresponding to the supercritical values of the Rayleigh number (Ra > 427). Enlargements of left and right boxes are displayed in Figs 8.2 and 8.6, respectively. Solid, dash-dot, dash-dot-dot, dash, and dot lines correspond to bifurcation branches of types 0, 1, 2, 3, and 4, respectively. Open circles identify critical conditions for pitchfork bifurcations. Filled circles identify critical conditions for the "bifurcations from infinity". Filled diamonds and open squares identify conditions selected for illustration of evolution of flow structures for Ra = 450 and 480, respectively.*

8.1.1 Pitchfork bifurcation

In this section, we shall elucidate the flow evolution associated with pitchfork bifurcations for the case of Ra = 450 illustrated in **Figure 8.2**. For convenience we call solutions corresponding to the middle, upper and lower branches as branches of type 0, 1 and 2, respectively, and we focus attention on the segment of the slot on the right side of the hot spot located at x = 0.

Branch of type 0 has a simple topology involving one large flow cell extending over half period of heating with the fluid moving upwards above the hot spot as shown in **Figure 8.3**. This topology does not change over a wide range of heating wavelengths (for

α <~0.25). This branch loses stability for $\alpha < \alpha_B = 0.093$.

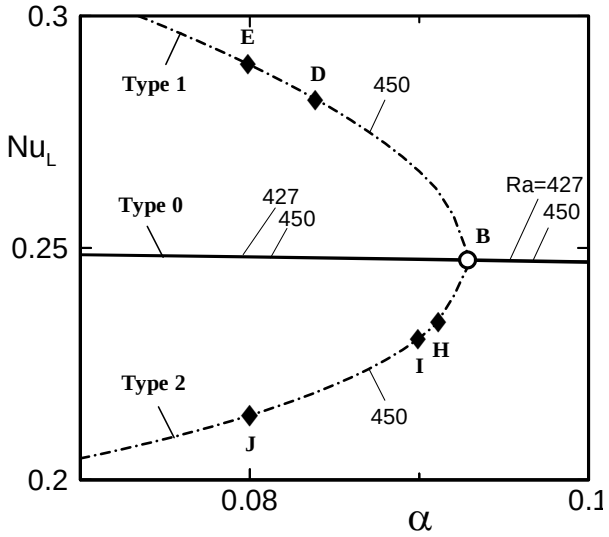

Figure 8.2. *Enlargement of the left box from Fig.8.1: pitchfork bifurcation.*

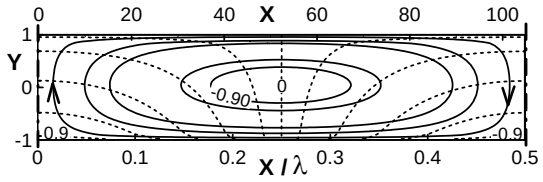

Figure 8.3. *Evolution of flow structures associated with branch of type 0 for the heating wave number $\alpha = 0.03$ for the heating corresponding to the Rayleigh number Ra = 450. Solid and dash lines identify streamlines and isotherms. Plotted values of the stream function and temperature correspond to ψ/ψ_{max} = 0, -0.1, -0.3, -0.45, -0.8, -0.9 and θ/θ_{max} = ±0.9, ±0.7, ±0.5, ±0.3, ±0.1, 0, unless otherwise noted. Figure displayed here is marked with letter C in Fig.8.1 and the flow structures marked by letters A,B in Fig.8.1 are similar to C.*

Variations of topology of flow structures associated with branch of type 1 are illustrated in **Figure 8.4**. It can be observed that the flow re-arrangement begins with the formation of a small separation bubble at the upper wall above the hot spot which grows to form a secondary roll attached to the hot spot, as shown in **Figure 8.4**A. The reader should note

that there is another similar secondary roll on the other side of the hot spot. All nomenclature used in this discussion and roll counting starting with **Figure 8.4** will refer to flow structures on the right side of the hot spot. The secondary roll rotates in the conterclockwise direction (opposite to the primary roll) and brings colder fluid into contact with the lower wall resulting in an increase of Nu_L, as shown in **Figure 8.2**. Decrease of α results in firming up of the secondary roll and formation of a new pair of rolls. The beginning of the pair formation process is visible for $\alpha = 0.084$ where one roll is being pinched off (with formation of an in-flow stagnation point) and the second one arises as a separation bubble at the upper wall away from the hot spot (see **Figure 8.4**B). Formation of this pair is finished when $\alpha = 0.08$ (**Figure 8.4**C). Further decrease of α to $\alpha = 0.05$ and then to $\alpha = 0.03$ results in a sequential formation of additional pairs following the process described above. The process of creation of additional pairs continues indefinitely with a decrease of α while the size of the already existing rolls approaches an asymptotic limit of $\Omega = 2.01$ (Drazin and Reid 1981) predicted by the RB instability in the case of a uniformly heated wall. The characteristic feature of this family of solutions is that there is always an odd number of secondary cells, as all new cells with exception of the first one are created in pairs. The secondary branches can loose stability but this issue has not been investigated during present study.

Topology of flow structures associated with branch of type 2 are illustrated in **Figure 8.5**. Formation of secondary rolls begins with the appearance of an inflow stagnation point (**Figure 8.5**A), creation of a small separation bubble at the upper wall away from the hot spot at $\alpha = 0.091$ (**Figure 8.5**B) and occurence of a distinctive pair of rolls at $\alpha = 0.09$ (**Figure 8.5**C). Roll closests to the hot spot rotates in the clockwise direction (the same as the primary roll) and thus brings warmer fluid into contact with the wall resulting in a decrease of Nu_L, as shown in **Figure 8.2**. Further decrease of α to 0.08 initiates formation of a second pair (**Figure 8.5**D). These rolls are well developed at $\alpha = 0.05$. Four pairs exist at $\alpha = 0.03$ (**Figure 8.5**F). Process of creation of additional pairs continues indefinitely with a decrease of α, similarly as in the case of branch 1, while the size of the already existing rolls approach the same asymptotic limit of $\Omega = 2.01$. The characteristic

feature of this family of solutions is that there is always an even number of secondary rolls, as all new rolls are created in pairs. The process of formation of rolls is very similar to that found in the case of branch 1 with exception of the first roll which accounts for a different direction of rotation at the hot spot.

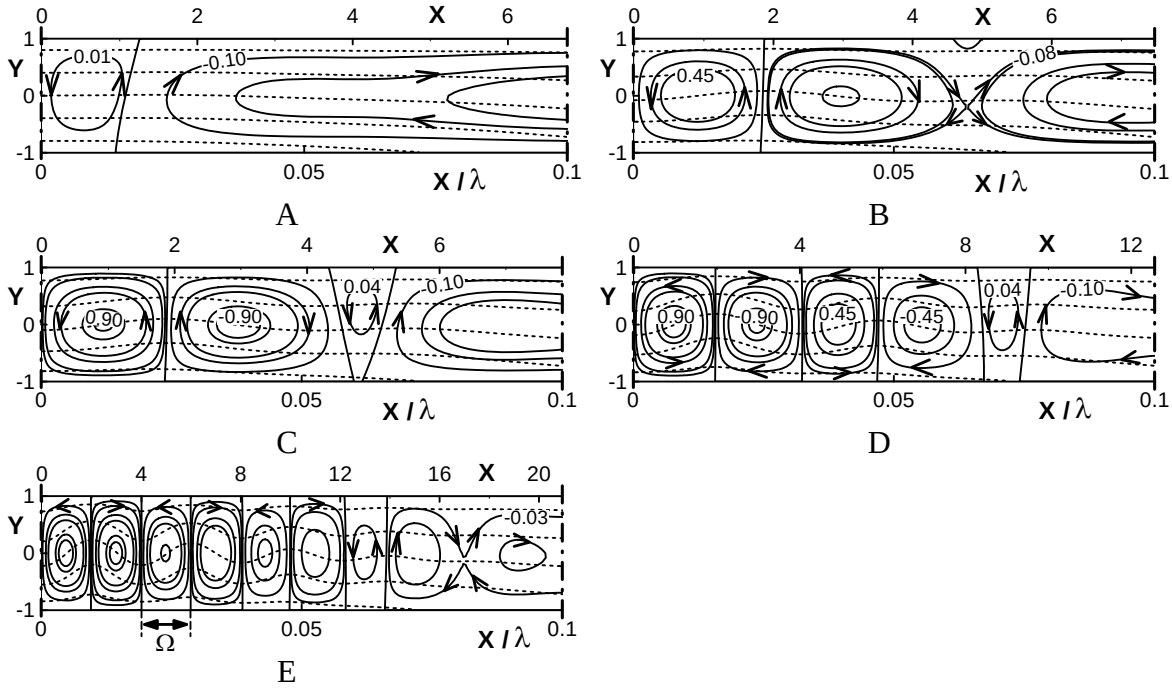

Figure 8.4. *Evolution of flow structures associated with branch of type 1 as a function of the heating wave number α for the Rayleigh number Ra = 450. Flow conditions in Figs 8.4A-E correspond to α = 0.093, 0.084, 0.08, 0.05, 0.03 and are marked with letters B, D, E, F and G in Figs 8.1-8.2, respectively. Ω denotes length of a single cell. Plot parameters as in Fig.8.3.*

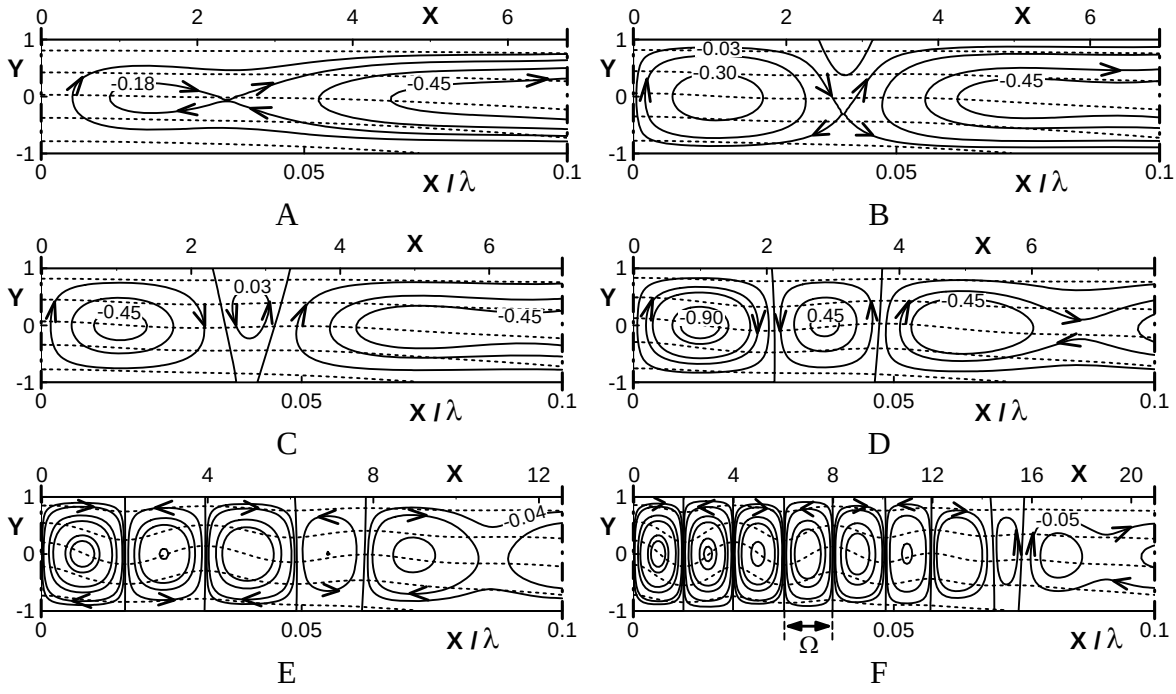

Figure 8.5. *Evolution of flow structures associated with branch of type 2 as a function of the heating wave number α for the Rayleigh number Ra = 450. Flow conditions in Figs 8.5A-F correspond to α = 0.093, 0.091, 0.09, 0.08, 0.05, 0.03 and are marked with letters B, H, I, J, K and L in Figs8.1-8.2, respectively. Ω denotes length of a single cell. Plot parameters as in Fig.8.3.*

8.1.2 Bifurcation from infinity

We shall now turn our attention to "bifurcations from infinity". This type of bifurcation occurs for the higher values of Ra, i.e., Ra > ~470. We shall carry out detailed discussion using the case of Ra = 480 illustrated in **Figure 8.6** as the reference case. For convenience we refer to solutions corresponding to the finite and infinite branches as branches of types 3 and 4, respectively.

Topology of flow structures associated with branch of type 3 are illustrated in **Figure 8.7**. The flow forms one big roll at he left limit of the lower part of this branch (**Figure 8.7**A). Increse of α results in initiation of the formation of a secondary roll rotating in the

direction opposite to the direction of the primary roll. At $\alpha = 0.177$ this roll has the form of a separation bubble attached to the upper wall (**Figure 8.7**B). This bubble extends to the lower wall at $\alpha = 0.178$ (**Figure 8.7**C), increases in size as α changes in the fourth digit (plot in **Figure 8.7**D is for the nominally the same α as plot in **Figure 8.7**C) and increases further in size as α begins to decrease (see **Figure 8.7**E). Beginning of a pinching process that results in the formation of additional rolls is visible at $\alpha = 0.12$ (**Figure 8.7**F) and a new pair of rolls is formed at $\alpha = 0.1$. This process is repeated sequentially with new rolls appearing in pairs. At $\alpha = 0.05$ two pairs are visible as well as beginning of the pinching process that leads to the formation of the third pair. The process of formation of new rolls is similar to that observed in the case of branch of type 1 resulting in the creation of an odd number of rolls with the size of the rolls approaching limit of $\Omega = 2.01$ when α becomes sufficiently small. The lower part of this branch is unstable for $\alpha < \alpha_R = 0.179$ (point R in **Figure 8.6**).

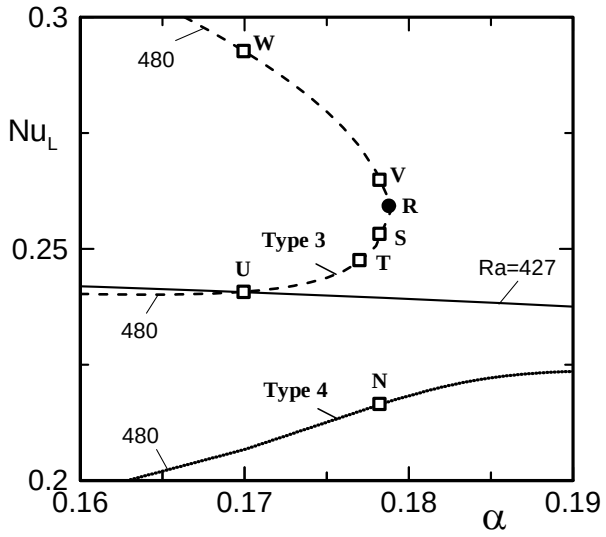

Figure 8.6. *Enlargement of the right box of the Fig. 8.1:"bifurcation from infinity".*

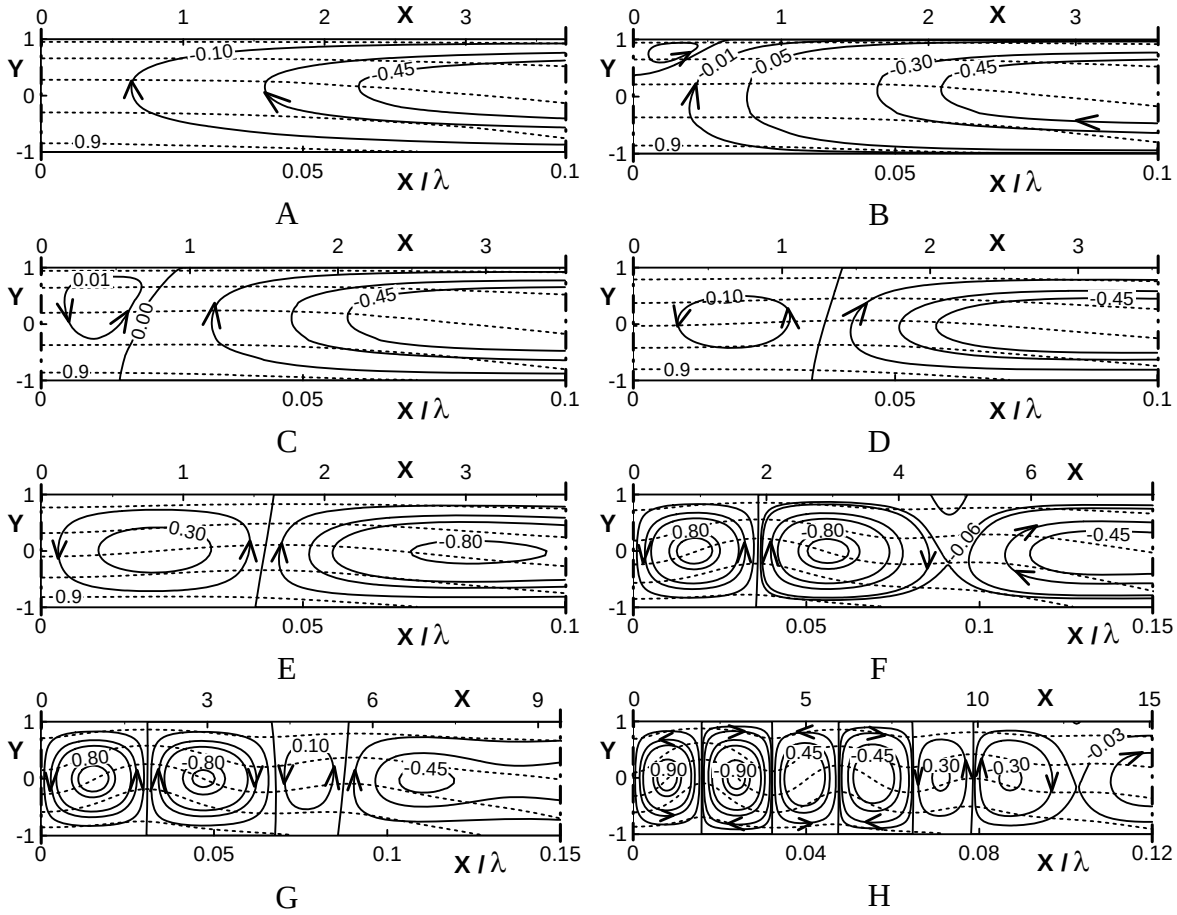

Figure 8.7. *Evolution of flow structures associated with branch of type 3 as a function of the heating wave number* α *for the Rayleigh number Ra = 480. Flow conditions in Figs 8.7A-H correspond to* α *= 0.17, 0.177, 0.178, 0.178, 0.17, 0.12, 0.1, 0.05 and are marked with letters U, T, S, V, W, X, Y and Z in Figs 8.1 and 8.6, respectively. Plot parameters as in Fig. 8.3.*

Evolution of flow structures associated with branch of type 4 is illustrated in **Figure 8.8**. There is one primary roll when α = 0.25 (**Figure 8.8**A). Reduction of α to 0.178 results in the formation of an inflow stagnation point (**Figure 8.8**B) and formation of a small separation bubble at the upper wall away from the hot spot at α = 0.16 (**Figure 8.8**C). The pinching process results in the formation of a distinct pair of rolls at α = 0.1 (**Figure 8.8**D). Further reduction of α results in a sequential formation of additional pairs of rolls with three pairs exisitng when α = 0.05 (**Figure 8.8**E). This process is very

similar to that observed in the case of branch of type 2 with the size of the rolls approaching limit of $\Omega = 2.01$ when α becomes sufficiently small.

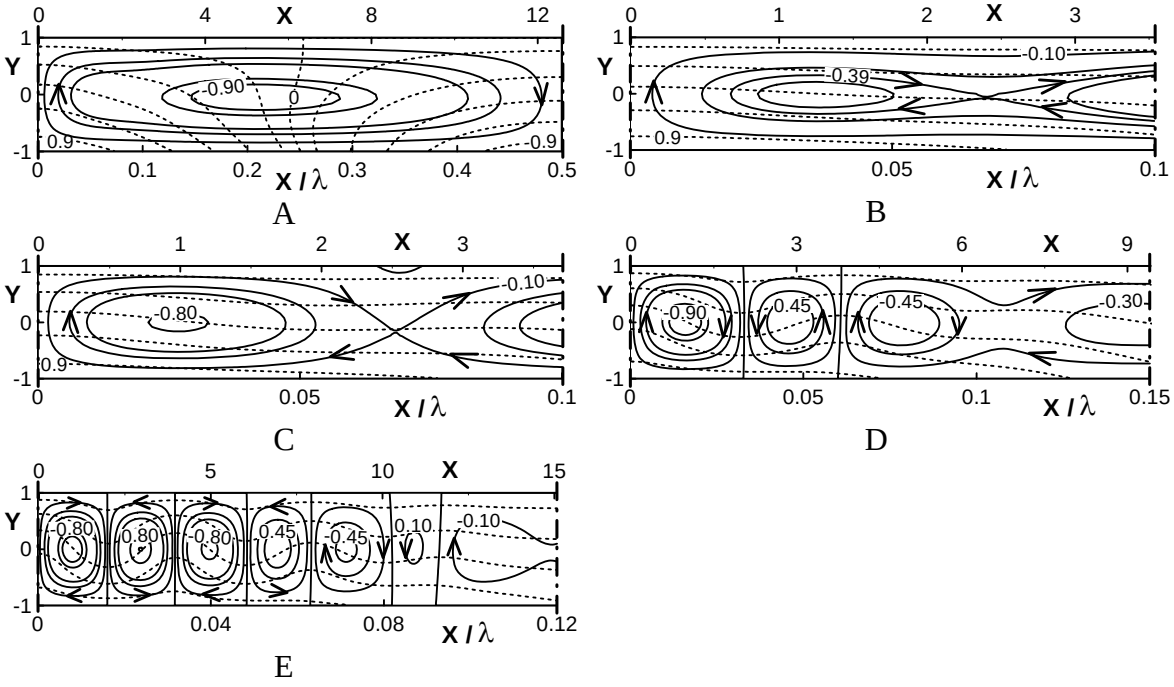

Figure 8.8. *Evolution of flow structures associated with branch of type 4 as a function of the heating wave number α for the Rayleigh number Ra = 480. Flow conditions in Figs 8.8A-E correspond to α = 0.25, 0.178, 0.16, 0.1, 0.05 and are marked with letters M, N, O, P and Q in Figs 8.1 and 8.6, respectively. Plot parameters as in Fig.8.3.*

It has been noticed that changes in the net heat transfer between the walls due to formation of secondary rolls cannot be demonstrated properly using the local Nusselt number defined in (8.1). A mean Nusselt number $\overline{\mathrm{Nu}}_{\mathrm{T}}$ associated with the zone where most of the activities related to the creation of secondary rolls occur (see **Figures 8.4-8.8**), i.e., $x \in (0, 0.12\pi/\alpha)$), is found to be better suited to explore the effect of the pinching process. **Figure 8.9**A shows increase of $\overline{\mathrm{Nu}}_{\mathrm{T}}$ due to formation of secondary rolls in the case of pitchfork bifurcation. Values of $\overline{\mathrm{Nu}}_{\mathrm{T}}$ associated with branches of types 1 and 2 keep crossing each other in a repetitive manner as α decreases. This type of variations is due to the fact that pinching of new pairs of rolls takes place at different

values of α for both branches and the branch having a larger number of cells at a given α has generally larger value of $\overline{Nu}_T$. **Figure 8.9**B shows similar data for Ra = 500 where "bifurcation from infinity" takes place. Values of $\overline{Nu}_T$ for the upper part of branch of type 3 and for branch of type 4 keep crossing each other in a repetitive manner as α decreases. This type of variations of $\overline{Nu}_T$ results from pinching off of new rolls at different values of α for both branches, similarly as in the case of the pitchfork bifurcation.

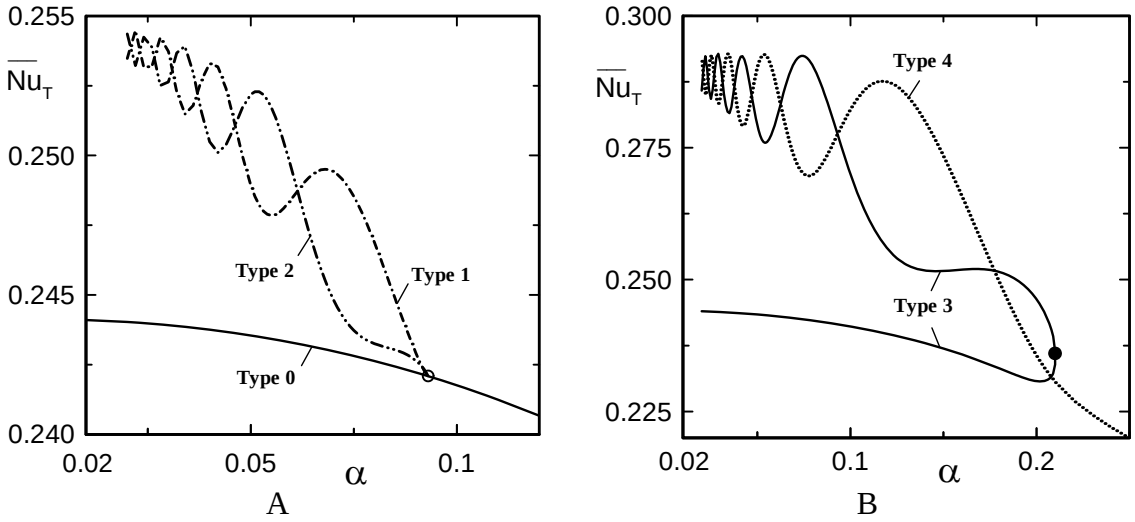

Figure 8.9. *Variations of the* $\overline{Nu}_T$ *(see text for definition) as a function of the heating wave number* α *for the Rayleigh numbers Ra = 450 (Fig.8.9A) and Ra = 500 (Fig.8.9B).*

8.2 Bifurcation diagram in (Nu_L, Ra) space

In the previous section we have discussed the bifurcation process by varying α at fixed values of Ra. Here we keep α fixed and vary Ra. This particular strategy could be more useful from experimental point of view, where the spatial distribution of heating would be fixed and one would be increasing the intensity of heating described in terms of the Rayleigh number. **Figure 8.10** displays bifurcation diagrams expressed in term of Nu_L resulting from variations of Ra for selected, fixed values of α. The forms of the bifurcation diagrams are similar to that found in the previous section. Supercritical

pitchfork bifurcations exist for $\alpha < \sim 0.14$ whereas "bifurcations from infinity" exist for $\alpha >\sim 0.14$.

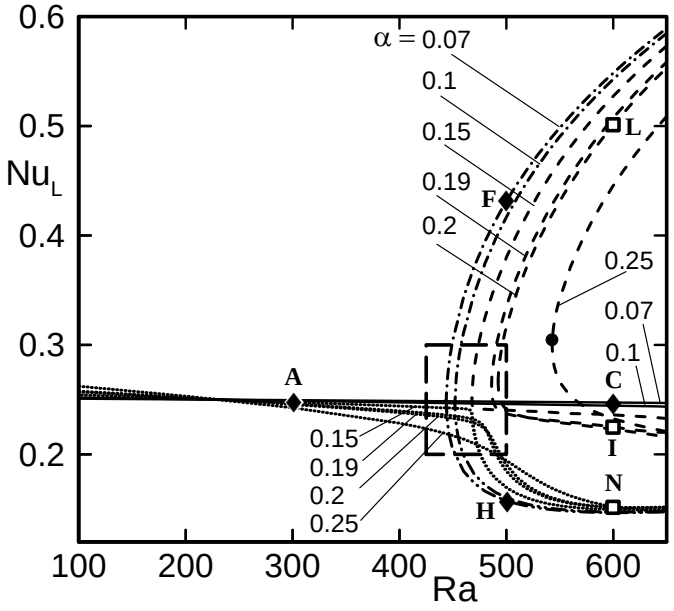

Figure 8.10. *Variations of the local Nusselt number Nu_L at x = 0, y = -1 as a function of the Rayleigh number Ra for selected values of the heating wave number α for a fluid with the Prandtl number Pr=0.71. Enlargement of box marked in Fig.8.10 is displayed in Fig.8.11. Solid, dash-dot, dash-dot-dot, dash, and dot lines correspond to bifurcation branches of types 0, 1, 2, 3, and 4, respectively. Open circles identify critical conditions for pitchfork bifurcations. Filled circles identify critical conditions for "bifurcations from infinity". Filled diamonds and open squares identify conditions selected for illustration of evolution of flow structures.*

Details of a typical pitchfork bifurcation are shown in **Figure 8.11** for $\alpha = 0.07$. This bifurcation consists of branch of type 0 passing through points A, B and C, and branches of types 1 and 2 that originate at point B and pass through points D, E, F and G, H, respectively. "Bifurcation from infinity", which is illustrated for $\alpha = 0.2$ (**Figure 8.11**), has two branches, i.e., branch of type 3 passing through points I, J, R, K, L and branch of type 4 passing through points N, M, O. The evolution of the flow structures for the branches of type 0, 1, 2, 3 and 4 are qualitatively similar to the corresponding branches discussed previous section in the **Figures 8.3-8.5**, **8.6-8.7**, respectively.

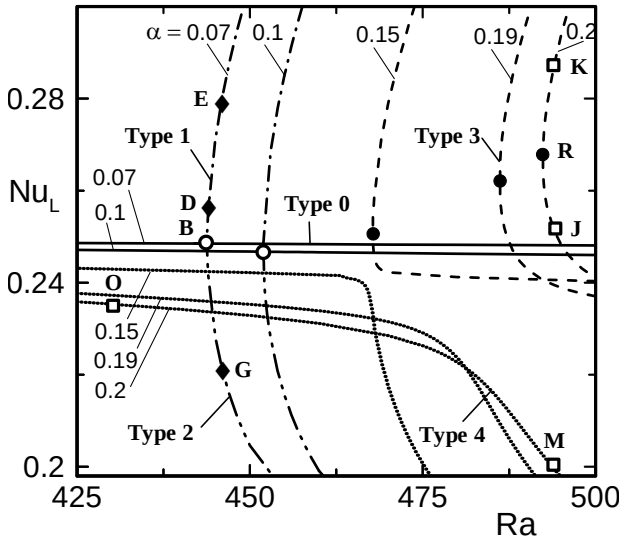

Figure 8.11. *Enlargement of the box marked in Fig.8.10.*

8.3 Effect of Prandtl number

Analysis of bifurcation diagrams displayed in **Figures 8.1** and **8.10** permits identification of critical conditions leading to the appearance of new, primary bifurcation branches. At this point we investigate how the critical Rayleigh number Ra_{cr} changes with the change of the Prandtl number of the fluid. **Figure 8.12** shows the varation of Ra_{cr} for Pr = 0.71, and Pr = 7 as functions of α. For both cases the decrease of α results in Ra_{cr} approaching the limit of 427, which agrees with the critical conditions for the RB instability for a uniformly heated lower wall (Drazin and Reid 1981). An increase of α leads to the primary convection with a strong spatial modulation and results in a rapid increase of Ra_{cr}. **Figure 8.12** also demostrates that the critical Rayleigh numbers Ra_{cr} remain very close for both types of fluids. The difference between them decreases as α decreases and Ra_{cr}'s for Pr = 0.71 and 7 approach the same asymptotic value.

The complete bifurcation diagram in the (Nu_L, α) plane for Pr = 7 overlaid with the diagram for Pr = 0.71 is displayed in **Figure 8.13**. The primary bifurcation points remain essentially unchanged while the branches corresponding to the saturations states exhibit

small differences increasing with distance away from the critical points. It may be concluded that the qualitative response of both fluids to the imposed heating is the same while quantitative differences remain small.

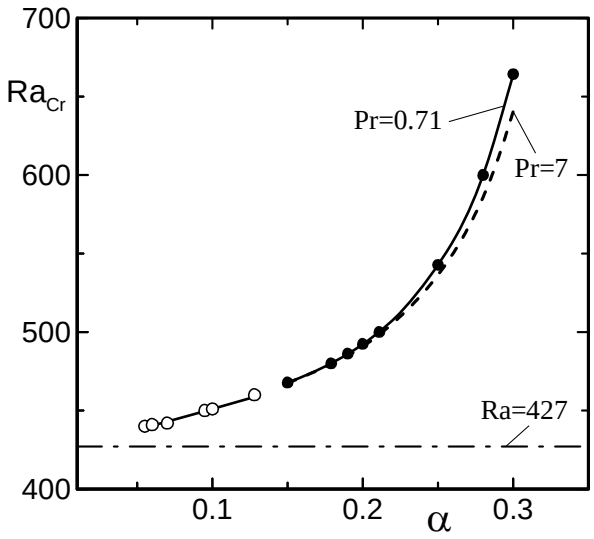

Figure 8.12. *Variation of the critical Rayleigh number Ra_{cr} as a function of the heating wave number α for fluids with Pr = 0.71 and Pr = 7. Open circles denote critical conditions for the pitchfork bifurcations and filled circles denote the critical points for the "bifurcations from infinity".*

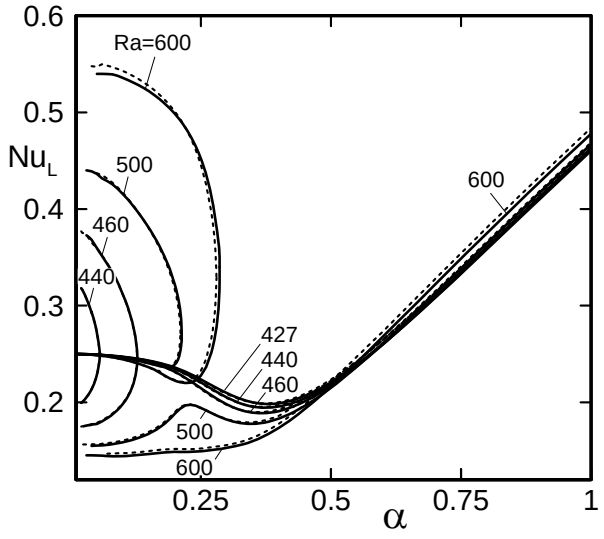

Figure 8.13. *Variations of the local Nusselt number Nu_L as a function of the heating wave number α for selected values of the Rayleigh number Ra for fluids with Prandtl numbers Pr = 0.71 (dash lines) and 7 (solid lines).*

Finally, bifurcation diagrams displayed in **Figure 8.13** demonstrates explicitely that the complex bifurcation patterns identified in this chapter describe phenomena strictly associated with the long wavelength heating and not taking place when $\alpha = O(1)$.

8.4 Summary

Natural convection in an infinite slot subject to periodic heating at the lower wall with wavelengths that are large when compared with the slot thickness has been studied. Secondary motions in the form of rolls aligned in the direction of primary rolls and concentrated around the hot spots occur for supercritical values of Ra ($Ra > 427$). Two types of bifurcations have been identified depending on the wave number of the heating α and on the intensity of the heating Ra.

When the heating intensity is sufficiently small but larger than the critical value, i.e., $427 < Ra < \sim 470$, the secondary motions correspond to supercritical pitchfork bifurcations and occur only for $\alpha < \sim 0.14$, i.e., when α is sufficiently small. One of the branches of such bifurcation always has an odd number of secondary rolls per half period, with rolls at the hot spots rotating in the direction opposite to the primary rolls. The other branch has an even number of secondary rolls per half period, with the rolls at the hot spots co-rotating with the primary rolls. The number of rolls increases without limit as α decreases with new rolls being pinched off in pairs. The pinching process for each branch occurs at different α's and as a result the branches alternate in producing larger net heat flow.

Increase of the intensity of the heating to $Ra > \sim 470$ results in secondary motions occurring at larger values of α (for $\alpha > \sim 0.14$), and bifurcation changing character into "bifurcations from infinity". The critical points for such bifurcations move towards higher α's with increase of Ra. The main branch of this bifurcation is associated with one pair of rolls per heating period for $\alpha > 0.25$ in the range of Ra studied. Decrease of α results in the formation of secondary rolls and the rolls at the hot spots co-rotating with the primary

rolls. The new rolls are always pinched off in pairs having always an even number of rolls per half period. The other branch is associated with one pair of rolls per heating period when α is very small. Increase of α results in pinching off of rolls counter-rotating with the primary rolls at the hot spots resulting in an odd number of rolls per half period.

The bifurcation processes are insensitive to variations of the Prandtl number for Pr = O(1) as only small differences have been observed between results for Pr = 0.71 and Pr = 7. It has been shown that the observed phenomena are strictly associated with the small wave number limit of the external heating.

9

Primary Convection with External Flow

So far we have discussed the primary and secondary convections generated solely due to the application of periodic heating. In this chapter, we elucidate changes in the primary convection due to the presence of an external flow. The external flow considered here has the form of a fully developed Poiseuille flow. Only fluid with the Prandtl number Pr = 0.71 is considered. The organization of the chapter is as follows. In Section 9.1 we reformulate the problem as the formulation presented in Chapter 2 does not contain any information about the external flow. Numerical solution procedure is illustrated again in Section 9.2. Discussion of the results is presented in Section 9.3. A short summary of the main findings is provided in Section 9.4.

9.1 Problem formulation

Consider steady flow of fluid confined in a channel bounded by two parallel walls extending to $\pm\infty$ in the x-direction and placed at a distance 2h apart from each other with the gravitational acceleration g acting in the negative y-direction, as shown in **Figure 9.1**. The flow is driven in the positive x-direction by a pressure gradient. The fluid is incompressible and Newtonian with thermal conductivity k_d, specific heat per unit mass c, thermal diffusivity $\kappa = k_d/\rho c$, kinematic viscosity ν, dynamic viscosity μ, thermal expansion coefficient Γ and variations of the density ρ that follow the Boussinesq approximation. All material properties are evaluated at the reference temperature defined below. The lower wall is subject to a periodic heating with temperatures of the lower (θ_L) and upper (θ_U) walls are specified as,

$$\theta_L(x) = 0.5\cos(\alpha x), \qquad \theta_U(x) = 0, \tag{9.1}$$

where α stands for the wave number of the heating ($\lambda=2\pi/\alpha$ is the wavelength), θ denotes the relative temperature, i.e., $\theta=T-T_{ref}$, T denotes the temperature and T_{ref} denotes the reference temperature. It is assumed that the mean temperatures of the both walls are equal and this defines the reference temperature.

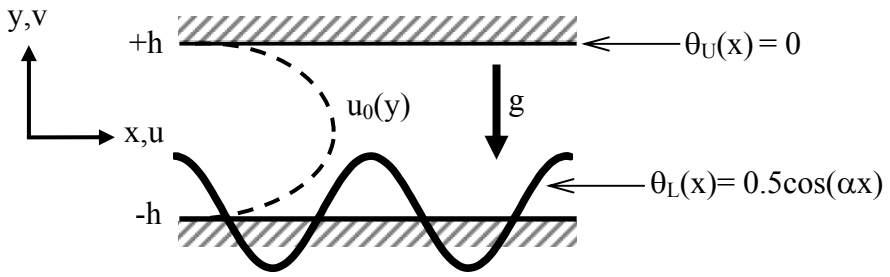

Figure 9.1. *Plane Poiseuille flow subject to a periodic heating.*

The velocity and pressure fields in the absence of any heating have the form (Poiseuille flow)

$$\mathbf{v}(x,y) = [u_0(y),\ 0] = [1-y^2,\ 0], \quad p_0(x,y) = -2x/\mathrm{Re}, \tag{9.2}$$

where $\mathbf{v}$ = (u,v) denotes the velocity vector scaled with the maximum of the x-velocity component U_p as a velocity scale, p stands for the pressure scaled with the dynamic pressure scale ρU_p^2, half-channel height h has been used as the length scale and Reynolds number is defined as $\mathrm{Re} = U_p h/\nu$. We shall refer to this flow as the reference flow. The applied heating produces flow modifications that can be represented in the form

$$\begin{aligned} &u_2(x,y) = \mathrm{Re}\,u_0(y) + u_1(x,y), \qquad v_2(x,y) = v_1(x,y), \\ &\theta_2(x,y) = \mathrm{Pr}^{-1}\,\theta_0(x,y) + \theta_1(x,y), \quad p_2(x,y) = \mathrm{Re}^2\,p_0(x,y) + p_1(x,y). \end{aligned} \tag{9.3}$$

In the above, (u_2,v_2), p_2 and θ_2 denote the complete velocity, pressure and temperature fields, respectively, (u_1,v_1) and p_1 denote the velocity and pressure modifications created by the heating, respectively, θ_0 stands for the conductive temperature field and θ_1 denotes deviations from the conductive temperature field induced by convective effects. The complete velocity vector and the velocity modifications have been scaled using the convective velocity scale $U_v = \nu / h$ where $U_p/U_v = Re$, and the pressure modifications have been scaled using the convective pressure scale ρU_v^2. The amplitude of temperature variations along the plates is used as the conductive temperature scale T_d and $T_v = T_d\nu/\kappa$ is used as the convective temperature scale, where $T_v/T_d = Pr$ and $Pr = \nu/\kappa$ denotes the Prandtl number.

The conductive temperature field θ_0 in (9.3) satisfying conditions in (9.1) can be easily determined, i.e,

$$\begin{aligned}\theta_0(x,y) &= \sum_{\substack{n=-\infty \\ n\neq 0}}^{n=+\infty} \theta_0^{(n)}(y)\, e^{in\alpha x} \\ &= \sum_{\substack{n=-\infty \\ n\neq 0}}^{n=+\infty} \left[\left(\theta_U^{(n)} - \theta_L^{(n)}\right) \frac{\sinh(n\alpha y)}{2\sinh(n\alpha)} + \left(\theta_U^{(n)} + \theta_L^{(n)}\right) \frac{\cosh(n\alpha y)}{2\cosh(n\alpha)} \right] e^{in\alpha x}\end{aligned} \tag{9.4}$$

with $\theta_L^{(\pm 1)} = 1/4$, $\theta_L^{(n)} = 0$ for $|n| \geq 2$ and $\theta_U^{(n)} = 0$ for $|n| \geq 1$.

The dimensionless field equations describing motion of the fluid and changes in the temperature field have the form

$$\left(Re\, u_0 + u_1\right)\frac{\partial u_1}{\partial x} + Re\, v_1 \frac{du_0}{dy} + v_1 \frac{\partial u_1}{\partial y} = -\frac{\partial p_1}{\partial x} + \nabla^2 u_1 \ , \tag{9.5a}$$

$$\left(Re\, u_0 + u_1\right)\frac{\partial v_1}{\partial x} + v_1 \frac{\partial v_1}{\partial y} = -\frac{\partial p_1}{\partial y} + \nabla^2 v_1 + Ra\theta_1 + Ra\, Pr^{-1}\, \theta_0 \ , \tag{9.5b}$$

$$\mathrm{Pr}\left((\mathrm{Re}\, u_0 + u_1)\frac{\partial \theta_1}{\partial x} + v_1 \frac{\partial \theta_1}{\partial y} \right) + (\mathrm{Re}\, u_0 + u_1)\frac{\partial \theta_0}{\partial x} + v_1 \frac{\partial \theta_0}{\partial y} = \nabla^2 \theta_1 \ , \tag{9.5c}$$

$$\frac{\partial u_1}{\partial x} + \frac{\partial v_1}{\partial y} = 0 \ , \tag{9.5d}$$

where $Ra = g\Gamma h^3 T_d/\nu\kappa$ is the Rayleigh number, ∇^2 denotes the Laplace operator and dissipation effects in the energy equation have been neglected. The boundary conditions take the form

$$u_1(\pm 1) = 0, \quad v_1(\pm 1) = 0, \quad \theta_1(\pm 1) = 0 \, . \tag{9.6}$$

The problem specification needs to be closed by specifying additional constraint. The presence of heating may alter the resistance that the fluid needs to overcome during its motion through the channel. The additional constraint may thus be specified in the form of requirement that the flow with or without the heating has to carry the same mass flow rate, i.e., fixed mass flow rate constraint. This constraint can be expressed as

$$Q = \int_{-1}^{1} u_2 dy = \int_{-1}^{1} (\mathrm{Re}\, u_0 + u_1) dy = 4\,\mathrm{Re}/3 \tag{9.7}$$

and its enforcement permits determination of the change in the average pressure gradient required in order to maintain the same flow rate. Another constraint of interest is the fixed pressure gradient constraint, i.e., the same pressure gradient is available for pushing the fluid through the channel with or without the heating. This constraint may be expressed as

$$\frac{\partial p_2}{\partial x} = \frac{\partial (p_0 + p_1)}{\partial x} = -2\,\mathrm{Re} \tag{9.8}$$

and permits determination of the change in the mass flow due to the imposition of the heating. The complete problem, which consists of the field equations (9.5), the boundary conditions (9.6) and either constraint (9.7) or (9.8), needs to be solved numerically.

9.2 Numerical Solution

We define the stream function ψ(x,y) in the usual manner, i.e., $u_1 = \partial\psi/\partial y$, $v_1 = -\partial\psi/\partial x$, and eliminate pressure from the momentum equations bringing the governing equations to the following form

$$\mathrm{Re}\,u_0 \frac{\partial}{\partial x}\left(\nabla^2\psi\right) - \mathrm{Re}\frac{d^2u_0}{dy^2}\frac{\partial\psi}{\partial x} + N_\psi = \nabla^4\psi - \mathrm{Ra}\frac{\partial\theta_1}{\partial x} - \mathrm{Ra}\,\mathrm{Pr}^{-1}\frac{\partial\theta_0}{\partial x}, \tag{9.9a}$$

$$\mathrm{Pr}\,\mathrm{Re}\,u_0\frac{\partial\theta_1}{\partial x} + \mathrm{Pr}\,N_{\theta 1} + \mathrm{Re}\,u_0\frac{\partial\theta_0}{\partial x} + N_{\theta 0} = \nabla^2\theta_1 \tag{9.9b}$$

where the nonlinear terms are written in the conservative form, i.e.,

$$N_\psi = \frac{\partial}{\partial y}\left(\frac{\partial}{\partial x}\langle u_1u_1\rangle + \frac{\partial}{\partial y}\langle u_1v_1\rangle\right) - \frac{\partial}{\partial x}\left(\frac{\partial}{\partial x}\langle u_1v_1\rangle + \frac{\partial}{\partial y}\langle v_1v_1\rangle\right),$$

$$N_{\theta 1} = \frac{\partial}{\partial x}\langle u_1\theta_1\rangle + \frac{\partial}{\partial y}\langle v_1\theta_1\rangle,$$

$$N_{\theta 0} = \frac{\partial}{\partial x}\langle u_1\theta_0\rangle + \frac{\partial}{\partial y}\langle v_1\theta_0\rangle.$$

The solution is assumed to be in the form of Fourier expansions, i.e.,

$$\psi(x,y) = \sum_{n=-\infty}^{n=+\infty}\varphi^{(n)}(y)e^{in\alpha x},\ \theta_1(x,y) = \sum_{n=-\infty}^{n=+\infty}\phi^{(n)}(y)e^{in\alpha x}, \tag{9.10a}$$

$$u_1(x,y) = \sum_{n=-\infty}^{n=+\infty}u_1^{(n)}(y)e^{in\alpha x},\ v_1(x,y) = \sum_{n=-\infty}^{n=+\infty}v_1^{(n)}(y)e^{in\alpha x}, \tag{9.10b}$$

$$p_1(x,y) = A_p\,x + \sum_{n=-\infty}^{n=+\infty}p_1^{(n)}(y)e^{in\alpha x} \tag{9.10c}$$

where $u_1^{(n)} = D\varphi^{(n)}$ and $v_1^{(n)} = -in\alpha\varphi^{(n)}$ and A_p denotes pressure gradient modification induced by the heating. The nonlinear terms are expressed in terms of Fourier expansions in the form

$$\langle u_1u_1\rangle(x,y)=\sum_{n=-\infty}^{n=+\infty}\langle u_1u_1\rangle^{(n)}(y)e^{in\alpha x}\ ,\ \langle u_1v_1\rangle(x,y)=\sum_{n=-\infty}^{n=+\infty}\langle u_1v_1\rangle^{(n)}(y)e^{in\alpha x}\ ,$$
$$\langle v_1v_1\rangle(x,y)=\sum_{n=-\infty}^{n=+\infty}\langle v_1v_1\rangle^{(n)}(y)e^{in\alpha x}\ ,\ \langle u_1\theta_1\rangle(x,y)=\sum_{n=-\infty}^{n=+\infty}\langle u_1\theta_1\rangle^{(n)}(y)e^{in\alpha x}\ , \qquad (9.10d)$$
$$\langle v_1\theta_1\rangle(x,y)=\sum_{n=-\infty}^{n=+\infty}\langle v_1\theta_1\rangle^{(n)}(y)e^{in\alpha x}\ ,\ \langle u_1\theta_0\rangle(x,y)=\sum_{n=-\infty}^{n=+\infty}\langle u_1\theta_0\rangle^{(n)}(y)e^{in\alpha x}\ .$$

Substitution of (9.10) into (9.9) and separation of Fourier components result in the following system of ordinary differential equations for the modal functions

$$D_n^2\varphi^{(n)}-in\alpha\,\mathrm{Re}\left(u_0D_n-\frac{d^2u_0}{dy^2}\right)\varphi^{(n)}-in\alpha Ra\phi^{(n)}=in\alpha Ra\,\mathrm{Pr}^{-1}\theta_0^{(n)}+N_\psi^{(n)}, \qquad (9.11a)$$

$$D_n\phi^{(n)}-in\alpha\,\mathrm{Pr}\,\mathrm{Re}\,u_0\phi^{(n)}=in\alpha\,\mathrm{Re}\,u_0\theta_0^{(n)}+N_{\theta0}^{(n)}+\mathrm{Pr}\,N_{\theta1}^{(n)} \qquad (9.11b)$$

where $-\infty<n<+\infty$, $D=d/dy$, $D^2=d^2/dy^2$, $D_n=D^2-n^2\alpha^2$,

$$N_\psi^{(n)}=in\alpha D\langle u_1u_1\rangle^{(n)}+D^2\langle u_1v_1\rangle^{(n)}+in^2\alpha^2\langle u_1v_1\rangle^{(n)}-in\alpha D\langle v_1v_1\rangle^{(n)},$$
$$N_{\theta1}^{(n)}=in\alpha\langle u_1\theta_1\rangle^{(n)}+D\langle v_1\theta_1\rangle^{(n)},$$
$$N_{\theta0}^{(n)}=in\alpha\langle u_1\theta_0\rangle^{(n)}+D\langle v_1\theta_0\rangle^{(n)}.$$

The linear terms have been placed on the left hand side, and the nonlinear and the known terms have been placed on the right hand side. The required boundary conditions for the modal functions have the form

$$D\varphi^{(n)}(\pm1)=0,\quad \phi^{(n)}(\pm1)=0\ ,\qquad \text{for } -\infty<n<+\infty\ . \qquad (9.12a,b)$$

$$\varphi^{(n)}(\pm1)=0,\quad \text{for } n\neq0 \qquad (9.12c)$$

$$\varphi^{(0)}(-1)=M_1,\quad \varphi^{(0)}(1)=M_2 \qquad (9.12d,e)$$

where the constants M_1, M_2 can be selected arbitrarily (Floryan 1997). One of these constants defines the arbitrary normalization condition in the definition of the stream function and the other one follows from a suitably chosen flow constraint. In the case of the fixed mass flow rate constraint these constants have been selected in the form

$$\varphi^{(0)}(-1)=0,\ \varphi^{(0)}(1)=0\,. \tag{9.13a,b}$$

In the case of the fixed pressure gradient constraint the closing conditions take the form

$$\varphi^{(0)}(-1)=0,\ \ A_p=0. \tag{9.14a,b}$$

The system (9.11) together with the boundary conditions (9.12a-c) and either constraints (9.13a,b) or (9.14a,b) needs to be solved numerically.

For the purpose of numerical solution, expansions (9.10) have been truncated after N_M Fourier modes. The discretization method uses Chebyshev collocation technique based on N_T collocation points. Gauss-Chebyshev-Lobatto points (Trefethen 2000) are used as the collocation points and their locations are computed from the following expression

$$y_k = \sin\left(\frac{\pi\left(N_T+1-2k\right)}{2\left(N_T-1\right)}\right),\quad k=0,1,2,\ldots N_T \tag{9.15}$$

which is advantageous in the floating-point arithmetic (Weideman and Reddy 2000). The resulting nonlinear algebraic system of equation is solved using an iterative technique combined with under-relaxation in the form

$$\Phi_{j+1} = \Phi_j + RF\left(\Phi_{comp} - \Phi_j\right) \tag{9.16}$$

where $\Phi = \left\{\varphi^{(n)}, \phi^{(n)}\right\}$, Φ_{comp} denotes the current solution, Φ_j denotes the previous solution, and Φ_{j+1} stands for the accepted value of the next iteration and RF denotes the

relaxation factor.

The solution process starts with solution of (9.11) with the nonlinear terms on the RHS assumed to be zero. Once solution of this problem has been completed, the first approximation of the nonlinear terms is computed on the basis of the available approximation of the velocity and temperature fields and system (9.11) is resolved with the new approximation of the nonlinear terms used on the RHS. This process is continued, with the update of the nonlinear terms taking place after each iteration, until a convergence criterion in the form

$$\max\left(\left|\Phi_{comp} - \Phi_j\right|\right) < \text{TOL} \tag{9.17}$$

is satisfied. TOL in (9.17) denotes tolerance at two consecutive iterations. The number of collocation points and the number of Fourier modes used in the solution were selected through numerical experiments so that the flow quantities of interest were determined with at least six digits accuracy.

The evaluation of the non-linear terms requires evaluation of products of two Fourier series. It is more efficient to evaluate these product in the physical space rather than in the Fourier space (Canuto et al. 2006). The required flow quantities, i.e., u_1, v_1, θ_1, are computed in the physical space on a suitable grid based on the collocation points in the y-direction and a uniformly distributed set of points in the x-direction, and the required products are evaluated. The Fast Fourier Transform (FFT) algorithm is used to express these products in terms of Fourier expansions (9.10d). The aliasing error is controlled using "padding" (Canuto et al. 2006), i.e., using of a discrete FFT transform with N_p rather than N_M points, where $N_p \geq 3N_M / 2$. Zeros are added for the additional Fourier modes as required.

Imposition of the fixed mass flow rate constraint (9.13a,b) is simple. Once the flow field has been determined, the pressure field is computed from the momentum equation. Insertion of (9.10) into (9.5a) and separation of Fourier modes lead to

$$p_1^{(n)} = \frac{1}{in\alpha}\left[\left(D^2 - n^2\alpha^2 - in\alpha\,Re\,u_0\right)D\varphi^{(n)} + in\alpha\,Re\frac{du_0}{dy}\varphi^{(n)} - in\alpha\langle u_1u_1\rangle - D\langle u_1v_1\rangle\right]$$

for $n\neq0$ (9.18a)

$$A_p = D^3\varphi^{(0)} - D\langle u_1v_1\rangle^{(0)} \qquad \text{for } n=0 \tag{9.18b}$$

Equation (9.18a) provides ability for direct evaluation of pressure modal functions for $n\neq0$. Equation (9.18b) can be used for determination of the additional pressure gradient required to maintain the mass flux in the heated channel as in the unheated reference channel. A form more suitable for computations (Floryan 1997) is obtained by integrating this equation between the walls resulting in

$$A_p = \frac{1}{2}\left[D^2\varphi^{(0)}\Big|_{y=1} - D^2\varphi^{(0)}\Big|_{y=-1}\right]. \tag{9.19}$$

The missing expression for determination of the 0^{th} modal function in the pressure field (see equation 9.10c) is obtained from the y-momentum equation. Substitution of (9.10) into (9.5b), extraction of mode zero and integration between both walls result in the following expression

$$p_1^{(0)} = Ra\int_{-1}^{y}\theta_1^{(0)}dy - \langle v_1v_1\rangle^{(0)} + \text{constant} \tag{9.20}$$

where the integration constant is arbitrary.

Imposition of the fixed pressure gradient constraint requires enforcement of (9.14a) in the same manner as above while imposition of condition (9.14b) is carried out with the help

of expression (9.19). The reader may note that the resulting problem is a mixed boundary value problem as conditions (9.19) involves quantities from both ends of the solution domain. The associated change in the flow rate is evaluated as

$$Q = \int_{-1}^{1} u_2 dy = \int_{-1}^{1} (\mathrm{Re}\, u_0 + u_1) dy = 4\,\mathrm{Re}/3 + Q_1 = 4\,\mathrm{Re}/3 + \varphi^{(0)}(1)\,. \tag{9.21}$$

9.3 Discussions of results

Due to the presence of the external flow the present problem becomes a three-parameter problem, and the parameters are (i) the heating wave number α which dictates the spatial distribution of the heating, (ii) the Rayleigh number Ra which defines the intensity of the heating, and (iii) the Reynolds number Re which describes the strength of the external flow. The structure of the temperature field in the absence of convection shown in **Figure 9.2** demonstrates that the space between the walls can be separated into heated and cooled zones resulting in the buoyancy force changing direction along the length of the channel. Such distribution of the driving force results in the onset of convection regardless of the amplitude of the heating.

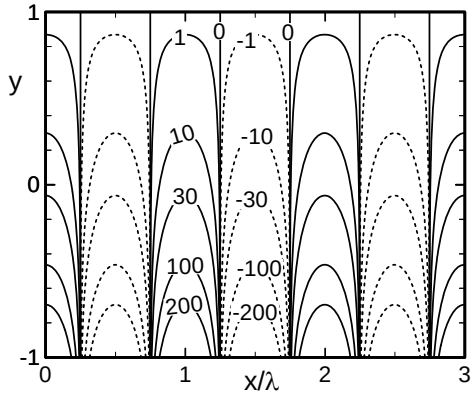

Figure 9.2. *Isotherms of the conductive temperature field for the heating wave number α = 3. Solid lines denote positive temperatures and dashed lines denote negative temperatures. Temperature magnitudes are multiplied by 1000. Note that this figure is same as the Fig.2.3 presented in Chapter 2. We show it here again.*

Convection motion has a fairly simple topology (as we have seen in Chapter 2) when there is no external flow, i.e., Re = 0. The fluid rises above the hot zones in the lower wall and descends above the cold zones forming pairs of counter-rotating rolls (see **Figure 9.3**A). When the external flow is introduced, flow topology starts to evolve away from the counter-rotating rolls. **Figure 9.3**B displays results for a weak external flow with Re = 1 and with the fixed mass constraint. It can be seen that a narrow stream tube has been formed. This stream tube separates rolls which are slightly displaced in the flow direction (as compared to the no flow case). The clock-wise rotating rolls are contained in the separation bubbles at the lower wall whereas the counter-clock-wise rolls are contained in the separation bubbles at the upper wall. If the intensity of the flow is increased to Re = 10 (**Figure 9.3**C), the heights of the separation bubbles are reduced. Further increase of the external flow to Re = 20 (**Figure 9.3**D) eliminates separation bubbles at the upper wall while retaining separation bubbles at the lower wall; these bubbles are concentrated near the cold regions of the wall. At Re = 100 (**Figure 9.3**E), no separation bubbles are visible at all since the external flow is strong enough to sweep them away. The motion of the bulk of the fluid is dominated by the external flow, and the influence of the buoyancy forces is limited to a thin zone near to the lower wall. We refer to such flow as the 'nearly parallel flow'. If the intensity of the external flow is further increased, the influence of the heating cannot be detected. It is noted that the separation bubbles at the lower and upper walls do not form in the same x-locations; usually the upper bubbles form above the hot spots while the lower bubbles form above the cold spots.

The isotherms corresponding to the above flow conditions are depicted in **Figure 9.4**. It is apparent from these figures that plumes are inclined along the flow direction with the inclination increasing with an increase of Re. It is also observed that only a very narrow portion (near the lower wall) of the channel remains cold. For low Re (see **Figure 9.4**A-C), the plume height covers almost the whole channel height; the size of the plume decreases with an increase of Re (**Figure 9.4**D-E).

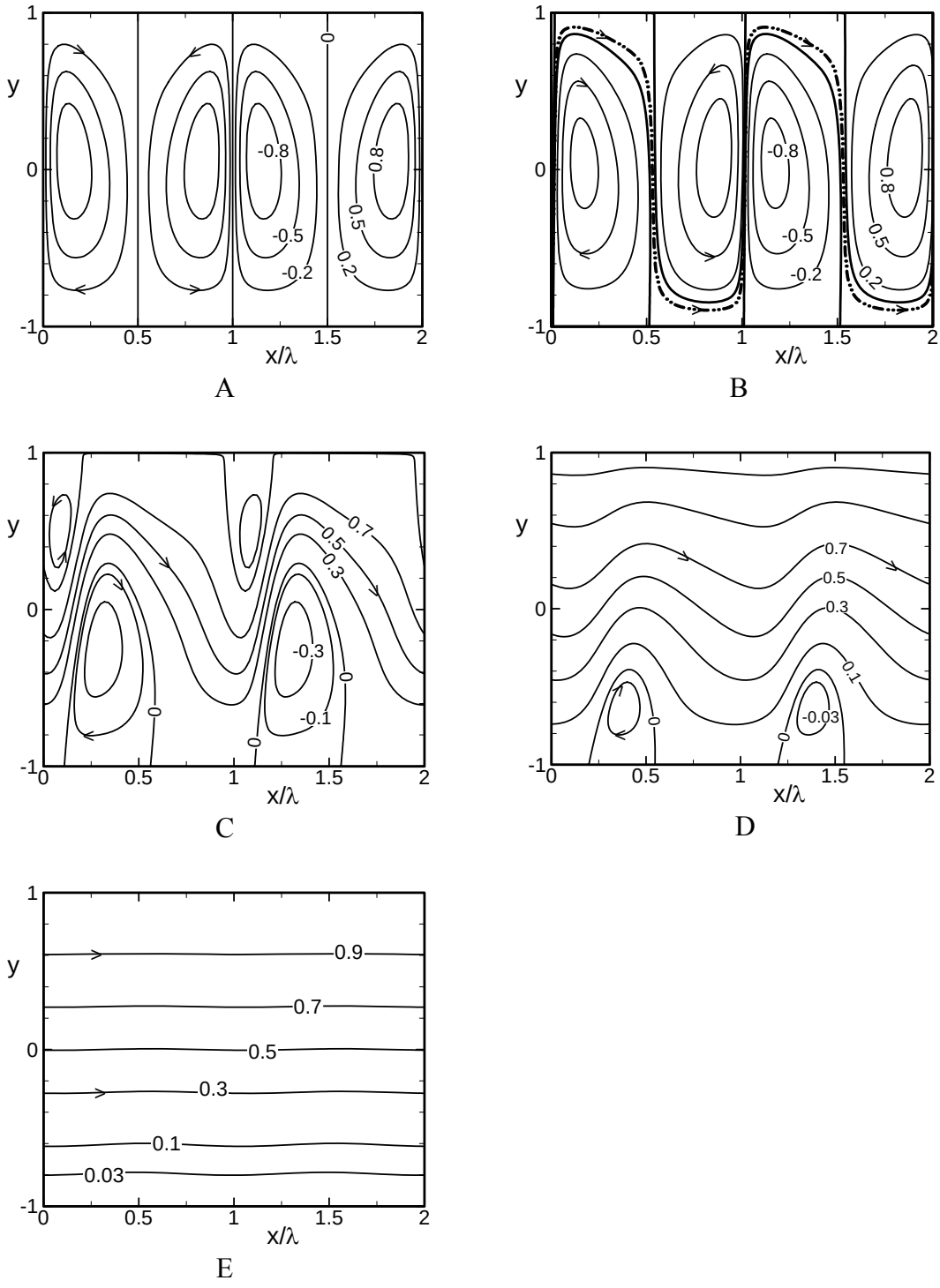

Figure 9.3. *Flow topology for the Rayleigh number Ra = 3500 and the heating wave number α = 1. Figures 9.3A-E correspond to the Reynolds number Re = 0,1,10,20,100, respectively. Stream function is normalized with its respective maxima. ψ_{max} for Figs 9.3A-E are 12.78, 13.34, 14.887, 26.667, 133.33, respectively. The dash-dot line in Fig.9.3B represents the center of the flow tube, whereas the thicker solid lines represent the boundaries of the lower and upper separation bubbles, respectively.*

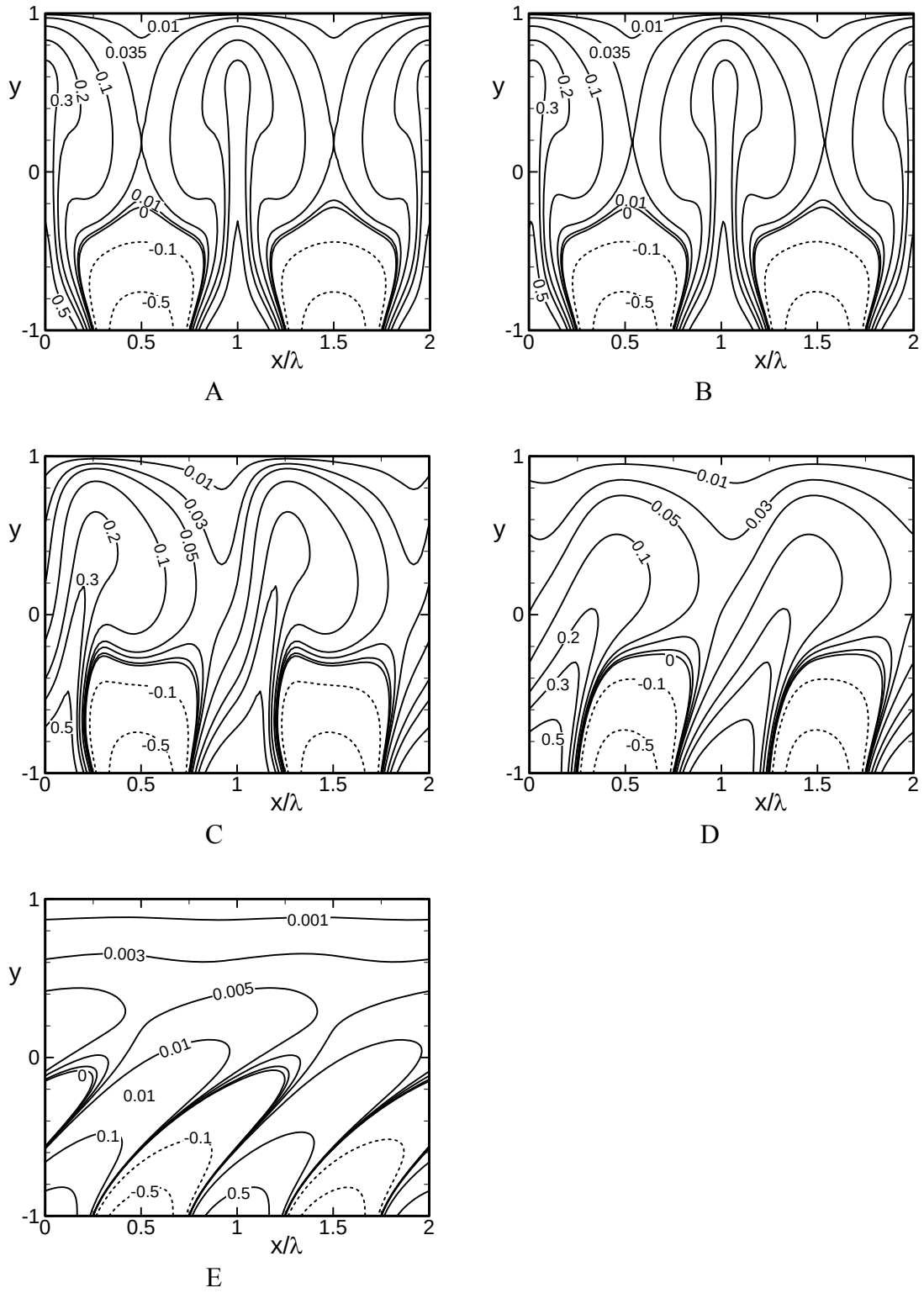

Figure 9.4. *Isotherms for the flow conditions shown in Fig.9.3.*

Flow patterns discussed above are usually observed when the heating wave number is low to moderate. A different evolution of flow topology is observed for large heating wave numbers. We have seen in the Chapter 2 that at Re = 0 the existence of the convection rolls was limited to the region near to the lower wall at large heating wave numbers, and the upper section of the channel experienced uniform x-independent temperature distribution. This phenomenon is shown again in **Figures 9.5A** and **9.6A**. Introduction of a weak Poiseuille flow (e.g., Re = 1) into the channel causes the rolls to begin to detach. The clockwise rolls form separation bubbles at the lower wall as before, but the counter-rotating rolls now form separation bubbles inside the flow; we refer to them as 'bubble-inside-the-flow' as shown in **Figure 9.5**B. Existence of the inflow stagnation points is detected. These bubbles divide the flow stream into two sections: one stream flows above the bubbles and the other flows below the bubbles. The lower stream meanders, whereas the upper stream is almost straight. This type of flow topology is usually observed at large heating wave numbers α. If the intensity of the external flow is increased to Re = 10 (see **Figure 9.5**C), the bubbles inside the flow disappear but bubbles attached to the lower wall remain. Further increase of Re to 40 eliminates the lower bubbles and the flow becomes nearly parallel as depicted in **Figure 9.5**D. It is noted that creation of separation bubbles at the upper wall at large heating wave number requires high intensity of the heating (e.g., Ra = 5000 at Re = 1 for $\alpha = 5$). In this case, the flow topology consists of three types of bubbles: bubbles at the lower wall, bubbles at the upper wall and 'bubble-inside-the-flow'. **Figure 9.5**E well illustrates such flow topology.

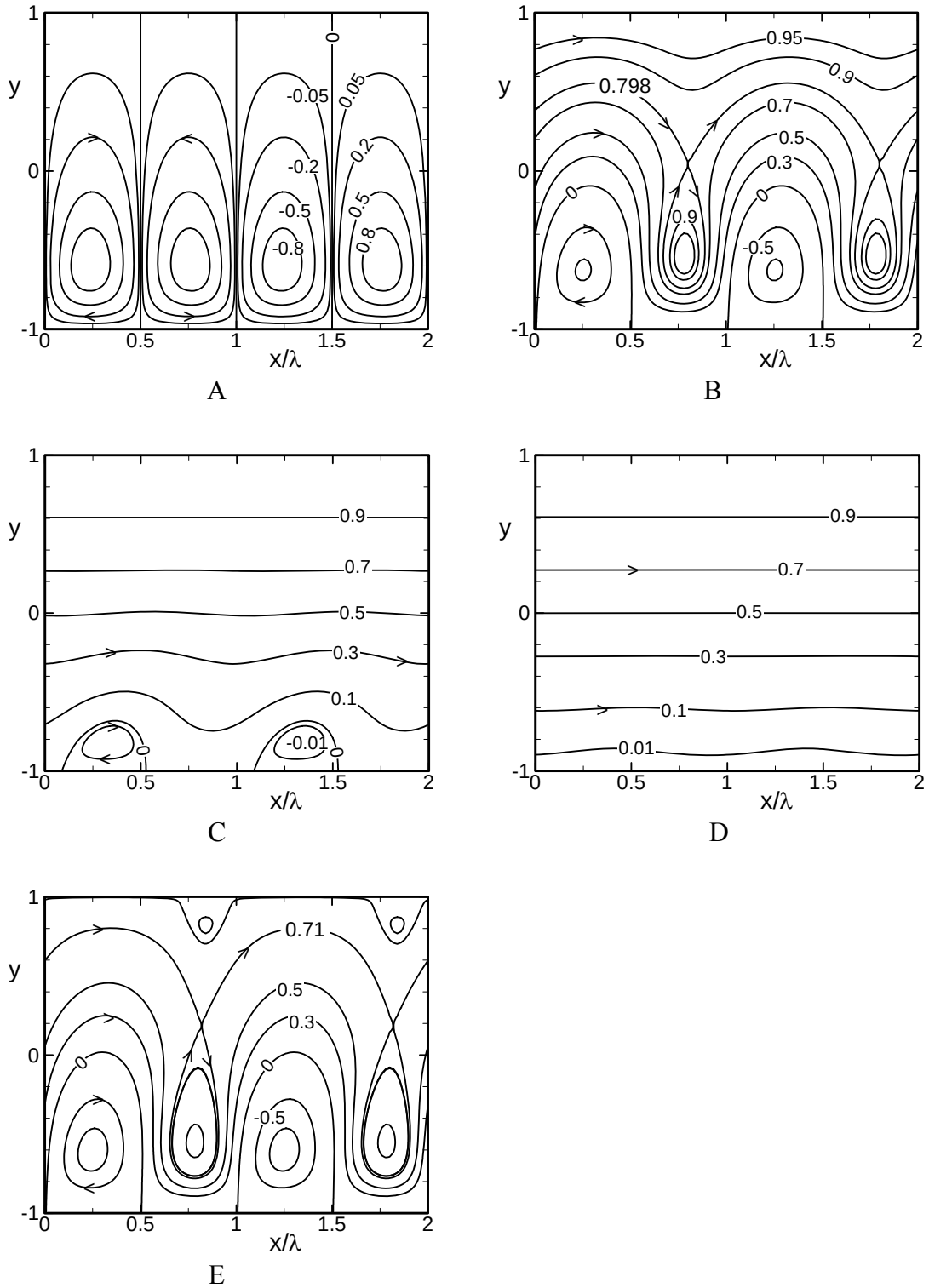

Figure 9.5. *Flow topology for the heating wave number α = 5. Figs 9.5A-E correspond to the Reynolds number Re = 0,1,10,40,1, respectively. The Rayleigh number Ra = 3500 for Figs 9.5A-D, and 5000 for Fig.9.5E. Stream function is normalized with its respective maxima. ψ_{max} for Figs 9.5A-E are 1.248, 1.365, 13.333, 53.333, 1.772, respectively.*

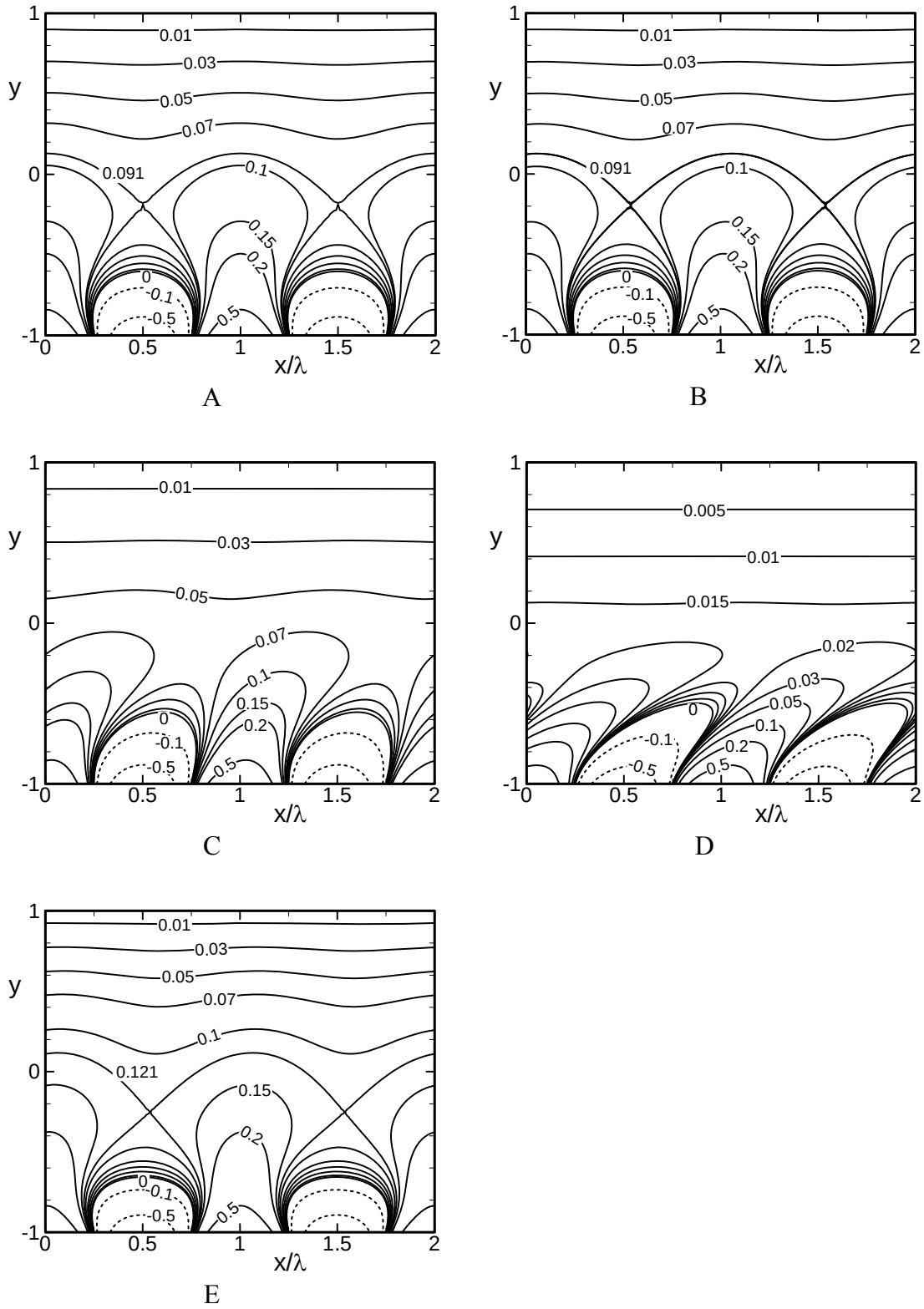

Figure 9.6. *Isotherms for the flow conditions shown in Fig.9.5.*

In **Figure 9.7** we elucidate the relationship between the heating wave number α and the Rayleigh number Ra at a fixed value of the Reynolds number Re that guarantees existence of various aforementioned flow structures. For a fixed value of Re, we obtain four types of zones. In zone I (which is below the solid lines) no bubbles are formed and the flow structure corresponds to the 'nearly parallel flow'. This zone exists for all α when either the intensity of the external flow is sufficiently high or the intensity of the heating is sufficiently low. In zone II (above the solid line) separation bubbles form at the lower wall. Bubbles start to appear at the upper wall when the flow conditions correspond to zone III. It is evident from **Figure 9.7** that if the upper wall bubbles form, the lower wall bubbles must also form; formation of only the upper bubbles is not possible. For higher values of α, intense heating (higher Ra) needs to be used in order to generate bubbles at the upper wall. Lastly, zone IV (above the dash-dot line) emerges when the heating is sufficiently high and, at the same time, α is also sufficiently high. Here at Re = 1 zone IV does not emerge at all if $\alpha \sim< 3.9$.

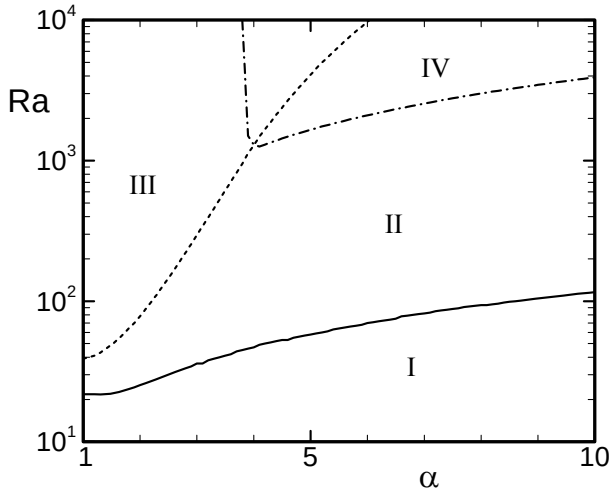

Figure 9.7. *Conditions for existence of various separation bubbles for the external flow with the Reynolds number Re = 1. Note that above the solid line bubbles at the lower wall exists, above the dotted line bubbles at the upper wall exist, and above the dash-dot line 'bubbles-inside-the-flow' exist.*

Conditions for the formation of bubbles at the lower and upper walls for selected values of Re are illustrated in **Figure 9.8**. These results demonstrate that in order to create bubbles at each of the walls one needs to increase the Reynolds number Re and the Rayleigh number Ra at the same time. It is found that for the range of Ra considered in this study the upper wall bubbles do not form when Re >~20 whereas the lower wall bubbles do not form if Re >~70.

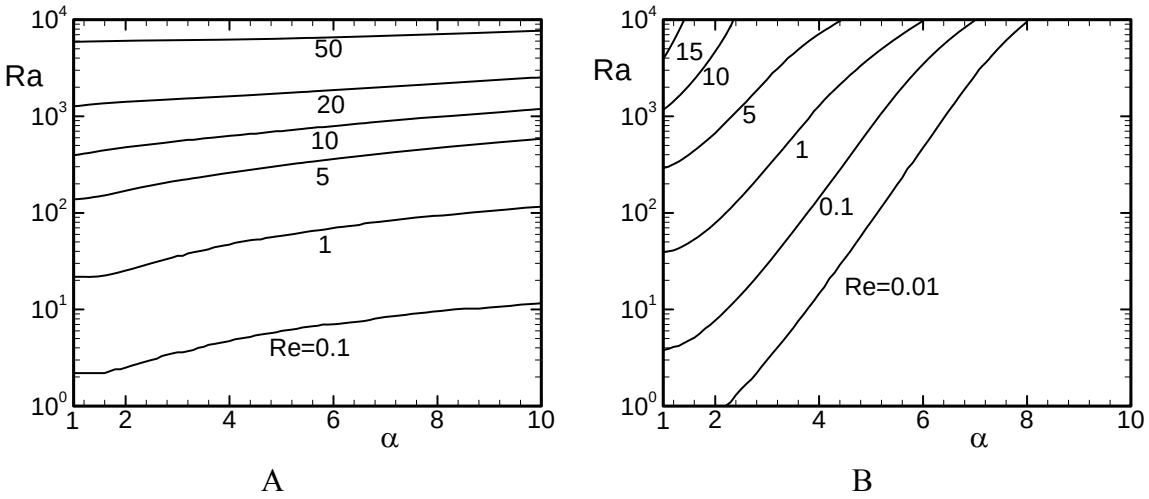

Figure 9.8. *Conditions for existence of bubbles at the lower wall (Fig. 9.8A) and at the upper wall (Fig. 9.8B) for selected values of the Reynolds number Re. Below each of the line bubbles do not exit, above each of the lines bubbles do exist.*

At this point, we focus our attention on the streamwise pressure gradient modifications (defined by Eq. 9.19) that may be induced by the applied heating. **Figure 9.9** shows the variations of the pressure gradient modification A_p as a function of the heating wave number α and the intensity of the reference flow Re at a constant intensity of the heating Ra. One may note that negative A_p contributes to the increase of drag whereas positive A_p contributes to the reduction of the drag experienced by the flow. For the range of parameters considered here we always obtain positive values of A_p , and with the increase of heating intensity Ra, the value of A_p usually increases.

To understand why drag force is reduced, we consider the force balance as follows:

Shear stress acting on the fluid at the lower wall, $\tau_L = -\left(\frac{\partial u}{\partial y} + \frac{\partial v}{\partial x}\right)_{y=-1}$

Shear stress acting on the fluid at the upper wall, $\tau_U = +\left(\frac{\partial u}{\partial y} + \frac{\partial v}{\partial x}\right)_{y=1}$

Shear force acting on the fluid at the lower wall per one wavelength of the heating, $F_{SL} = \int_{x=0}^{x=\lambda} \tau_L dx$ where, $\lambda = 2\pi/\alpha$

Shear force acting on the fluid at the upper wall per one wavelength of the heating, $F_{SU} = \int_{x=0}^{x=\lambda} \tau_U dx$.

The force balance along the x-direction requires that the total shear force per one wavelength ($F_s = F_{sL} + F_{sU}$) has to be equal to the pressure force acting on surfaces perpendicular to the walls placed at a distance equal to one wavelength, i.e., $F_p = -2\left(\frac{dp}{dx}\Delta x\right) = -2\left(-2\,\mathrm{Re} + A_p\right)\lambda$.

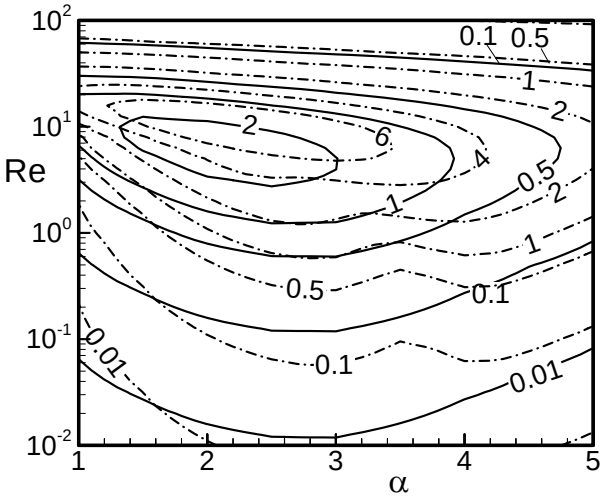

Figure 9.9. *Variation of the streamwise pressure gradient modification induced by the heating A_p as functions of the heating wave number α, and the Reynolds number Re for the Rayleigh numbers Ra=2000(solid line) and 5000(dash-dot lines) for the constant mass flux constraint. The maximum values of A_p at Ra=2000 and 5000 are 2.722 (at α=2) and 8.175 (at α=2.25), respectively.*

Consider situation when A_p takes the maximum value for Ra = 2000, i.e., Re = 6.3 and $\alpha = 2$. The shear force acting on the fluid on both walls and the percentage reduction of the drag force ϑ as compared with the non-heated case are shown in Table 9.1.

$$\vartheta_{\%} = \left(F_s\big|_{\text{withheating}} - F_s\big|_{\text{withoutheating}}\right) 100 / F_s\big|_{\text{withoutheating}} \tag{9.22}$$

Table 9.1: Shear force at Re = 6.3, $\alpha = 2$, Ra = 2000, $A_p = 2.722$.

	Lower wall (F_{SL})	Upper wall (F_{UL})	Total (F_S)	Percentage Reduction, ϑ(%)
Without heating	-39.58	-39.58	-79.16	**21.6**
Ra=2000	-14.17	-47.89	-62.06	

The above results show that presence of the heating results in 21.6% drag reduction.

The flow topology and the pressure field for the above conditions are displayed in **Figure 9.10**A. The flow structure contains separation bubbles at the lower and upper walls. Here we see that the size of the lower wall bubble is moderate, and the size of the upper wall bubble is small. This combination of the bubbles' size provides maximum drag reduction. It may be noted that if the bubbles' size is too large drag reduction is very small. We shall come to this issue again.

Figure 9.10B illustrates shear stress distributions at the lower and upper walls. Shear stress is positive in the separation regions. Because of that, instead of opposing the flow, the shear assists the flow as it acts along the flow direction. The overall result is the reduction of the total shear force when compared with the non-heated channel.

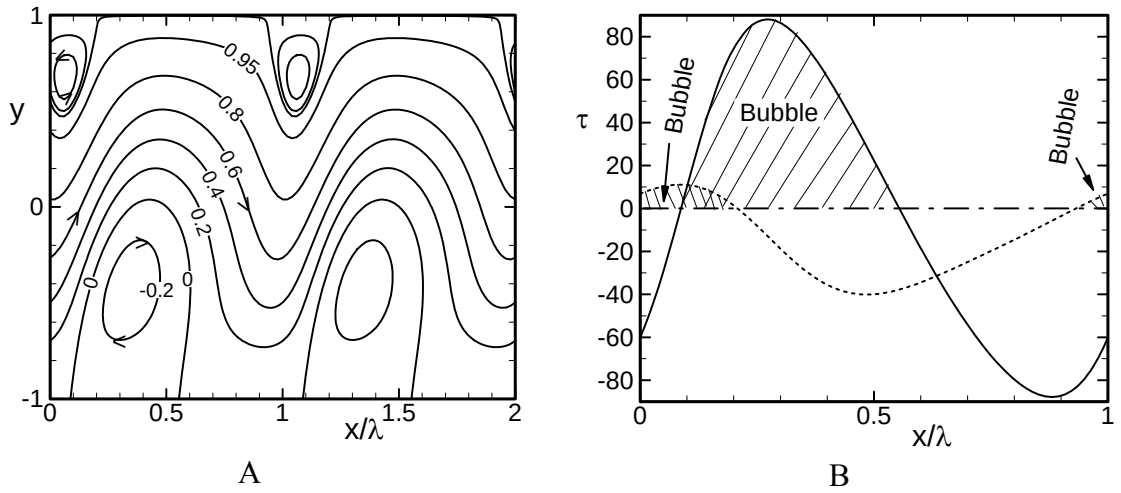

Figure 9.10. *Flow structure is shown in Fig.9.10A, and shear stress τ distributions at the lower wall (solid line) and the upper wall (dotted line) are shown in Fig.9.10B for the conditions when the streamwise pressure gradient modification induced by the heating A_p is maximum, i.e., Re = 6.3, α = 2, Ra = 2000. Shaded areas in Fig.91.0B show the regions of separation bubbles.*

Figure 9.11 depicts velocity profiles at different x-locations over one heating wavelength. It is evident that the maximum of the horizontal velocity component is greater than that for the unheated flow. This increase of the local velocity is due to the formation of the separation zones which reduce the cross-sectional flow area available to the flow.

Figure 9.12 describes distribution of shear stress at the upper and lower walls at selected values of the Reynolds number Re. It confirms that the bubble size diminishes with the increase of Re, and at high enough Re the bubbles disappear.

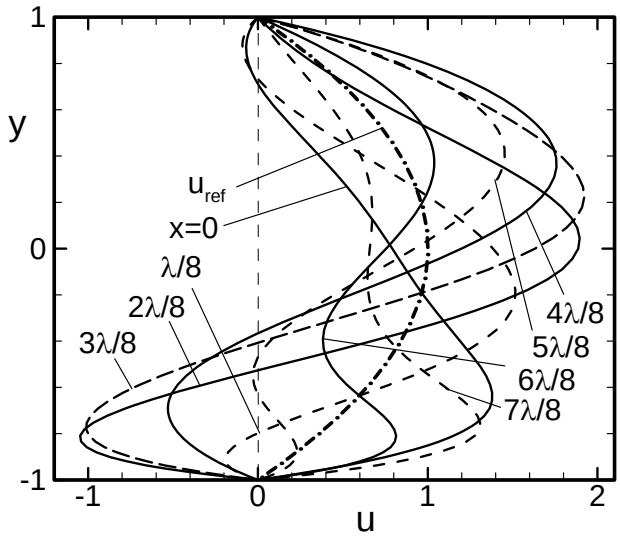

Figure 9.11. *Horizontal velocity profiles at different x-locations for the Reynolds number Re = 6.3, the heating wave number α = 2 and the Rayleigh number Ra = 2000. The thick dash-dot line shows the velocity profile without heating. Horizontal velocity is normalized by the maximum of u_{ref}.*

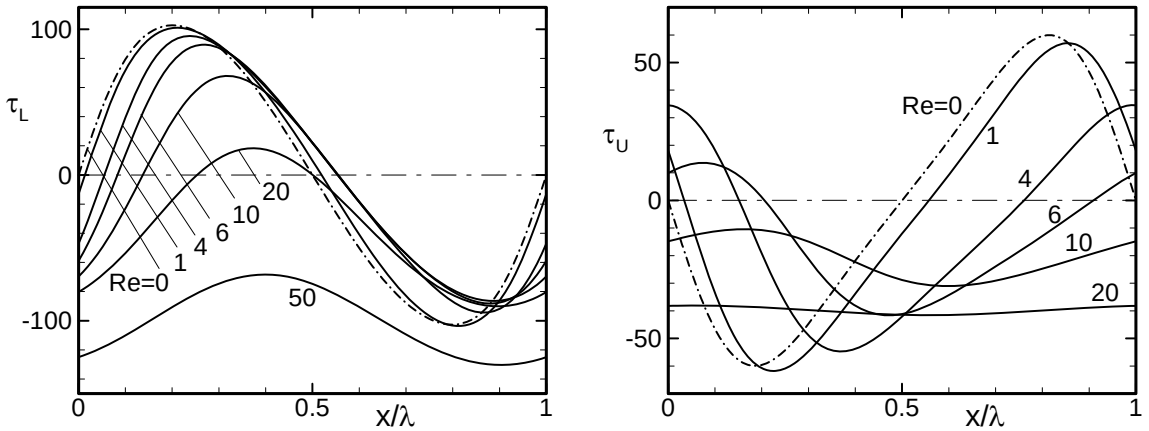

A B

Figure 9.12. *Shear stress τ distributions at the lower (Fig.9.12A) and the upper (Fig.9.12B) walls for selected values of the Reynolds number Re at the heating wave number α = 2 and the Rayleigh number Ra = 2000. Subscripts L and U are for the lower and upper walls, respectively.*

To identify the heating pattern (i.e., the heating wave number α) which leads to the maximum drag reduction, we refer to the plot shown in **Figure 9.13**. It can be seen that the heating pattern defined by α = 2~3 provides the maximum possible drag reduction at Reynolds numbers Ra = 2000 and 5000 considered here. The range of the Reynolds numbers that provides meaningful drag reduction is identified as Re = 1~20 for the case of Ra = 2000; this range increases to Re = 0.5~50 for Ra = 5000. The magnitude of A_p is reduced at higher Re because of reduction of the size of the separation zones. It is found that at low Re the magnitude of A_p decreases proportionally to the decrease of Re. To explain the reduction of A_p at smaller values of Re we explore the flow structures at very low Re. A typical example is shown at **Figure 9.3**B. It is observed that at very low Re, the presence of the heating results in large and almost vertical plumes (as the reference flow is too weak to tilt them along the flow direction) covering most of the channel height resulting in the formation of very big separation bubbles at both walls leaving a very narrow meandering flow tube for the fluid to pass through. The overall effect of such flow re-arrangement is the reduction of the pressure gradient modification A_p.

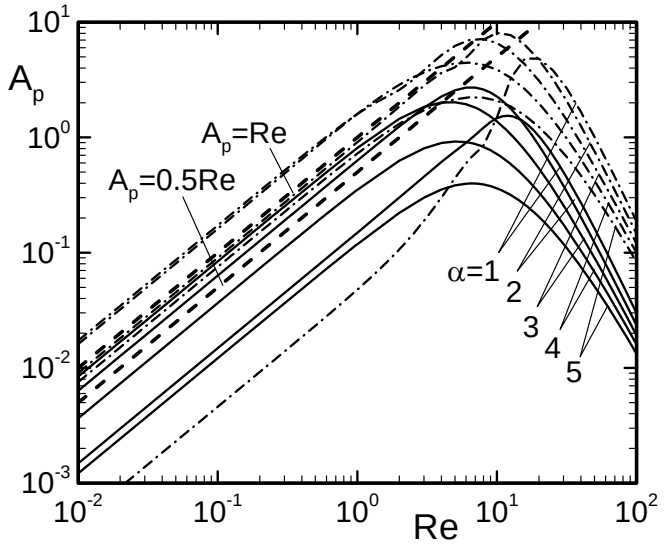

Figure 9.13. *Variation of the streamwise pressure gradient modification induced by the heating A_p as a function of the Reynolds number Re for the Rayleigh numbers Ra = 2000 (solid line) and Ra = 5000 (dash-dot line) for selected values of the heating wave number α.*

Figure 9.14 illustrates variations of the pressure gradient modification A_p with the change of the heating intensity Ra at selected values of the flow Reynolds number Re. We consider α = 2 and 3 only as these values correspond to the most efficient heating patterns. A_p initially increases proportionally to Ra^2 but this increase eventually saturates and any additional heating does not increase A_p.

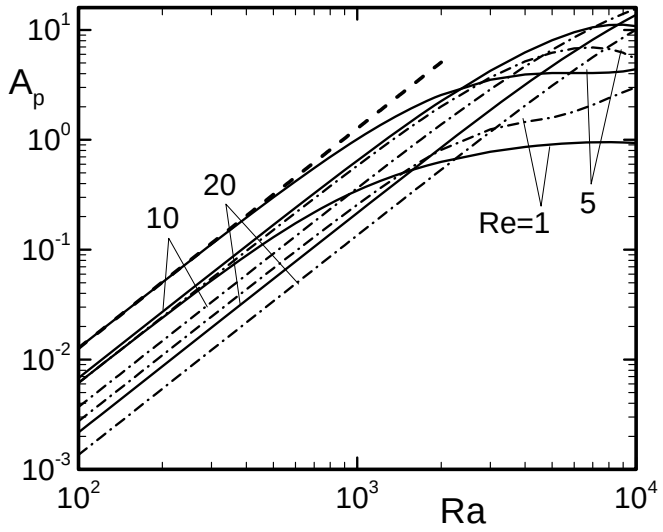

Figure 9.14. *Variation of the streamwise pressure gradient modification induced by the heating A_p as a function of the Rayleigh number Ra at selected values of the Reynolds number Re for the heating wave numbers α = 2(solid line) and α = 3(dash-dot line).The thick dash line represents the relation $A_p \propto Ra^2$.*

The nonlinear interactions associated with the convection and the reference Poiseuille flow give rise to the mean vertical temperature gradient that results in the net heat transfer between both walls. The net heat flow between both walls per unit length is expressed in terms of the Nusselt number defined as

$$\mathrm{Nu} = \frac{\mathrm{Pr}}{\lambda}\int_0^{\lambda}\left(-\left.\frac{\mathrm{d}\theta}{\mathrm{dy}}\right|_{y=-1}\right)\mathrm{dx} = -\mathrm{Pr}\left.\frac{\mathrm{d}\phi^{(0)}}{\mathrm{dy}}\right|_{y=-1} \quad . \tag{9.23}$$

Figure 9.15 shows the net transfer between the walls. It is observed that with the increase of the Reynolds number Re, the Nusselt number Nu decreases. This is because the external flow dominates the bulk motion of the fluid and the transverse heat transfer is limited to conduction only.

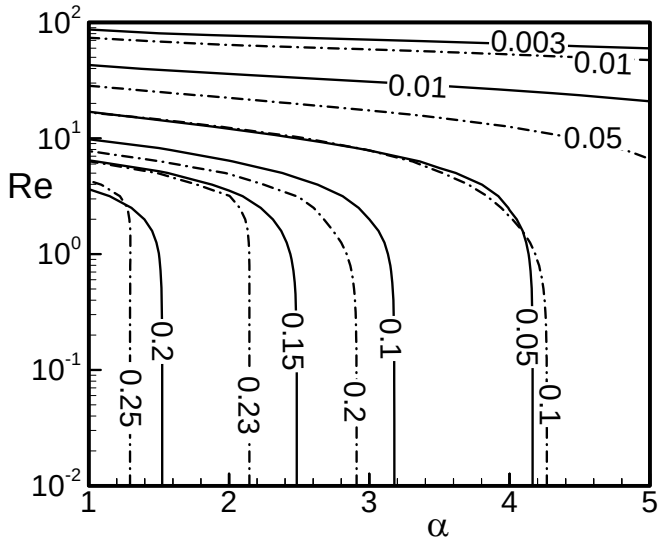

Figure 9.15. *Variation of the heat flow between the walls expressed in terms of the Nusselt number Nu as functions of the Reynolds number Re and the heating wave number α. Solid line corresponds to the Rayleigh number Ra = 2000, and dash-dot line to Ra = 5000.*

9.4 Summary

Channel flow subject to a periodic heating at the lower wall has been considered. The flow has Poiseuille form in the absence of any heating. The flow with the heating exhibits five distinct topologies, i.e., (i) nearly parallel flow, (ii) flow with separation bubbles at the lower wall, (iii) flow with separation bubbles at the upper wall, (iv) flow with bubble-inside-the flow, and (v) flow with a combination of the lower, upper and inside bubbles. It is found that the pressure gradient modification induced by the heating is always positive indicating the reduction of the overall drag. The formation of the separation bubbles provides recirculation zones which contribute to the reduction of the wall shear

force, and thus to the reduction of the drag. Maximum drag reduction occurs when the separation bubbles at the lower and the upper wall exist simultaneously and have optimum sizes.

10

Conclusions, Applications and Recommendations

10.1 Conclusions

Thermal convection (buoyancy-driven) of a Boussinesq fluid contained in an infinite slot has been analyzed. The slot is subject to a spatially distributed heating and the gravity is directed across the slot. It is assumed that the mean temperatures of both walls are the same and thus the convection occurs only due to the spatial variability of the heating. Detailed results are presented for the case of sinusoidal variations of temperature of the lower wall while the temperature of the upper wall is kept constant. The spatial pattern of the heating is described in terms of the heating wave number α while the intensity of the heating (heating amplitude) is expressed in terms of a suitable defined Rayleigh number Ra. Fluids with Prandtl numbers in the range $10^{-2} < Pr < 10^{3}$ have been considered which covers the range of interest in most of potential applications.

The primary response of the system consists of convection in the form of rolls whose orientation is determined by the heating wave number α and structure is dictated by the particular values of Ra and α. Heating with small and moderate values of α results in convection spreading throughout the whole fluid domain. When α is sufficiently large, convection is confined to a thin zone adjacent to the lower wall and a uniform conductive layer with temperature independent of the x-direction emerges above this zone. Sufficient increase of Ra causes convection to expand back into the bulk of the fluid. The nonlinear interactions associated with convection give rise to the mean vertical temperature gradient that results in the net heat transfer between both walls, with the heat flow being larger for smaller α. The upper section of the fluid layer has always an unstable mean temperature gradient with thickness of this zone decreasing with a decrease of α.

Linear stability of the primary convection has been considered and conditions leading to the emergence of secondary convection have been identified. Depending on the heating wave number α, the secondary convection may take the form of either the longitudinal rolls, or the transverse rolls, or the oblique rolls, or have an oscillatory character. The longitudinal rolls are parallel to the primary rolls and the transverse rolls are orthogonal to the primary rolls, and both of them result in striped patterns. The oblique rolls lead to the formation of convection cells with aspect ratio dictated by their inclination angle.

Three mechanisms of instability at the onset have been identified. In the case of small and moderate α the parametric resonance leads to the pattern of instability that is locked-in with the pattern of the heating according to the relation $\delta_{cr} = \alpha/2$, where δ_{cr} denotes component of the disturbance wave vector parallel to the heating wave vector. This resonance may be combined with variations in patterns of vertical temperature gradients, and patterns and strength of the primary convection currents. These patterns represent the second mechanism which may by itself dominate the form of secondary convection, as in the case with the transverse rolls. The third mechanism is active in the case of large α, where the instability is driven by the mean vertical temperature gradient created by the primary convection with the magnitude of the critical disturbance wave vector approaching limiting value of $\delta_{cr} = 1.56$ regardless of the roll orientation. Rolls in this limit show weak preference for the transverse orientation and the fluid response is similar to that found in the case of a uniformly heated wall. The first two mechanisms dominate for small and intermediate values of α where the spatial modulation of the flow is sufficiently strong while the third mechanism dominates in the case of weak spatial modulation. The strength of the modulation is a monotonic function of Pr and α but a non-monotonic function of Ra.

In the case of the longitudinal rolls, mechanisms associated with parametric resonance and mean vertical temperature gradient, i.e., the first and the third mechanisms, are observed. Competition between these mechanisms gives rise to commensurable and non-commensurable states for the longitudinal rolls. The commensurable states can be categorized according to the wavelength of the flow system N_δ measured using the

disturbance wavelength as the length scale. Branches corresponding to N_δ = 39, 78, 156, 234 and 468 have been explored in details for some selected values of Pr. In the "large α" zone the modulation is always limited to the area around the lower (heated) wall and the flow structures in the bulk of the fluid are dominated by δ_{cr}. Depending on the type of fluid, a decrease of α causes flow patterns to morph into the "beating", "wavy", "double wavy", "wavy-like", "double-parallel" and other forms that cannot be easily characterized, including formation of soliton lattices.

The possible system responses in the case of longitudinal rolls can be divided into four types depending on the value of Pr. In type A, the pattern of instability is locked-in with the pattern of heating for smaller values of α and no direct relation between both patterns exists for larger values of α. In type B, the lock-in does not occur at all. Type C response is similar to Type A, the difference involves only in the rate of change of the lock-in conditions as a function of Pr; this change is very rapid for type C and insignificant for type A. In type D, two different critical instability branches have been identified. Branch one exists for lower values of α and corresponds to disturbances whose structure is locked-in with the heating pattern whereas branch two exists for larger values of α and describes disturbance patterns that have no direct relation with the heating patterns. Morphing between different patterns of instability motion may occur in response to change in the heating pattern in types A and C, while such process is not possible in types B and D.

In the case of the transverse rolls, the main role is played by mechanisms associated with spatial modulation and with the mean vertical temperature gradient, i.e., the second and the third mechanisms. The modulation mechanism is active for heating patterns corresponding to the heating wave numbers O(1) for all values of Pr. Domination of this mechanism leads to the formation of very deformed transverse rolls. The zone where the other mechanism is active shifts towards higher values of the heating wave number as Pr decreases. The interplay between both mechanisms results in two types of fluid response depending on Pr. One of them produces a single-minimum critical curve when both

mechanisms are active in the same range of heating wave numbers, and the other produces a two-minimum critical curve when both mechanisms are active in distinctly different ranges of the heating wave numbers. A zone of a fairly stable primary convection occurs in the latter case for the heating patterns corresponding to the heating wave numbers from the in-between zone.

In the case of the oblique rolls, all three mechanisms are active. It has been found that, within the range of Ra being of interest, these rolls can change orientation from 0° to 35° with respect to the primary rolls depending on the heating wave number and the Prandtl number of the fluid. A rapid stabilization of the primary convection is observed when the heating wave number is sufficiently small. Analysis of temperature field created by the primary convection at the onset suggests that reduction of the thickness of zone with an unstable temperature gradient is likely responsible for the observed stabilization. The zone of dominance of the oblique rolls increases (moves toward “large α” zone) with the decrease of Pr. The x-component of the critical disturbance wave vector δ_{cr} varies as $\delta_{cr} = \alpha/2$ for all of the Prandtl numbers considered. Morphing between the oblique and longitudinal rolls occurs only for fluids with $\sim 0.3 < Pr < \sim 1$.

In the case of long wavelength heating, secondary motions in the form of longitudinal rolls concentrated around the hot spots occur for supercritical values of Ra ($Ra > 427$). Pitchfork bifurcations and "bifurcations from infinity" have been identified depending on the wave number of the heating α and on the intensity of the heating Ra. The secondary convective motions of each of the bifurcation branches contain either an odd number of secondary rolls per half period, with rolls at the hot spots rotating in the direction opposite to the primary rolls, or an even number of secondary rolls per half period, with the rolls at the hot spots co-rotating with the primary rolls. The number of rolls increases without limit as α decreases with new rolls being pinched off in pairs. The pinching process for each branch occurs at different α's and as a result the branches alternate in producing larger net heat flow. The bifurcation processes are insensitive to variations of the Prandtl number for $Pr = O(1)$.

The topology of the primary convection changes with the presence of an external flow. Five distinct flow compositions have been identified; they include separation bubbles at the lower wall, separation bubbles at the upper wall, 'bubbles-inside-the-flow', combination of the lower, upper and inside flow bubbles, and a nearly parallel flow. The pressure modification gradient induced by the heating always appears to be positive indicating reduction of the overall drag. The formation of separation bubbles provides some recirculation zones which contribute to the reduction of the wall shear force which leads to the reduction of the drag. Maximum drag reduction is achieved when the flow contains separation bubbles both at the lower and upper walls with an optimum size.

Overall, it is can be concluded that the heating wave number α can be used as a pattern control parameter and its judicious selection provides means for creation of a large range of flow responses.

10.2 Applications

The distributed heating or, particularly, the periodic heating in sinusoidal form studied in this dissertation provides unevenly heated surfaces. We have seen that this type of heating produces convection regardless of the intensity of heating, no matter how small the heating amplitude is. Some of the proposed applications are discussed below:

- To create convection and thereby enhance mixing in micro- and nano-devices by inserting electrically heated micro- or nano-wires in a suitable interval on the surface.

- To contribute to modeling of transport processes in atmosphere where local convective motions may be occurring in the presence of unevenly heated surfaces (ocean, lake/forest system, urban environment, local fires etc.). Local convection may have dominant effect on transport of contaminants, especially in urban environment and in sea.

- To develop new efficient heat exchangers working with low temperature differences between the heat source and the heat target. The primary application area would be geothermal heating and cooling. Use of geothermal energy is of great interest at present due to concerns associated with environmental pollution, greenhouse gases and the cost of traditional sources of energy.

- To help in the analysis of transport processes occurring during transportation of petroleum products such as natural gas using pipelines. Pipelines usually extend over large distances and thus must be exposed to different temperatures which could be modeled using periodic heating. In this sense, this study may be helpful in petroleum industry.

- RB convection is suitable for performing thermally activated chemical reactions that require temperature cycling. One example that requires frequent changes in temperature is the polymerase chain reaction (PCR) that is typically carried out by heating and cooling a sample volume repeatedly. Krishnan et al. (2002) conducted PCR for DNA amplification using RB convection cell. Various convection cells obtained in this study may also be used for such PCR.

- The analysis of the noninvasive measurement of blood perfusion (Liu and Xu 1999) and the analysis of cancer hyperthermia or thermal comfort (Deng and Liu 2002) in biological bodies involve the use of spatial sinusoidal heating. Consequently, this study may be a potential use for these types of problems.

10.3 Recommendations for future works

Primary and secondary convection in a fluid layer exposed to a sinusoidal heating at the lower wall has been considered for a wide range of Prandtl numbers Pr. The primary convection is assumed to be two-dimensional while the secondary convection is assumed to be three dimensional. Analysis of the secondary convection is based on the linear

stability theory. In order to advance research presented in this dissertation, analysis of the following problems may be undertaken in the future:

i) In this dissertation various secondary flow structures have been identified at the onset conditions. The next step would be to perform the direct numerical simulation (DNS) to obtain saturation states, as saturation properties dictate the actual behavior of the system.

ii) The distributed heating defined here may have many forms. The simplest pattern described by sinusoidal function has been investigated in details. More complex forms of heating can be considered. Examples of possible patterns include heating with temperature in the form of a saw-tooth, or in the form of a sine-bump, among many others.

iii) The heating pattern considered in this dissertation varies along the length of the slot, i.e., f(x). Variations across the slot can be studied by considering heating to be function of both dimensions, i.e., f(x,z). In the later case, the primary convection will be three-dimensional, and the corresponding linear stability will follow formulation presented in Appendix C.

iv) In RB convection a non-linear stability theory is used to obtain final patterns, e.g., spiral-defect chaos, etc. (Bodenschatz et al. 2000). Non-linear stability theory may be developed to gain further understanding of periodically heated systems.

v) This dissertation describes only the primary convection when an external flow is present. This analysis can be extended by considering the secondary convection in the presence of an external flow.

References

Arnold, V.I., 1983, *Geometrical Methods in the Theory of Ordinary Differential Equations*, Springer-Verlag, New York.

Asgrian, A., 2000, *Natural Convection in a Slot Subject to a Long Wavelength Heating*, M.A.Sc. Dissertation, Faculty of Engineering, The University of Western Ontario, London, ON, Canada.

Beltrame, P., Knobloch, E., Hanggi, P. and Thiele, U., 2011, Rayleigh and depinning instabilities of forced liquid ridges on heterogeneous substrates, *Phys. Rev. E*, 83, 016305.

Bodenschatz, E., Pesh, W. and Ahlers, G., 2000, Recent developments in Rayleigh-Benard convection, *Ann. Rev. Fluid Mech.*, 32, 709-778.

Busse, F.H., 1972, The oscillatory instability of convection rolls in a low Prandtl number fluid, *J. Fluid Mech.*, 51, 97-112.

Busse, F.H. and Clever, R.M., 1979, Instabilities of convection rolls in a fluid of moderate Prandtl number, *J. Fluid Mech.*, 91, 319-335.

Canuto, C., Hussaini, M.Y., Quarteroni, A., and Zang, T.A., 2006, *Spectral Methods Fundamentals in Single Domain*, Springer.

Clever, R.M. and Busse, F.H., 1974, Transition to time dependent-convection, *J. Fluid Mech*., 65, 625-645.

Deng, Z.S. and Liu, J., 2002, Analytical Study on Bioheat Transfer Problems with Spatial or Transient Heating on Skin Surface or Inside Biological bodies, *ASME J. of Bio-mechanical Engineering*, 124, 638-649.

Ding, Y. and Kawahara, M., 1998, Linear stability of incompressible flow using a mixed finite element method, *J. Comput. Phys.*, 139, 243–273.

Drazin, P.G. and Reid W.H., 1981, *Hydrodynamic Stability*, Cambridge University Press.

Dubief, Y. and Delcayre, F., 2000, On coherent-vortex identification in turbulence, *J. of Turbulence*, 1, 011.

Floryan, J.M., 1997, Stability of wall bounded shear layers with simulated distributed surface roughness, *J. Fluid Mech.*, 335, 29-55.

Floryan, J.M., 2003, Vortex instability in a diverging-converging channel, *J. Fluid Mech*., 482, 17-50.

Floryan, J.M,. 2005, Two-dimensional instability of flow in a rough channel, *Phys. Fluids*, 17, 044101.

Freund, G., Pesch, W. and Zimmermann, W., 2011, Rayleigh-Bénard convection in the presence of spatial temperature modulations, *J. Fluid Mech*., 673, 318-348.

Furlani, E.P. and Hanchak, M.S., 2010, Nonlinear analysis of the deformation and breakup of viscous microjets using the method of lines, *Int. J. Numer. Meth. Fluids*, doi: 10.1002/fld.2205.

Golub G.H. and Loan C. F., 1996, *Matrix Computations*, Baltimore: Johns Hopkins Univ. Press, 3rd ed.

Hignett, P., Ibbetson, A. and Killworth, P.D., 1981, On rotating thermal convection driven by non-uniform heating from below, *J. Fluid Mech.,* 109, 161-187.

Jenkins, D.R., 1988, Interpretation of shadowgraph patterns in Rayleigh-Benard convection, *J. Fluid Mech.,* 190, 451-469.

Kelly, R.E. and Pal, D., 1978, Thermal convection with spatially periodic boundary conditions: resonant wavelength excitation. *J. Fluid Mech.,* 86, 433-456.

Kierzenka, J. and Shampine, L.F., 2008, A BVP Solver that Controls Residual and Error, *JNAIAM*, 3, 27-41.

Kierzenka, J. and Shampine, L.F., 2001, A BVP Solver Based on Residual Control and the MATLAB PSE., *ACM Trans. Math. Softw*., 27, 299-316.

Killworth, P.D. and Manins, P.C., 1980, A model of confined thermal convection driven by non-uniform heating from below, *J. Fluid Mech.*, 98, 587-607.

Kim, J., Moin, P. and Moser, R, 1987, Turbulence statistics in fully developed channel flow at low Reynolds number, *J. Fluid Mech*., 177, 133-166.

Krishnan, M., Ugaz, V.M. and Burns M.A., 2002, PCR in a Rayleigh-Benard Convection Cell, *Science*, 298, 793-793.

Liu, I.C., 2004, Effect of modulation on onset of thermal convection of a second-grade fluid layer. *Int. J. Non-Lin Mech.*, 39, 1647-1657.

Liu, J. and Xu, L.X., 1999, Estimation of Blood Perfusion Using Phase Shift in Temperature Response to Sinusoidal Heating at the akin surface, *IEEE Trans. Biomed. Eng.*, 46(9), 1037-1043.

Lowe, M. and Gollub, J.P., 1985, Solitons and the commensurate-incommensurate transition in a convective nematic fluid, *Phys. Rev. A*, 31, 3893-3897.

Lyubimov, T.P., Lyubimov, D.V., Morozov, V.A., Scuridin, R.V., Hadid, H.B. and Henry, D., 2009, Stability of convection in a horizontal channel subjected to a longitudinal temperature gradient. Part 1. Effect of aspect ratio and Prandtl number, *J. Fluid Mech.*, 635, 275-295.

Mancho, A.M., Herrero, H. and Burguete J., 1997, Primary instability in convective cells due to nonuniform heating, *Phys. Rev. E* 56(3), 2916-2923.

Manor, A., Hagberg, A. and Meron, E., 2008, Wave-number locking in spatially forced pattern-forming systems, *Europhys. Lett*, 83, 10005.

Manor, R., Hagberg, A. and Meron, E., 2009, Wave number locking and pattern formation in spatially forced systems, *New J. Phys*., 11, 063016.

McCoy, J.H, Brunner, W., Pesch W. and Bodenschatz, E., 2008, Self-Organization of Topological Defects due to Applied Constraints, *Phys. Rev. Lett.*, 101, 254102.

Mullarney, J.C., Griffiths, R.W. and Hughes, G.O., 2004, Convection driven by differential heating at a horizontal boundary, *J. Fluid Mech.,* 516, 181–209.

Natarajan, E., Basak, T. and Roy, S., 2008, Natural convection flows in a trapezoidal enclosure with uniform and non-uniform heating of bottom wall, *Int. J. Heat Mass. Trans.*, 51, 747-756.

Or, A.C. and KELLY, R.E., 1999, Time-modulated convection with zero mean temperature gradient, *Phys. Rev. E,* 60(2), 1741-1747.

Or, A.C., 2001, Onset condition of modulated Rayleigh-Benard convection at low frequency, *Phys. Rev. E,* 64, 050201 (R).

Pal, P., Wahi, P., Paul, S., Verma, M.K., Kumar, K. and Mishra, P.K., 2009, Bifurcation and chaos in zero-Prandtl-number convection, *EPL,* 87, 54003.

Pal, D. and Kelly, R. E., 1979. Three-Dimensional Thermal Convection Produced by Two-Dimensional Thermal Forcing. *Proc. Joint ASME/AIChE 18th Nat. Heat Transfer Conf., San Diego, Calif.,* ASME Publication 79-HT-109, 1-8.

Paul, M. R., Chiam, K.-H., Cross, M. C., Fischer, P. F., and Greenside, H. S., 2003, Pattern formation and dynamics in Rayleigh-Benard convection: numerical simulations of experimentally realistic geometries, *Physica D,* 184(1-4), 114-126.

Pesch, W., Palaniappani, D., Tao, J. and Busse, F.H., 2008, Convection in heated layers subjected to time-periodic horizontal accelerations, *J. Fluid Mech.,* 596, 313-326.

Rosenblat, S. and Davis, S.H., 1979, Bifurcation from infinity, *SIAM J. Appl. Math.*, 37, 1-19.

Rossby, T., 1998, Numerical experiments with a fluid heated non-uniformly from below, *Tellus,* 50A, 242-257.

Saad, Y., 2011, *Numerical Methods for Large Eigenvalue Problems*, SIAM, 2nd ed.

Schmid, P.J. and Henningson, D.S., 2000, *Stability and Transition in Shear Flows*, Springer.

Seiden, G., Weiss S., McCoy, J.H., Pesch, W. and Bodenschatz, E., 2008, Pattern Forming System in the Presence of Different Symmetry-Breaking Mechanisms, *Phys. Rev. Lett.,* 101, 214503.

Singh, J. and Bajaj, R., 2009, Temperature modulation in a ferrofluid convection, *Phys. Fluids,* 21, 064105.

Tao, J. and Busse, F.H., 2009, Oblique roll instability in inclined buoyancy layers, *Euro. J. Mech. B/Fluids*, 28, 532-540.

Theofilis, V., 2011, Global Linear Instability, *Annu. Rev. Fluid Mech*., 43, 319-352.

Trainoff, S.P. and Cannel, D.S., 2002, Physical optics treatment of the shadowgraph, *Phys. Fluids*, 14(4), 1340-1363.

Trefethen, L.N., 2000, *Spectral Methods in MATLAB*, SIAM, Philadelphia.

Verzicco, R. and Camussi, R., 1999, Prandtl number effects in convective turbulence, *J. Fluid Mech.*, 383, 55-73.

Vozovoi, L.P., Nepomnyashchy, A.A, 1974, Convection in a horizontal layer in the presence of spatial modulation of temperature at the boundaries, *Gidrodynamika*, 7, 105-117.

Walton, I.C., 1982, The effect of slow spatial variations on Benard convection, *Q. J. Mech. Appl. Math.*, 35(1), 33-48.

Wang, W. and Huang, R.X., 2005, An experimental study on thermal circulation driven by horizontal differential heating, *J. Fluid Mech.,* 540, 49-73.

Weideman, J. A. C. and Reddy, S. C., 2000, A MATLAB Differentiation Matrix Suite, *ACM Trans. Math. Softw.*, 26(4), 465-519.

Appendix-A

Calculation of Pressure Field for the Primary Convection

This appendix describes method used to determine the pressure field from the computed velocity field for the primary convection described in Section 2.4.2.2.

The non-dimensional x- and y-momentum equations (2.5a-b) can be written in the conservative form as

$$\frac{\partial}{\partial x}\langle uu\rangle + \frac{\partial}{\partial y}\langle uv\rangle = -\frac{\partial p}{\partial x} + \nabla^2 u\,, \tag{A.1a}$$

$$\frac{\partial}{\partial x}\langle uv\rangle + \frac{\partial}{\partial y}\langle vv\rangle = -\frac{\partial p}{\partial y} + \nabla^2 v + Ra\theta_1 + Ra\,Pr^{-1}\theta_0\,. \tag{A.1b}$$

The flow variables u, v and p can be expressed using Fourier expansion as

$$u(x,y) = \sum_{n=-\infty}^{n=+\infty} u^{(n)}(y)e^{in\alpha x}\,, \tag{A.2a}$$

$$v(x,y) = \sum_{n=-\infty}^{n=+\infty} v^{(n)}(y)e^{in\alpha x}\,, \tag{A.2b}$$

$$p(x,y) = \sum_{n=-\infty}^{n=+\infty} p^{(n)}(y)e^{in\alpha x}\,. \tag{A.2c}$$

The convective terms can also be expressed in terms of the Fourier expansions as

$$\langle uu\rangle(x,y) = \sum_{n=-\infty}^{n=+\infty} \langle uu\rangle^{(n)}(y)e^{in\alpha x}\,, \tag{A.3a}$$

$$\langle uv\rangle(x,y)=\sum_{n=-\infty}^{n=+\infty}\langle uv\rangle^{(n)}(y)e^{in\alpha x}\ , \tag{A.3b}$$

$$\langle vv\rangle(x,y)=\sum_{n=-\infty}^{n=+\infty}\langle vv\rangle^{(n)}(y)e^{in\alpha x}\ . \tag{A.3c}$$

Insertion of the above Fourier expansions into (A.1) and separation of Fourier components lead to

$$in\alpha p^{(n)}=\left(D^2-n^2\alpha^2\right)u^{(n)}-in\alpha\langle uu\rangle_n-D\langle uv\rangle_n\,, \tag{A.4a}$$

$$Dp^{(n)}=\left(D^2-n^2\alpha^2\right)v^{(n)}-in\alpha\langle uv\rangle_n-D\langle vv\rangle_n+Ra\theta_1^{(n)}+Ra\,Pr^{-1}\,\theta_0^{(n)}\ . \tag{A.4b}$$

Equation (A.4a) written for mode n≠0 provides expression for the evaluation of $p^{(n)}(y)$

$$p^{(n)}(y)=\frac{1}{in\alpha}\left[\left(D^2-n^2\alpha^2\right)u^{(n)}-in\alpha\langle uu\rangle_n-D\langle uv\rangle_n\right],\qquad \text{for } n\neq 0. \tag{A.5}$$

The last quantity, i.e., $p^{(0)}(y)$, needs to be computed from the y-momentum equation (A.4b). This equation written for mode 0 results in

$$Dp^{(0)}=-D\langle vv\rangle_0+Ra\theta_1^{(0)}+Ra\,Pr^{-1}\,\theta_0^{(0)} \tag{A.6}$$

which, after integration, leads to

$$p^{(0)}(y)=-D\langle vv\rangle_0+Ra\int_{-1}^{y}\theta_1^{(0)}dy+\text{constant}\ . \tag{A.7}$$

Expressions (A.5) and (A.7) provide the complete pressure field. Integration constant in (A.7) is arbitrary and usually taken to be zero.

Appendix-B

Formulation of the Field Equations Describing Three-Dimensional Primary Convection

In this Appendix we derive the three-dimensional governing equations for the primary convection created by spatially distributed heating varying in the longitudinal and transverse directions, i.e., *f(x,z)*. The reader may note that this formulation includes externally imposed flow.

Consider flow confined in a channel bounded by walls at y = ±1 and extending to ±∞ in the x- and z- directions, as shown in **Figure B.1**. The reference flow is the Poiseuille flow directed along the positive x-axis and driven by a pressure gradient. The fluid is incompressible and Newtonian. This flow is modified by distributed heating applied at the bottom wall resulting in the temperatures of the walls in the form

$$\theta_L(x,z) = \sum_{n=-\infty}^{n=+\infty} \sum_{m=-\infty}^{m=+\infty} \theta_L^{(n,m)} e^{i(\alpha n x + \mu m z)} , \tag{B.1a}$$

$$\theta_U(x,z) = 0 \tag{B.1b}$$

where $\alpha = 2\pi/\lambda_x$, $\mu = 2\pi/\lambda_z$,and λ_x and λ_z denote wavelengths in the streamwise and spanwise directions, respectively. θ denotes the relative temperature, i.e., $\theta = T-T_{ref}$, T denotes the temperature and the temperature of the upper wall is selected as the reference temperature T_{ref}.

The dimensional field equations for a Boussinesq fluid are scaled using two sets of scales, i.e., one to characterize the Poiseuille flow and the other to characterize the convective structures resulting from the heating. Scales are defined as follows:

Length scale: h - half channel height;

Velocity scales:

i) for Poiseuille flow: U_p = maximum x-velocity component of Poiseuille flow;

ii) for convective flow: $U_v = \nu/h$;

Temperature scales:

(i) conductive scale: T_d = amplitude of the temperature variations

ii) convective scale: $T_v = T_d \nu / \kappa$,

Pressure scales:

(i) for Poiseuille flow: $P_p = \rho U_p^2$,

(ii) for convective flow: $P_v = \rho U_v^2$,

Time scale: $t = d / U_v$.

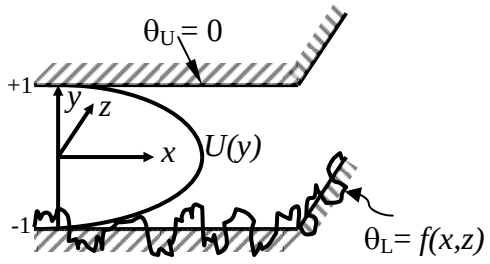

Figure B.1. Plane Poiseuille flow subject to a spatially distributed wall heating.

The resulting non-dimensional parameters are defined as follows:

$$\mathrm{Re} = \frac{U_p\, d}{\nu} = \frac{U_p}{U_v}, \qquad \mathrm{Pr} = \frac{\nu}{\kappa} = \frac{T_v}{T_d}, \qquad \mathrm{Ra} = \frac{g\gamma h^3 T_d}{\kappa\nu}$$

where Re stands for the Reynolds number, Pr denotes the Prandtl number and Ra stands for the Rayleigh number. In the above, ν is the kinematic viscosity, κ is the thermal

diffusivity, g stands for acceleration due to gravity, γ is the volumetric coefficient of expansion and ρ denotes the density of the fluid.

The velocity and pressure fields associated with the Poiseuille flow have the form

$$[u_0(y),\ 0,\ 0] = [1 - y^2,\ 0,\ 0],\ p_0(x,y,z,t) = -2x/\mathrm{Re}. \tag{B.2}$$

The flow quantities are assumed to have the following form

$$\left.\begin{aligned} u_2(x,y,z) &= \mathrm{Re}\, u_0(y) + u_1(x,y,z), \\ v_2(x,y,z) &= v_1(x,y,z), \\ \theta_2(x,y,z) &= \mathrm{Pr}^{-1}\theta_0(x,y,z) + \theta_1(x,y,z), \\ p_2(x,y,z) &= \mathrm{Re}^2\, p_0(x,y,z) + p_1(x,y,z) \end{aligned}\right\} \tag{B.3}$$

where subscript 1 denotes flow modifications due to the heating and θ_0 is the conduction temperature field defined as

$$\theta_0(x,y,z) = \theta_{0,\mathrm{uni}}(y) + \theta_{0,\mathrm{nun}}(x,y,z) \tag{B.4}$$

where $\theta_{0,\mathrm{uni}}$ stands for the part of the temperature field generated by the mean temperature difference between the channel walls, i.e.,

$$\theta_{o,\mathrm{uni}}(y) = (1-y)/2, \tag{B.5}$$

and $\theta_{0,\mathrm{nun}}$ stands for the spatially non-uniform part described by the following problem

$$\frac{\partial^2\theta_{0,\mathrm{nun}}}{\partial x^2} + \frac{\partial^2\theta_{0,\mathrm{nun}}}{\partial y^2} + \frac{\partial^2\theta_{0,\mathrm{nun}}}{\partial z^2} = 0 \tag{B.6}$$

subject to boundary conditions that can be deduced from (B.1). The solution is assumed to be in the form

$$\theta_{0,nun}(x,y,z)=\sum_{n=-\infty}^{n=+\infty}\sum_{m=-\infty}^{m=+\infty}\theta_{0,nun}^{(n,m)}(y)e^{i(n\alpha x+m\mu z)}$$

which leads to the analytical expression in the form

$$\theta_{o,nun}(x,y,z)=\sum_{\substack{n=-\infty\\ n\neq 0}}^{n=+\infty}\sum_{\substack{m=-\infty\\ m\neq 0}}^{m=+\infty}\left[\frac{-\theta_L^{(n,m)}}{2\sinh(k_{n,m})}\sinh(k_{n,m}y)+\frac{\theta_L^{(n,m)}}{2\cosh(k_{n,m})}\cosh(k_{n,m}y)\right]e^{i(n\alpha x+m\mu z)} \tag{B.7}$$

where $k_{n,m}^2=n^2\alpha^2+m^2\mu^2$.

Flow quantities represented by Eq. (B.3) are substituted into the three-dimensional Navier-Stokes, continuity and energy equations resulting in the following form of the governing equations,

$$\frac{\partial v_1}{\partial y}+\frac{\partial w_1}{\partial z}=0, \tag{B.8}$$

$$(Re\,u_0+u_1)\frac{\partial u_1}{\partial x}+Re\,v_1\frac{\partial u_0}{\partial y}+v_1\frac{\partial u_1}{\partial y}+w_1\frac{\partial u_1}{\partial z}=-\frac{\partial p_1}{\partial x}+\nabla^2 u_1, \tag{B.9}$$

$$(Re\,u_0+u_1)\frac{\partial v_1}{\partial x}+v_1\frac{\partial v_1}{\partial y}+w_1\frac{\partial v_1}{\partial z}=-\frac{\partial p_1}{\partial y}+\nabla^2 v_1+Ra\left(Pr^{-1}\theta_0+\theta_1\right), \tag{B.10}$$

$$(Re\,u_0+u_1)\frac{\partial w_1}{\partial x}+v_1\frac{\partial w_1}{\partial y}+w_1\frac{\partial w_1}{\partial z}=-\frac{\partial p_1}{\partial z}+\nabla^2 w_1, \tag{B.11}$$

$$(Re\,u_0+u_1)\left(Pr^{-1}\frac{\partial\theta_0}{\partial x}+\frac{\partial\theta_1}{\partial x}\right)+v_1\left(Pr^{-1}\frac{\partial\theta_0}{\partial y}+\frac{\partial\theta_1}{\partial y}\right)+w_1\left(Pr^{-1}\frac{\partial\theta_0}{\partial z}+\frac{\partial\theta_1}{\partial z}\right)=Pr^{-1}\left(\nabla^2\theta_1\right). \tag{B.12}$$

To eliminate pressure from the momentum equations, the governing equations have been expressed in terms of the wall-normal vorticity ($\zeta=\partial u_1/\partial z-\partial w_1/\partial x$), the wall-normal

velocity and the temperature (Kim et al. 1987), resulting in a form suitable for computations, i.e.,

wall-normal vorticity (ζ) equation:

$$\frac{\partial \zeta}{\partial t} = \nabla^2 \zeta - \mathrm{Re}\, u_0 \frac{\partial \eta}{\partial x} - \mathrm{Re} \frac{du_0}{dy} \frac{\partial v}{\partial z} + N_\zeta \ , \tag{B.13}$$

wall-normal velocity (v) equation:

$$\frac{\partial}{\partial t}\left(\nabla^2 v_1\right) = \nabla^2\left(\nabla^2 v_1\right) - \mathrm{Re}\, u_0 \frac{\partial}{\partial x}\left(\nabla^2 v_1\right) + \mathrm{Re} \frac{\partial^2 u_0}{\partial y^2} \frac{\partial v_1}{\partial x} + \mathrm{Ra}\left(\frac{\partial^2}{\partial x^2} + \frac{\partial^2}{\partial z^2}\right)\left(\mathrm{Pr}^{-1} \theta_0 + \theta_1\right) + N_v \ , \tag{B.14}$$

energy equation:

$$\frac{\partial \theta_1}{\partial t} = \mathrm{Pr}^{-1}\left(\nabla^2 \theta_1\right) - \mathrm{Re}\, u_0 \left(\mathrm{Pr}^{-1} \frac{\partial \theta_0}{\partial x} + \frac{\partial \theta_1}{\partial x} \right) - \mathrm{Pr}^{-1} N_{\theta_0} - N_{\theta_1} . \tag{B.15}$$

In the above, N_ζ, N_v, N_{θ_0} and N_{θ_1} are defined as,

$$N_\zeta = \frac{\partial H_w}{\partial x} - \frac{\partial H_u}{\partial z},$$

$$N_v = \frac{\partial}{\partial y}\left(\frac{\partial H_u}{\partial x} + \frac{\partial H_w}{\partial z} \right) - \left(\frac{\partial^2}{\partial x^2} + \frac{\partial^2}{\partial z^2} \right) H_v ,$$

$$N_{\theta 0} = u_1 \frac{\partial \theta_0}{\partial x} + v_1 \frac{\partial \theta_0}{\partial y} + w_1 \frac{\partial \theta_0}{\partial z}, \ N_{\theta 1} = u_1 \frac{\partial \theta_1}{\partial x} + v_1 \frac{\partial \theta_1}{\partial y} + w_1 \frac{\partial \theta_1}{\partial z},$$

where,

$$H_u = \frac{\partial}{\partial x} < u_1 u_1 > + \frac{\partial}{\partial y} < u_1 v_1 > + \frac{\partial}{\partial z} < u_1 w_1 >$$

$$H_v = \frac{\partial}{\partial x} < u_1 v_1 > + \frac{\partial}{\partial y} < v_1 v_1 > + \frac{\partial}{\partial z} < v_1 w_1 >$$

$$H_w = \frac{\partial}{\partial x} < u_1 w_1 > + \frac{\partial}{\partial y} < v_1 w_1 > + \frac{\partial}{\partial z} < w_1 w_1 > .$$

Here the special symbol '<..>' is used to represent the product terms of the flow quantities (u_1, v_1, w_1 and θ_1).

Method of solution

The unknowns are assumed in the form of Fourier expansions

$$\zeta(x,y,z,t) = \sum_{n=-\infty}^{n=+\infty}\sum_{m=-\infty}^{m=+\infty} \zeta^{(n,m)}(y,t)\, e^{i(\alpha n x + \mu m z)} \quad ,$$

$$v_1(x,y,z,t) = \sum_{n=-\infty}^{n=+\infty}\sum_{m=-\infty}^{m=+\infty} v_1{}^{(n,m)}(y,t)\, e^{i(\alpha n x + \mu m z)} \quad ,$$

$$\theta_1(x,y,z,t) = \sum_{n=-\infty}^{n=+\infty}\sum_{m=-\infty}^{m=+\infty} \theta_1{}^{(n,m)}(y,t)\, e^{i(\alpha n x + \mu m z)} \quad .$$

Substitution of the above expansion into the governing equations and separation of Fourier modes lead to the following system of modal equations:

wall-normal vorticity (ζ) equation:

$$\frac{\partial}{\partial t}\zeta^{(n,m)} = \left(D_{n,m} - in\alpha\, Re\, u_0\right)\zeta^{(n,m)} - im\mu\, Re \frac{du_0}{dy} v_1{}^{(n,m)} + N_\zeta^{(n,m)}, \tag{B.16}$$

wall-normal velocity (v) equation:

$$\frac{\partial}{\partial t} D_{n,m} v_1{}^{(n,m)} = \left[D_{n,m}^2 + in\alpha\, Re\left(-u_0 D_{n,m} + \frac{d^2 u_0}{dy^2} \right) \right] v_1{}^{(n,m)} - k_{n,m}^2 Ra\left(Pr^{-1}\theta_0^{(n,m)} + \theta_1^{(n,m)} \right) + N_v^{(n,m)}, \tag{B.17}$$

energy equation:

$$\frac{\partial}{\partial t}\theta_1^{(n,m)} = Pr^{-1} D_{n,m}\theta_1{}^{(n,m)} - in\alpha\, Re\, u_0 \left(Pr^{-1}\theta_0^{(n,m)} + \theta_1^{(n,m)} \right) - Pr^{-1} N_{\theta_0}^{(n,m)} - N_{\theta_1}^{(n,m)} \tag{B.18}$$

where $D_{n,m} = d^2/dy^2 - k_{n,m}^2$, $D = d/dy$,

$$N_{\zeta}^{(n,m)} = in\alpha H_{w}^{(n,m)} - im\mu H_{u}^{(n,m)},$$

$$N_{v}^{(n,m)} = iD\left(n\alpha H_{u}^{(n,m)} + m\mu H_{w}^{(n,m)}\right) + k_{n,m}^{2} H_{v}^{(n,m)},$$

$$N_{\theta_0}^{(n,m)} = in\alpha < u_1\theta_0 >^{(n,m)} + D < v_1\theta_0 >^{(n,m)} + im\mu < w_1\theta_0 >^{(n,m)},$$

$$N_{\theta_1}^{(n,m)} = in\alpha < u_1\theta_1 >^{(n,m)} + D < v_1\theta_1 >^{(n,m)} + im\mu < w_1\theta_1 >^{(n,m)}$$

$$H_{u}^{(n,m)} = in\alpha < u_1u_1 >^{(n,m)} + D < u_1v_1 >^{(n,m)} + im\mu < u_1w_1 >^{(n,m)},$$

$$H_{v}^{(n,m)} = in\alpha < u_1v_1 >^{(n,m)} + D < v_1v_1 >^{(n,m)} + im\mu < v_1w_1 >^{(n,m)},$$

$$H_{w}^{(n,m)} = in\alpha < u_1w_1 >^{(n,m)} + D < v_1w_1 >^{(n,m)} + im\mu < w_1w_1 >^{(n,m)}.$$

Various terms present in (B.13-B.15) have been replaced by their Fourier expansions in the form

$$N(x,y,z,t) = \sum_{n=-\infty}^{n=+\infty} \sum_{m=-\infty}^{m=+\infty} N^{(n,m)}(y,t) e^{i(\alpha nx + \mu mz)}$$

where N stands for N_{ζ}, N_{v}, N_{θ_0} and N_{θ_1}.

The modal functions ${u_1}^{(n,m)}$ and ${w_1}^{(n,m)}$ for velocity components can be computed as

$${u_1}^{(n,m)} = k_{n,m}^{-2}\left(in\alpha D\,{v_1}^{(n,m)} - im\mu\zeta^{(n,m)}\right),$$

$${w_1}^{(n,m)} = k_{n,m}^{-2}\left(im\mu D{v_1}^{(n,m)} + in\alpha\zeta^{(n,m)}\right).$$

The reader may note that the aforementioned two relations are valid for n ≠0, m ≠0 and special relations are needed for the mode (0,0). Equations for mode (0,0) have been derived from equations (B.8-B.12) and have the following form in the Fourier space

$$\frac{1}{\mathrm{Re}} D^2(u_{00}) + v_{00} D(u_0) + Nu_{00} = -A_p \ , \tag{B.19a}$$

$$v_{00} = 0 \ , \tag{B.19b}$$

$$w_{00} = 0 \ , \tag{B.19c}$$

$$\frac{1}{\mathrm{Re\,Pr}} D^2(\theta_{00}) + N\theta_{00} = 0 \tag{B.19d}$$

where A_p is the streamwise pressure gradient induced by the heating, and Nu_{00} and $N\theta_{00}$ are the respective nonlinear terms associated with the mode (0,0).

Equations (B.16-B.18) are subject to the no-slip and no-penetration conditions at both walls. The no-slip boundary conditions translate into $\zeta^{(n,m)} = 0$ and $Dv_1^{(n,m)} = 0$ to be imposed at the walls. No-penetration condition translates into $v_1^{(n,m)} = 0$ to be imposed at both walls. The boundary condition for temperature is simply $\theta_1^{(n,m)} = 0$ at both walls.

Appendix-C

General Three-Dimensional Stability Equation

In the case of a three-dimensional primary convection described in Appendix B, the disturbances have the form

$$\bar{v}_3(x,y,z,t)=\sum_{q=-\infty}^{q=+\infty}\sum_{p=-\infty}^{p=+\infty}\left[g_u^{(p,q)}(y),g_v^{(p,q)}(y),g_w^{(p,q)}(y)\right]e^{i[(\delta+p\alpha)x+(\beta+q\mu)z-\sigma t]}+\text{c.c.}\ , \tag{C.1a}$$

$$\theta_3(x,y,z,t)=\sum_{q=-\infty}^{q=+\infty}\sum_{p=-\infty}^{p=+\infty}\left[g_\theta^{(p,q)}(y)\right]e^{i[(\delta+p\alpha)x+(\beta+q\mu)z-\sigma t]}+\text{c.c.}\ . \tag{C.1b}$$

The disturbance equations (3.14) become

$$A^{(p,q)}\xi^{(p,q)}=\sum_{n=-\infty}^{n=+\infty}\sum_{m=-\infty}^{m=+\infty}\left[H_\xi^{(p-n,q-m)}\xi^{(p-n,q-m)}+H_v^{(p-n,q-m)}g_v^{(p-n,q-m)}\right], \tag{C.2a}$$

$$B^{(p,q)}g_v^{(p,q)}-Rak_{p,q}^2g_\theta^{(p,q)}=-\sum_{n=-\infty}^{n=+\infty}\sum_{m=-\infty}^{m=+\infty}\left[I_\xi^{(p-n,q-m)}\xi^{(p-n,q-m)}+I_v^{(p-n,q-m)}g_v^{(p-n,q-m)}\right]\ , \tag{C.2b}$$

$$it_pg_u^{(p,q)}+Dg_v^{(p,q)}+it_qg_w^{(p,q)}=0, \tag{C.2c}$$

$$C^{(p,q)}g_\theta^{(p,q)}=Pr\sum_{n=-\infty}^{n=+\infty}\sum_{m=-\infty}^{m=+\infty}\left[\begin{matrix}J_\xi^{(p-n,q-m)}\xi^{(p-n,q-m)}+J_v^{(p-n,q-m)}g_v^{(p-n,q-m)}\\+J_\theta^{(p-n,q-m)}g_\theta^{(p-n,q-m)}\end{matrix}\right] \tag{C.2d}$$

where $A^{(p,q)}=D^2-k_{p,q}^2+i\sigma$, $B^{(p,q)}=\left(D^2-k_{p,q}^2\right)^2+i\sigma\left(D^2-k_{p,q}^2\right)$,

$C^{(p,q)}=D^2-k_{p,q}^2+i\,Pr\,\sigma$,

$\xi^{(p,q)}=t_pg_w^{(p,q)}-t_qg_u^{(p,q)}$,

$t_p=\delta+p\alpha$, $t_q=\beta+q\mu$, $k_{p,q}^2=t_p^2+t_q^2$,

$$
\begin{aligned}
H_{\xi}^{(p-n,q-m)} &= i\left[t_p F_u^{(n,m)} + t_q F_w^{(n,m)}\right] + k_{p-n,q-m}^{-2}\left(t_p t_{q-m} + t_q t_{p-n}\right)\left[in\alpha F_w^{(n,m)} - im\mu F_u^{(n,m)}\right] \\
&\quad + \left[1 + k_{p-n,q-m}^{-2}\left(n\alpha t_{p-n} - m\mu t_{q-m}\right)\right] F_v^{(n,m)} D \\
H_v^{(p-n,q-m)} &= \left[-t_q D F_u^{(n,m)} + t_p D F_w^{(n,m)}\right] \\
&\quad + k_{p-n,q-m}^{-2}\left(t_p t_{p-n} - t_q t_{q-m}\right)\left[n\alpha F_w^{(n,m)} - m\mu F_u^{(n,m)}\right] D, \\
&\quad + k_{p-n,q-m}^{-2}\left(in\alpha t_{q-m} + im\mu t_{p-n}\right) F_v^{(n,m)} D^2 \\
I_v^{(p-n,q-m)} &= i\, k_{p-n,q-m}^{-2}\left[n\alpha\left(t_q t_{q-m} - t_p t_{p-n}\right) - 2m\mu t_p t_{q-m}\right] D F_u^{(n,m)} D \\
&\quad + i\, k_{p-n,q-m}^{-2}\left[m\mu\left(t_p t_{p-n} - t_q t_{q-m}\right) - 2n\alpha t_q t_{p-n}\right] D F_w^{(n,m)} D \\
&\quad + k_{p,q}^2\, k_{p-n,q-m}^{-2}\left[t_{p-n} t_{p-2n} - t_{q-m} t_{q-2m}\right] F_v^{(n,m)} D \\
&\quad + i\, k_{p-n,q-m}^{-2}\left[-t_p k_{p-n,q-m}^2 + 2n\alpha t_q t_{q-m} - 2m\mu t_p t_{q-m}\right] D F_u^{(n,m)} D^2, \\
&\quad + i\, k_{p-n,q-m}^{-2}\left[-t_r k_{p-n,q-m}^2 + 2m\mu t_p t_{p-n} - 2n\alpha t_q t_{p-n}\right] D F_w^{(n,m)} D^2 \\
&\quad - k_{p-n,q-m}^{-2}\left[t_p t_{p-n} + t_q t_{q-m}\right] F_v^{(n,m)} D^3 \\
&\quad + ik_{p,q}^2\left[t_{p-2n} F_u^{(n,m)} + t_{q-2m} F_w^{(n,m)}\right] + it_p D^2 F_u^{(n,m)} + it_q D^2 F_w^{(n,m)} \\
I_{\xi}^{(p-n,q-m)} &= k_{m-n}^{-2}\left\{\left(t_p t_{q-2m} - t_q t_{p-2n}\right)\left[t_{p-n} F_u^{(n,m)} + t_{q-m} F_w^{(n,m)}\right] D\right. \\
&\quad + \left(n\alpha t_q - m\mu t_p\right)\left[\left(t_p + t_{p-n}\right) D F_u^{(n,m)} + \left(t_q + t_{q-m}\right) D F_w^{(n,m)}\right], \\
&\quad \left. + ik_{p,q}^2\left(-n\alpha t_{q-m} + m\mu t_{p-n}\right) F_v^{(n,m)} + i\left(-t_p t_{q-m} + t_q t_{p-n}\right) F_v^{(n,m)} D^2\right] \\
J_{\xi}^{(p-n,q-m)} &= ik_{p-n,q-m}^{-2}\left(-n\alpha t_{q-m} + m\mu t_{p-n}\right) F_{\theta}^{(n,m)}, \\
J_v^{(p-n,q-m)} &= -k_{p-n,q-m}^{-2}\left(n\alpha t_{p-n} + m\mu t_{q-m}\right) F_{\theta}^{(n,m)} D + D F_{\theta}^{(n,m)}, \\
J_{\theta}^{(p-n,q-m)} &= it_{p-n} F_u^{(n,m)} + F_v^{(n,m)} D + it_{q-m} F_w^{(n,m)}.
\end{aligned}
$$

The boundary conditions (3.15) take the form

$$\xi^{(n,m)}(\pm 1) = 0,\ g_v^{(n,m)}(\pm 1) = 0,\ Dg_v^{(n,m)}(\pm 1) = 0,\ g_{\theta}^{(n,m)}(\pm 1) = 0 \quad \text{for } -\infty<n<+\infty. \tag{C.3}$$

The required expressions for the basic state (3.16) have the form

$$\bar{v}_2(x,y,z) = \sum_{n=-\infty}^{n=+\infty}\sum_{m=-\infty}^{m=+\infty}\left[F_u^{(n,m)}(y), F_v^{(n,m)}(y), F_w^{(n,m)}(y)\right] e^{in\alpha x + im\mu z}, \tag{C.4a}$$

$$\theta_2(x,y,z) = \sum_{n=-\infty}^{n=+\infty}\sum_{m=-\infty}^{m=+\infty} F_{\theta}^{(n,m)}(y) e^{in\alpha x + im\mu z}. \tag{C.4b}$$

Appendix-D

This appendix describes the classical Newton-Raphson and the 'inverse iteration' methods that are used to evaluate a single eigenvalue as discussed in Section (3.3). It also describes the Newton-Raphson search method used for eigenvalue tracing.

D.1 Newton-Raphson search method

To solve the homogeneous system (3.14) together with the boundary conditions (3.15), let us take an initial guess of the eigenvalue σ_a. Since all of the boundary conditions are homogeneous, we alter one of the boundary conditions to a non-zero value, for example, we alter the original boundary condition

$$BC(\sigma) = Dg_v^{(n)}(-1) = 0 \qquad \text{to} \qquad D^2 g_v^{(n)}(-1) = 1. \qquad \text{(D.1a-b)}$$

Now the system (3.14) with the new boundary condition becomes non-homogeneous and can be solved directly. Our goal is to search iteratively for the correct value of σ so that the original boundary condition is satisfied. We use the Newton-Raphson method for this purpose. A suitable relaxation factor (σ_{relax}) is used to guarantee convergence.

The following form of the Newton-Raphson search procedure has been used for computing the eigenvalue,

START: assume, $\sigma_0 = \sigma_a$, $\sigma_0^{step} = S_1\sigma_0$, $\sigma_{relax} = S_2|\sigma_0|$

where S_1, and S_2 are small percentages of σ_0, usually (S_2<S_1).

Solve the system using σ_0, and store the value of boundary condition as BC_0

Compute $\sigma_1 = \sigma_0 + \sigma_0^{step}$.

REPEAT for k=1,2,3… UNTILL $BC_k < \varepsilon$ (here, ε is the tolerance in BC)

1) Solve the system with σ_k , and store the value of boundary condition as BC_k

2) Compute $\sigma_k^{step} = -\dfrac{BC_k\, \sigma_{k-1}^{step}}{BC_k - BC_{k-1}}$

3) If $\left|\sigma_k^{step}\right| > \left|\sigma_{relax}\right|$ then,

$\sigma_k^{step} = \sigma_{relax}\, \sigma_k^{step}$.

End if

4) Compute $\sigma_{k+1} = \sigma_k + \sigma_k^{step}$.

END.

D.2 Inverse Iteration method

In this work, the following form of the Inverse Iteration Method has been used:

START: λ_0 – initial approximation of an eigenvalue

$\mathbf{z}_0$ – initial approximation of an eigenvector

$p_0 = 0$

REPEAPT for k = 0, 1, 2,…

1) Solve $(\mathbf{A} - \sigma_0 \mathbf{B})\mathbf{w}_{\mathbf{k}+1} = \mathbf{B}\,\mathbf{z}_{\mathbf{k}}$

2) Compute $p_{k+1} = \langle \mathbf{w}_{\mathbf{k}+1}, \mathbf{z}_{\mathbf{k}} \rangle^{-1}$

3) If $|p_{k+1} - p_k| > \varepsilon$, then

normalize $\mathbf{z}_{\mathbf{k}+1} = \mathbf{w}_{\mathbf{k}+1} / \|\mathbf{w}_{\mathbf{k}+1}\|_2$

go to step 1

Else

compute the eigenvalue $\sigma = \sigma_0 + p_{k+1}$

compute the normalized eigenvector $\mathbf{z} = \mathbf{w}_{\mathbf{k}+1} / \|\mathbf{w}_{\mathbf{k}+1}\|_2$

STOP

End If

END.

D.3 Eigenvalue tracing

To trace the eigenvalue in the parameter space we use the multidimensional Newton-Raphson method. We use several combinations of parameters for the eigenvalue tracing. Here we show one example, iteration on the Rayleigh number Ra and the real part of the eigenvalue σ_r keeping the imaginary part of the eigenvalue σ_i constant. For this case, the boundary condition function (D.1a) becomes

$$BC(\sigma_r, Ra) = f = 0 .$$

Taking the total derivative one obtains

$$\Delta f = \left(\frac{\partial f}{\partial Ra}\right)\Delta Ra + \left(\frac{\partial f}{\partial \sigma_r}\right)\Delta\sigma_r .$$

Let us assume $\Delta f = f_1 + if_2$, $\frac{\partial f}{\partial Ra} = r_1 + ir_2$, $\frac{\partial f}{\partial \sigma_r} = \sigma_1 + i\sigma_2$

$$f_1 + if_2 = (r_1 + ir_2)\Delta Ra + (\sigma_1 + i\sigma_2)\Delta\sigma_r .$$

Separating the real and imaginary part, one obtains

$$f_1 = r_1\Delta Ra + \sigma_1\Delta\sigma_r ,$$
$$f_2 = r_2\Delta Ra + \sigma_2\Delta\sigma_r .$$

Solving the above two equations, one obtains

$$\Delta Ra = \frac{\sigma_1 f_2 - \sigma_2 f_1}{\sigma_1 r_2 - \sigma_2 r_1},$$

$$\Delta\sigma_r = \frac{r_2 f_1 - r_1 f_2}{\sigma_1 r_2 - \sigma_2 r_1} .$$

Appendix-E

Numerical Accuracy

This appendix describes testing of the numerical accuracy of solution processes used in this dissertation. The numerical accuracy of the primary convection and the secondary convection are discussed in Section E.1 and E.2, respectively.

E.1 The primary convection

Various quantities of the primary convection (Chapter 2) are obtained by using three different types of numerical solvers, i.e. (i) finite difference-complex notation (Section 2.3.1), (ii) finite difference-real notation (Section 2.3.2), and (iii) spectral complex notation (Section 2.3.3). Results from each of the solvers are matched. All of the solvers give the same accuracy (the error bounds are set at 10^{-6}). Some of the critical points were tested with error bounds 10^{-10} and no significant changes in flow and temperature field were observed.

Certain cases have been computed using the finite-volume discretization method applied to the governing equations expressed in terms of primitive variables (see equation 2.5) as implemented in the FLUENT commercial software package. Use of this method was limited due to its cost and the need to change grid structure (and repeat grid convergence tests) whenever wave number of heating has been altered. The cost of this method was higher by at least 0(100) as compared with the other methods discussed above.

For large wavelength heating (Section 2.4.2) an analytical solution (see equation 2.31) using asymptotic expansion has been obtained. This analytical solution well agrees with the solution obtained numerically at small values of the heating wave number α.

E.2 Secondary convection

Results of numerical tests presented in Tables E.1-E.3 assist in identifying the correct values of various numerical parameters to be used in the computations. It is evident that the primary convection determined using $N_M = 14$ Fourier modes with the error bounds in the primary convection solver set at 10^{-6} permits determination of eigenvalues for the secondary convection with accuracy no worse than four digits using $N_T = 51$ Chebyshev collocation points and the same number $N_M = 14$ Fourier modes used for discretization of the disturbance equations.

a)	Number of Fourier modes used to represent disturbance field	Number of Fourier modes used in the solution of the primary convection (error bounds in the solver set at 10^{-6})			
		8	11	14	17
	8	0.4821714	0.4822135	0.4822138	0.4822139
	11	0.4820305	0.4820344	0.4820354	0.4820361
	14	0.4820282	0.4820327	0.4820333	0.4820333
	17	0.4820282	0.4820321	0.4820335	0.4820329

b)	Number of Chebyshev collocation points	21	31	41	51	61
	σ_i	0.4820290	0.4820308	0.4820335	0.4820333	0.4820336

Table E.1: Disturbance amplification rate σ_i for α=2.1, δ=1.05, β=0.66, Ra=6000 obtained using (a) number of Chebyshev collocation points N_T=51, and (b) number of Fourier modes N_M=14 to represent both the primary convection and the disturbance field. The primary convection has been obtained with the convergence criterion set at 10^{-6}.

a)	Number of Fourier modes used to represent disturbance field	Number of Fourier modes used in the solution of the primary convection (error bounds in the solver set at 10^{-5})			
		8	11	14	17
	8	0.4821684	0.4822083	0.4822087	0.4822086
	11	0.4820275	0.4820293	0.4820299	0.4820294
	14	0.4820255	0.4820271	0.4820271	0.4820276
	17	0.4820248	0.4820271	0.4820276	0.4820275

b)	Number of Chebyshev collocation points	21	31	41	51	61
	σ_i	0.4820234	0.4820277	0.4820277	0.4820271	0.4820293

Table E.2: Disturbance amplification rate σ_i for α=2.1, δ=1.05, β=0.66, Ra=6000 obtained using (a) number of Chebyshev collocation points N_T=51, and (b) number of Fourier modes N_M=14 to represent both the primary convection and the disturbance field. The primary convection has been obtained with the convergence criterion set at 10^{-5}.

a)	Number of Fourier modes used to represent disturbance field	Number of Fourier modes used in the solution of the primary convection (error bounds in the solver set at 10^{-7})			
		8	11	14	17
	8	0.4821723	0.4822124	0.4822127	0.4822132
	11	0.4820316	0.4820332	0.4820344	0.4820337
	14	0.4820300	0.4820312	0.4820321	0.4820320
	17	0.4820300	0.4820316	0.4820322	0.4820319

b)	Number of Chebyshev collocation points	21	31	41	51	61
	σ_i	0.4820276	0.4820322	0.4820321	0.4820321	0.4820339

Table E.3: Disturbance amplification rate σ_i for α=2.1, δ=1.05, β=0.66, Ra=6000 obtained using (a) number of Chebyshev collocation points N_T=51, and (b) number of Fourier modes N_M=14 to represent both the primary convection and the disturbance field. The primary convection has been obtained with the convergence criterion set at 10^{-7}.

It is noted that the numerical accuracy presented in the Tables E.1-E.3 are well suited for the heating wave numbers $\alpha \leq 1$. Below this limit one has to increase the number of Fourier modes for the determination of the primary convection, and hence the secondary convection, to get the desired accuracy. Below we present short discussion of the numerical accuracy required for the computations in the case of the long wavelength heating.

Methods discussed in Section 2.3 are used for determination of stationary states in the case of long wavelength heating. The solution procedure uses Fourier expansions in the x-direction and either finite-difference or collocation discretization in the y-direction. The finite-difference scheme has automatic grid adjustment procedure build in to guarantee the desired level of accuracy and thus there is no need for further discussion of this method. The collocation method provides spectral accuracy and also does not require any further discussion. The convergence of the Fourier series represents a limiting factor and requires explanation. **Figure E.1** displays variations of kinetic energy associated with different Fourier modes as a function of the mode number. It can be seen that convergence of Fourier series (2.8) is very rapid (exponential) for heating wave numbers α=0.5 and 0.2. Reduction of the convergence rate for smaller α is clearly visible and is associated with the flow bifurcations and the need to resolve very small secondary flow structures. Computations require in excess of 100 modes for $\alpha < 0.03$ which places a practical limit on the analysis of secondary structures.

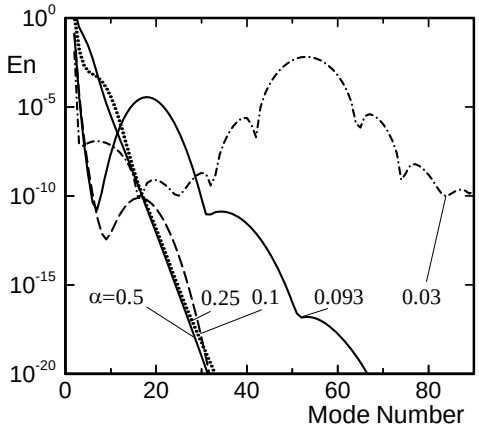

Figure E.1. *Variations of kinetic energy associated with different Fourier modes as a function of the mode number for fluids with the Prandtl number Pr=0.71 subject to heating with the Rayleigh number Ra=450.*

Appendix-F

This appendix describes derivation of the correlation (4.3) presented in Chapter 4.

From the primary convection in Chapter 2 the correlation (2.14) gives

$$Nu = 0.00192Ra/\alpha^3 \quad \text{as } \alpha\to\infty. \tag{F.1}$$

From the secondary convection in Chapter 4, the asymptotic relation (4.1) provides,

$$Ra_{cr} = 236\,\alpha^{1.5} \quad \text{as } \alpha\to\infty. \tag{F.2}$$

Thus, using (F.2) into (F.1) gives,

$$Nu = 0.00192*236/\alpha^{1.5} = 0.4531\alpha^{-1.5} \text{ along the critical curve as } \alpha\to\infty. \tag{F.3}$$

It may be noted that the asymptotic relation (F.3) is also obtained from the direct computation of the Nusselt number Nu for the primary convection along the critical curve as shown in **Figure 4.4**B.

We know that Nu defines the average temperature gradient in the vertical direction for the primary convection, i.e., we know how this gradient varies when $\alpha\to\infty$. We also know that thickness of the convection layer $h_v\to 0$ as $\alpha\to\infty$ (see relation (4.2c) and **Figure 4.4**B), which means that thickness of the conduction layer approaches 2 when $\alpha\to\infty$.

Our definition of the Rayleigh number is $Ra = \dfrac{\hat{g}\hat{\Gamma}\hat{h}^3\hat{T}_d}{\hat{\nu}\hat{\kappa}}$. Definition of the Rayleigh number used in the RB convection is $Ra_{uni} = \dfrac{\hat{g}\hat{\Gamma}\hat{H}^3\Delta\hat{T}}{\hat{\nu}\hat{\kappa}}$ where quantities with 'hat' are dimensional. Evaluation of ratio of both Rayleigh numbers gives

$$\frac{Ra}{Ra_{uni}} = \left(\frac{\hat{h}}{\hat{H}}\right)^3 \left(\frac{\hat{T}_d}{\Delta\hat{T}}\right)$$

$$\Rightarrow \qquad Ra = Ra_{uni}\left(\frac{\hat{T}_d}{\Delta\hat{T}}\right)\left(\frac{\hat{h}}{\hat{H}}\right)^3 = Ra_{uni}\left(\frac{\hat{T}_v}{Pr\,\Delta\hat{T}}\right)\left(\frac{\hat{h}}{\hat{H}}\right)^3 \qquad \text{note: } \frac{\hat{T}_v}{\hat{T}_d} = Pr$$

$$\Rightarrow \qquad Ra = Ra_{uni}\left(\frac{1}{Pr\,\Delta\theta}\right)\left(\frac{\hat{h}}{\hat{H}}\right)^3 \qquad \text{note: } \Delta\theta = \frac{\Delta\hat{T}}{\hat{T}_v}$$

$$\Rightarrow \qquad Ra = Ra_{uni}\left(\frac{2-h_v}{(2-h_v)Pr\,\Delta\theta}\right)\left(\frac{\hat{h}}{\hat{H}}\right)^3$$

$$\Rightarrow \qquad Ra = Ra_{uni}\left(\frac{1}{(2-h_v)Nu}\right)\left(\frac{\hat{h}}{\hat{H}}\right)^3 \qquad \text{as } Nu = Pr\frac{d\theta}{dy} \rightarrow Pr\frac{\Delta\theta}{2-h_v}$$

Since $h_v \rightarrow 0$, $\frac{\hat{h}}{\hat{H}} = \frac{1}{2}$, $Nu \rightarrow 0.4531\alpha^{-1.5}$, $Ra_{uni} = 1708$,

we obtain

$$Ra = 1708\left(\frac{\alpha^{1.5}}{2*0.4531}\right)\frac{1}{2^3} = 235.6\,\alpha^{1.5}.$$

Curriculum Vitae

Name: Mohammad Zakir Hossain

Post-secondary Education and Degrees:

B.Sc. in Mechanical Engineering (1999)
Bangladesh University of Engineering and Technology
Department of Mechanical Engineering
Dhaka, Bangladesh.

M.Sc. in Mechanical Engineering (2003)
Bangladesh University of Engineering and Technology
Department of Mechanical Engineering
Dhaka, Bangladesh.

Ph.D (2011)
The University of Western Ontario
Department of Mechanical and Materials Engineering
London, Ontario, Canada.

Publications (Journals):

Hossain, M. Z. and Floryan, J. M., "Natural Convection in a Fluid Subject to Periodic Heating". Submitted to Journal of Fluid Mechanics, Cambridge University Press.

Publications (Conference):

Hossain, M.Z. and Floryan, J.M, "Natural Convection in a Fluid Layer Subject to periodic Heating", accepted for *64th Annual Meeting of the APS Division of Fluid Dynamics*, to be held on November 20-22, 2011, Baltimore, MD, USA.

Asgarian, A., Hossain, M.Z. and Floryan, J.M., "Numerical Bifurcation Study of Natural Convection in a Layer of Fluid Subject to Spatially Distributed Heating", *International Conference on Applied Mathematics, Modeling & Computational Science (AMMCS-2011)*, July 25-29, Waterloo, Ontario, Canada.

Asgarian, A., Hossain, M.Z. and Floryan, J.M., "Rayleigh-Benard Convection and Thermal Bifurcation in a Fluid Layer Subject to a Long Wavelength Heating", Proceedings of the *19th Annual Conference of the CFD Society of Canada*, April 27-29, 2011, Montreal, Quebec, Canada.

Hossain, M.Z. and Floryan, J.M, "Natural Convection in a Slot Subject to a Spatially Distributed Heating", *Bulletin of the American Physical Society*, Vol-55, No-16, Nov. 2010, pp. 127.

Hossain, M.Z. and Floryan, J.M., "Convection Roll Instability due to Spatially Distributed Heating", Proceedings of the *Canadian Society for Mechanical Engineering Forum 2010*, June 7-9, 2010, Victoria, British Columbia, Canada.

Hossain, M.Z. and Floryan, J.M., "Roll Instability of a Stationary Fluid Exposed to Spatially Distributed Thermal Forcing", Proceedings of the *18th Annual Conference of the CFD Society of Canada*, May 17-19, 2010, London, Ontario, Canada.

Hossain, M.Z. and Floryan, J.M., "Instability of Flow in a Channel with Distributing Heating", *Proceedings of the 11th Pan-American Congress on Applied Mechanics*, Jan. 4-8, 2010, Foz du Iguacu, PR, Brazil.

Hossain, M.Z. and Floryan, J.M., "Thermal instability of Stationary Fluid Subject to Spatially Periodic Wall Heating", Book of Abstracts of *CAIMS 2009, Canadian Applied and Industrial Mathematics Society, June 10-14, 2009, London, Ontario, Canada.*

Hossain, M.Z. and Floryan, J.M., "Stability of Stationary Fluid Subject to Spatially Distributed Wall Heating", *Proceedings of the 17th Annual Conference of the CFD Society of Canada*, May 3-5, 2009, Ottawa, Ontario, Canada.

Floryan, J.M. and Hossain, M.Z., "Analysis of Stability of Channel Flow subject to Distributing Heating", *Bulletin of the American Physical Society* , Vol-53, No-15, Nov. 2008, pp. 250.

Hossain, M.Z. and Floryan, J.M., "Analysis of Stability of Channel Flow Subject to Distributing Heating", *Proceedings of the CSME Forum 2008*, June 5-8, Ottawa, Ontario, Canada.

Hossain, M.Z.; Fotia, M.L. and Floryan, J.M., "Direct Numerical Simulation of Channel Flow with Distributed Heating," *Proceedings of the 21st Canadian Congress of Applied Mechanics*, June 3-7, 2007, Toronto, Ontario, Canada.

Fotia, M.L.; Hossain, M.Z. and Floryan, J.M., "Thermal Instability of Poiseuille Flow Subjected to Spatially-Distributed Heating", *Proceedings of the 21st Canadian Congress of Applied Mechanics*, June 3-7, 2007, Toronto, Ontario, Canada.

Hossain, M.Z. and Floryan, J.M., "Direct Numerical Simulation of Flows Modulated by Distributed Heating", *Proceedings of the 15th Annual Conference of the CFD Society of Canada*, May 27-31, 2007, Toronto, Ontario, Canada.